3D studies of coarserning kinetics of individual grains

Poulsen, Stefan Othmar; Lauridsen, Erik Mejdal; Juul Jensen, Dorte

Publication date:
2012

Document Version
Publisher's PDF, also known as Version of record

Citation (APA):
Poulsen, S. O., Lauridsen, E. M., & Juul Jensen, D. (2012). 3D studies of coarserning kinetics of individual grains. Kgs. Lyngby: Department of Energy Conversion and Storage, Technical University of Denmark.

3D studies of coarsening kinetics of individual grains

Stefan Othmar Poulsen

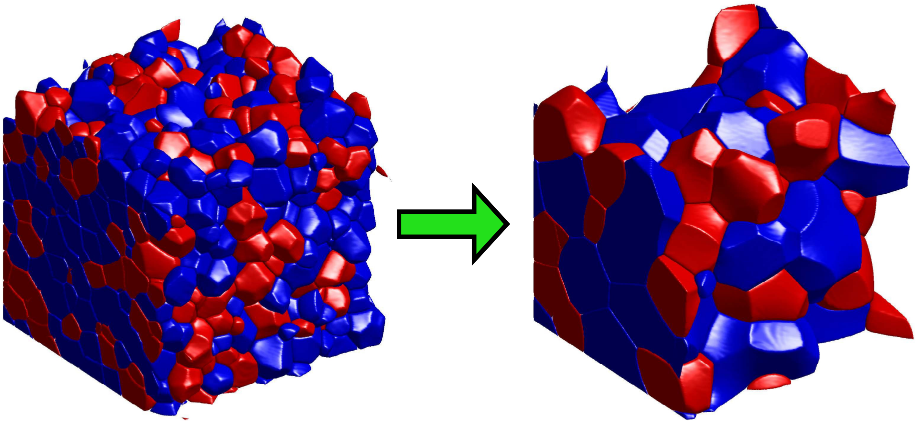

Roskilde 2011
RISØ-PHD-2011-87

Risø DTU
National Laboratory for Sustainable Energy

Cover: Simulated microstructural evolution of the grain structure of a 40/60 volume ratio dual-phase material by a phase-field model. Minority phase grains are red, and majority phase grains are blue. Some grains are not shown to reveal the internal grain structure.

Risø DTU
Materials Research Division
Building 228, DK-4000 Roskilde, Denmark
Phone +45 46775701, Fax +45 46775758
www.risoe.dtu.dk
RISØ-PHD-2011-87
ISBN 978-87-550-3950-6

Abstract

Techniques for fast, non-destructive characterization of the microstructure of materials using synchrotron X-ray radiation have in recent years become an important tool in materials science. The non-destructive nature of the techniques allows for time-resolved characterization of three-dimensional microstructures, i.e. direct probing of the evolution of *specific* microstructural features.

Synchrotron X-ray radiation techniques have in the present work been employed for experimental characterization of microstructural evolution in individual grains during isothermal annealing: For a study of individual grains during recrystallization, where the recrystallization kinetics of individual grains and the temperature dependence of the recrystallization rate is examined, and for a study of grain structure and grain growth, where growth predictions are put forth in terms of the grain size and topology of individual grains, and compared to the observed growth of a small number of grains.

A phase-field model has been developed and implemented efficiently for parallel execution on computer clusters for simulation of a third annealing phenomenon: Coupled grain growth and coarsening in polycrystalline, dual-phase materials, under phase ratio conserving conditions. This is used to investigate the microstructural evolution in a 50/50 volume ratio material and in a 40/60 volume ratio material by large-scale three-dimensional simulations, in both liquid/liquid and polycrystalline/polycrystalline states. These are used to make general predictions of the coarsening kinetics of polycrystalline, dual-phase materials, specifically the coarsening mechanism, steady state distributions of grain size and topology, and interface morphology.

Resumé

3D undersøgelser af individuelle korns vækst kinetik

Teknikker til hurtig, ikke-destruktiv karakterisering af materialers mikrostruktur ved hjælp af synkrotron Röntgen stråling er i de senere år blevet et vigtigt værktøj til materialeforskning. Disse teknikkers ikke-destruktive natur tillader tidsopløst karakterisering af tre-dimensionelle mikrostrukturer, dvs. direkte undersøgelser af *specifikke* mikrostrukturelle elementers tidsudvikling.

Synkrotron Röntgen strålingsteknikker er i dette Ph.D. projekt belevet anvendt til eksperimentel karakterisering af individuelle korns mikrostrukturelle udvikling under isoterm varmebehandling: Til en undersøgelse af rekrystallisation, hvor individuelle korns rekrystallisationskinetik og rekrystallisationsrates temperaturafhængighed blev undersøgt, og til en undersøgelse af kornstruktur og kornvækst, hvor vækstforudsigelser blev beregnet ud fra individuelle korns størrelser og topologi. Disse forudsigelser blev sammenlignet med vækst observeret i et lille antal korn.

En phase-field model blev udviklet og implementeret til effektiv afvikling på computer klynger til simulation af et tredie varmebehandlingsfænomen: Koblet kornvækst og coarsening (da: forgrovning) i polykrystallinske, to-fase materialer, under forhold der bevarer fasernes rumfang. Denne blev anvendt til undersøgelser af den mikrostrukturelle udvikling i materialer med fase forholdene 50/50 og 40/60 vha. tre-dimensionelle simulationer af materialer i både flydende/flydende og polykrystallinsk/polykrystallinsk tilstande. Disse blev brugt til at fremføre generelle forudsigelser om polykrystallinske to-fase materialers vækst kinetik, mere specifikt vækst mekanismen, fordelinger af kornstørrelser og topologi under dynamisk ligevægt, og fasegrænsemorfologi.

Preface

This thesis is submitted in partial fulfillment of the requirements for obtaining the Ph.D. degree at the Technical University of Denmark (DTU).

The research detailed within was carried out at the Materials Research Division (AFM) at Risø DTU, National Laboratory for Sustainable Energy.

The work was supervised by Erik Mejdal Lauridsen, and co-supervised by Dorte Juul Jensen, both from AFM at Risø DTU.

Funding was provided by Grundforskningsfonden. The Danish national research foundation.

Roskilde, November 2011

Stefan Othmar Poulsen

Papers included in the thesis

[B.1] S.O. Poulsen, E.M. Lauridsen, A. Lyckegaard, J. Oddershede, C. Gundlach, C. Curfs, and D. Juul Jensen. In situ measurements of growth rates and grain-averaged activation energies of individual grains during recrystallization of 50% cold-rolled aluminium. *Scripta Materialia* 64(11):1003–1006, 2011

[B.2] S.O. Poulsen, A. Lyckegaard, J. Oddershede, E.M. Lauridsen, C. Gundlach, C. Curfs, and D. Juul Jensen. Recrystallization kinetics of 50% cold-rolled aluminium. In N. Hansen, D. Juul Jensen, S.F. Nielsen, and B. Ralph, editors, *31st Risø International Symposium on Materials Science*, pages 391–397, 2010

[B.3] S.O. Poulsen, P.W. Voorhees, and E.M. Lauridsen Towards a phase field model of the microstructural evolution of duplex steel with experimental verification. Accepted for publication in *Proceedings of ReX&GG IV - 4th International Conference on Recrystallization and Grain Growth*

Following papers are based on work performed during the Ph.D. candidacy, but are not a direct basis for this thesis.

[B.4] L.K. Aagesen, A.E. Johnson, J.L. Fife, P.W. Voorhees, M.J. Miksis, S.O. Poulsen, E.M. Lauridsen, F. Marone, M. Stampanoni Universality and self-similarity in pinch-off of rods by bulk diffusion. *Nature Physics*, 6(10):796–800, 2010.

[B.5] L.K. Aagesen, A.E. Johnson, J.L. Fife, P.W. Voorhees, M.J. Miksis, S.O. Poulsen, E.M. Lauridsen, F. Marone, M. Stampanoni Pinch-off of rods by bulk diffusion *Acta Materialia*, 59(12):4922–4932, 2011.

Following papers are in preparation, and are therefore not included in the appendix

S.O. Poulsen, P.W. Voorhees, E.M. Lauridsen Three-dimensional simulations of microstructural evolution in polycrystalline dual-phase materials with conserved volume ratios In preparation for submission to *Acta Materialia.*

S.O. Poulsen, E.M. Lauridsen, W. Ludwig, I.M. McKenna, R.W. Fonda, D. Juul Jensen Non-destructive observations of 3D grain topology and grain growth in β titanium In preparation for submission to *Scripta Materialia.*

I.M. McKenna, E.M. Lauridsen, S.O. Poulsen, W. Ludwig, P.W. Voorhees Grain growth in 4D: A comparison of simulation and experiment In preparation for submission to *Acta Materialia.*

Acknowledgements

I would like first and foremost to thank my two advisors Erik Mejdal Lauridsen and Dorte Juul Jensen, and to thank Peter W. Voorhees, in whose group at Northwestern University in Evanston, Illinois I was fortunate to spend six months. All three are thanked for their seemingly endless patience, and willingness to find time in their busy schedules for me, and my fumbling attempts at learning materials science. Their enthusiasm and guidance has been invaluable to me.

During my Ph.D. candidacy I have participated in a number of experiments at the European Synchrotron Radiation Facility (ESRF) and the Swiss Light Source (SLS). I would like to thank the staff and scientists at the respective beam lines, ID11 and ID19 at ESRF, and TOMCAT at SLS. In particular, I must thank Wolfgang Ludwig from ESRF for help and expertise. I am also grateful to the technicians at AFM without whom the experiments had been impossible.

Ian M. McKenna is thanked for many fruitful discussions on implementation and optimization of numeric simulations, and I am grateful to him and the rest of the Voorhees group for making me feel at home during my stay in Evanston.

Allan Lyckegaard is thanked for advice and discussions on various algorithms for data analysis.

Finally, I would like to thank the rest of the M4D group at Risø DTU for all the help, and the many scientific and not so scientific discussions during the least three years.

Contents

Chapter 1

Introduction

The microstructure of materials is known to affect a wide range of their properties: Strength, toughness, resistance to corrosion and fatigue, electric and magnetic susceptibility, to name a few. An understanding of the relationship between processing techniques and the resulting microstructure is therefore important for the development and understanding of materials with properties that are tailored towards specific purposes.

Knowledge of the true three-dimensional microstructure is recognized as important, as e.g. size and morphology of individual microstructural features may not be deduced from two-dimensional cross sections with stereological methods without introducing assumptions [1]. Three-dimensional characterization of bulk materials has historically been difficult, since most materials of interest are opaque to visible light. Serial sectioning provides a means of three-dimensional characterization through a series of two-dimensional characterizations: Layers of material is successively removed, followed by characterizations of the newly formed surfaces using whichever characterization technique is most appropriate for the problem at hand, such as e.g. optical microscopy or scanning electron microscopy (SEM), which may also be combined with electron back scatter diffraction (EBSD) microscopy. Serial sectioning has been automated with focused ion beam (FIB) microscopes [2] and with robotic setups, e.g. [3], and may thus characterize three-dimensional microstructures fast, and with high spatial resolution, but the techniques are inherently destructive.

Non-destructive three-dimensional characterization may be accomplished by neutron scattering experiments at a purpose-built nuclear reactor, or a spallation neutron source. Neutron scattering e.g. provides unique possibilities for characterization of magnetic [4], and biological [5] materials, but for microstructural investigations that require μm spatial resolutions, X-ray photons produced at a modern synchrotron light source may be a more appropriate tool [6]: The flux of X-ray photons can be orders of magnitude higher than the corresponding flux of neutrons, resulting in significantly faster characterization. Hard X-rays, here meaning photon energies $E \gtrsim 50$ keV, has appreciable penetration depths (e.g. 5 mm in steel, and considerably more in lighter materials [7]), and may therefore be employed to characterize the microstructure of samples of dimensions that are orders of magnitude larger than the typical size of microstructural features, which are typically measured in units of μm. The introduction of the dedicated three-dimensional X-ray diffraction (3DXRD) microscope at the European Synchrotron Radiation Facility (ESRF) as a joint venture with Risø National Laboratory in 2000 [8] provided a novel method for characterization of microstructural features of polycrystalline materials with μm resolution using synchrotron X-ray radiation. Since then, a number of X-ray techniques have been developed. Some of these methods provide direct insight into the morphology of individual microstructural features, while others must be coupled with tomographic reconstruction methods [9] to extract this knowledge.

The strength of non-destructive characterization is that it allows for the direct investigation of microstructural evolution. This is best appreciated in contrast with destructive characterization: Using destructive techniques, the usual experimental approach would be to prepare a number of samples identically, inducing varying degrees of microstructural evolution, and characterizing the samples. This means that insight into microstructural evolution must be inferred by comparing and contrasting characterizations of different samples, and so continuity is lost: When a microstructural feature of interest has been observed, no observations of how and from what that feature evolved may have been performed, and observations of how that feature would continue to evolve during continued microstructural evolution are likewise impossible. With non-destructive characterization techniques, the evolution of microstructural features of interest may be directly probed. If the data acquisition is sufficiently fast compared to the evolution of the microstructural features of interest, it may even be possible, i.e. if the experimental setup allows, to observe the evolution *in situ*.

Theoretical predictions of microstructural evolution is done with models, which are usually designed to reproduce certain experimentally observed behaviours. Models of the evolution of complex microstructures can only in the simplest cases be treated analytically. In general, the models must be solved iteratively by a computer. Simulations of three-dimensional microstructural evolution on mm length scales, and time scales sufficient for considerable microstructural evolution are computationally intensive. However, models where interactions between simulated microstructural elements are localized to some degree may be executed efficiently in parallel on computer clusters. As the computational power of computer clusters continue to increase, so does the feasible length and time scales of simulations, and in recent years, results from large-scale simulations of microstructural evolution on the mesoscale have become possible [7].

Non-destructive three-dimensional characterization of microstructures using synchrotron radiation, and large-scale simulations of microstructural evolution may each provide important insight in their own right. A combination of the two approaches, however, provide unique opportunities [7]: As the non-destructive nature of the techniques allows for characterization of the same sample at varying degrees of microstructural evolution, these experimental techniques may be used to generate initial conditions for large-scale simulations of microstructural evolution, and by comparison of simulated and experimentally determined microstructural evolution, the validity of the employed model may be gauged. Such a comparison also conceivably allows for tuning of those model parameters that are not directly related to measurable quantities, thereby increasing the correspondence between simulation output and the experimental characterization in an iterative manner. Furthermore, hypotheses regarding the physical mechanisms responsible for microstructural evolution may be examined, as these mechanism may often be included in models as seen fit, their relative importance varied, and simulation output compared to experimental characterizations. If the model is found to reproduce experimentally observed microstructural evolution with a high degree of fidelity, simulations may be used as guidance for future experiments.

1.1 Overview of this text

This text presents experimental synchrotron X-ray radiation methods for three-dimensional microstructural characterization. These are employed to study the evolution of individual grains during isothermal annealing due to different driving forces: During *recrystallization*, where new, almost defect-free grains nucleate and grow in a deformed matrix, driven by the energy stored plastically in the matrix during deformation [10], and during *grain growth*, where a fully recrystallized microstructure evolves by grain boundary migration to decrease the total interfacial area, driven by the energy stored in the grain boundaries [11].

Two experimental synchrotron X-ray methods were also employed to characterize the microstructural evolution of a dual-phase steel during isothermal annealing with conserved phase ratio. This microstructural evolution may be described as a combination of grain growth, i.e. migration of grain boundaries separating grains of same phase, and coarsening, which here is taken to be the reduction of interphase interfacial area through long-range diffusion of mass. This combination is sometimes referred to as *coupled grain growth and coarsening* in the literature, and this nomenclature shall be kept. The experimental characterizations were to be coupled to large-scale three-dimensional phase-field simulations of microstructural evolution, but this coupling could unfortunately not be achieved, as segmentation and reconstruction of the experimental data from one of the methods could not be accomplished satisfactorily. This is explained in further detail in chapter 5. The phase-field model was developed, implemented, and tested during the failed attempts at segmentation and reconstruction, and was found to reproduce the intended physical behaviour. It has therefore been employed to make more general predictions about coupled grain growth and coarsening in dual-phase materials with conserved phase ratios, without experimental verification.

This text is organized as follows:

Chapter 2 Synchrotron X-ray radiation for characterization of microstructure contains descriptions of four synchrotron radiation methods employed during this Ph.D. project, including sketches of the underlying physics. It is important to note that these methods have merely been employed, but not subjects of original research. *They are presented here for completeness.*

Chapter 3 Recrystallization kinetics in cold-rolled aluminium presents a time resolved *in situ* study of the recrystallization kinetics of individual grains in cold-rolled aluminium and the temperature dependence of the recrystallization rate of these by synchrotron X-ray radiation. The non-destructive nature of the characterization technique is crucial for examining the deviations from mean behaviour of individual grains, and for determining activation energies for recrystallization of individual grains. A simple model of recrystallization of a single grain is employed to support a hypothesis of the influence of the deformed microstructure on the observed recrystallization kinetics.

Chapter 4 Grain topology and grain growth in β titanium presents the application of a synchrotron X-ray radiation method to characterization of the grain structure of a titanium alloy. Growth predictions are put forth by application of the three-dimensional Von Neumann-Mullins equation presented by MacPherson and Srolovitz in 2007 [12], and these predictions are examined statistically in terms of topology and grain size. Grain growth was induced through an annealing step, and the grain structure characterized a second time. The observed growth of a small number of individual grains is compared to the theoretically predicted growth rate.

Chapter 5 Coupled grain growth and coarsening of dual-phase materials presents a phase-field model of coupled grain growth and coarsening in polycrystalline dual-phase materials with conserved phase fractions, along with details of the computer implementation. Results from four simulations with "artificial" initial conditions are presented: Two 50/50 volume ratio, and two 40/60 volume ratio simulations, one of each being in a liquid/liquid state, and the other of each being in a polycrystalline/polycrystalline state. The topology and morphology of the simulation output is examined.

It is on the work detailed in chapter 5 that the main emphasis of this text is placed.

CHAPTER 2

Synchrotron X-ray radiation for characterization of microstructure

---

A beam of X-rays from an insertion device at a synchrotron light source is with good approximation a cone with a very low angular divergence, typically < 0.1 mrad. The distance between the source (insertion device) and the sample stage may be very long, > 50 m, and the flux vastly higher than that which may be produced by current laboratory sources [13]. The X-ray energy may be varied substantially: At the materials science beamline ID11 at the European Synchrotron Radiation Facility (ESRF), the energy may be varied between 29 keV and 140 keV as of November 2011 [14], corresponding to wavelengths between 0.43 Å and 0.09 Å. This combination of a small beam size and the significant penetration power of the high energy, high flux X-rays makes this radiation well suited for several X-ray techniques for fast, non-destructive characterization of bulk microstructures.

A vast number of different X-ray methods and algorithms to extract microstructural information from the acquired data exist, and the development of new, as well as improvement on existing, techniques and algorithms are very active areas of research. This is not the focus of the present work. Rather, four known techniques have been employed for microstructural characterization of different

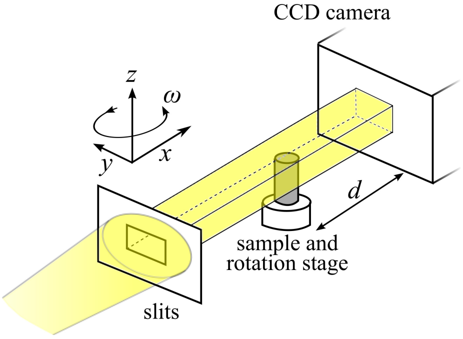

Figure 2.1: A schematic of the common experimental setups for microstructural characterization with hard X-rays employed in present work. The beam is directed along the x-axis. The sample-detector distance d may be varied.

systems. These will be described in the rest of this chapter. Complete treatments of the techniques and the underlying physics are impossible in the scope of this text. The reader is referred to [13] for a general introductory treatment of X-ray physics including synchrotron radiation, and to [15] for a comprehensive treatment of X-ray diffraction.

The four employed techniques have similar experimental setups: A sample is illuminated with hard X-rays, and two-dimensional images of the resulting intensity distribution are acquired with an area detector placed downstream from the sample and centered on the beam. A sketch of the common setup is shown in figure 2.1, where the coordinate system is indicated. The sample is then rotated a fixed angle about the vertical ω-axis, and another image is acquired (or alternatively, the image may be acquired during the rotation), and this is repeated for the desired angular range. The main difference between the experimental setups are the sample-detector distances. The images (or projections), are then used to reconstruct the microstructural features of interest in the sample through tomographic reconstruction algorithms for three of the four techniques. The current bottleneck for these methods is the spatial resolution of the detectors, which is around $\sim 0.5\ \mu$m [8].

The methods employed may be divided into two classes: Phase methods (note that "phase" is in reference to the phase of the X-ray wave) of section 2.1, which are sensitive to variations in electron density, and Bragg diffraction methods of section 2.2, which are sensitive to the crystallographic orientations in the sample. The two classes thus exploit different physical properties of the interaction of X-rays with matter. The application of these techniques to specific physical systems and results thereof are presented in the following chapters of this work.

Note that the time dependence of the X-ray wave function is unimportant for the present applications, and so will be suppressed in the following.

2.1 Phase methods

A propagating X-ray wave in the absence of Bragg diffraction may experience attenuation, phase shifts and refractions. These phenomena are conveniently described in terms of the complex refractive index n, which for X-rays are conventionally written as

$$n = 1 - \delta + i\beta \tag{2.1}$$

and $n = 1$ only in vacuum. The refractive index decrement δ may be expressed as [16]

$$\delta = \frac{r_0 N \lambda^2}{2\pi} \approx 1.3 \times 10^{-6} \rho \lambda^2 \tag{2.2}$$

where r_0 is the classical electron radius, N the electron density, and λ is the X-ray wavelength, which in the approximate expression must be specified in Å, and ρ is the density of the material specified in g/cm^3. This gives values of $\delta \approx 10^{-6} - 10^{-5}$ for typical materials, so the real part of n is always less than, but close to unity.

As a beam travels between domains of different refractive index, an angular deviation may occur, as described e.g. by Snell's law [17]. The refractive angular deviations in going from vacuum into a material at non-grazing conditions are typically of the order of δ [18], and the angular deviations experienced while travelling through a sample are typically even lower. All angular deviations will therefore be assumed sufficiently small so as to be unimportant during propagation through a sample. This assumption is argued to be justified up to sample sizes of $\sim$ 1 cm with X-ray wave lengths of 1 Å and a detector resolution of 1 μm in [18].

With the assumption of straight propagation through the sample, the X-ray wave exiting the sample in the plane $x = x_1$ may be related to the X-ray wave entering the sample in the plane $x = x_0$ by projection along the x-axis through the complex refractive index of the sample [17]

$$u_{\text{out}}(\mathbf{r}) = u_{\text{in}}(\mathbf{r}) \exp\left(i\Delta_0\right) \exp\left(-i\Delta(\mathbf{r})\right) \exp\left(-B(\mathbf{r})\right) \tag{2.3}$$

where $\mathbf{r} \equiv (y, z)$, $k \equiv 2\pi/\lambda$ is the wave number of the X-ray wave in vacuum, and

$$\Delta_0 \equiv \int_{x_0}^{x_1} k dx = k(x_1 - x_0) \tag{2.4a}$$

$$\Delta(\mathbf{r}) \equiv k \int_{x_0}^{x_1} \delta(x, \mathbf{r}) dx \tag{2.4b}$$

$$B(\mathbf{r}) \equiv k \int_{x_0}^{x_1} \beta(x, \mathbf{r}) dx \tag{2.4c}$$

are non-negative quantities. Δ_0 represents the phase shift the X-ray beam would have acquired by propagation in vacuum, Δ represents the deviation from the vacuum phase shift experienced by propagation through the sample, and B represents the attenuation of the beam. This linear relation is conveniently described in terms of a transmission function T, and so

$$u_{\text{out}}(\mathbf{r}) = T(\mathbf{r})\ u_{\text{in}}(\mathbf{r}) \tag{2.5}$$

An absorption projection, as is routinely performed for medical diagnostics, is determined by placing an area detector on the $x = x_1$ plane (or as close as possible, i.e. minimizing the sample-detector distance d). The detected intensity is given by the squared modulus of equation (2.3) (we will for brevity ignore physical constants of proportionality)

$$I_{d=0}(\mathbf{r}) = |u_{\text{out}}(\mathbf{r})|^2 = |u_{\text{in}}(\mathbf{r})|^2\, |T(\mathbf{r})|^2 = |u_{\text{in}}(\mathbf{r})|^2 \exp\big(-2B(\mathbf{r})\big) \tag{2.6}$$

whereby all information about the phase shift $\Delta(\mathbf{r})$ is seen to be lost. Absorption imaging may be adequate for many applications, e.g. where there is substantial difference in the absorption between the domains sought visualized. For e.g. weakly absorbing materials, and in biological systems where the deposition of a large dose of X-ray energy is unwanted, phase based methods may be used to advantage [19], and may also provide better resolution [18].

The phase information may be retrieved by letting the transmitted X-ray wave interfere with a reference wave in a Bonse-Hart type interferometer setup [19, 20] before acquiring projections of the intensity of the superposition of the two waves. The required experimental setup is however not trivial, and is susceptible to errors introduced by instabilities in the setup.

The present approaches instead rely on free space propagation of the transmitted beam. Assuming the sample dimensions are small compared to the sample-detector distance d, the wave in this plane, $u_d(\mathbf{r})$ is given by the Fresnel diffraction approximation integral [17]

$$u_d(\mathbf{r}) = -\frac{i}{\lambda d} \exp\left(i\frac{2\pi}{\lambda} d\right) \int u_{\text{out}}(\mathbf{r}') \exp\left(i\frac{\pi}{\lambda d} |\mathbf{r} - \mathbf{r}'|^2\right) d\mathbf{r}' \tag{2.7}$$

where the integration is performed over the x-plane. The approximation of the integrand is valid for those point pairs where [18]

$$\frac{\pi}{4\lambda} |\mathbf{r} - \mathbf{r}'|^4 \ll d^3 \tag{2.8}$$

As the integration of equation (2.7) is performed over all $\mathbf{r}'$, this criterion is not trivially fulfilled for all points, but by inspection of the integrand it is seen that the exponential function fluctuates rapidly when the magnitude of its argument "becomes large", thus largely cancelling out the contributions where the requirement (2.8) is invalid.

This observation also gives insight into the effect of varying the sample-detector distance d, since d scales the argument of the exponential function: The wave in the detector plane $u_d(\mathbf{r}_0)$ at some point $\mathbf{r}_0$ will be dominated by the values of the wave transmitted through the sample, $u_{\text{out}}(\mathbf{r})$, in an area centered on $\mathbf{r} = \mathbf{r}_0$. Increasing d increases this area. A wave front transmitted through the sample at $\mathbf{r}_0$ will thus experience interference with wave fronts transmitted at points increasingly distant from $\mathbf{r}_0$ as a function of d. Thus a projection through a plate with an image defined by variations in the refractive index decrement δ becomes increasingly "blurry" with increasing d, and the image ultimately becomes unrecognizable from the projection, which is illustrated e.g. in figure 1 in [21]. This prompts the definition of two regimes: The *direct imaging regime*, where d is "small" and the image is recognizable from the projection, and the *holographic regime*, where d is "large", and the image becomes unrecognizable from the projection. The holographic regime is named as such, as projections acquired in this regime are described by the principle of in-line holography [22].

It is seen that the Fresnel integral (2.7) is in the form of a convolution, and so in Fourier space will take the form of a simple product of the respective Fourier transforms of the two factors [23]. Taking $\mathcal{FT}\left\{\cdot\right\}$ to be the Fourier transform from $\mathbf{r}$ to the conjugate variable $\mathbf{f}$ of spatial frequencies, we have

$$\mathcal{FT}\left\{u_d\right\}(\mathbf{f}) = \mathcal{FT}\left\{u_{\text{out}}\right\}(\mathbf{f})\mathcal{FT}\left\{F_d\right\}(\mathbf{f}) \tag{2.9}$$

where F_d is the integrand of equation (2.7) excluding u_{out}, known as the *propagator*, the Fourier transform of which is given simply by [21]

$$\mathcal{FT}\left\{F_d\right\}(\mathbf{f}) = \exp\left(i\frac{2\pi}{\lambda}d\right)\exp\left(-i\pi\lambda d\mathbf{f}^2\right) \tag{2.10}$$

which together conveniently expresses the Fourier transform of the X-ray wave in the detector plane.

2.1.1 Edge enhanced tomography

Restricting attention to the near-field where we can take λd to be small compared to $\mathbf{f}^2$, i.e. the frequency of spatial features of interest, the second exponential function of equation (2.10) is Taylor expanded to first order in its argument, whereby equation (2.9) becomes

$$\mathcal{FT}\left\{u_d\right\}(\mathbf{f}) = \mathcal{FT}\left\{u_{\text{out}}\right\}(\mathbf{f}) \exp\left(i\frac{2\pi}{\lambda}d\right)\left(1 - i\pi\lambda d\mathbf{f}^2\right) \tag{2.11}$$

$-\mathbf{f}^2$ is recognized as the Fourier transform of the Laplacian operator $\nabla^2_{\mathbf{r}}$ in $\mathbf{r}$. Inserting equation (2.3), assuming the variation of $u_{\text{in}}(\mathbf{r})$ to be negligible, neglecting terms of second order in $\Delta(\mathbf{r})$ and $B(\mathbf{r})$, and assuming that the sample is weakly or homogeneously absorbing, the term with $\nabla^2_{\mathbf{r}} B(\mathbf{r})$ is neglected, and so we may write

$$I_d(\mathbf{r}) = I_{d=0}(\mathbf{r}) \left|1 + \frac{\lambda d}{4\pi}\nabla^2_{\mathbf{r}}\Delta(\mathbf{r})\right|^2 \tag{2.12}$$

which allows a physical interpretation of the detected intensity (for a more rigorous derivation of this, see e.g. [24]). So a necessary condition for the detected intensity to vary from that found by an absorption projection is that the Laplacian in the detector plane of the projection of the phase shift is non-zero. It also shows that the variation of the detected intensity from that detected by absorption tomography increases with sample-detector distance d within the stated assumptions.

With images acquired at many different equally spaced sample rotation angles, e.g. 720 images and so $\Delta\omega = 0.5°$, and a sample distance $d > 0$, a "qualitative" tomographic reconstruction of $\nabla^2\delta$ [24, 25] may be produced, where the boundaries between microstructural domains are visualized. For some applications this is sufficient, i.e. visualizations of cracks, inclusions, etc., and was the approach taken in the present work to visualize the grain structure of titanium through a second phase precipitated preferentially on the grain boundaries, as will be elaborated upon in chapter 4. A cross section of the reconstructed microstructure is shown in figure 2.2. The raw data contain ring artifacts, and the decorated grain boundaries are difficult to see with the naked eye, but this was corrected with an image filter algorithm, which will be sketched in chapter 4. Acquiring an additional set of images at a distance $d \approx 0$ allows for a fully quantitative tomographic reconstruction algorithm [24, 26] to be employed as needed.

2.1.2 Holotomography

An alternative method to edge contrast tomography is afforded by holotomography. The experimental setup is essentially the same, but holotomography employs projections from additional distances, typically a total of four. This makes a quantitative phase reconstruction possible, and for holotomography to resolve smaller differences in refractive index decrement δ than edge contrast

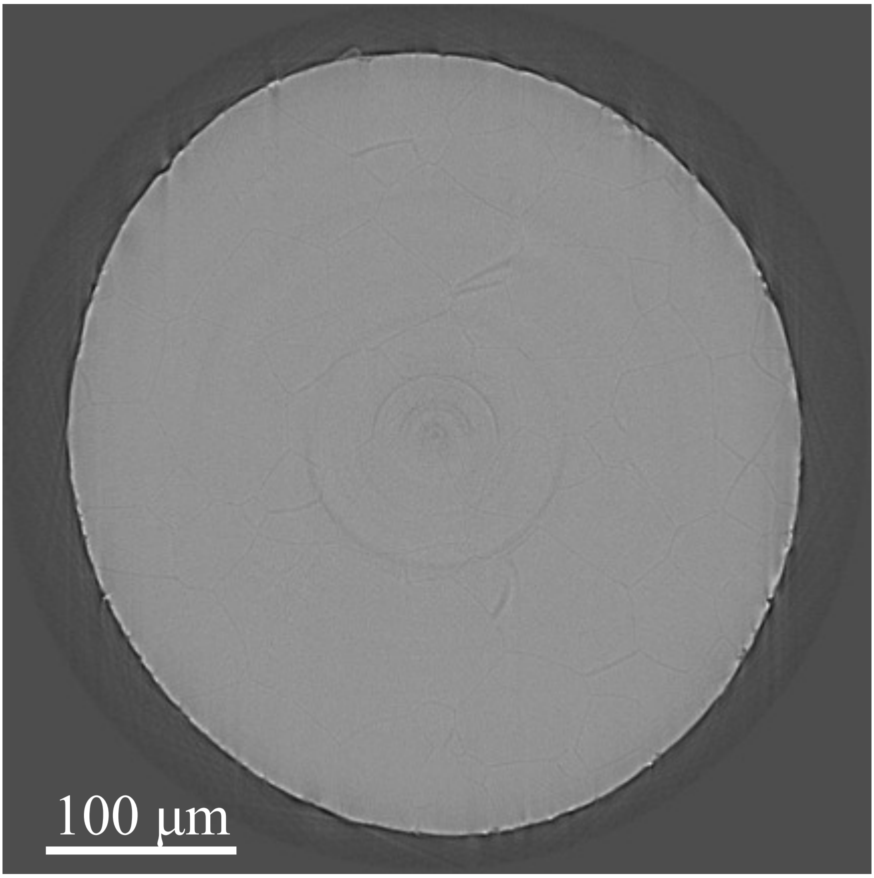

Figure 2.2: A cross section of a reconstruction of the grain structure of titanium visualized through a second phase precipitated preferentially on the matrix phase grain boundaries using edge contrast tomography.

tomography, at the cost of longer scan times. A second benefit is a better resolution of different spatial frequencies: Quoting [27] *"the need for data recorded at several distances is made clear by the Talbot effect: a periodic phase object with period* a *produces no contrast at distances* pa^2/λ, λ *being the wavelength and* p *an integer."*, meaning that some spatial frequencies will not cause contrast at any given sample-detector distance.

In the original implementation presented in [18, 27], there are three conceptual steps to be taken before a three-dimensional reconstruction has been determined from the acquired data:

1. An initial estimate of the projections of the refractive index decrement δ is constructed using the *paraboloid method* devised for high resolution transmission electron microscopy (HRTEM) [28], where the perturbation stemming from interference between multiple diffracted waves is neglected.
2. This estimate is refined by an iterative method, e.g. a non-linear least squares method, to include the neglected perturbation, until the desired degree of self-consistency has been achieved.
3. Finally, the three-dimensional reconstruction is put together from these projections by the filtered back projection method [9].

The paraboloid method will be sketched, rather than presented in full detail, which may be found in [18]. The Fourier spectrum of the detected intensity is given as an autocorrelation

$$\mathcal{FT}\left\{I_d\right\}(\mathbf{f}) = \int \mathcal{FT}\left\{u_d\right\}(\mathbf{p}+\mathbf{f})\mathcal{FT}\left\{u_d^*\right\}(\mathbf{p})d\mathbf{p} \tag{2.13}$$

Consider for simplicity an incoming plane wave of unit intensity so $|u_{\text{in}}(\mathbf{r})|^2 = 1$, so this equation by insertion of (2.9) becomes

$$\begin{aligned}\mathcal{FT}\left\{I_{d_n}\right\}(\mathbf{f}) &= \exp\left(-i\pi\lambda d_n \mathbf{f}^2\right) \\ &\times \int \mathcal{FT}\left\{T\right\}(\mathbf{p}+\mathbf{f})\mathcal{FT}\left\{T^*\right\}(\mathbf{p}) \exp\left(-2\pi\lambda d_n \mathbf{f}\cdot\mathbf{p}\right) d\mathbf{p}\end{aligned} \tag{2.14}$$

here the subscript n has been added to the sample-detector distance d to indicate that there are several, and $*$ denotes complex conjugation. The real space transmission function is now written as a sum of the mean value κ, and the fluctuations around the mean $\psi(\mathbf{r})$, so

$$T(\mathbf{r}) \equiv \kappa + \psi(\mathbf{r}) \Leftrightarrow \mathcal{FT}\left\{T\right\}(\mathbf{f}) = \kappa\delta_{\text{D}}(\mathbf{f}) + \mathcal{FT}\left\{\psi\right\}(\mathbf{f}) \tag{2.15}$$

where $\mathcal{FT}\left\{\psi\right\}(\mathbf{0}) = 0$ by definition, and δ_{D} is the Dirac delta distribution. The phase of the transmission function may be chosen arbitrarily since it does not alter the detected intensity, as is easily seen from equation (2.14), and so is chosen so κ is real. In Fourier space κ corresponds to a direct beam, the phase of which is unaltered by the transmission as compared to a beam travelling in vacuum, and ψ corresponds to Fresnel diffracted parts of the wave. Insertion, straight forward integration over the Dirac delta distribution, and rewriting gives

$$\begin{aligned}\exp(i\pi\lambda d_n\mathbf{f}^2)\mathcal{FT}\left\{I_{d_n}\right\}(\mathbf{f}) = \kappa^2\delta_D(\mathbf{f}) + \kappa\mathcal{FT}\left\{\psi\right\}(\mathbf{f})\\ + \exp(2\pi i\lambda d_n\mathbf{f}^2)\kappa\mathcal{FT}\left\{\psi^*\right\}(-\mathbf{f}) + I_{NL}(\mathbf{f}) \quad (2.16)\end{aligned}$$

where the non-linear term is

$$I_{NL}(\mathbf{f}) \equiv \int \exp(-2\pi i\lambda d_n\mathbf{p}\cdot\mathbf{f})\mathcal{FT}\left\{\psi\right\}(\mathbf{p}+\mathbf{f})\mathcal{FT}\left\{\psi^*\right\}(\mathbf{p})d\mathbf{p} \quad (2.17)$$

The first term on the right hand side of equation (2.16) is related to the direct beam. The second and third are due to interactions between the direct beam and Fresnel diffracted waves, and the fourth term to non-linear interactions between different Fresnel diffracted waves. Summing the equation over the N available distances gives

$$\begin{aligned}\sum_{n=1}^{N}\exp(i\pi\lambda d_n\mathbf{f}^2)\mathcal{FT}\left\{I_{d_n}\right\}(\mathbf{f}) = N\kappa^2\delta_{\mathrm{D}}(\mathbf{f}) + N\kappa\mathcal{FT}\left\{\psi\right\}(\mathbf{f})\\ + \kappa\mathcal{FT}\left\{\psi^*\right\}(-\mathbf{f})\sum_{n=1}^{N}\exp(2\pi i\lambda d_n\mathbf{f}^2) + \sum_{n=1}^{N}I_{NL}(\mathbf{f}) \quad (2.18)\end{aligned}$$

The strength of employing images acquired at multiple distances now become more apparent: Summing over the exponentials in the third and fourth terms in the right hand side of equation (2.18) decreases the relative importance of the third and fourth terms for $\mathbf{f} \neq \mathbf{0}$.

Assuming the last term to be negligible, equation (2.18) and its complex conjugate for $\mathbf{f} \neq \mathbf{0}$ where $\delta_{\mathrm{D}}(\mathbf{f}) = 0$ may be used to isolate the product $\kappa\mathcal{FT}\left\{\psi\right\}(\mathbf{f})$.

To separate the contributions from the average and the fluctuations about average, equation (2.18) is evaluated in the limit $\mathbf{f} \to \mathbf{0}$. For mathematical consistency, the limits of the terms without Dirac delta distributions are taken to be $\lim_{\mathbf{f}\to 0} X(\mathbf{f}) = \int X(\mathbf{f})\delta_D(\mathbf{f})d\mathbf{f}$, where the integration is over a domain containing the origin. Doing so gives

$$\sum_{n=1}^{N}\mathcal{FT}\left\{I_{d_n}\right\}(\mathbf{0}) = N\kappa^2 + \underbrace{\frac{1}{\kappa^2}\int\left|\kappa\mathcal{FT}\left\{\psi\right\}(\mathbf{p})\right|^2 d\mathbf{p}}_{\lim_{\mathbf{f}\to\mathbf{0}} I_{NL}} \quad (2.19)$$

where $1/\kappa^2$ has been taken out of the I_{NL} term to show the explicit dependence on the known product $\kappa\mathcal{FT}\{\psi\}(\mathbf{f})$. This equation can be rewritten in the form of a quadratic equation to determine κ^2, assuming that the largest-κ solution is the applicable one, which thereby completes the estimation of the transmission function T. Note that I_{NL} was neglected while determining $\kappa\mathcal{FT}\{\psi\}(\mathbf{f})$ for $\mathbf{f} \neq \mathbf{0}$, and retained for determining κ^2 for $\mathbf{f} = \mathbf{0}$.

The estimated transmission function may in certain cases be sufficient, i.e. weak objects or a very large number N of different distances employed, but in general, corrections are applied to increase the quality of the reconstruction. The simplest way to do so is to use an iterative method:

I_{NL} is estimated from its definition (2.17) using the transmission function just determined and the experimentally determined images, and this is used to determine a new estimate of $\kappa\mathcal{FT}\{\psi\}(\mathbf{f})$ and κ^2 by repeating the steps described above. Alternatively, to increase convergence, the new estimate of $\kappa\mathcal{FT}\{\psi\}(\mathbf{f})$ may be determined as a weighted superposition of the old and the new estimates. This procedure may then be repeated until self-consistency is reached, meaning an optimal solution has been determined. Alternatively, a less intuitive but more computationally efficient non-linear least-squares method may be employed [29]. Computational efficiency is desirable, as these steps must be performed for every set of images acquired at a given sample rotation, e.g. 720 times.

With all transmission functions determined, the three-dimensional reconstruction may be performed by any standard tomographic reconstruction method, in this case usually a filtered back projection [9].

The fundamentals of edge enhanced tomography and holotomography have been sketched. A comparison between cross sections of three-dimensional reconstructions of the same sample of duplex steel 2205 is found in figure 2.3, published in [30], clearly shows the benefits of employing holotomography rather than edge enhanced tomography in this case, which is due to the significant absorption, and small density difference between the phases of this alloy.

2.2 Bragg diffraction methods

An X-ray wave interacting with an electron density experiences scattering. This scattering is taken to be Thomson, i.e. elastic, scattering, but a momentum transfer between the X-ray wave and the electron density may occur, even when no energy is exchanged. An incoming X-ray photon of wave vector $\mathbf{k}$ may after

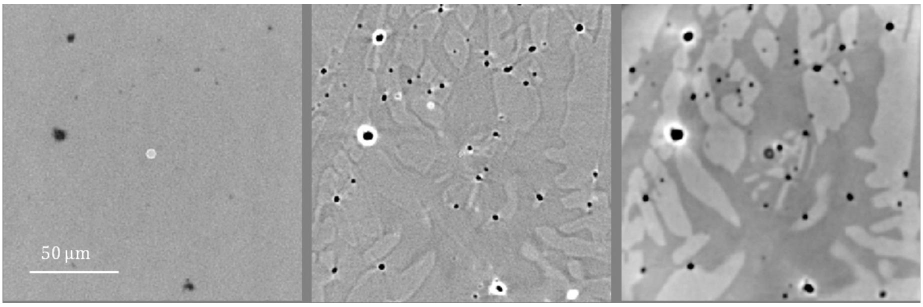

Figure 2.3: Three cross sections of reconstructions of the same sample of duplex steel 2205 in the as-cast condition, courtesy of Dr. Wolfgang Ludwig, ESRF. Left: Absorption tomography, only the largest voids are visible. Middle: Edge enhanced tomography. All voids are visible, but the phases are not easily distinguished. Right: Holotomography. Both voids and phases are clearly visible. Published in [30].

a scattering event have the wave vector $\mathbf{k}'$, which prompts the definition of the scattering vector $\mathbf{Q} = \mathbf{k} - \mathbf{k}'$, where elastic scattering requires $|\mathbf{k}| = |\mathbf{k}'|$. The scattered wave incident on a detector is the sum of contributions from all illuminated volumes containing electron density, but waves taking different paths will have different phases. This is illustrated on figure 2.4. Coherent waves scattering at the point of origin and $\mathbf{r}$ by the scattering vector $\mathbf{Q}$ will be out of phase by the amount $\mathbf{Q} \cdot \mathbf{r}$. Adding the infinitesimal contributions from scattering on the electron density distribution ρ gives the Fourier transform

$$f(\mathbf{Q}) = \int \rho(\mathbf{r}) \exp(i\mathbf{Q} \cdot \mathbf{r}) d\mathbf{r} \tag{2.20}$$

which is termed the scattering length of the electron density ρ. In particular, if ρ is the electron density of an atom, equation (2.20) is the atomic form factor. This gives a good description of the magnitude of the scattering with scattering vector $\mathbf{Q}$ when the X-ray energy is far removed from absorption edge energies [13, 15].

Scattering on multiple atoms at locations $\mathbf{r}_n$ is with good approximation describable as a sum of atomic form factors and phase shifts

$$F(\mathbf{Q}) = \sum_n f_n(\mathbf{Q}) \exp(i\mathbf{Q} \cdot \mathbf{r}_n) \tag{2.21}$$

This is since the perturbations to the spatial distribution of the electron density of an atom when forming part of a molecule or crystal are largely confined to the highest energy orbitals as compared to a free atom.

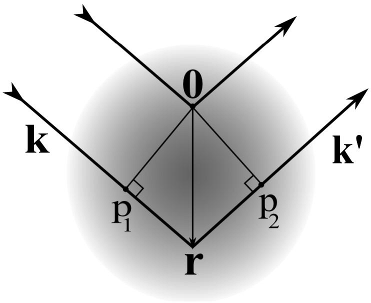

Figure 2.4: Scattering from electron density. Recreated after [13]. A coherent wave of wave vector $\mathbf{k}$ is elastically scattered at the origin, and at the point $\mathbf{r}$ into direction $\mathbf{k}'$. The waves are in-phase until the waves reach the points 0 and p_1 respectively. The waves reaching a detector will be out of phase by the longer distance traversed by the bottom wave, $|\mathbf{p}_1 - \mathbf{r}| + |\mathbf{r} - \mathbf{p}_2|$, which may be conveniently written as $\mathbf{k} \cdot \mathbf{r} - \mathbf{k}' \cdot \mathbf{r} = \mathbf{Q} \cdot \mathbf{r}$.

For crystalline materials, it is possible to define a unit cell containing one or more atoms, from which the whole crystallite may be constructed by spatial translations of the lattice vectors

$$\mathbf{R}_m \equiv n_1\mathbf{a}_1 + n_2\mathbf{a}_2 + n_3\mathbf{a}_3 \tag{2.22}$$

where n_1, n_2 and n_3 are integers and $\mathbf{a}_1, \mathbf{a}_2$ and $\mathbf{a}_3$ are basis vectors chosen as convenient. This allows for a decomposition of the scattering length into the product of a sum over the unit cell (first factor), and a sum over the lattice (second factor)

$$F_{\text{crystal}}(\mathbf{Q}) = \sum_n f_n(\mathbf{Q}) \exp(i\mathbf{Q} \cdot \mathbf{r}_n) \sum_m \exp(i\mathbf{Q} \cdot \mathbf{R}_m) \tag{2.23}$$

The lattice sum will largely cancel, becoming appreciable only when the argument is an integer multiple of 2π for all m, so

$$\left| \sum_m \exp(i\mathbf{Q} \cdot \mathbf{R}_m) \right| = \left\{ \begin{array}{c} \sim 1 \\ N \end{array} \right. \text{ for } \begin{array}{c} \mathbf{Q} \cdot \mathbf{R}_m \neq 2\pi n \\ \mathbf{Q} \cdot \mathbf{R}_m = 2\pi n \end{array} \tag{2.24}$$

where N is the number of unit cells in the crystallite, which relates the scattered intensity to the volume of the scattering crystallite. The reciprocal lattice vectors

$$\mathbf{G}_{hkl} \equiv h\mathbf{a}_1^* + k\mathbf{a}_2^* + l\mathbf{a}_3^* \tag{2.25}$$

where h, k and l are integers are introduced to fulfill this requirement for scattering. Note that the notation $\{\cdot\}^*$ is chosen for historical reasons, and does not mean complex conjugation in the present context, but are simply to differentiate the real space lattice vectors of equation (2.22) from the reciprocal space lattice vectors of equation (2.25). The reciprocal lattice basis vectors are defined from the real space basis vectors as

$$\mathbf{a}_1^* = 2\pi \frac{\mathbf{a}_2 \times \mathbf{a}_3}{\mathbf{a}_1 \cdot (\mathbf{a}_2 \times \mathbf{a}_3)} \quad \mathbf{a}_2^* = 2\pi \frac{\mathbf{a}_3 \times \mathbf{a}_1}{\mathbf{a}_1 \cdot (\mathbf{a}_2 \times \mathbf{a}_3)} \quad \mathbf{a}_3^* = 2\pi \frac{\mathbf{a}_1 \times \mathbf{a}_2}{\mathbf{a}_1 \cdot (\mathbf{a}_2 \times \mathbf{a}_3)} \tag{2.26}$$

and it may be shown that $\mathbf{G}_{hlk}$ is perpendicular to the crystallographic plane with Miller index (h, k, l). A necessary condition for constructive interference of scattering may thus be imposed on the scattering vector

$$\mathbf{Q} = \mathbf{G}_{hkl} \tag{2.27}$$

which is known as the Laue condition. This may be shown to be equivalent to the more familiar Bragg condition [13], where scattering is taken to occur on atomic planes

$$n\lambda = 2d_{hkl} \sin\theta_{hkl} \tag{2.28}$$

where θ_{hkl} is half the angle between the incoming and the scattered beams ($\mathbf{k}$ and $\mathbf{k}'$), and d_{hkl} is the distance between planes of Miller index (h, k, l), which for the important special case of cubic unit cells are $d_{hkl} = a/\sqrt{h^2 + k^2 + l^2}$, a being the lattice parameter. This means that appreciable scattering occurs only at a number of discrete angles to the incoming beam. The cones that the scattered intensity is confined to are known as Debye-Scherrer cones, and their intersection with an area detector as in the case for the common setup shown on figure 2.1 are known as Debye-Scherrer rings.

The Laue, or equivalently, Bragg condition is necessary but not sufficient for appreciable scattering, as the unit cell sum (first factor) of equation (2.23) may vanish, which is termed systematic extinction. E.g. for the case of an FCC crystal which is relevant to present work, the unit cell structure factor is [13]

$$F_{hkl} = \left\{ \begin{array}{lcl} 4f(\mathbf{Q}) & \text{when} & h,\ k \text{ and } l \text{ are of same parity} \\ 0 & & \text{otherwise} \end{array} \right. \tag{2.29}$$

where $f(\mathbf{Q})$ is the atomic form factor of the element in question, and so there will be no appreciable scattering caused when the indices of the scattering plane (h, k, l) are of mixed parity. The Laue (or Bragg) condition and the condition that no systematic extinction be present are known collectively as the diffraction condition.

The scattered intensity from a crystallite in diffraction condition will constitute sharp peaks. A quantitative interpretation of the total intensity of such a peak for an experimental setup like that shown in figure 2.1 is presented in [15]:

$$I_{\text{crystal}} = I_0 \left(\frac{d\omega}{dt} \right)^{-1} \frac{\lambda^3 r_0^2 \left| F_{hkl} \right|^2}{v^2} P_{hkl} L V_{\text{crystal}} \tag{2.30}$$

where I_o is the incoming X-ray intensity, v is the volume of the unit cell, and V_{crystal} is the volume of the diffracting crystallite. The factor P_{hkl} is known as the polarization factor, which for a synchrotron light source where the polarization is in the horizontal plane, is given by $P_{\text{hkl}} = \cos^2\phi$, where ϕ is the angle between the incoming beam and the diffracted beam in the horizontal plane. For high energy X-rays, the diffraction angles are typically sufficiently small that we may take $P_{hkl} = 1$.

The factor L of equation (2.30) is known as the Lorentz factor, and is given by the geometry of the setup. Equation (2.30) is derived as a volume integral in reciprocal space so L contains a factor related to the magnitude of a reciprocal space volume element. The Lorentz factor also relates the time a given crystallite remains in diffraction condition to the position of the diffraction spot on the Debye-Scherrer ring. This is sought illustrated in figure 2.5: The reciprocal lattice vectors $\mathbf{G}_{hkl}$ of some family of lattice planes (h, k, l) point to the surface of a sphere. The points where diffraction may occur are dependent on the incoming X-ray wave vector $\mathbf{k}$ and $\mathbf{G}_{hkl}$ and trace a circle on the surface of the sphere. As the sample is rotated about the vertical ω-axis, the reciprocal lattice vectors may cross this circle, and diffraction will occur. A reciprocal lattice vector pointing close to the pole will spend more time in diffraction condition than one near the equator as it moves slower. It may be shown geometrically, using that the angles 2θ are small for hard X-rays, that this factor with good approximation is given by [8]

$$L = \frac{1}{\sin 2\theta_{hkl} \ \ |\sin\eta|} \tag{2.31}$$

where η is the angle in the detector-plane to the positive z-axis, as is indicated on figure 2.6, and the first factor is related to the reciprocal space volume element.

For a powder sample, the result for the intensity scattered to any point on a Debye-Scherrer ring is written as [15]

$$I_{\text{powder}} = I_0 t \frac{\lambda^3 r_0^2}{v^2} \frac{m_{hkl} \left|F_{hkl}\right|^2 P_{hkl}}{4 \sin\theta_{hkl}} V_{\text{gauge}} \tag{2.32}$$

where t is the exposure time, m_{hkl} is the multiplicity of the hkl reflection, and V_{gauge} is the illuminated volume of the powder sample. A powder sample may be regarded as being composed of a large number of small crystallites of random orientation, while a sufficiently deformed metal may be regarded as a "textured powder", meaning that it is composed of a large number of small crystallites of orientations statistically given by the texture of the material. The powder diffraction equation will be employed in chapter 3 for a deformed material, where this will be argued in more detail.

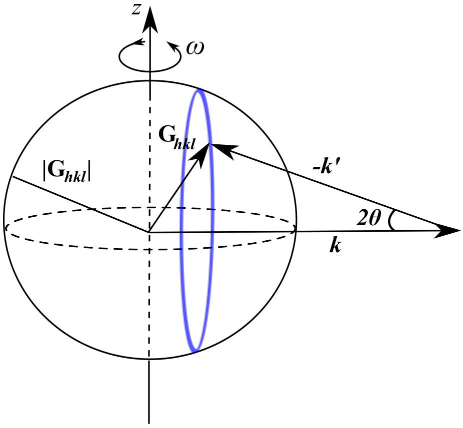

Figure 2.5: Diffraction in reciprocal space. The surface of the sphere is the possible end points for a given set of reciprocal lattice vectors $\mathbf{G}_{hkl} = \mathbf{Q} = \mathbf{k} - \mathbf{k}'$, with one specific indicated. The blue circle represents the points where diffraction may occur, and so $\mathbf{G}_{hkl}$ is depicted as being in diffraction condition.

2.2.1 Three-Dimensional X-ray Diffraction (3DXRD)

The principles behind 3DXRD are readily understood by the physics presented in previous chapter, however 3DXRD has proved a versatile tool, and the specifics are too numerous to fit in the scope of this text. Quoting [31]: *"the 3DXRD concept has developed over time so that it now comprises a set of methods optimized for spatial, angular, or time resolution"*. Present text will focus on a setup used for an *in situ* study of recrystallization kinetics of individual grains as described in chapter 3 focussing on time resolution. See e.g. [8] for an introduction to other approaches.

A 3DXRD experimental setup is shown in figure 2.6. A typical sample-detector distance for this setup is $d \approx 20$ cm or more. Using hard X-rays, i.e. "small" 2θ values cf. equation (2.28), this means that multiple Debye-Scherrer rings may be monitored simultaneously, while there are few overlapping diffraction spots, so contributions to the diffraction pattern from individual grains may be isolated, provided the sample dimensions are "reasonable". For lightly absorbing materials such as aluminium where the penetrative depth of hard X-rays are several cm, the need for few overlapping diffraction spots is the factor restricting the sample size. Large rotation steps $\Delta\omega \sim 0.25° - 1°$ are employed when high precision orientations of individual grains are not required, which results in fast scan times. The angular ω window may be restricted as appropriate for the symmetry of the lattice in question without loss of information. Sample

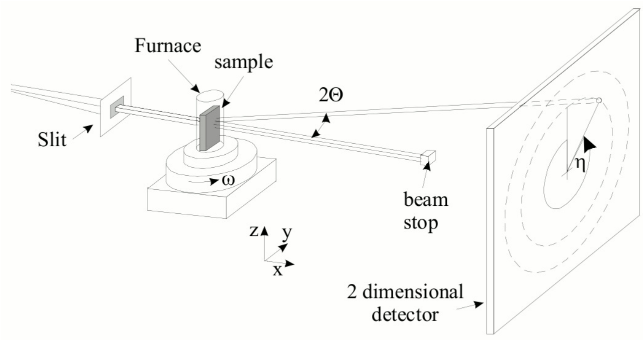

Figure 2.6: A 3DXRD setup for *in situ* experimental studies involving annealing. Modified from [32].

diameters of $d \sim 0.5$ mm may be scanned with exposure times of about $t \sim 2$ s with current FReLoN cameras. A beam stop that absorbs the direct beam after passage through the sample is inserted to spare the FReLoN camera the high intensity beam, and to reduce contributions to the detected intensity from scattering on air.

The technique has the inherent advantage that the distance between sample and detector allows for additional equipment to be fitted for true *in situ* studies, e.g. a furnace as on figure 2.6 or a stress rig.

The positions of diffraction spots in $(2\theta, \eta, \omega)$ and their intensities may be used as input for an indexing algorithm, e.g. GrainSpotter [33], which can determine center-of-mass positions to within 5 μm (detector limited) [31] and orientations of individual grains. However, the detector distance makes extraction of high resolution morphological information difficult, since the diffraction spots are isolated to a few detector pixels. Approximations may be constructed by e.g. Laguerre tessellations using the determined volumes and center-of-mass [34], or morphological information may be acquired using e.g. a line focus beam setup [35], but this increases acquisition time considerably.

2.2.2 Diffraction Contrast Tomography (DCT)

An alternative approach which allows for extraction of morphological data is provided by DCT. The sample-detector distance of a few mm is used, and slits define the beam tightly around the sample. A sketch of the principle is seen in figure 2.7: As a grain enters diffraction condition, an extinction spot appears in

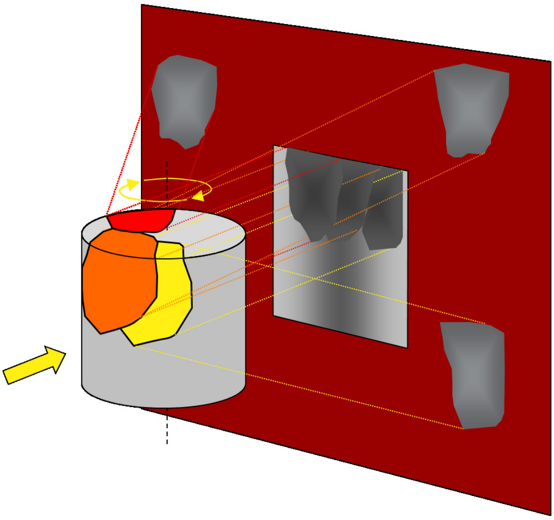

Figure 2.7: Illustration of the principle of DCT. Courtesy of Dr. Wolfgang Ludwig, ESRF. Three individual grains are shown in diffraction condition simultaneously.

the direct beam area where intensity is being scattered at some 2θ angle to the direction of the direct beam, and a diffraction spot appears outside the direct beam area. Both the extinction spot and diffraction spot may be considered projections through the diffracting grain, and thus carries information about the morphological shape of the grain.

In the original implementation, only the extinction spots were used for reconstruction [36]. This was later refined so both extinction spots and diffraction spots were employed [37]. In the present implementation, which is the one focussed on in present text, only the diffraction spots are used [38], as this has been found to lead to increased accuracy.

Data acquisition proceeds over the full range of sample rotations $0^\circ \leq \omega < 360^\circ$ in small rotation steps, typically $\Delta\omega \sim 0.1^\circ$, which increases the accuracy of the determination of the crystallographic orientation, and decreases the amount of overlap between diffraction spots stemming from scattering from different grains. Each individual grain will typically display on the order of $20 - 30$ diffraction spots [37] during a full rotation, which for bulk samples results in a very large number of diffraction spots that must be indexed in order to trace them to the diffracting grain. The current methodology is to look for Friedel pairs: Using that a diffraction spot from a lattice plane (h, k, l) at $\omega = \omega_0$ will also have a diffraction spot from the lattice plane $(-h, -k, -l)$ at $\omega = \omega_0 + 180^\circ$. In a coordinate system where the sample is kept fixed and the beam and detector are rotated about the sample center, these Friedel pairs may be pictured as being projected in directions $\mathbf{k}'$ and $-\mathbf{k}'$, thus straight lines connecting them will pass through the diffracting grain. Matching up many Friedel pairs makes it possible to trace (index) the diffraction spots to individual grains by a combination of finding the lines that are close to intersecting at a point (not exactly, due to experimental uncertainty), and comparing with the known possible 2θ angles, assuming the crystallography of the sample is known. The large number of diffraction spots allows for the discarding of overlapping diffraction spots, with only a small loss of morphological information.

When the diffraction spots are indexed, a varying number of discrete projections through each individual grain have been determined. These are then used as input for a tomographic reconstruction on a grain by grain basis using an algebraic reconstruction technique (ART) [9], where the problem is cast as a system of linear equations, which may be solved by matrix inversion or more conventionally by an iterative relaxation method. ART has for the present case been found to give results superior to those of a filtered back projection due to the low number of projections.

Finally, since the grains have been reconstructed individually, the reconstruction will show regions of overlapping grains and voids due to experimental error and uncertainty, the low number of projections and the poor contrast on the edges of the diffracting grains. A space-filling grain structure is then constructed by assuming the errors are distributed evenly and performing a simple expansion or contraction of the grains until all voxels of the reconstruction are occupied once. This has been shown to give good results by comparison to a grain map of titanium produced by the edge contrast method described in section 2.1.1 [38].

Chapter 3

Recrystallization kinetics in cold-rolled aluminium

As a metal or alloy is plastically deformed, some small portion of the work, around 1% [10], is retained in the material as crystal defects. The presence of crystal defects, dislocations in particular, increases the stored energy of the material, and therefore also the free energy, and so may provide the driving force for recrystallization, which is the thermally activated process by which new grains nucleate, and grow, until the deformed matrix has been replaced by a polycrystalline microstructure.

Recrystallization kinetics has historically been studied with destructive characterization techniques, such as hardness tests or optical microscopy of cross sections of a series of partly recrystallized samples to e.g. determine the recrystallized fraction as a function of annealing time and temperature. Average growth rates may be determined with e.g. the Cahn-Hagel [39] or extended Cahn-Hagel methods [40]. See [10] for a comprehensive review of experimental methods.

These experimental methods have been successful in determining the mean kinetics of recrystallization. The results thereof were sought described by the analytical theory by Johnson and Mehl [41], Avrami [42] and Kolmogorov [43], known collectively as JMAK theory, which was originally developed as a model for phase transformations, but shown to apply equally well to recrystallization.

In JMAK theory, grains are assumed to nucleate at random sites, and grow at constant and equal radial rates until impinging on other recrystallizing grains. The theory has been extended several times, most notably by Vandermeer and Rath [44], which included an orientation dependence in the growth rate. However, the growth rate of individual grains was still assumed to be constant for grains of a given orientation, and no direct experimental evidence disproving this assumption could be produced.

The introduction of 3DXRD as presented in section 2.2.1 provided a means of non-destructive *in situ* characterization of the recrystallization kinetics of large numbers of *individual* grains, which showed that the recrystallization kinetics would vary substantially between grains [45, 46]. Later experiments also showed that the recrystallization of individual grains occur in a complex manner [47].

The remainder of this chapter describes an experimental investigation of the recrystallization of individual grains in 50% cold-rolled aluminium AA1050 using 3DXRD. Recrystallization kinetics in the same alloy has previously been investigated in [46] for 244 individual grains, but for a deformation of 90% cold-rolling, and at comparable strain (42% cold-rolling), but for a single grain in [47]. The emphasis of the present study is on the relation between growth rate and annealing temperature which is quantified using grain-averaged activation energies. The concept of grain-averaged activation energies is introduced in section 3.1, and the experimental details and data analysis is presented in sections 3.2 and 3.3. Results are presented and discussed in section 3.4, which includes the introduction of a simple cellular automaton model to explain the observed recrystallization kinetics. Finally, the conclusions drawn will be emphasized in section 6.1.

3.1 Grain-averaged activation energies

As a recrystallizing grain grows into the deformed matrix, it does so through grain boundary migration. There is a large body of experimental evidence supporting that the velocity of a grain boundary during migration may be written as the product of a mobility M and the driving pressure for grain boundary migration P [48]

$$v = MP \tag{3.1}$$

Note that this driving pressure may be found equivalently in the literature as a driving force. The driving pressure for grain boundary migration is taken to be the possibility for a reduction of the stored energy caused by the high density of dislocations introduced during deformation, and so is taken to strictly be a function of the local microstructure close to the grain boundary. The grain boundary mobility M has been shown to approximately follow a modified Arrhenius equation [49]

$$M \propto \frac{1}{RT} \exp\left(-\frac{Q}{RT}\right) \tag{3.2}$$

where R is the universal gas constant, T the absolute temperature and Q the activation energy of the migration of the grain boundary in question. The combination of equations (3.1) and (3.2) may thus be written as

$$v = m_0 \exp\left(-\frac{Q}{RT}\right) P \tag{3.3}$$

where the preexponential dependence on RT has been expressed by the mobility m_0. If radial growth rates v_1 and v_2 are determined at temperatures T_1 and T_2, we may use equation (3.3) to determine an activation energy as

$$Q = R\left(\frac{1}{T_1} - \frac{1}{T_2}\right) \ln\left(\frac{v_2}{v_1}\right) \tag{3.4}$$

provided that the local microstructure has not changed significantly between measurements, and that the magnitude of the difference of T_1 and T_2 is small so the variation in m_0 due to temperature is negligible.

This activation energy is termed a grain-averaged activation energy, because when it is measured for an individual grain it expresses the mean of the activation energies of the boundaries of the grain weighted by the respective areas of the boundaries. Bulk activation energies for recrystallization, like those determined calorimetrically and presented in e.g. [50] may then be determined by taking the mean of a representative set of grain-averaged activation energies. Grain-averaged activation energies were introduced in [51] for a study of 8 grains recrystallizing in copper, where they were denoted *apparent activation energies*.

3.2 Experimental details

A sheet of commercially pure aluminium AA1050 was chosen for the investigation, and cold-rolled 50%. That specific alloy was chosen as it had been the subject of previous 3DXRD investigations after 90% cold-rolling, and since the Zener pinning force [52] for the impurities in the alloy have been estimated to be a factor ~ 10 lower than the driving pressure for comparably strained (42% cold-rolled) samples [47], so observed complex recrystallization kinetics was argued not to be attributed to pinning and depinning of boundaries [47].

Three cubic samples of approximate side lengths (850 μm $\times$850 μm $\times$2000 μm) were cut from the middle of the sheet. As it is well known that scratches and notches caused by mechanical cutting supplies preferred nucleation sites along the surface of the samples, these were removed by electropolishing.

A number of larger cubic samples were cut from the same deformed material, to roughly determine the recrystallized fraction as a function of annealing time, by a series of Vickers hardness tests. It was concluded that annealing for 120 min at a temperature of 310°C would result in a recrystallized fraction of $\sim$ 20%, and this result was used to guide the *in situ* 3DXRD experiment.

The experiment was conducted at the extended ID11 beamline at the European Synchrotron Radiation Facility (ESRF) in Grenoble, France, with the standard 3DXRD setup, as may be seen in figure 2.6 in section 2.2.1, with a "hot finger" type furnace with an X-ray transparent enclosure that could be sealed airtight mounted on the rotation stage. A sample was mounted in the furnace, and the enclosure filled with argon. A beam of hard (65 keV) X-rays was defined in the vertical direction by slits distanced $h_0 = 400$ μm from each other. The beam was wider in the horizontal direction than the samples, meaning that the beam illuminated a gauge volume of $V_{\text{gauge}} = 400$ μm $\times$ 850 μm $\times$ 850 μm. It was estimated that this setup sets a detection limit on the size of grains of $d \sim 5$ μm, and so the early stages of nucleation could not be observed with the present setup.

The furnace temperature was set to $T_1 = 310$°C, and data collection began. The sample was rotated around the vertical ω-axis from $\omega = -15°$ to $\omega = 15°$ in individual rotations of $\Delta\omega = 0.5°$, which would last 2 s each. During each individual rotation, an image of the diffracted beam was collected with a 14-bit FReLoN camera located a distance of $d = 23$ cm from the sample. Including read out times for the camera and moving the rotation stage back to $\omega = -15°$ after all 60 images comprising a full rotation have been acquired, the time between images at same ω was 3.2 min.

After image acquisition at temperature $T_1 = 310$°C for a duration of 120 min, the furnace temperature was swiftly changed. For two of the samples the temperature was changed to $T_2 = 325$°C, and for the last sample to $T_2 = 320$°C. The temperature changes occured over a time $t \lesssim 2$ min.

Image acquisition now proceeded for a duration of 90 min, before the temperature was again lowered to $T_1 = 310$°C, and data acquisition continued for an additional 90 min. It was found that the recrystallization kinetics was dominated by impingement after the temperature decrease, so that data was not included in further analysis.

To ensure the quality of the acquired images, these were examined for signs of detector saturation during the experiment. If an image was found to be substantially saturated, the beam attenuation was increased to allow for detection of the increasingly intense diffraction spots corresponding to the increasing volumes of the growing grains.

This experimental setup does not allow for easy detection of grains that are impinging on the sample surface, but grains recrystallizing outside the gauge volume were identified by periodically increasing the vertical distance between the slits from $h_0 = 400\ \mu$m to $h_1 = 500\ \mu$m for a full rotation set of 60 images. Grains growing outside the gauge volume were revealed as the intensity of their diffraction spots would increase abruptly on increasing the slit separation to $h_1 = 500\ \mu$m, and again fall abruptly when the slit separation was lowered back to $h_0 = 400\ \mu$m, as the intensity of the diffraction spots are proportional to the illuminated volume of the grain. This procedure is explained and an example is shown in [32].

3.3 Data correction and analysis

The raw diffraction images must be corrected for four factors before analysis:

1. Dark current: This is an effect of thermal excitations in the FReLoN camera, and so is a function of exposure time. The dark current is determined by acquiring images with the X-ray shutter closed.
2. Synchrotron current: The incoming X-ray intensity is proportional to the current in the synchrotron ring, which varies during experiments.
3. Beam attenuation: The attenuator at ID11 is a piece of aluminium of stepped thickness, which may be introduced in the beam path. Thus, the X-ray intensity arriving at the sample is proportional to the transmission through the chosen thickness of the attenuator.
4. Spatial distortion: This is specific to the camera, and was corrected for with the FIT2D program [53].

At early times the diffracted intensity will be slowly varying profiles along the Debye-Scherrer rings, which are consequences of the texture of the deformed microstructure. An example of this is shown in figure 3.1a. As recrystallization progresses, the deformed microstructure is gradually replaced by sharp diffraction spots each of which may be traced back to an individual grain. This is shown in figure 3.1b.

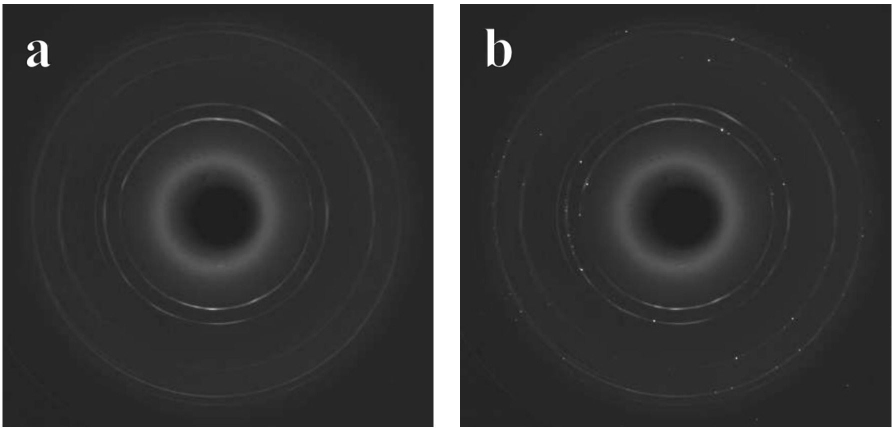

Figure 3.1: Debye-Scherrer rings from recrystallizing aluminium AA1050. a: Early time (low recrystallized fraction), the diffracted intensity is mainly from the deformed microstructure. b: Later time (higher recrystallized fraction), the diffracted intensity now shows both the remaining deformed microstructure and recrystallizing grains seen as sharp spots. The round smeared-out artifact near the center of both images is due to scattering from the glass enclosure of the furnace.

The "background" caused by the remaining deformed microstructure in partly recrystallized samples must be determined and subtracted from the images before the intensity diffracted by a recrystallizing grain may be used to determine the volume of that grain. First, a polar transformation of the images was performed using FIT2D [53] to transform the Debye-Scherrer rings to lines. This operation is not trivial, as the beam center and camera center will not coincide with mathematical precision, and the camera may be slightly rotated about several axes, which must be corrected for during transformation. The polar transformed Debye-Scherrer rings were then summed over their width in 2θ, i.e. the radial direction in the original images, to give one-dimensional profiles. A mathematical method to determine this background assuming it to be slowly varying, using only that specific profile was attempted, but found to be unreliable at early times when the intensity diffracted by the recrystallizing grains was of the same order as the intensity from the deformed matrix. Instead, the intensity from the deformed matrix was estimated as the mean of the two ω-adjacent profiles. This has two consequences: Firstly, that the images corresponding to $\omega = -15°$ and $\omega = 15°$ can only be used for background determination, as they do not have two neighboring images. Secondly, that diffraction spots in ω-adjacent images must be sufficiently far removed in η, the polar coordinate in the original images, so the estimated background does not contain intensity diffracted from a recrystallizing grain. This is believed to be a reliable method, since the deformation texture at 50% cold-rolling is known to be relatively weak, and thus the profiles are slowly varying in ω.

The intensity of a diffraction spot I_{grain} could then be determined as the sum over the range of the profile where the diffraction spot was localized. It was attempted to fit a pseudo-Voigt profile to the peaks, rather than simple summation, but it was found to be unreliable, likely due to the low resolution of the far-field detector employed, thus not supplying a sufficient number of data points for reliable fitting.

The volume of the diffracting grain was determined by first noting that the integrated intensity of the Debye-Scherrer rings before recrystallization starts is equal to that produced by a non-textured powder, since a texture simply redistributes the intensity in η and ω. So defining I_{powder} as the mean of the integrated intensity from images taken over the full 360° range before recrystallization starts, we can combine equations (2.30) and (2.32) to get

$$V_{\text{grain}} = \frac{d\omega}{dt}\frac{t}{2} m_{hkl} \cos\theta_{hkl} \left|\sin\eta\right| \frac{I_{\text{grain}}}{I_{\text{powder}}} V_{\text{gauge}} \tag{3.5}$$

where $d\omega/dt$ is the angular velocity of the sample rotation, t is the exposure time of the "powder" images, and m_{hkl} is the multiplicity of the hkl reflection. This method has the added feature that there is no dependence on the structure factor of the hkl reflection. However, due to this, it may not be employed for normalization of reflections on degenerate Debye-Scherrer rings, i.e. where multiple Debye-Scherrer rings coincide.

So, all diffraction spots in the six inner-most Debye-Scherrer rings were converted to volumes of the grain responsible for diffraction if

1. No other diffraction spots were overlapping in the image in question.
2. The background could be reliably determined, i.e. no other diffraction spots were found close in η in the ω-adjacent profiles.
3. The diffracting grain was found to be contained completely in the gauge volume.
4. The FReLoN camera did not saturate during the acquisition of that diffraction spot.

The diffraction spots were then indexed, i.e. were traced back to the unique grain responsible for the diffraction using the open source program GrainSpotter

[33]. The diffraction spots remaining in the analysis was traced to a total of 1406 unique grains. This allowed the volume of the same grain determined from different diffraction spots to be compared. A generally good correspondence was found by visual inspection. Discrepancies seemed to be mainly due to the background estimation.

3.4 Experimental results

3.4.1 Recrystallization kinetics of individual grains

The equivalent sphere diameter of the 1406 recrystallizing grains were examined as a function of annealing time. The diameters of different grains are found to increase at different rates, and the diameter of individual grains are found to increase at rates that vary in time. This was previously found to be the case for the same material cold-rolled to 90% reduction [46], and so is not a result of the larger strain. Many grains are found to display recrystallizaton kinetics that is approximately piecewise linear at times with constant temperature at the current time resolution. The dataset is too extensive to be visualized in fullness, so the evolution of the volume (left) and diameter (right) of six grains is shown in figure 3.2. The gap in data points occuring around $t = 160$ min is due to an increase of the ω window to a full rotation. Using GrainSpotter, this additional information could have been used to give good estimates of the centers of mass of the individual grains, and thus to estimate the degree of impingement of individual grains. This, however, was not undertaken due to time constraints.

Impingement is assumed to be responsible for most of the slow down of the kinetics at late times, as may be seen for grains 2-5. This is most often observed as a gradual, rather than abrupt slow down, and is assumed to be due to an increasing fraction of impinged surface area of the recrystallizing grains, and to the lower rate of recrystallization often observed when the recrystallized fraction is ~ 1.

Kinetic speed ups at constant temperature are also observed. The most notable examples for the grains shown in figure 3.2 is listed in table 3.1. These changes in growth rate are to some extent observed for $\sim 1/3$ of the recrystallizing grains in this analysis. Pinning and depinning of boundaries is an unlikely cause cf. [47] as noted in section 3.2, and it is therefore assumed to be a consequence of the structure of the deformed matrix, which for cold-rolled aluminium is of the "cell block" type [54, 55], where mosaic cells are grouped together, separated

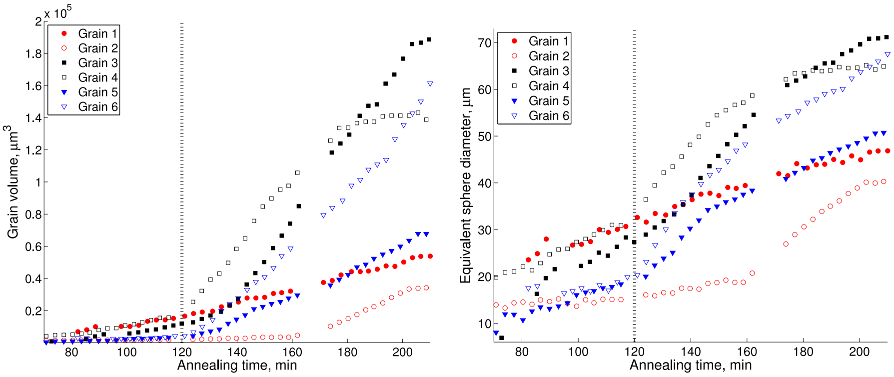

Figure 3.2: The evolution of the volume (left) and diameter (right) of 6 individual grains during recrystallization. The dashed line indicates where the temperature was raised from T_1 to T_2. For grains 2-5 the temperature was raised to $T_2 = 325°\text{C}$, and for grains 1 and 6 to $T_2 = 320°\text{C}$. The "missing" data points after time $t = 160$ min are due to ω range being increased to the full 360° so additional spatial information could be extracted using GrainSpotter [33] (see text).

	Grain number			
	2	3	5	6
Time of speed up (min)	160	141	138	195
Growth rate before speed up (μm/min)	0.10	0.50	0.42	0.24
Growth rate after speed up (μm/min)	0.54	0.71	0.62	0.40

Table 3.1: Quantification of selected kinetic speed ups at constant temperature for the recrystallizing grains shown in figure 3.2. Growth rate is defined as change in diameter per time. Note that the speed up for grain 2 is not typical for the data set, as it was the largest observed during the analysis.

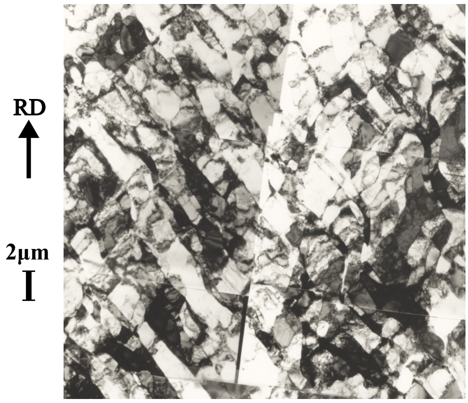

Figure 3.3: Transmission electron micrograph of the microstructure of 50% cold-rolled aluminium AA1050 courtesy of Dr. Xiaoxu Huang, Risø DTU.

by high angle boundaries, with cell blocks of typical size $\sim 4\ \mu$m for 50% cold-rolling. An example of this microstructure is shown in figure 3.3, where the cell blocks may seen to be aligned at approximately 45° to the rolling direction.

After a recrystallizing grain has reached a diameter of $d \gtrsim 4\ \mu$m, it will therefore have grain boundaries to multiple cell blocks of different orientations. Reiterating, the presently employed 3DXRD setup is estimated to have a lower detection limit of grains of diameter $d \sim 5\ \mu$m, so grains recrystallizing in a single cell block are not reliably detectable with the present method. The boundary migration rate detected with the present method is, like as was stated for the grain-averaged activation energies, a mean of the boundary migration rates of the individual boundaries weighted by the area of that boundary. Should a boundary migrate into a cell block where the boundary has a different mobility on the scale of the time resolution, then this may manifest itself as an abrupt change in recrystallization rate of the grain in question.

3.4.2 Cellular automaton model of recrystallization in aluminium

To investigate effects of the cell block microstructure on the recrystallization kinetics of an individual grain, a simple cellular automaton model was implemented. A three-dimensional array, P, representing the microstructure was set up. The array elements P_{ijk} could represent either deformed microstructure, or recrystallizing grain. The value of array elements that represented deformed matrix are referred to as a "switching probability", since the system was iter-

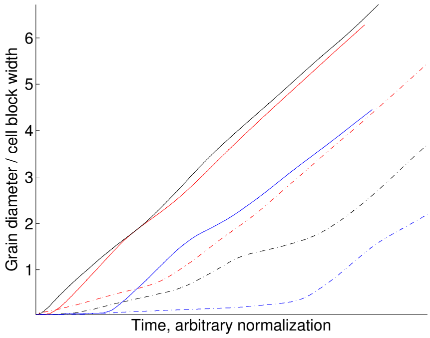

Figure 3.4: Simulated recrystallized grain diameter as a function of time. Each curve represents the output of a simulation, i.e. an individual recrystallizing grain. The cell block switching probabilities were chosen pseudorandomly from the discrete distribution (3.7).

ated forward in time by switching an array element P_{ijk} from representing the deformed matrix, to representing the recrystallizing grain, if

$$\frac{1}{6} N_{ijk} P_{ijk} > R \tag{3.6}$$

where N_{ijk} is the number of nearest neighbor array elements of array element P_{ijk} which represents the grain, rather than the deformed microstructure, and $0 \leq R \leq 1$ is a pseudorandom number. This conditional switching is done for all elements of P representing deformed matrix in each time step. The switching probability may therefore be thought of as being proportional to the mobility of the grain boundary through that particular part of the deformed matrix. For these simulations, a single array element near the center of P would be switched to represent the nucleus of the recrystallizing grain "by hand" before iteration began.

Using switching probabilities that are equal for all elements of P, and using switching probabilities that are completely random was found to lead to approximately spherical growth, and so diameter vs. time curves that were straight lines with very good approximation.

To simulate the cell block structure of cold-rolled aluminium, the elements of P was subdivided into a number of cubes of equal size representing cell blocks. All elements of a given cube were then assigned the same switching probability, which was chosen from some distribution. A nucleus was generated, and iteration began.

Six examples of simulated recrystallized grain diameters as functions of time is shown in figure 3.4. For these examples, the switching probabilities of all elements P_{ijk} within a cube was chosen from the discrete distribution

$$P_{ijk} = \begin{cases} 0.01 & \\ 0.04 & \text{for} \\ 0.16 & \end{cases} \begin{array}{l} 0 \leq R \leq \frac{1}{3} \\ \frac{1}{3} < R \leq \frac{2}{3} \\ \frac{2}{3} < R \leq 1 \end{array} \tag{3.7}$$

and $0 \leq R \leq 1$ chosen pseudorandomly.

Several different kinds of distributions, both discrete and continuous, were examined, and were found to give similar results as long as the assigned cell block switching probabilities varied sufficiently about the mean.

The resulting simulated grain sizes may in most cases be described as piecewise linear, or with changes in growth rate occuring over a short time span, which would appear piecewise linear with a poorer sampling rate. Changes in radial growth rates are observed for many simulations when the diameter of the grain is less than about 4 cell block diameters, after which the growth rate of most simulations tend towards the same value related to the average boundary mobility of the setup.

This simple model is a gross simplification of recrystallization in cold-rolled aluminium, e.g. the boundary mobilities of the cell blocks are taken to be uncorrelated spatially, and the orientation of the recrystallizing grain is not taken to be of significance. However, as the simple model predicts recrystallization rates that qualitatively resemble the observed growth rates, it is taken as supporting evidence that the recrystallization kinetics in cold-rolled aluminium is strongly affected by the cell block structure of the deformation microstructure.

3.4.3 Measurements of grain-averaged activation energies

The determination of grain-averaged activation energies with equation (3.4) was achieved by least squares fitting straight lines to a number of diffraction spots before and after the temperature increase from T_1 to T_2. This was done under visual inspection, and the specific number of diffraction spots used was selected individually both before and after the temperature increase, and for each series of diffraction spots, to give the best fit in each case. All diffraction spots would be excluded from further analysis if it was found that the grain responsible for diffraction had not grown above the detection limit ($d \sim 5$ μm) at the time of the temperature increase or if the data was too noisy for a linear fit to at least three diffraction spots both before and after the temperature increase. The reason for using series of diffraction spots rather than grain diameters was to reduce the

	Grain number					
	1	2	3	4	5	6
Q (kJ/mol)	0	98	182	199	279	547

Table 3.2: Grain-averaged activation energies of the six recrystallizing grains shown in figure 3.2.

uncertainty caused by the noise from the background, which the grain-averaged activation energies were found to be sensitive to.

These selection criteria are strict and excludes about 44% of the individual grains, but was not found to introduce significant bias, except that grains nucleated at late times (close to or after the time of the temperature increase) could not be included in the analysis.

Diffraction spots from a total of 793 individual grains were used to determine grain-averaged activation energies in the three samples. The grain-averaged energies of the 6 recrystallizing grains shown in figure 3.2 are reported in table 3.2, while the distribution of grain-averaged activation energies of the 793 individual grains may be seen in figure 3.5. Comparing table 3.2 to figure 3.2 documents that the six specific grains show the breadth of the distribution of grain-averaged activation energies. The mean of the grain-averaged activation energies is found to be $\langle Q \rangle = 187$ kJ/mol (indicated by the dashed line in figure 3.5), which is in excellent agreement with the activation energy presented for impurity-controlled recrystallization of aluminium in [50].

The activation energy for boundary migration of well-defined boundaries as a function of misorientation is presented in [48] and the references therein for various metal and alloys. The misorientation causes an approximate factor ~ 2 variation in activation energy, but this is for migration of large, almost flat boundaries of well-defined misorientation, and even so would only imply variations of a factor of ~ 2 in grain-averaged activation energies, which is significantly less than what is displayed in figure 3.5. This is an indication that the boundary migration during recrystallization occurs in a more complicated manner. The same conclusion was recently drawn [56] for examinations of recrystallization of individual grains in 96% cold-rolled nickel with a series of EBSD mappings following *ex situ* annealing steps. Stepwise and protruded boundary migration was observed with a time resolution that was comparable to the time resolution of the present 3DXRD investigation. It was argued that this more complicated boundary migration was due to atomic rearrangements occuring in the deformed matrix prior to migration of the grain boundary. This is an interesting proposition, which may explain present findings, but could not, however, be further examined with the 3DXRD data at hand.

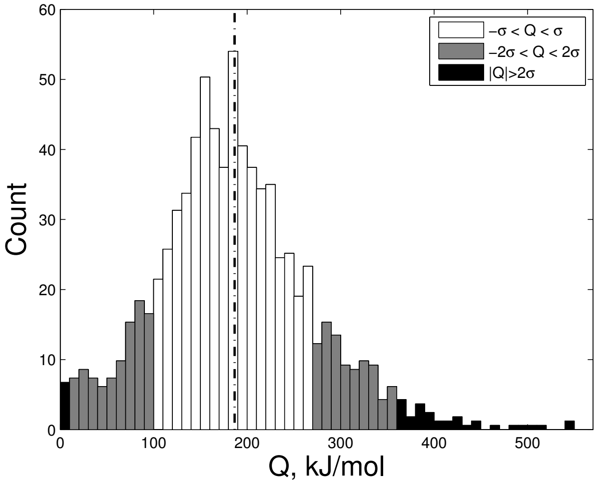

Figure 3.5: The distribution of grain-averaged activation energies of 793 individual grains recrystallizing in 50% cold-rolled aluminium. The standard deviation is found to be $\sigma = 82.9$ kJ/mol. The color of the bars indicate the confidence intervals.

The grains displaying very low grain-averaged activation energies, here taken to be $Q < 10$ kJ/mol, and exemplified by grain 1 of figure 3.2 are rare, in that they account for a total of less than 1% of the individual grains in the data sets, but are of particular interest, as the observed recrystallization rate implies that the boundary mobility is not a thermally activated process. Similar results were found in [57] through molecular dynamics simulations, where an inverse relationship between some boundary mobilities and temperature for some temperature ranges were found. This type of non-activated boundary migration was substantiated by other molecular dynamics simulations [58, 59] where diffusion-less boundary migration was observed. These findings might explain the present observations of very low grain-averaged activation energies, however the molecular dynamics investigation employed an artificial driving pressure, and simulated migration of boundaries of well-defined misorientations, which may not be applicable to present studies of recrystallization. An alternative, simpler explanation may be that a thermally activated increase in boundary migration rate was counterbalanced by a lower driving force for recrystallization, which may occur if the boundary migrates into volumes of lower dislocation density around the time of the temperature increase.

3.5 Outlook

The present investigation could have been further supported if time had permitted the analysis of the additional data (mentioned in section 3.4.1) to estimate the degree of impingement of individual grains on other grains and the sample surface.

Investigations into recrystallization kinetics of individual grains may be carried further with the experimental method described in this chapter by reducing the window of the angular rotation, thereby increasing the time resolution, at the price of a lowered statistical basis. Mapping of the deformed microstucture local to a recrystallizing grain, and comparing to the growth kinetics of that grain would seem to be the next conceptual step to be taken, but the 3DXRD method is not able to do so, and to the best knowledge of this author, no other experimental method is able to do so presently. It is possible that insight may be gained with the novel technique three-dimensional orientation mapping in the TEM (3D-OMiTEM) [60], however the limitation on the thickness of the sample is prohibitive to the study of bulk recrystallization, and so such a study would likely have to focus on recrystallization in nanocrystalline materials.

An interesting theoretical undertaking would be to attempt to incorporate a broad distribution of grain-averaged activation energies into an analytical theory such as JMAK, and compare to experiments.

Chapter 4

Grain topology and grain growth in β titanium

After recrystallization, the microstructure of a metal is polycrystalline, and so characterized as being composed of grains, which are regions of low dislocation density and almost constant crystallographic orientation, delineated by grain boundaries. The grains form an irregular, space-filling network known as the grain structure.

The presence of the grain boundaries raise the free energy of the material above that which would be found in a single crystal, and so may provide a driving force for microstructural evolution: When thermally activated, the grain boundaries will migrate to reduce the total grain boundary energy. This process is known as grain growth, and is a competitive growth process, as an increase in the size of one grain must be counterbalanced by a decrease of the size of one or more other grains to maintain the space-filling nature of the grain structure. As grain growth progresses, the number of grains in the system will decrease, thereby increasing the mean grain size of the material.

Although grain boundaries were likely the first microstructural feature discovered [48], not much progress in understanding was achieved before a seminal lecture was delivered by Smith [61] in 1948, where connections between grain boundary energies and the geometry of the grain structure, in particular the dihedral angle at a triple junction, were made. These considerations were carried further by Von Neumann in 1952 [62], working on two-dimensional soap froths, which may be taken as an approximation of a grain structure with isotropic grain boundary energies and faces of constant curvature. Von Neumanns result was rederived for an idealized grain structure by Mullins in 1956 [63], where the curvature need not be constant across grain faces:

For a grain structure with isotropic grain boundary energy per area γ, and mobility M, the rate of the local boundary migration by capillarity is taken to be the following well-known relation for migration of curved grain boundaries [48]

$$v = -M\gamma\ \kappa \tag{4.1}$$

where κ is the signed local curvature, i.e. the signed inverse radius of curvature, so $|\kappa| = 1/R$. The local dihedral angles are fixed at 120° due to the isotropy of the grain boundary energy. Together, these assumptions lead to the Von Neumann-Mullins law, relating the rate of change of the area A of a given grain to its number of faces n [63]:

$$\frac{dA}{dt} = -2\pi M\gamma \left(1 - \frac{n}{6}\right) \tag{4.2}$$

This simple expression is remarkable, as the number of faces is a purely topological quantity. Grains with more than six sides grow, grains with six sides do not grow, and grains with fewer than six sides shrink. This may be understood intuitively by considering that a grain with six sides may fulfill the requirement of dihedral angles of 120° while having faces with vanishing curvature. Grains with more than six faces will have convex faces which cf. equation (4.1) will migrate away from the grain center, thus increasing the area of the grain, and vice versa for grains with fewer than six faces.

Generalization of this result to three dimensions proved difficult, but was achieved in 2007 by MacPherson and Srolovitz [12]. The equivalent to equation (4.2) for the rate of change of a grains volume V may be written as

$$\frac{dV}{dt} = -2\pi M\gamma \left(\mathcal{L}(\mathbf{D}) - \frac{1}{6}\sum_{i=1}^{n} e_i(\mathbf{D})\right) \tag{4.3}$$

where $\mathbf{D}$ is a grain (mathematically, a bounded domain), $\mathcal{L}$ is the mean width, a measure of the size of the grain, and e_i is the length of the i^{th} triple line. The dependence on the morphology of the grain $\mathbf{D}$ is explicit in equation (4.3) to show that the pure dependence on topological quantities is broken in transitioning from two dimensions to three dimensions.

The mean width $\mathcal{L}$ is equal to twice the mean caliper diameter of the grain if the grain is convex. For any polyhedron, such as a closed, triangulated surface which may be produced by e.g. the marching cubes algorithm [64], which is relevant for the present work, the mean width may be written as (supplementary information of [12])

$$\mathcal{L} = \frac{1}{2\pi} \sum_{\forall i} \epsilon_i \beta_i \tag{4.4}$$

ϵ_i is the length of edge i, and β_i is the exterior angle at edge i, i.e. the angles between the two polygons sharing edge i measured outside the surface. Furthermore, the exterior angle must be taken positive for convex segments and negative for concave segments. The mean width of any polygonized surface is guaranteed to converge to the mean width of the smooth object, as the polygonized mesh becomes finer [12].

The three-dimensional Von Neumann-Mullins law, equation (4.2), does not readily provide analytical insight. If the problem is approached by considering a three-dimensional ensemble of grains averaged over their topological class, analytical expressions for the growth rate of these averages may be derived [65, 66]. These agree on the number of faces below which grains tend to shrink, and above which grains tend to grow of $F \approx 13.4$. Simulations with the Surface Evolver method [67], which simulated microstructural evolution due to boundary migration by capillarity, placed the number of faces higher, $F \approx 15$ [68].

In the following, these assertions will be examined by characterizations of the grain structure of a titanium alloy with edge enhanced tomography. The experimental details and segmentation procedure is explained in section 4.1. A smoothing procedure was applied to the grain structure prior to analysis, which is detailed in section 4.2. Growth predictions are determined by application of the three dimensional Von Neumann-Mullins law, and compared to a recent experimental investigation with the same focus by Rowenhorst *et al.* [69] in section 4.3. Grain growth was induced, and a second characterization is employed to experimentally investigate the validity of the growth predictions of the three-dimensional Von Neumann-Mullins law, which is presented in section 4.4.

4.1 Data acquisition and segmentation

Edge enhanced tomography was employed to characterize a sample of β titanium, Ti-21S from TIMET (datasheet is available online [70]) at the beamline ID19 at the European Synchrotron Radiation Facility (ESRF). Contrast was produced by preferentially precipitated α phase on the grain boundaries. The as-received sample was annealed for 2 hours at 725°C and air-cooled to cause α phase precipitation. An example of a cross section of the resulting data may be seen in figure 2.2 in section 2.1.1, where it is seen that the α phase precipitates preferentially, but not solely, on the grain boundaries, and some grain boundaries are decorated more than others. Segmentation of the tomographically reconstructed volume into a quantitative, computer readable form is therefore not completely trivial. The raw data was initially processed by an image filter algorithm by Dr. A. Lyckegaard, Risø DTU as detailed in [71], which corrects for ring artifacts, and enhances contrast at grain boundaries. Following this, segmentation was accomplished with the following steps:

1. The filtered volume was thresholded to a binary volume. The binary volume showed the grain structure, but not all grain boundaries were continuous, and precipitated α phase in bulk grains was common.
2. The α phase precipitated inside bulk grains was cleaned manually.
3. The cleaned volume was transformed with a Euclidian distance transform algorithm, resulting in a gray scale image where the intensity of each voxel gave its proximity to the nearest grain boundary voxel.
4. The distance transformed volume was processed with a topological watershed algorithm [72]. This algorithm may be thought of as tracing "ridges" in the distance transformed volume, i.e. locates discontinuities in the gradient, and so filled in the missing sections of grain boundary. The output was a continuous grain boundary "skeleton".
5. The grain boundary "skeleton" was visually compared to the filtered volume. Oversegmented grains, i.e. single grains that had mistakenly been subdivided by the algorithm, were merged, and the missing grain boundaries of undersegmented grains were manually defined.

A cross section of the raw images with the grain boundary "skeleton" overlaid, as was used for visual inspection of quality in step 5 of above list is shown in figure 4.1.

The data thus segmented contained 1073 grains, of which 556 are bulk grains, i.e. do not touch the sample edges. This is shown in figure 4.2. Topological quantities such as number of faces may be readily determined, and grain sizes may be determined with high precision from the voxelized data. For application of the three-dimensional Von Neumann-Mullins law (4.3), where morphology is important, a smoothing procedure is first applied, which is detailed in next section.

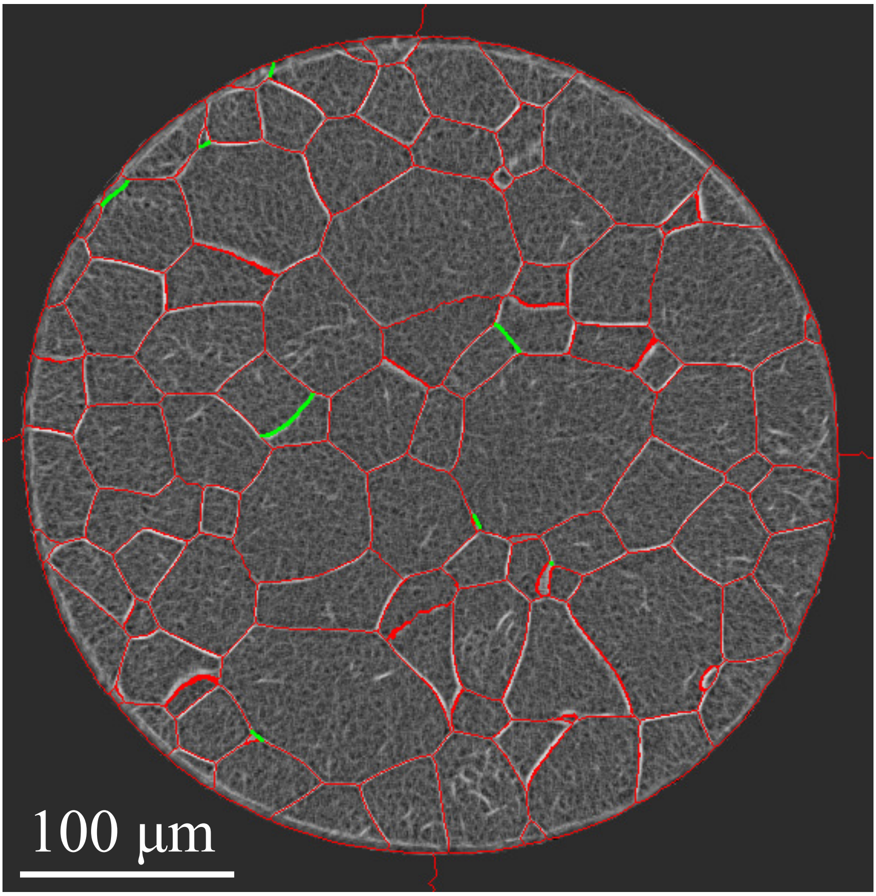

Figure 4.1: A cross section of the filtered tomographic reconstruction of the grain structure of β titanium with the grain boundary "skeleton" overlaid. Red represents the grain boundaries stemming from the watershed algorithm, green represents the grain boundaries that have been manually defined.

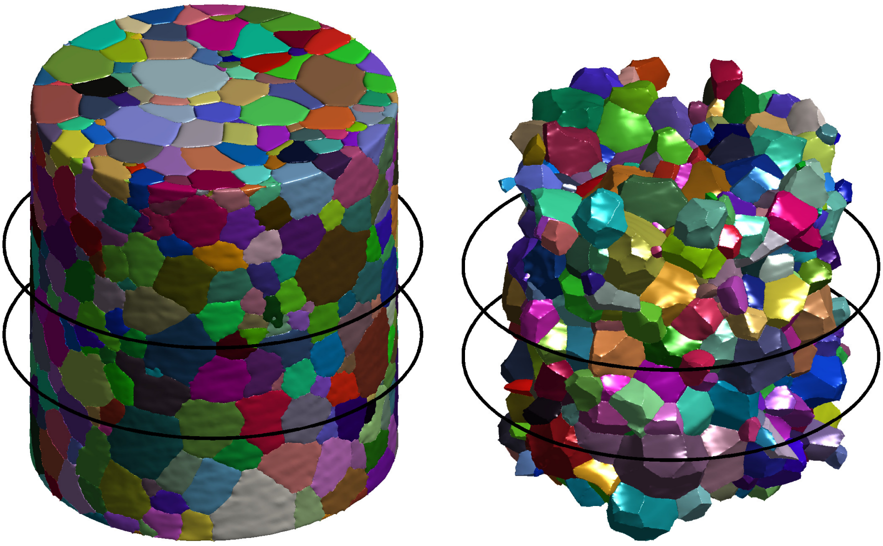

Figure 4.2: The grain structure of β titanium in the first data set. Left: All 1073 segmented grains. Right: The 556 bulk grains. The volume between the rings is a volume successfully segmented in the second data set, shown here for future reference. A smoothing procedure has been applied prior to visualization. Its details and parameters are given in section 4.2.

4.2 Iterative smoothing of the grain structure

The voxelized grain structure was triangulated on a grain by grain basis with a simplified marching cubes algorithm, which guaranteed that triangle vertices on grain faces were paired, and thus created a space-filling grain structure of triangulated grains. The vertices of each grain were divided in two classes: Face vertices, and triple line vertices, and these were treated differently during iterative smoothing:

The face vertices were moved to reduce an approximation to the Laplacian ∇^2 at that point: Vertex i at position $\mathbf{v}_i$ is iterated by [73]

$$\mathbf{v}_i^{t+1} = \mathbf{v}_i^t + \lambda \sum \left(\mathbf{v}_j^t - \mathbf{v}_i^t \right) \tag{4.5}$$

λ is a small relaxation parameter, and the sum is performed over all vertices that the i^{th} vertex is connected to by triangle edges.

The triple line vertices were first sorted according to which triple line they belong to. A cubic spline curve with fitting parameter $0 \leq p \leq 1$ was fitted to these points, using the Matlab function "csaps" from the Spline toolbox. A value of $p = 0$ gives a curve that is the least squares fitted straight line approximation, while $p = 1$ gives a smooth curve that passes through all points used for the fitting. For iterative smoothing, this should be chosen so $p \lesssim 1$. The triple line vertices were smoothed by

$$\mathbf{v}_i^{t+1} = \mathbf{v}_i^t + w \left(\mathbf{S}_i^t - \mathbf{v}_i^t \right) \tag{4.6}$$

where $\mathbf{S}_i^t$ is the point on the spline curve with the shortest distance to the i^{th} vertex, and w is a relaxation parameter akin to λ from equation (4.5).

This smoothing operation, given the relaxation parameters are chosen sufficiently small to ensure numeric stability, preserves the space-filling nature of the grain structure. An example of a grain at various degrees of smoothing is shown in figure 4.3. 70 smoothing iterations have been applied to the grain structure for the analysis in the present work. This degree of smoothing is shown in the rightmost part of figure 4.3. This two step approach was taken mainly to preserve the sharp nature and length of the triple junction lines.

A smoothing process inevitably introduces a degree of arbitrariness into the grain structure, but it was found that the smoothing applied to the grain shown in figure 4.3 caused a mean displacement of the vertices of only $\langle D \rangle \approx 0.67$ μm. The evaluation of the three-dimensional Von Neumann-Mullins equation (4.2) requires the determination of two terms. The effect of smoothing on these terms is shown in figure 4.4, where it is seen that although the effect of smoothing is substantial on both terms, it largely cancels when the difference is determined.

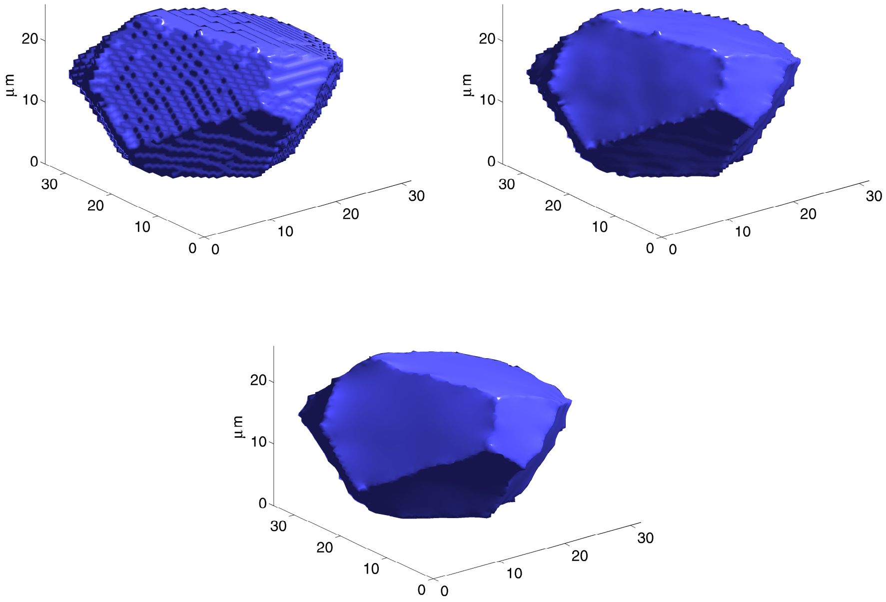

Figure 4.3: A grain with 12 faces at three stages of smoothing. The parameters were chosen as $\lambda = 0.04$, $p = 0.999$, and $w = 0.05$. Top left: 0 iterations. Top right: 10 iterations. Bottom: 70 iterations. The smoothing slows down considerably as the grain becomes smoother due to the nature of the algorithm.

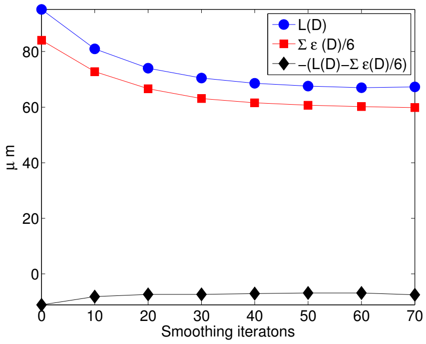

Figure 4.4: An illustration of the effect of smoothing the grain structure on the terms of the three-dimensional Von Neumann-Mullins law (4.2) for the grain shown in various stages of smoothing in figure 4.3.

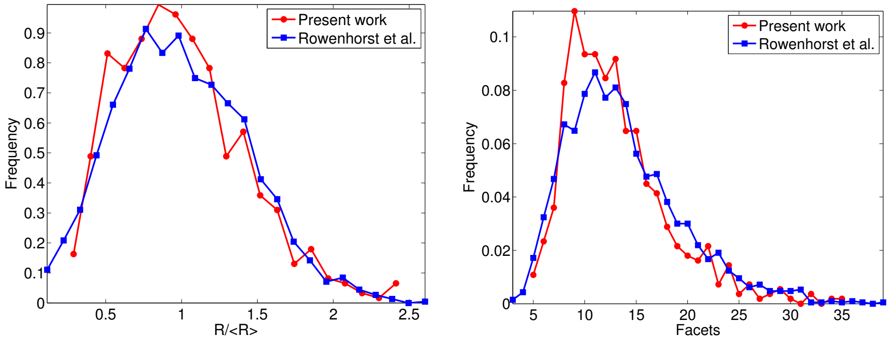

Figure 4.5: Left: Grain size distribution. Right: Distribution of faces. Data is from present work with 556 bulk grains, and from Rowenhorst *et al.* [69] with 2098 grains.

4.3 Grain structure and growth predictions

The grain size and face distributions for the 556 bulk grains of the first data set are shown in figure 4.5. Results for comparison from 2098 grains in β titanium produced by serial sectioning, published in [69] show a good correspondence, thus validating the experimental procedure. The mean grain size was found to be $\langle d\rangle \approx 37.2$ μm. The mean number of faces in the present work is found to be $\langle F\rangle \approx 13.1$, while it was $\langle F\rangle \approx 13.7$ in [69]. The relationship between grain size and number of faces is shown in figure 4.6, the mean of which shows a roughly linear relationship, but with considerable variation about the mean.

4.3.1 Growth predictions

The predicted normalized growth rate G is defined from equation (4.3) as

$$G \equiv \frac{1}{2\pi M\gamma}\frac{dV}{dt} = -\left(\mathcal{L}(\mathbf{D}) - \frac{1}{6}\sum_{i=1}^{n} e_i(\mathbf{D})\right) \tag{4.7}$$

and has been determined for the 556 individual bulk grains. This is shown in figure 4.7, along with the two terms necessary to determine this. Note that "normalized" in this context means that the G is normalized to the product $M\gamma$, so the right-hand side is independent of the materials parameters.

Focussing on the left side of figure 4.7, a linear interpolation between the two closest mean value data points was used to determine where the sign change of

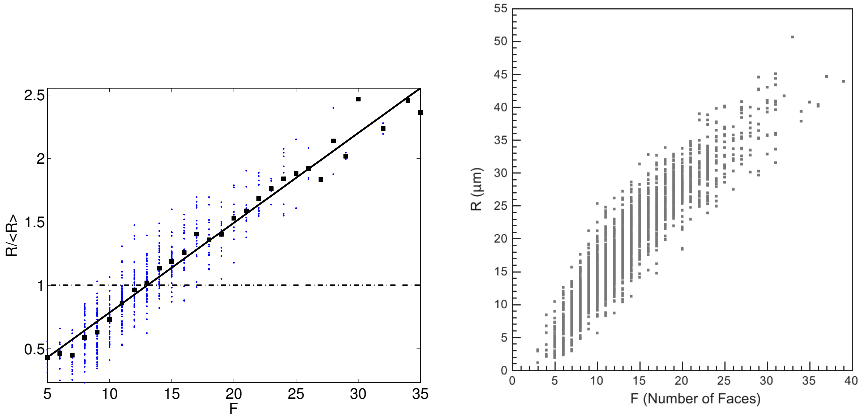

Figure 4.6: Grain size vs. faces. Left: From present work. Blue markers represent individual grains. Black dots represent average for the topological class. The black line is the least squares fit given by $R/\langle R\rangle = 0.071F + 0.078$. Right: From Rowenhorst *et al.* [69], where the mean grain radius is reported as $\langle R\rangle = 19.5\ \mu$m.

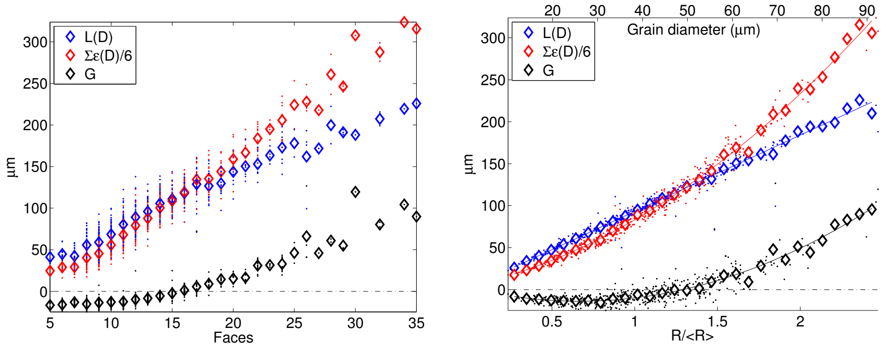

Figure 4.7: Mean width $\mathcal{L}(\mathbf{D})$, edge length $\sum \epsilon(\mathbf{D})/6$ and predicted normalized growth rate G for 566 individual grains in the present work. Left: As a function of number of grain faces. Right: As a function of normalized grain radius. Individual points are shown as dots, while mean values are shown as diamonds. Solid lines are least-squares fitted polynomials. Blue: Mean width. Fitting line is $2.38d + 3.27$. Red: Total edge length. Fitting curve is $0.017d^2 + 1.14d + 6.15$. Black: Predicted normalized growth rate. Fitting curve is $0.017d^2 + (1.14 - 2.38)d + (6.15 - 3.27)$.

the predicted growth rate G occur. This is found to be $F \approx 15.65$. The value of $F \approx 15.65$ is consistent with the value reported by Rowenhorst *et al.* [69] ($F \approx 15.5$).

The curve for G in the left part of figure 4.7 is seen to flatten significantly towards the left for $F \leq 10$. Approximative theoretical results by Glicksman [66] finds a minimal rate of shrinkage at $F = 6$. Such a minimal rate of shrinkage is not clearly observed when G is shown as a function of the number of faces, but the relative occurrence of grains with few faces is low, cf. figure 4.5, and so the statistics too poor for definitive conclusions to be drawn.

Turning attention to the right side of figure 4.7, the sign change of the normalized predicted growth rate is found by linear interpolation of two nearest data points to be at $R \approx 1.35\,\langle R\rangle$. It also shows a minimal shrinkage rate occurring for a relative grain size of $R \approx 0.7\,\langle R\rangle$, which due to the relationship between grain size and number of faces shown in figure 4.6 hints that such a minimal growth rate might also be found for G as a function of the number of faces, had data for a higher number of individual grains been available. Interestingly, the variation in mean width and total edge length (note that total edge length is divided by 6 for easy comparison with mean widths) seems to be more conveniently described by the grain size, rather than number of faces. The morphology of the grains is such, that the mean width as a function of grain size falls on a straight line with good approximation, while the total edge length is approximately parabolic. The average values of the mean width and total edge length have been fitted with polynomials, and this is also shown in figure 4.7 (right), along with the fitting curves (parameters in figure text), where it is seen that the polynomials give an excellent fit. The fitting curve of the predicted normalized growth rate G predict the sign change to occur at $R = 1.3\,\langle R\rangle$, and the predicted normalized growth rate appears to be (keeping in mind that this is an extrapolation) increasing with grain size for large grain sizes, as was found by Glicksman [66] to be the case for growth rate of grains with many faces. No underlying topological and/or morphological explanation for this observation will be offered. The roughly approximate linear relationship between number of grain faces and grain sizes, figure 4.6 puts a minimal growth rate at $\langle F\rangle \approx 9$ but this must be taken as a hypothesis, due to the many averagings and two polynomial fittings employed. However, that the mean width with good approximation is given by a straight line is interesting: Such a scaling is expected as a simple size effect, cf. equation (4.4), but the grains considered here are of many different topological classes, thus it seems that this grain structure is such that the topological class of the grains do not affect the average mean width much.

The growth predictions put forth by Rowenhorst *et al.* are presented in terms of a slightly different quantity called *normalized integral mean curvature* $\mathcal{G}$ which is dimensionless. The mathematical correspondence is $2\pi G/V^{1/3} = \mathcal{G}$, where V

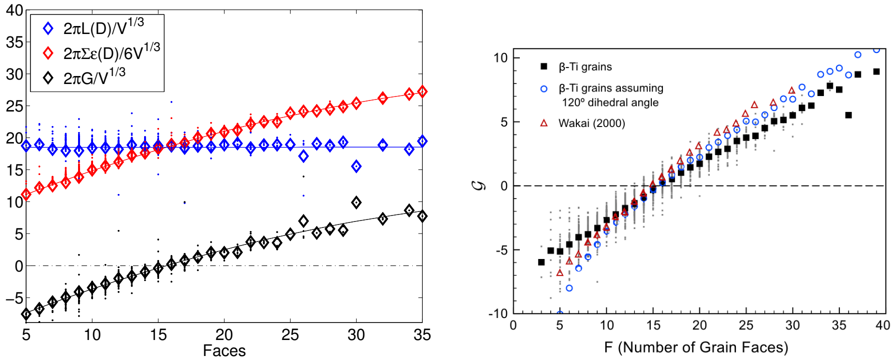

Figure 4.8: Normalized predicted growth rates. Left: From the present work. Solid lines are least-squares fitted polynomials. Red: Mean width $2\pi\mathcal{L}(\mathbf{D})/V^{1/3}$, fitting line is $0.0006F+18.50$. Blue: Edge length $2\pi\sum\epsilon(\mathbf{D})/6V^{1/3}$, fitting curve is $-0.0085F^2+0.8693F+7.0$. Black: Normalized integral mean curvature $\mathcal{G}=2\pi G/V^{1/3}$, fitting curve is $-0.0085F^2+(0.8693-0.0006)F+(7.0-18.50)$. Right: From Rowenhorst *et al.* [69]. Blue points: $\mathcal{G}$ determined with the same method as in present work. Black points: $\mathcal{G}$ determined with a variation of the method employed in present work. This is argued to result in higher fidelity than the method employed in present work.

is the volume of the grain in question. The correspondence is shown in figure 4.8, with the results from present work left and the results from Rowenhorst *et al,* [69] right. This normalization results in average quantities that are very well described in terms of the number of grain faces. The method employed to determined mean widths and edge lengths in the present work corresponds to the blue points on the the right of figure 4.8, but inspection shows that the values of the normalized integral mean curvature $\mathcal{G}$ for the present work correspond better to the black points on the right of figure 4.8. Rowenhorst *et al.* argues that the method employed to determine the integral mean curvature $\mathcal{G}$ shown as the black points give more accurate results than the one employed to determine the blue points. That the results from the present work correspond better to the black points is assumed to be the result of the smoothing scheme employed in the present work, which seems to preserve the sharp nature of the triple junctions better than the scheme employed by Rowenhorst *et al.* The good fit of the straight line to the mean width $\mathcal{L}(\mathbf{D})$ in figure 4.7 (right, blue line), as well as the extrapolated mean width of vanishing grain $\mathcal{L}(\mathbf{D})\approx 0$ is taken to be evidence that the smoothing procedure does not show dependence on the grain size for the grain sizes investigated in the present work. The "flatness" of the fitting line corresponding to mean width $\mathcal{L}(\mathbf{D})$ in figure 4.8 (left, blue) is taken as a consequence of this as well.

4.4 Grain growth of 31 individual grains

After the characterization resulting in the data set investigated in previous sections, a second characterization was performed: The sample was annealed for 2 hours at 860°C as both solution treatment and to induce grain growth. The recommended solution time and temperature is $3 - 30$ min at $816 - 843$°C [70], and so the α precipitates are assumed to dissolve fast compared to the grain growth of the β phase. The sample was water quenched, and annealed for 11 hours at 730°C to again allow α phase precipitation, before the sample was characterized again. The quality of this second raw data set, however, was significantly poorer than the first, due to a higher fraction of α phase precipitation in bulk grains. The segmentation procedure thus became very time consuming, and only 150 contiguous voxel layers (105 μm) of the sample was successfully segmented. Note that the poor quality of the raw data of the second data set increased the segmentation time, but is not believed to have lowered the fidelity of the segmented volume.

Examinations of the second data set reveals that approximately 7/8 of the grains in the first data set have been eliminated, corresponding to an increase in the mean grain size by a factor of ~ 2, and so significant grain growth has occurred.

As the crystallographic orientation of the grains are not determined with the described experimental method, there is no simple, direct way of determining the correspondence between grains in the two data sets. An identification has been performed by Dr. I. M. McKenna, Northwestern University. The procedure is described in detail in [74]. The procedure consisted of determining the center of mass of all grains in the segmented part of the second data set, and projecting them into the first data set. If the projected point was in the bulk of a grain in the first data set, the grains were assumed to be identical. This is believed to give good results when the growth is not highly directional, and the growth has been sufficiently small. This procedure identified 31 individual grains completely contained in the segmented volumes of the two data sets. These are shown in figure 4.9 at the two stages of grain growth. It is important to note that a significant bias has been introduced: Grains that have been eliminated during the grain growth has not been identified, and grains that are large compared to the segmented volume of the second data set are underrepresented, as their large sizes make it improbable that they are completely contained in the small segmented volume of the second data set. The 31 grains therefore do not constitute a representative set, and strongly favor small grains.

The observed grain sizes, and number of faces of the 31 grains before and after grain growth is shown in figure 4.10. Shrinkage is observed for grains 1-25, no appreciable size change for grains 26 and 27, and slight growth is observed for

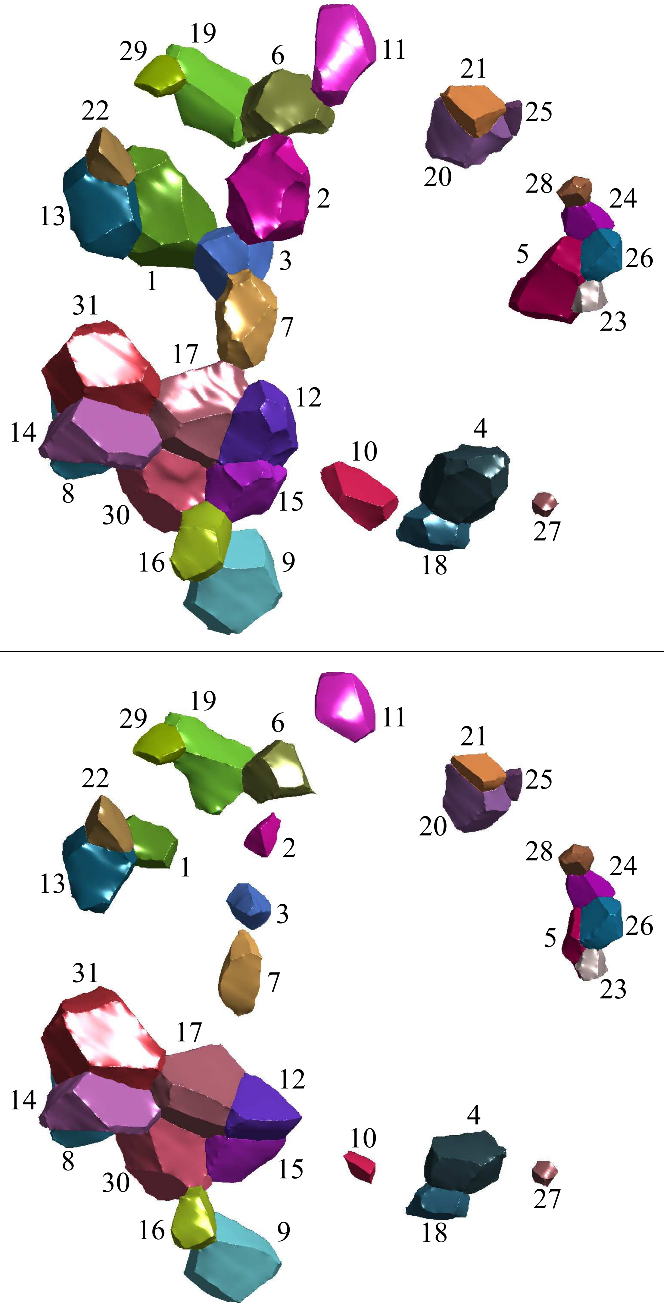

Figure 4.9: Top view of the 31 grains in β titanium contained in the segmented volume as they are located in the sample. Top: First data set (before grain growth). Bottom: Second data set (after grain growth).

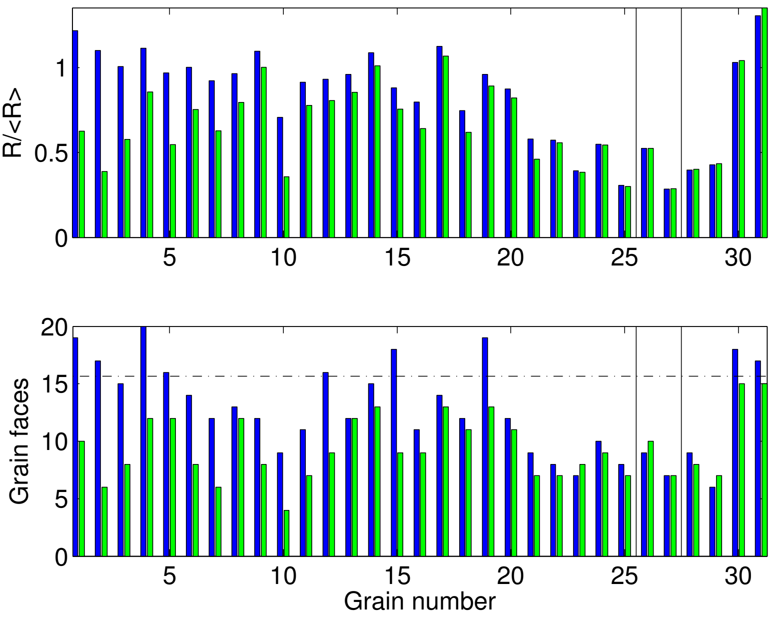

Figure 4.10: Normalized grain size (top) and number of faces (bottom). The normalizing grain size is the mean grain size of the first data set. Blue bars: Time 1 (before grain growth). Green bars: Time 2 (after grain growth). Grains are sorted so the largest measured net growth is rightmost. The dash-dotted line in the bottom figure marks the number of faces above which a grain on average is predicted to grow, $F = 15.65$. All 31 grains are smaller than the predicted size necessary for growth, $R = 1.3 \langle R \rangle$. Negative, approximately zero, and positive net growth rates are grouped by vertical lines.

grains 28-31. All grains are observed to lose at least one face, except grains 13 and 27 for which the number of faces is unchanged, and grains 23, 26 and 29 which gain a single face. Note that all grains are of a smaller size than is predicted to cause growth on average $R \approx 1.35 \langle R \rangle$, while grains 1, 2, 4, 5, 12, 15, 21, 30 and 31 have more faces than that the number that is predicted to cause growth on average $F \approx 15.65$.

The normalized predicted growth rate G as defined in equation (4.7) gives predictions for the growth of individual grains. The quantity G is defined as a time derivative, and is therefore subject to change on the time scale of grain boundary migration in the system. Such variations will not be captured by the two acquired data sets, so only the sign of the normalized predicted growth rate will be considered. The observed relative change in volume $\Delta V/V$ is shown alongside G in figure 4.11.

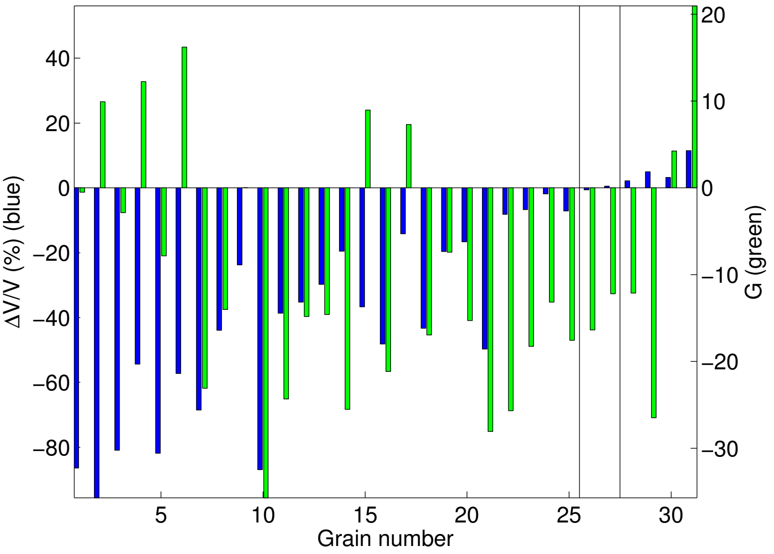

Figure 4.11: Comparison between the observed relative change in volume (blue bars, left axis), and the normalized predicted growth rate G (green bars, right axis) of the 31 individual grains. Negative, approximately zero, and positive net growth rates are grouped by vertical lines as in figure 4.10.

The grains which are observed to undergo negative growth, are found to mainly have normalized predicted growth rates that are also negative, however, 5 are seen to be positive. To investigate this discrepancy, the normalized predicted growth rates are determined for these grains in the second data set, i.e. after grain growth. These are all negative. The observed negative net growth rate of these grains may thus in some cases be explained by these grains undergoing a topological and/or morphological change during growth, which changes the sign of the growth rate, so that an initially growing grain begins shrinking. Such topological and/or morphological changes causing a transition from positive to negative growth rate must occur with some frequency during grain growth, as a necessity for competitive growth.

The two grains with an observed net growth rate of approximately zero, grains 26-27, show a predicted negative growth rate, and this is also the case when G is determined for the grains after the grain growth. It seems unlikely that a topological and/or morphological change should occur twice, i.e. that an negative growth rate becomes positive, and then again negative, resulting in a net growth rate of zero. The two grains with the lowest positive net growth rate, grains 28-29, are likewise seen to have a predicted negative growth rate in both data sets. The two grains with the highest positive net growth rate observed, grains 30-31, both have a positive predicted growth rate.

In total, the sign of the growth of 22 grains is correctly predicted by the three-dimensional Von Neumann-Mullins equation (4.3). The growth of 5 additional grains may arguably have been predicted correctly, but this cannot be investigated further without a higher time resolution. This gives between $71 - 87\%$ correct predictions. When considering the problem at hand, and the experimental method employed for this study, the discrepancy between experimental observations and theoretical growth predictions are not surprising, mainly due to two factors: Firstly, the considerable grain growth occurring between experimental characterizations (mean grain size increasing a factor of ~ 2). The three-dimensional Von Neumann-Mullins equations (4.3) is a differential quantity, and thus the growth predictions should ideally be compared to experimental characterizations with a very fine time resolution to examine the validity of the predictions. Secondly, the three-dimensional Von Neumann-Mullins equation (4.3) is derived for a three-dimensional infinite soap froth, meaning that surface effects are neglected, and isotropy is assumed, which is never realized for metals. Although a correlation between predicted and observed growth has been observed, further studies should be performed. Finally, α phase precipitates slow to dissolve during the solution treatment would affect the grain boundary migration. The α phase precipitates are assumed to not interfere significantly with the grain growth, mainly due to the temperature and length of the combined solution treatment and grain growth (2 hours at 860°C, compared to a recommended solution treatment of 3-30 min at $816-843$°C), but this may also have affected the grain growth.

4.5 Outlook

It has been shown that edge enhanced tomography may provide three-dimensional data sets of high fidelity. The method described should therefore be applied to larger samples, so the application of the three-dimensional Von Neumann-Mullins equation (4.3) could be done with a better statistical basis. In particular, additional statistics on grains with a low number of faces would reveal if a minimal growth rate could be observed for a topological class of grains, which is hinted at by the normalized growth rate G in figure 4.7. The simple polynomial forms of the average mean width and edge length are intriguing, and it would be interesting to seek an explanation related to the geometry of the grain structure.

The experimental method applied for characterization of grain structure is not sensitive to crystallographic orientation, and so the relationship between grains at different stages of grain growth must be inferred, which is a weakness of the technique. Application of a different technique, e.g. diffraction contrast tomography (DCT) from section 2.2.2, would allow direct investigations into grain growth with a good time resolution, at the price of a poorer resolution of the grain boundaries, which could however be applied to a larger class of materials, because it does not require precipitation of a second phase on the grain boundaries. Alternatively, a 3DXRD scan could be employed to determine crystallography and center of mass of the grains using e.g. GrainSpotter [33], which gives center of mass positions accurate to about 5 μm. These could then be mapped into the grain structure determined by edge enhanced tomography to positively identify the grains through their crystallographic orientation. By 3DXRD, it would be possible to follow the grain sizes during growth *in situ*, with detailed morphological information determined at the beginning and end by edge enhanced tomography.

Chapter 5

Coupled grain growth and coarsening of dual-phase materials

As stated in the introduction, the original intention was to study coupled grain growth and coarsening by a combination of experimentally characterized microstructures and large-scale phase-field simulations. The chosen material was duplex steel 2205, which is an austenitic/ferritic alloy. The characterization was attempted by a combination of two techniques:

Holotomography, as is described in section 2.1.2, was employed to produce a high-resolution map of the phase structure. Other well-known methods, e.g. absorption tomography, could not be employed, as there is only a slight difference between the magnitudes of the X-ray attenuation in the two phases. A proof-of-concept holotomographic reconstruction of a sample of this specific alloy, and comparisons to reconstructions produced by other methods has been published in [30], and was shown in figure 2.3. The holotomographic reconstruction was of good quality. A cross section of the reconstruction is shown in figure 5.1 (right).

Diffraction Contrast Tomography (DCT) as is described in section 2.2.2 was employed in order to generate a grain map including crystallographic information.

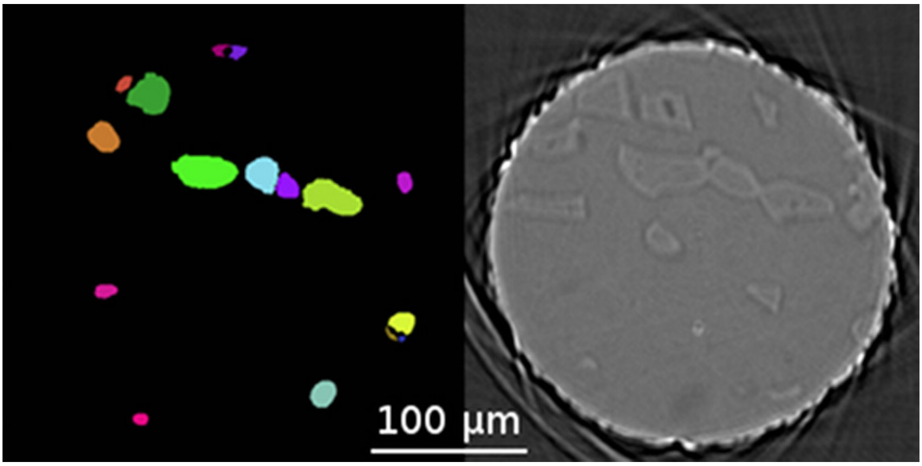

Figure 5.1: Cross sections of tentative reconstructions of duplex steel 2205, courtesy of Dr. Wolfgang Ludwig, ESRF. Left: DCT reconstruction of austenite grains. Right: Holotomographic reconstruction. Lighter domains are austenitic.

DCT is in principle sufficient to fully characterize the grain and phase structure of the stainless steel, but there are two main points to using both techniques: First, that holotomography gives a higher resolution, space-filling phase map, which may be used to assist in the dilation procedure, which as is mentioned in section 2.2.2 is necessary to ensure that grain maps produced by DCT are space-filling. Second, that the phase map may supply information to the DCT reconstruction algorithm about phase and spatial position of grains that may not have otherwise been found by the algorithm.

The experimental characterization failed, as the DCT reconstruction algorithm was unable to properly segment smaller austenite grains. This is believed to be due to residual stresses between the austenitic and ferritic phases which would tend to blur the diffracted images, thus reducing contrast. An example of a DCT reconstruction alongside a holotomographic reconstruction is found in figure 5.1, which clearly shows austenitic domains in the holotomographic reconstruction that the DCT reconstruction algorithm has not been able to find.

The DCT reconstruction algorithm is a sophisticated piece of software, that is under continual development. Extending the algorithm to better accommodate reconstruction of duplex steel 2205 was unfortunately deemed outside the scope of current Ph.D. project, and so experimentally determined initial conditions, and reconstructions of microstructures characterized after annealing could not be acquired. Focus was therefore shifted to simulations of coupled grain growth and coarsening from "artificial" initial conditions.

In the following, the phase-field method will be sketched briefly in section 5.1 for readers unfamiliar with the method. The method will be discussed and compared to other well-known modelling frameworks in section 5.2, and applied to the specific case of coupled grain growth and coarsening in polycrystalline dual-phase materials in section 5.3. The mathematical details of the model employed is found in section 5.3. Details regarding numeric implementation of the solver is found in section 5.4, and finally simulations are presented and quantified in section 5.5.

5.1 Phase-field modelling of microstructural evolution

In recent years phase-field modelling has emerged as one of the preferred mesoscale modelling methods in materials science. That the method has been used to simulate phenomena as diverse as grain growth, both isotropic, e.g. [75–77] and anisotropic, e.g. [78, 79], solidification, e.g. [80–82], Ostwald ripening, e.g. [83], crack propagation, e.g. [84], domain coarsening in dual-phase structures, e.g. [85], and many more, is a testament to its unique versatility.

The phase-field framework has been largely developed in a series of papers by Cahn, Hilliard and Allen [86–88]. This development predates the widespread access to computer power that is taken for granted today, and so was applied only to systems where insight could be gained analytically. The practical applicability of the phase-field method has increased enormously with computing power, but is still based on the original derivation. Several reviews and texts providing comprehensive introductions to the method with varying focus have been published, see e.g. [82, 89–91], however, citing [91] *"An exhaustive review of the field is nearly impossible due to the broad range of applications."*

5.1.1 Phase-field variables

An idea central to the method is to describe all microstructural features of interest by *phase-field variables.* The phase-field variables are defined in the entire system, and are required to be smooth in space and time (the dependence on space and time will be suppressed for brevity in the following). Interfaces are then represented by a smooth variation between some equilibrium values in one or more phase-field variables. The method therefore belongs to the class called *diffuse interface* methods, as all interfaces in the system take on a width that is non-zero and specific to the type of interface.

Diffuse interface theory may be traced back to the early work on gas/liquid interfaces by Van der Waals, see e.g. [92], in which the density of the fluid was taken to vary smoothly across interfaces, and the work of Landau [93] on second-order phase transitions. The phase-field method may be viewed as a continuation of this work.

Specific examples of phase-field variables are e.g. one representing a molar fraction of some chemical constituent in a system with several chemically distinct phases, or one representing the solid/liquid state in a solidification problem. A molar fraction has an intuitive physical interpretation, and equilibrium values given by the problem, but a solid/liquid state is more ambiguous. Its equilibrium values may be set arbitrarily, but are usually taken to be 0 and 1 in the literature. Domains where the phase-field variable attains values ~ 0 could then be interpreted as the system being completely liquid in those domains, and values ~ 1 as the system being completely solid. Domains containing values in between are considered interfacial regions.

5.1.2 Free energy of a system with interfaces

Since the phase-field variables are taken to describe all microstructural features of interest, i.e. defines the state of the system everywhere, it must be possible to express the Gibbs free energy F as a functional of these (F could also be taken as the Helmholtz free energy, if more applicable to the problem at hand).

For a system defined by N phase-field variables, $\phi_1, \phi_2 \cdots \phi_N$, the free energy is first taken to be a functional of a local free energy, f, which in turn is taken to be a function of all phase-field variables and their gradients up to second order

$$F = \int_\Omega f\left(\phi_1, \cdots, \phi_N, \nabla\phi_1, \cdots, \nabla\phi_N, \nabla^2\phi_1, \cdots, \nabla^2\phi_N\right) d\mathbf{r} \tag{5.1}$$

Here Ω denotes the entire system volume. So the local free energy is assumed to only be a function of the local microstructural configuration and its immediate surroundings.

Taking f to be a smooth function, it may be Taylor expanded about f_0, termed the bulk free energy, which is the local free energy of a homogeneous microstructure, i.e. a system with no gradients, and is an inherently non-linear quantity. The expanded expression is truncated, and a series of symmetry considerations then lead to the simplified expression [86]

$$F = \int_{\Omega} \left(f_0 \left(\phi_1, \cdots, \phi_N \right) + \sum_{i=1}^{N} \frac{\epsilon_i}{2} \left| \nabla \phi_i \right|^2 \right) d\mathbf{r} \tag{5.2}$$

The constants ϵ_i are called gradient energy coefficients. They may be viewed as "energy penalties" associated with interfaces, and should therefore be taken non-negative, to ensure positive interfacial energies. The magnitude of the gradient energy coefficients are related to the width of the interface in question: "small" gradient energy coefficients result in numerically "large" gradients, i.e. narrow interfaces, and vice versa.

The bulk free energy, f_0, should have a number of minima defining the position in phase-field space of the equilibria of the system, i.e. minimas should be placed at positions in phase-field space corresponding to the microstructural configurations that are in equilibrium far from interfaces. For a solidification problem where the solid/liquid state of the system is expressed by a single phase-field variable ϕ, $f_0(\phi)$ could be a simple double-well function with minima placed at $\phi = 0$ (liquid) and $\phi = 1$ (solid).

The interfacial energy σ which expresses the excess free energy associated with having interfaces in the system may be determined as [86]

$$\sigma = \int_{\Omega} \left(\Delta f + \sum_{i=1}^{N} \frac{\epsilon_i}{2} \left| \nabla \phi_i \right|^2 \right) d\mathbf{r} \tag{5.3}$$

where Δf is defined as the difference between the bulk free energy, f_0, and the free energy found by the common tangent plane approximation. The interfacial energy is thus composed of contributions from both Δf and from gradients in the phase-field variables.

5.1.3 Governing equations

If the free energy functional F, equation (5.2), is not at a minimum, the excess free energy will provide a driving force for microstructural evolution. Before proceeding, a distinction must be made between phase-field variables that are conserved, e.g. a molar fraction of a constituent, and those that are non-conserved, e.g. solid/liquid state in a solidifying system. For clarity, conserved variables are designated C_i, while non-conserved variables are designated ϕ_i, so

$$\frac{\partial}{\partial t} \int_{\Omega} C_i d\mathbf{r} = 0 \tag{5.4}$$

$$\frac{\partial}{\partial t} \int_{\Omega} \phi_i d\mathbf{r} \neq 0 \tag{5.5}$$

The requirement (5.4) assumes conservative boundary conditions, e.g. periodic or reflective. If non-conservative boundary conditions were used, the right-hand side should be replaced by the flux into the volume Ω at the boundary $\partial\Omega$. The conserved phase-field variables are *required* to fulfill (5.4), while the non-conserved variables are *allowed* to fulfill (5.5), as a given subset of initial conditions may cause any or all ϕ_i to be conserved.

The minima of the free energy functional, and so the equilibrium microstructural configurations, are characterized by a vanishing functional derivative with respect to all phase-field variables [23]

$$\frac{\delta F}{\delta C_i} = \frac{\delta F}{\delta \phi_j} = 0 \text{ for all } i \text{ and } j \tag{5.6}$$

The functional derivative may be thought of as a generalized gradient: Where the gradient of a scalar function of several variables points in the direction of steepest increase, the functional derivative of a scalar functional gives the "direction" in function space that the functions should be changed to increase the functional most steeply. This is the justification for assuming that the non-conserved phase-field variables evolve in time according to [88]

$$\frac{\partial \phi_i}{\partial t} = -L_i \frac{\delta F}{\delta \phi_i} = -L_i \left(\frac{\partial f_0}{\partial \phi_i} - \nabla \cdot \epsilon_i \nabla \phi_i \right) \tag{5.7}$$

The ϵ_i of this equation is the gradient energy coefficient of the phase-field variable in question, and the L_i are mobilities. This equation is known as the Allen-Cahn equation or the Time-Dependent Ginzburg-Landau equation, and is a second-order in space, first order in time partial differential equation.

The conserved phase-field variables are governed by the Fick's first law diffusion equation. The flux of the i^{th} conserved phase-field variable $\mathbf{j}_i$, is taken to be given by

$$\mathbf{j}_i = -M_i \nabla \frac{\delta F}{\delta C_i} \tag{5.8}$$

Here M_i is a mobility. The intuitive understanding of this equation is that the negative variational derivative expresses the "direction" the phase-field variable should be changed to lower the free energy of the system, while the spatial derivative gives the direction of the flow, so that density will flow from domains where it causes excess free energy, to domains where it causes less excess free energy.

Conservation is guaranteed by subjecting the flux to the continuity equation

$$\frac{\partial C_i}{\partial t} = -\nabla \cdot \mathbf{j}_i = \nabla \cdot M_i \nabla \frac{\delta F}{\delta C_i} = \nabla \cdot M_i \nabla \left(\frac{\partial f_0}{\partial C_i} - \nabla \cdot \epsilon_i \nabla C_i \right) \tag{5.9}$$

This equation is known as the Cahn-Hilliard equation [86], which is a fourth order in space, first order in time partial differential equation.

In the Allen-Cahn and Cahn-Hilliard equations, (5.7) and (5.9), the mobilities L_i and M_i and the gradient energy coefficients ϵ_i need not be constant, although they are taken as such in the present work. See e.g. [90] for a review of approaches.

5.2 Discussion of the method

The phase-field framework has been sketched. It is a method rooted in thermodynamics, where the time evolution of a system with N conserved - and M non-conserved phase-field variables in general is accomplished by solving N fourth order in space, first order in time, and M second order in space, first order in time partial differential equations, that are coupled through the non-linear bulk free energy, f_0. Therefore, solution of the system of equations may be performed using standard numeric methods for non-linear partial differential equations as may be found in e.g. [94], while analysis of simple cases, e.g. planar boundaries, may be performed with approximate methods known from e.g. boundary layer theory in fluid dynamics, as may be found in e.g. [95]. The method is completely deterministic (unless stochastic effects are deliberately added), in contrast to Monte-Carlo Potts methods for microstructural evolution, as presented in e.g. [96].

The most immediate advantage of using the phase-field method to model microstructural evolution is inherent in the diffuse interfaces: The lack of a need for front tracking. Consider, as an example, a physical system where particles in a liquid matrix are undergoing Ostwald ripening. This could be analyzed by solving a diffusion equation subject to boundary conditions on the surfaces of the particles. The surfaces, however, are not fixed in time, as matter is transported from regions of larger mean curvature to regions of smaller mean curvature. This type of problem, where boundary conditions must be imposed on moving boundaries, is known as a Stefan problem, and is considerably more difficult to solve than when all boundaries are stationary [97]. No such considerations are necessary within the phase-field framework, as all interfaces are handled implicitly by solving the governing equations (5.7) and (5.9). Here, boundary conditions need only be imposed on the external boundaries of the system.

The width of the diffuse interfaces are a possible concern: The widths of physical interfaces between microstructural features, e.g. grain boundaries, are usually measured in Å or nm. In phase-field simulations of complex microstructures, this width must currently be taken significantly higher, on the order of μm, to allow numeric resolution of the interfaces on a computational grid. This has been shown to not necessarily be a problem by Fan *et al.* using a phase-field model of grain growth. Quoting [98]: *if there are enough grid points to resolve a diffuse boundary, the migration velocity of a diffuse grain boundary is exactly the same as that of a sharp grain boundary, even for a very small grain whose size is comparable to the grain boundary width.* The sufficient number of grid points through the interface is there found to be 7, but the sufficient width of the interfaces should be investigated in any new phase-field model prior to large-scale simulations, to ensure that the simulated microstructural evolution is not a consequence of the numeric resolution.

As a modelling framework, the phase-field method has similarities to the level set method, see [99, 100] for reviews, in that microstructural features there are also represented by smooth functions, known as level set functions, and that microstructural evolution is simulated by solving first order in time partial differential equations. The level set functions only represent features with fronts: They are positive inside the feature in question, negative outside, and the interface is taken to be where the level set function vanishes. Microstructural evolution is simulated by subjecting the level set functions to a continuity equation, where a front velocity is supplied which may depend on the front orientation and may be coupled to external physics. It is known that the accuracy of the solution is dependent on the initial choice of profile. This effect is so important that it has led to the notion of *reinitialization*, where the interface contour is periodically determined, so the level set profile may be reset to one beneficial for numerical accuracy. This increases programming complexity and reduces execution speed when done frequently, a problem which is not present in the phase-field framework. Even if reinitialization is not required, the interfaces must oftentimes be continually tracked. In e.g. [101] the level set method is applied to growth of faceted crystals, front tracking is employed to halt growth when crystal interfaces come into contact.

When developing a phase-field model, the main difficulty is in determining a bulk free energy function, f_0 of equation (5.2), to capture the physics of the problem. In the literature, there are two main branches in how to approach this problem: The bulk free energy function may be supplied by a thermodynamics database or chosen phenomenologically, with the vast majority of publicized models favoring the latter. Using a thermodynamic database, e.g. [90] provides a measure of confidence in the simulation output, at the cost of reduced transparency. The phenomenological models are usually constructed as Landau polynomials [93]. Correspondence to physical systems is then sought by tuning model parameters until the model output reproduces physically measurable quantities, e.g. equilibrium triple junction angles, boundary migration rates, etc. with a top-down approach.

5.3 Phase-field model for simulation of coupled grain growth and coarsening in dual-phase materials

The phase-field model employed is presented in detail in this section. The model was used to simulate grain growth and coarsening in systems where the two phases were taken to be identical in the sense that all materials parameters were equal for the two phases, which are distinguished by a chemical difference. All grain boundary mobilities and grain boundary energies were taken equal and isotropic. The model will, however, be presented in more generality, and the choice of parameters leading to the specific case used for simulation in present work will be noted.

5.3.1 Phase-field variables

We consider a dual-phase material where the phases are denoted α and β. The α phase is taken to be subdivided into N_α grains, each having a unique crystallographic orientation, and β phase likewise subdivided into N_β grains. A non-conserved phase-field variable is assigned to represent each unique crystallographic orientation. The α phase grains are thus described by N_α phase-field variables which are denoted $\alpha_1, \alpha_2, \ldots, \alpha_{N_\alpha}$, while the β phase grains are described by N_β phase-field variables, denoted $\beta_1, \beta_2, \ldots, \beta_{N_\beta}$.

The chemical composition of the system is taken to be defined by a single conserved phase-field variable, C, which may be interpreted as a molar fraction. If the model is to be applied to many-component alloys, C should represent the slowest diffusing element, under assumption that the diffusion kinetics is dominated by this constituent. The equilibrium composition in the two phases are taken to be given by C_α and C_β, where we take $C_\alpha < C_\beta$ by definition.

Altogether, $N_\alpha + N_\beta + 1$ phase-field variables are used to describe the microstructure. The $N_\alpha + N_\beta$ degenerate equilibria in phase-field variable space, as will be made to correspond to minima of the bulk free energy f_0, are taken to be given by

$$\alpha_i = 1,\, \alpha_{j\neq i} = 0,\, \beta_k = 0,\, C = C_\alpha \tag{5.10a}$$

$$\beta_l = 1,\, \beta_{m\neq l} = 0,\, \alpha_n = 0,\, C = C_\beta \tag{5.10b}$$

where $i = 1, 2, \cdots, N_\alpha$, $k = 1, 2, \cdots, N_\beta$, $l = 1, 2, \cdots, N_\beta$ and $n = 1, 2, \cdots, N_\alpha$. Thus equilibria will be placed where a single α phase-field variable has the value

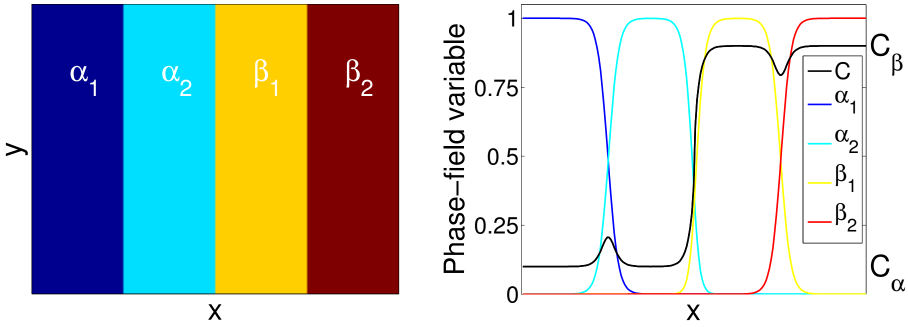

Figure 5.2: Four planar grain boundaries at equilibrium. Left: Qualitative cross section. Right: Equilibrium phase-field profiles in the model presented in present chapter. The composition profile clearly shows segregation at the grain boundaries. This will be covered in section 5.3.8.1.

1, $C = C_\alpha$, and all other phase-field variables have the value 0, and vice versa for β. In other words, the equilibria are to be placed so free energy is minimized if spatial domains are occupied by only one α grain given that the composition is $C = C_\alpha$, or equivalently one β grain if the composition is $C = C_\beta$.

An illustration of a system with two α grains and two β grains is shown in figure 5.2.

5.3.2 Bulk free energy function f_0

The free energy of the system (5.2) may be written as

$$F = \int_\Omega \left(f_0 + \frac{\epsilon_\alpha}{2} \sum_{i=1}^{N\alpha} |\nabla \alpha_i|^2 + \frac{\epsilon_\beta}{2} \sum_{i=1}^{N\beta} |\nabla \beta_i|^2 \right) d\mathbf{r} \tag{5.11}$$

as all grain boundary energies of the same type ($\alpha\alpha, \alpha\beta$ and $\beta\beta$) are considered equal, the gradient energy coefficients has been taken outside the summations in the more general equation (5.2). Note that there is no gradient energy coefficient associated with the compositional variable C. This does not mean that the compositional profile across an interphase boundary will be sharp. Coupling between the compositional variable C, and the other phase-field variables in the system will be introduced in this section. Without a gradient energy coefficient in C, the Cahn-Hilliard equation governing the time evolution of this conserved phase-field variable, equation (5.9), reduce to a first order in time, second order in space partial differential equation, which improves the numerical stability of the system. The price, however, is that it becomes more difficult (but not impossible) to tune the $\alpha\beta$ boundary energies, which will be elaborated on briefly later in this section.

The bulk free energy, f_0, is in present work chosen as a phenomenological quantity, a Landau polynomial of fourth order in α_i, β_i and C. It is defined as

$$f_0 = f_C + \sum_{i=1}^{N\alpha} f_{C\alpha} + \sum_{i=1}^{N\beta} f_{C\beta} + \sum_{i=1,j\neq i}^{N\alpha} f_{\alpha\alpha} + \sum_{i=1,j\neq i}^{N\beta} f_{\beta\beta} + \sum_{i=1}^{N\alpha}\sum_{j=1}^{N\beta} f_{\alpha\beta} \tag{5.12}$$

Defining $C_m = \frac{1}{2}(C_\alpha + C_\beta)$, the 6 functions in the bulk free energy are defined as

$$f_C = -\frac{A}{2}\left(C - C_m\right)^2 + \frac{B}{4}\left(C - C_m\right)^4 + \frac{D_\alpha}{4}\left(C - C_\alpha\right)^4 + \frac{D_\beta}{4}\left(C - C_\beta\right)^4 \tag{5.13a}$$

$$f_{C\alpha} = \frac{\gamma_\alpha}{2}\left(\left(C - C_\alpha\right)^2 - \left(C - C_\beta\right)^2\right)\alpha_i^2 + \frac{\delta_\alpha}{4}\alpha_i^4 \tag{5.13b}$$

$$f_{C\beta} = \frac{\gamma_\beta}{2}\left(\left(C - C_\beta\right)^2 - \left(C - C_\alpha\right)^2\right)\beta_i^2 + \frac{\delta_\beta}{4}\beta_i^4 \tag{5.13c}$$

$$f_{\alpha\alpha} = \frac{\epsilon_{\alpha\alpha}}{2}\alpha_i^2\alpha_j^2 \tag{5.13d}$$

$$f_{\beta\beta} = \frac{\epsilon_{\beta\beta}}{2}\beta_i^2\beta_j^2 \tag{5.13e}$$

$$f_{\alpha\beta} = \frac{\epsilon_{\alpha\beta}}{2}\alpha_i^2\beta_j^2 \tag{5.13f}$$

$A, B, D_\alpha, D_\beta, \gamma_\alpha, \gamma_\beta, \delta_\alpha, \delta_\beta, \epsilon_{\alpha\alpha}, \epsilon_{\beta\beta}$ and $\epsilon_{\alpha\beta}$ are positive parameters, many of which will be fixed due to thermodynamic concerns in section 5.3.5, as the wanted positions of the minima, (5.10) have not yet been enforced. Note that $\epsilon_{\alpha\alpha}$, $\epsilon_{\alpha\beta}$ and $\epsilon_{\beta\beta}$ should not be confused with the gradient energy coefficients ϵ_α and ϵ_β.

The 6 terms of the bulk free energy (5.12) have specific functions. As implied by the subscripts, $f_{C\alpha}$ and $f_{C\beta}$ creates coupling between the compositional phase-field variable C and α and β type phase-field variables respectively. Coupling between α type phase-fields is introduced by $f_{\alpha\alpha}$ and by $f_{\beta\beta}$ for β type phase-fields, while coupling between α and β type phase-fields is introduced by $f_{\alpha\beta}$. These affect the respective boundary widths and boundary energies, and so $f_{\alpha\beta}$ may be used to gain some control over the energy and width of the $\alpha\beta$ boundary, which due to the lack of a gradient energy coefficient related to C would otherwise not have been possible. Exactly how much control this gives has not been quantified, as it has not been important in the present work. All the terms containing products of squares may be intuitively understood as raising the free energy when both terms are non-zero: e.g. $f_{\alpha\alpha}$ will reduce overlap between α type phase-field variables, as having two α type phase-fields be non-zero at any point in space will raise the local free energy. The function f_C as well as the fourth order terms in $f_{C\alpha}$ and $f_{C\beta}$ are introduced to ensure enough mathematical degrees of freedom to allow the parameters to be set in a way which ensures thermodynamic consistency.

5.3.3 Governing equations

All grain boundary mobilities and the diffusional mobility are considered constant and isotropic. With these assumptions the model parameters may be taken outside the differential operator ∇ so the time evolution of the compositional phase-field variable C governed by the Cahn-Hilliard equation (5.9) simplify to

$$\frac{\partial C}{\partial t} = M\nabla^2 \frac{\partial f_0}{\partial C} \tag{5.14a}$$

and the Allen-Cahn equation (5.7) governing the α and β type phase-field variables simplify to

$$\frac{\partial \alpha_i}{\partial t} = -L_\alpha \left(\frac{\partial f_0}{\partial \alpha_i} - \epsilon_\alpha \nabla^2 \alpha_i \right), \; i = 1, 2, \ldots, N_\alpha \tag{5.14b}$$

$$\frac{\partial \beta_i}{\partial t} = -L_\beta \left(\frac{\partial f_0}{\partial \beta_i} - \epsilon_\beta \nabla^2 \beta_i \right), \; i = 1, 2, \ldots, N_\beta \tag{5.14c}$$

Here M is the diffusional mobility, while L_α and L_β are grain boundary mobilities. Thus, the Laplacian ∇^2 is the only spatial differential operator in the partial differential equations governing the time evolution of the simulations.

5.3.4 Normalization of governing equations

The governing equations as presented in equations (5.14) contain degrees of freedom which are mathematically superfluous. A partial normalization of the governing equations can be performed by normalizing space and time by defining

$$\mathbf{r}' = \frac{\mathbf{r}}{\sqrt{\epsilon_\alpha}} \qquad t' = L_\alpha t \qquad M' = \frac{M}{L_\alpha \epsilon_\alpha} \qquad L'_\beta = \frac{L_\beta}{L_\alpha} \qquad \epsilon'_\beta = \frac{\epsilon_\beta}{\epsilon_\alpha}$$

and writing the governing equations in terms of these primed variables. This is mathematically equivalent to setting $L_\alpha = \epsilon_\alpha = 1$ in the governing equations (5.14b), which can therefore be done with no loss of generality. Thus, this method is chosen, rather than the introduction of the primed variables above.

5.3.5 Conditions for thermodynamic equilibrium

The minimas of the bulk free energy f_0 are to be placed according to equations (5.10), which is achieved by fixing the values of some model parameters. First requiring the bulk free energy to have extrema at these positions in phase-field space is done by requiring

$$\left.\frac{\partial f_0}{\partial \alpha_i}\right|_{C=C_\alpha}^{\alpha_i=1} = \left.\frac{\partial f_0}{\partial \alpha_i}\right|_{C=C_\beta}^{\alpha_i=0} = 0, \text{ where all } \alpha_{j\neq i} = 0 \text{ and all } \beta_j = 0$$

$$\left.\frac{\partial f_0}{\partial \beta_i}\right|_{C=C_\beta}^{\beta_i=1} = \left.\frac{\partial f_0}{\partial \beta_i}\right|_{C=C_\alpha}^{\beta_i=0} = 0, \text{ where all } \beta_{j\neq i} = 0 \text{ and all } \alpha_j = 0$$

which gives the four requirements

$$\gamma_\alpha = \frac{1}{8}BX^2 - \frac{1}{2}A + D_\beta X^2 \tag{5.15a}$$

$$\gamma_\beta = \frac{1}{8}BX^2 - \frac{1}{2}A + D_\alpha X^2 \tag{5.15b}$$

$$\delta_\alpha = X^2\gamma_\alpha \tag{5.15c}$$

$$\delta_\beta = X^2\gamma_\beta \tag{5.15d}$$

where $X \equiv C_\beta - C_\alpha$ has been defined. Requiring that these extrema are minima

$$\left.\frac{\partial^2 f_0}{\partial \alpha_i^2}\right|_{C=C_\alpha}^{\alpha_i=1} > 0, \text{ where all } \alpha_{j\neq i} = 0 \text{ and all } \beta_j = 0$$

$$\left.\frac{\partial^2 f_0}{\partial \alpha_i^2}\right|_{C=C_\beta} > 0, \text{ where all } \alpha_j = 0 \text{ and all } \beta_j = 0$$

$$\left.\frac{\partial^2 f_0}{\partial \beta_i^2}\right|_{C=C_\beta}^{\beta_i=1} > 0, \text{ where all } \beta_{j\neq i} = 0 \text{ and all } \alpha_j = 0$$

$$\left.\frac{\partial^2 f_0}{\partial \beta_i^2}\right|_{C=C_\alpha} > 0, \text{ where all } \beta_j = 0 \text{ and all } \alpha_j = 0$$

along with the usual common tangent assumption across an interphase boundary

$$\left.\frac{\partial f_0}{\partial C}\right|_{C=C_\alpha}^{\alpha_i=1} = \left.\frac{\partial f_0}{\partial C}\right|_{C=C_\beta}^{\beta_i=1} = 0 = \frac{f_0|_{C=C_\alpha}^{\alpha_i=1} - f_0|_{C=C_\beta}^{\beta_i=1}}{C_\alpha - C_\beta}$$

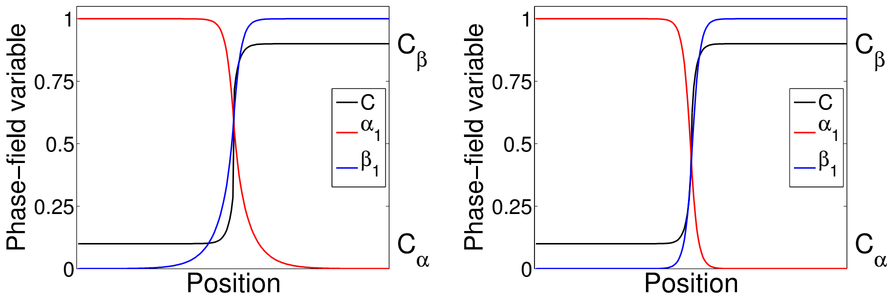

Figure 5.3: A planar $\alpha\beta$ grain boundary. Left: Using the bulk free energy function by Chen and Fan presented in [102–105]. Right: Using the bulk free energy function from present work.

gives two additional requirements of positivity

$$\gamma_\alpha > 0 \tag{5.16a}$$

$$\gamma_\beta > 0 \tag{5.16b}$$

5.3.6 Comparison to Chen and Fan model

The employed model is derived from that presented by Chen and Fan in [102–105], which was used to investigate the topological evolution of coupled grain growth and coarsening in two dimensions. That model seems to be an extension of the model presented in [83], which was used to simulate Ostwald ripening.

The model employed in present work uses a bulk free energy function f_0 that differs from that by Chen and Fan. Two new terms, $f_{\alpha\alpha}$ and $f_{\beta\beta}$, equations (5.13d) and (5.13e) have been added. This is done to be able to vary the width of the $\alpha\alpha$ and $\beta\beta$ boundaries, and allows for determination of asymptotic solutions of planar boundary profiles, as shown in section 5.3.7.

Examinations of intraphase boundaries using the model of Chen and Fan reveals that the phase-fields representing crystallographic orientation couple rather weakly to the composition, resulting in crystallographic interfaces that are significantly wider than the compositional interface. This is shown in the left side of figure 5.3. These differing interface widths may be unwanted, as they may result in e.g. two grains of the same phase interacting through an intermediate grain of the other phase. The reason for this behaviour is revealed by examination of the terms responsible for coupling between crystallographic phase-fields and composition. In the notation of present work, the equivalent of equation (5.13b) in the work by Chen and Fan is

$$f_{C\alpha} = -\frac{\gamma_\alpha}{2}\left(C - C_\beta\right)\alpha_i^2 + \frac{\delta_\alpha}{4}\alpha_i^4 \qquad \text{(Chen \& Fan)}$$

It is seen that C expanded around $C = C_\beta$ does not have a linear term: An α type phase-field variable forming an interface with a β type phase-field variable tapers off towards 0 as C approaches $C = C_\beta$. However, when $C \sim C_\beta$ the local excess free energy will be a product of two small factors squared and thus not significant enough to couple strongly. Vice versa for β.

This coupling has been strengthened in the bulk free energy function in current work by using the coupling term (5.13b):

$$f_{C\alpha} = \frac{\gamma_\alpha}{2}\left(\left(C - C_\alpha\right)^2 - \left(C - C_\beta\right)^2\right)\alpha_i^2 + \frac{\delta_\alpha}{4}\alpha_i^4 \qquad \text{(this author)}$$

which is seen to always have a term linear in C, which strengthens the coupling considerably, as is shown in the right side of figure 5.3.

5.3.7 Asymptotic solutions and width of planar interfaces

The equations governing the time evolution of the phase-field variables (5.14a), (5.14b) and (5.14c) have been investigated analytically for the simple cases of a planar ($\alpha\alpha$, $\alpha\beta$, or $\beta\beta$) boundary. Exact solutions have not been determined, and it is doubtful if these can be expressed in terms of well-known functions, but sets of approximate solutions forming planar interfaces have been determined. Details may be found in appendix A.1.

It was found that choosing $D_\alpha = D_\beta$, and thus $\gamma_\alpha = \gamma_\beta$ ensures that all planar interfaces in the system attain same width, and allows asymptotic solutions to planar grain boundaries to be determined: Choosing

$$\epsilon_{\alpha\alpha} = \epsilon_{\alpha\beta} = \epsilon_{\beta\beta} = 3X^2\gamma_\alpha - \frac{16X^2\gamma_\alpha^2}{3BX^2 + 12D_\beta X^2 - 4A} \qquad (5.17)$$

ensures that the asymptotic solutions are in good correspondence to numeric solutions where the phase-field variables are ~ 1. This in turn allows the width of the interfaces to be expressed as

$$W = \frac{8}{\sqrt{\xi}} \quad \text{where} \quad \xi = \epsilon_{\alpha\alpha} - X^2\gamma_\alpha \qquad (5.18)$$

with the interface width defined as the length between where the α and/or β type phase-field variable forming the planar interface attains values of 0.98.

Note that this definition of interface width is arbitrary. The model parameters mentioned in this section were set as prescribed here, to allow for comparisons between simulation output and numeric solutions.

5.3.8 Model parameters for large-scale simulations

The computational requirements for large-scale three-dimensional simulations prohibit a real parameter study. Therefore, the model parameters not yet fixed were chosen with a degree of arbitrariness. These were chosen as

$$C_\alpha = 0.1, \;\; C_\beta = 0.9, \;\; A = 5, \;\; B = 4.5, \quad D_\alpha = 6, \;\; M = 1, \;\; L_\beta = 1 \tag{5.19}$$

and so the remaining parameters are fixed due to the normalization of section 5.3.4, to ensure correspondence between numeric and asymptotic solutions, section 5.3.7, and by the requirement of thermodynamic consistency, section 5.3.5.

Numeric determination of the boundary energies of the three types of planar boundaries, as given by equation (5.3) gives the following energetic ratios

$$R_\alpha = \frac{\sigma_{\alpha\alpha}}{\sigma_{\alpha\beta}} = R_\beta = \frac{\sigma_{\beta\beta}}{\sigma_{\alpha\beta}} \approx 0.8 \tag{5.20}$$

which according to the analysis by Cahn [106] means that the three types of triple junctions ($\alpha\alpha\alpha, \alpha\alpha\beta, \alpha\beta\beta$, and $\beta\beta\beta$) are stable with equilibrium triple junction angles of

$$120.0^\circ, 120.0^\circ, 120.0^\circ \quad \text{for } \alpha\alpha\alpha \text{ and } \beta\beta\beta \tag{5.21a}$$

$$113.6^\circ, 113.6^\circ, 132.8^\circ \quad \text{for } \alpha\alpha\beta \text{ and } \alpha\beta\beta \tag{5.21b}$$

where the larger angle in (5.21b) is the angle between the two interphase boundaries. Also, according to [106], no quadrijunctions may be stable. These assertions have been confirmed by inspection of output from simulations. The interface widths are cf. appendix A.1 found to be equal to $W \approx 6.95$.

5.3.8.1 Boundary segregation

Segregation of solute to $\alpha\alpha$ interfaces and away from $\beta\beta$ interfaces is an unavoidable phenomenon in the present model, as was also found in [102]. As impurity drag is known to affect boundary migration rates, see e.g. [48], it has been investigated in some detail here, as impurity drag was not the focus of this study.

Examining the asymptotic solution for the compositional profile at an e.g. $\alpha\alpha$ boundary, equation (A.4) reveals that $\gamma_\alpha = 0$ is a necessary criteria for a flat compositional profile, and this is forbidden by the criteria for thermodynamic consistency (5.16). In other words, $\gamma_\alpha = 0$ would decouple the compositional phase-field variable from the α type phase-field variables, and lead to simulated behaviour that would not reflect the physical problem in question.

A reductio ad absurdum treatment to show that boundary segregation is unavoidable in current model which does not rely on approximate solutions requires solving the Cahn-Hilliard equation (5.14a) in its time independent form, across an e.g. $\alpha\alpha$ interface (phase-field variables α_1 and α_2), while requiring that $C = C_\alpha$ everywhere:

$$0 = \nabla^2 \frac{\partial f_0}{\partial C}\bigg|_{C=C_\alpha} \Rightarrow \nabla^2 \left(1 - \sum_{i=1}^{2} \alpha_i^2\right) = 0$$

which due to the boundary conditions valid for a planar $\alpha\alpha$-interface

$$\lim_{x\to-\infty} \alpha_1 = 1, \quad \lim_{x\to\infty} \alpha_1 = 0, \lim_{x\to-\infty} \alpha_2 = 0, \quad \lim_{x\to\infty} \alpha_2 = 1$$

give the requirement

$$1 - \sum_{i=1}^{2} \alpha_i^2 = 0$$

which, when imposed on the two equations governing α_1 and α_2, equation (5.14b) in their time invariant form leads to

$$\nabla^2\alpha_1 = \nabla^2\alpha_2 = 0$$

and as this is incompatible with solutions with interfaces, it is concluded that boundary segregation is an inherent feature of this model.

As the model is too complicated to readily give analytical insight into solute segregation to moving boundaries, this has been examined numerically with simulations using the solver also employed for large-scale simulations. A two-dimensional simulation where a round α grain was embedded in another α grain was set up on a grid of 512^2 points and a grid spacing of $\Delta h = 2/3$. The round grain was represented by the phase-field variable α_1, and the embedding grain by α_2. The composition was set to $C = C_\alpha$ everywhere, periodic boundary conditions were imposed, and the simulation was executed until the round grain had been eliminated.

The position of the interface and the radial interface profile as a function of time is shown in figure 5.4 for various times. It is seen that the round grain retains

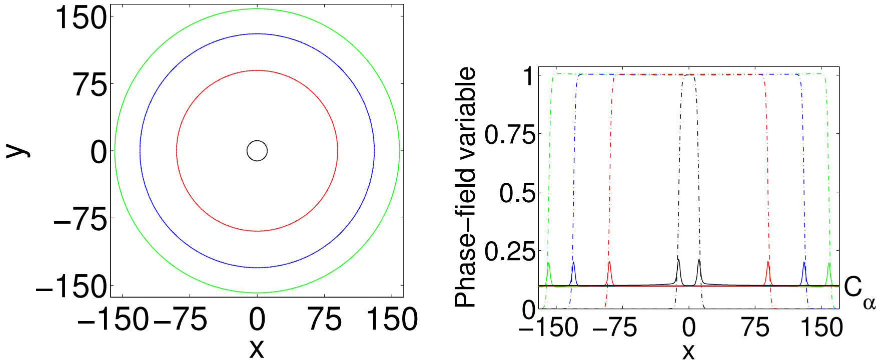

Figure 5.4: Two-dimensional simulation of a round α grain embedded in an α grain. Left: Position of the interface at times (outermost to innermost) $t = 50.000, t = 500.000, t = 1.000.000$, and $t = 1.440.000$. Right: Radial profiles of the phase-field variable representing the round grain (broken lines), and the composition profile, C (full lines), at the times corresponding to left figure. The profiles of the surrounding grain are not shown.

its shape while shrinking, and that profiles of both α_1 and C largely retain their shape.

The area of the round grain vs. time is shown in figure 5.5. The evolution of the area is found to be given by a straight line with very good approximation, except at times very close to the elimination of the grain. When close to elimination, the grain area vs. time is observed to speed up, rather than slow down, which supports that it is not an effect of impurity drag. It has been found by inspection of simulation output to be due to the grain radius becoming too small to support local equilibrium phase-field variable profiles, rather than an effect of boundary segregation. The departure from linearity is found to occur at a grain size of $d \approx 8$, which is less than the width (cf. section 5.3.8) needed to support two interfaces, $d \approx 8 < 2W \approx 13.90$.

This implies that the grain boundary velocity is proportional to the radius of curvature of the grain, $\kappa = 1/R$, where R is the radius of the grain, and so $v \propto \kappa$, as is known for grain growth in pure materials [11, 48]. Thus, it is concluded that boundary segregation at most affects the grain boundary migration rate by introducing a new, effective grain boundary migration rate in the present model with the chosen parameters at the radii of curvature the model in its current setup can simulate accurately.

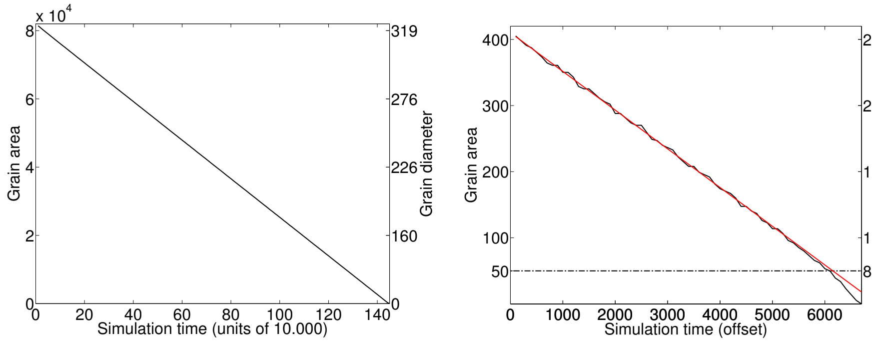

Figure 5.5: Area of a round α grain embedded in an α grain as function of time. Left: For all simulation times. Right: Zoom in on late times. Time is here offset by 144.000. Black line shows simulation output, red line is a least squares fitted straight line. A departure from the straight line is at a grain size of $d \approx 8$.

5.4 Implementation

Details regarding the implementation of the solver used for large-scale simulations is found in this section. Systems of partial differential equations can be solved easily by simple numeric methods, but efficient solution of large-scale problems requires both careful optimization and choice of methods and algorithms.

For present work, a numeric solver has been implemented in High Performance Fortran (HPF) [107], which is an extension of Fortran 90. The code was parallellized for execution on computer clusters using the MPI-2.0 [108] specifications. Both HPF and MPI-2.0 are *de facto* standards in high-performance computing, and have both commercial and open source implementations. Furthermore, MPI-2.0 gives a high degree of flexibility, as correctly written code may be executed efficiently on distributed memory clusters which may be composed of shared memory machines that need not be homogeneous.

5.4.1 Discretization of space and time

Numeric solution of partial differential equations on computers requires discretization of the continuous governing equations. The Laplacian is in current

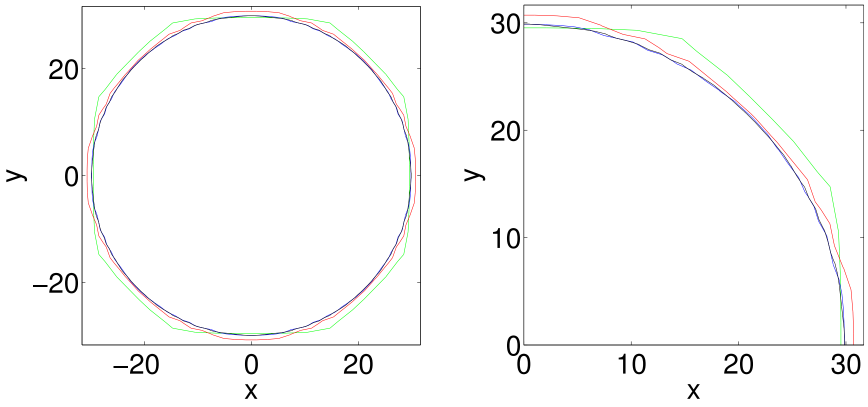

Figure 5.6: Equilibrium shape of a β grain embedded in an α grain for different grid spacings. Green curve: $\Delta h = 2$, red curve: $\Delta h = 1$, blue curve: $\Delta h = 2/3$, black curve: $\Delta h = 1/2$.

implementation discretized on a regular grid by the finite difference stencil

$$\nabla^2 x_i \approx \frac{1}{\Delta h^2} \sum_{j \in n.n.} (x_j - x_i) \tag{5.22}$$

where Δh is the grid spacing, and the sum extends over the nearest neighbor grid points, and so has six terms for a three-dimensional grid. The grid spacing is of particular importance: too large a grid spacing will introduce grid oriented anisotropy, as the interfaces then become non-smooth. On the other hand, too small a grid spacing will increase the computational time, as this is proportional to the number of grid points in the computational domain. The effect of changing the grid spacing has been illustrated by determining the two-dimensional equilibrium shape of a β phase grain embedded in an α phase grain for various grid spacings in figure 5.6. It is seen that the grain attains the round shape expected for an isotropic boundary energy at grid spacings $\Delta h = 2/3$ and $\Delta h = 1/2$. The grid spacing was thus set to $\Delta h = 2/3$ for all large-scale simulations.

This choice of grid spacing results in profiles with 12 grid points through planar interfaces, with equation (5.18) as the definition of interface width, as shown for an $\alpha\beta$ interface on figure 5.7. If the width of an interface was instead defined as the width of the region where phase-field variables attain values between 0.1 and 0.9, the presently chosen grid spacing results in 7 points through planar interfaces.

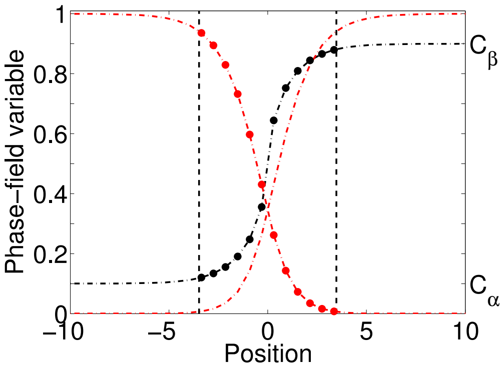

Figure 5.7: Planar $\alpha\beta$ interface with grid point positions shown. Dashed lines marks the interface.

Time stepping is done by the forward Euler method, where

$$\left.\frac{\partial x}{\partial t}\right|_{t=t_0} \approx \frac{x(t_0+\Delta t)-x(t_0)}{\Delta t} \tag{5.23}$$

where Δt is the time step, which was set to $\Delta t = 0.01$ for the large-scale simulations. This value was found to not introduce significant numeric errors by comparing output from simulations with this time step to output from simulations with shorter time steps.

The chosen numeric scheme has thus transformed the system of coupled partial differential equations into a system of algebraic equations with an explicit time stepping method. Methods based on discrete Fourier transforms may be found in the literature, e.g. [109], which allows for longer time steps to be taken over the methods presented here. When these simple schemes were still chosen for present problem, there were two reasons: First, for ease of writing parallellized code to be executed on computer clusters. Fourier methods are generally non-local, and although parallellized Fourier methods exist (e.g. the open source FFTW library [110]), the efficiency drops due to communication overhead. Second, to be able to easily accommodate non-periodic boundary conditions.

5.4.2 Sparse matrix data structure for α and β type phase-field variables

The main computational problems when performing simulations with many phase-field variables are the high computer memory requirements and computational time necessary for large-scale simulations. Both the memory required, and the duration of the calculation will increase linearly with the number of phase-field variables. Consider a simulation on a grid of 512^3 grid points. Holding a single phase-field variable in memory with an array of 8 byte floating point variables requires 1 GB of RAM, thus to simulate 1000 unique grain orientations with the present model would require ~ 1 TB of memory, rendering large-scale simulations impossible, even on modern hardware.

Various approaches to extend the possible scale of phase-field simulations with many phase-field variables representing unique crystallographic orientations may be found in the literature, but all begin from the observation that only a few phase-field variables are appreciably different from 0 at any point in space, e.g. for the present model, a phase-field variable of α or β type has appreciable values only in and near the domain containing the grain represented by that phase-field variable, i.e. grain bulk and boundary.

A scheme for simulating grain growth using a fixed number of phase-field variables to represent the grain orientation were presented in [75] for two-dimensional simulations. Several different grain orientations were represented in a single phase-field variable. This introduces the problem that growth may now proceed by coalescence, rather than by boundary migration, i.e. grain orientations represented by the same phase-field variable may come into contact. It was found that setting the required fixed number of phase-field variables to $p \gtrsim 36$. It was later argued that $p \gtrsim 100$ is required [76]. There, an adaptive redistribution of the non-zero volumes of a fixed number of phase-field variables were introduced, i.e. assigning one of two grains about to coalesce to another phase-field variable. A number of $p \gtrsim 20$ was found to limit coalescence. This was in two-dimensions still, so in three dimensions the number must be expected to be substantially higher, to allow for a higher number of grain neighbors in three dimensions.

A bounding box algorithm was proposed in [111] to accommodate an in principle infinite number of phase-field variables during grain growth. The position of the appreciably non-zero regions ($\geq \eta$, for some suitable value of η) of a phase-field variable were tracked, and a box were defined containing those values, one for each phase-field variable. This algorithm effectively provides a means to avoid storing and solving for the domains of the phase-field variables where the values were close to 0.

For the present work, a sparse data structure for the α and β type phase-field variables was implemented, following [112]. A data type, *grid_entry*, containing an integer identifier I, a real value V, and a pointer to a *grid_entry* was introduced. Here, I distinguishes between different phase-field variables with the convention that $I < 0$ is an α type phase-field variable, and $I \geq 0$ is β type. The pointer allows the *grid_entry*s to form a singly linked list, so entries may be added and removed on-the-fly as needed.

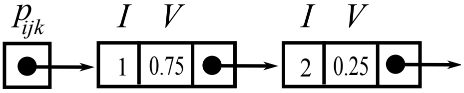

Figure 5.8: Sketch of the sparse matrix data structure for a single grid point, p_{ijk}. Two phase-field variables are non-zero at the grid point, both of β type: $\beta_1 = 0.75$ and $\beta_2 = 0.25$.

A three-dimensional grid of pointers to *grid_entry*s was set up to represent the computational grid. This is sketched for a single point in the computational grid in figure 5.8. A grid of integers, *num_entries* was introduced to hold the length of the list at each grid point.

A small cut off value η was introduced, and entries were inserted into or removed from the structure at each time step, according to the entries found at the nearest neighbor grid points:

- An entry with $I = i$ and $V < \eta$ is removed from a grid point, if no nearest neighbor grid point has an entry with $I = i$ and $V \geq \eta$.
- An entry with $I = i$ and $V = 0$ is added to a grid point, if the grid point does not already have an entry with $I = i$ and a nearest neighbor grid point has an entry with $I = i$ and $V \geq \eta$.

This is depicted qualitatively in figure 5.9 for a grain boundary during migration. The cut off value was set to $\eta = 0.0001$ for the large-scale simulations. This value was shown in [112] to result in negligible differences between simulations with and without sparse data structures, which was confirmed for the present model by comparing output from simulations with varying cut off values.

This approach allows for an unlimited number of α and β type phase-field variables. The memory required scales with the interfacial area in the system, as does the computational time needed for an Euler time step. The method can furthermore be easily extended to include, e.g. anisotropic effects.

When the cut off value η is increased, the simulations show lower boundary migration rates, and a degree of grid oriented anisotropy as unwanted artifacts of the numeric scheme. The anisotropy would likely be decreased if the criteria for adding and removing entries were not based on nearest neighbor grid points, but on both nearest- and next-nearest neighbor points. The choice to not do so was to increase the efficiency of the parallellization, which is elaborated upon in section 5.4.4.

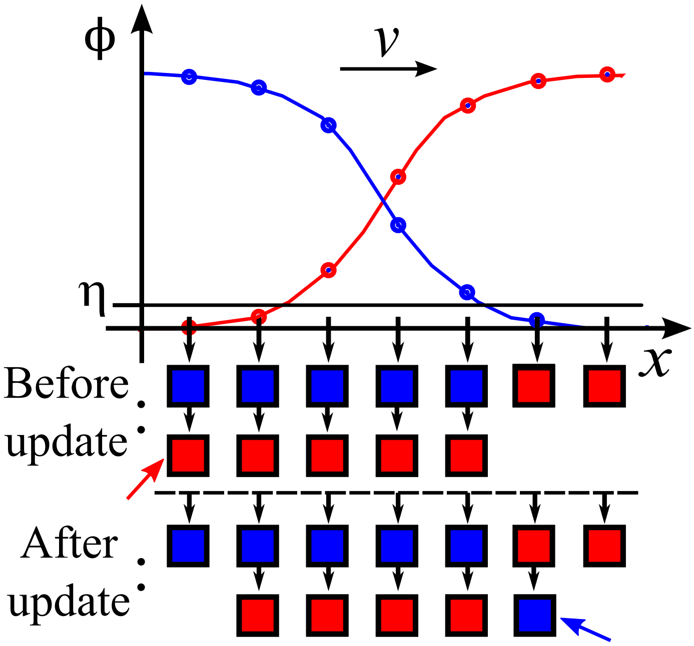

Figure 5.9: A qualitative sketch of the sparse matrix data structure, and the update algorithm in the case of a migrating grain boundary. The grain boundary has migrated towards the right since last update, and the sparse matrix data structure is shown before, and after the update algorithm has been executed. Ticks show the location of the discrete grid points. Boxes represent sparse matrix entries, where the color signify the identifier, I, i.e. which phase-field variable the entry represents. The red arrow points to an entry which is removed when the update algorithm is executed, as the value of the entry of the same identifier at the right neighboring grid point has fallen below η. The blue arrow points to an entry that is introduced, since the value of the entry of the same identifier at the left neighboring grid point has risen above η.

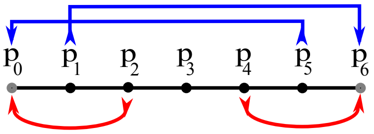

Figure 5.10: Sketch of periodic and reflective boundary conditions on a one-dimensional chain with $N = 5$ grid points in the computational domain. Grey grid points are the two grid points introduced to accommodate boundary conditions. Blue arrows correspond to periodic boundary conditions, red arrows correspond to reflective boundary conditions.

5.4.3 Discretization of boundary conditions

When discretizing the system of partial differential equations, the conditions imposed by the physics of the problem on the external boundaries of the computational domain must also be discretized. The choice of finite difference stencil described in section 5.4.1 requires nearest neighbor information to determine the Laplacian, thus for the grid points on the edges, i.e. those grid points lacking one or more nearest neighbors in the grid, information must be supplied by the boundary conditions. To be able to treat all grid points in a uniform manner, the grid was extended by one grid point on all sides, so introducing a new boundary that is not part of the computational domain. This new boundary must be assigned values consistent with the boundary conditions before each determination of the Laplacian. In the present work, only periodic boundary conditions are applied. Reflective boundary conditions have also been implemented in the solver for use with experimentally characterized microstructures, and so is presented here for completeness.

For a one-dimensional chain of $N + 2$ grid points, $p_0, p_1, \cdots, p_N, p_{N+1}$, where the first and last points in the chain are introduced to deal with the boundary conditions, and so is outside the computational domain, the boundary conditions are

$$p_0 = p_N \quad \text{and} \quad p_{N+1} = p_1 \qquad \text{(Periodic)} \tag{5.24a}$$

$$p_0 = p_2 \quad \text{and} \quad p_{N+1} = p_{N-1} \qquad \text{(Reflective)} \tag{5.24b}$$

and these generalize easily to higher dimensions. Periodic boundary conditions are intuitively understood as the two ends of the chain of grid points being linked together. This is sketched with the blue arrows in figure 5.10. Periodic boundary conditions are useful for problems displaying periodicity (which must be rare in microstructural studies), or when boundary effects are unwanted. In the latter case, the features investigated must be considerably smaller than the simulation domain, so these features do not interact with themselves across the boundary.

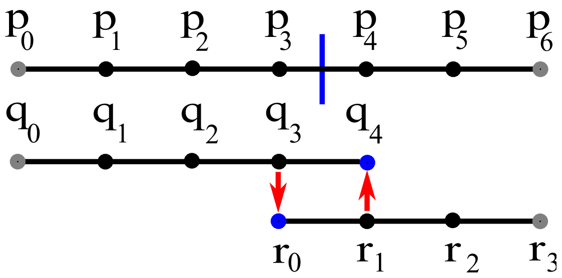

Figure 5.11: Sketch of how a chain p with $N = 5$ grid points in the computational domain may be split into subdomains q and r with $S = 3$ and $T = 2$ grid points in their respective computational domains. The blue line shows where chain p is split, grey dots show grid points the values of which are given by external boundary conditions, blue dots are grid points the values of which must be transferred from the other subdomain as indicated by the red arrows.

Reflective boundary conditions are sketched with the red arrows in figure 5.10. These prohibit flux across boundaries by ensuring that the derivative vanishes on the boundaries.

5.4.4 Parallellization

A grid based problem may be parallellized by splitting the computational domain into a number of subdomains, and solving in each subdomain as mutually independent processes, which may be distributed amongst e.g. nodes in a compute cluster. With MPI this conceptually works by letting each node included in the execution run identical, but independent instances of the program. Each node is issued a unique ID at run-time, which may be used to identify that node and its position in the computational domain.

Splitting in subdomains introduces a boundary along the subdomain edges, on which the conditions are dependent on the values of the edge grid points of the subdomain it neighbors. Cf. earlier this section, the subdomains were extended by a grid point in all directions to accommodate both external boundary conditions and subdomain boundary conditions. A one-dimensional chain may be split into two subdomains as

$$p_0, p_1, \cdots, p_{N+1} \Leftrightarrow q_0, q_1, \cdots, q_{S+1} \text{ and } r_0, r_1, \cdots, r_{T+1} \text{ where } S + T = N$$

If we take q_1 to correspond to p_1 and r_T to correspond to p_N, i.e. placing the subdomain boundary between q_S and r_1 we get the subdomain boundary

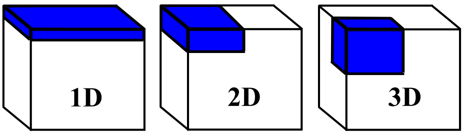

Figure 5.12: Examples of how a computational domain may be divided into three different virtual topologies with $P = 8$ subdomains, with one subdomain highlighted. $(P_i, P_j, P_k) = (8, 1, 1)$, $(4, 2, 1)$ and $(2, 2, 2)$ for 1D, 2D and 3D respectively.

condition

$$q_{S+1} = r_1 \text{ and } r_0 = q_S \tag{5.25}$$

while the conditions on q_0 and r_{T+1} are given by whichever external boundary conditions are imposed. An example with $N = 5$, $S = 3$ and $T = 2$ is shown in figure 5.11. It is a necessity that a node at any given time step has both received and sent subdomain boundary conditions from and to its neighbors before iteration, to ensure that all grid points are in a state corresponding to the same simulation time.

5.4.4.1 Domain decomposition

MPI-2.0 provides a set of highly optimized methods for exchanging data between nodes in a cluster, the speed of which scales roughly with the amount of data sent and received, with only a small overhead related to the setting up of the data transfer. When transferring data between nodes, the communication is best performed in as few operations as possible, e.g. transferring N array elements should be done in one operation rather than in N separate operations, motivated by the overhead. If this is done, the overhead is of no practical importance when using modern hardware, see e.g. [108, 113].

Part of optimizing the parallellization is thus to minimize the area of the subdomain boundaries, and so the amount of data which must be transferred. A cubic computational domain of N^3 grid points may be divided into a regular grid of P subdomains in several different manners, which is commonly referred to as *decomposition*. A specific division is termed a *virtual topology*, and shall be denoted (P_i, P_j, P_k), where P_i is the number of subdomains in the first dimension, etc., and $P_i P_j P_k = P$ by definition.

Different virtual topologies of same number of subdomains may differ in total subdomain area. Consider a subdomain in one-, two- and three-dimensional

	Nearest neighbors	Virtual topology	Subdomain area	Optimal range
1D	2	$(P, 1, 1)$	$2N^2$	$P < 4$
2D	4	$(\sqrt{P}, \sqrt{P}, 1)$	$4N^2/\sqrt{P}$	$4 \leq P < 12$
3D	6	$(\sqrt[3]{P}, \sqrt[3]{P}, \sqrt[3]{P})$	$6N^2/P^{2/3}$	$P \geq 12$

Table 5.1: Optimal choice of virtual topology for a grid of N^3 points as function of number of nodes P. This may be derived simply by considering the number of grid points on the subdomain boundaries.

virtual topologies, as shown in figure 5.4.4.1. For a system with periodic boundary conditions, or a subdomain not forming part of an external boundary, the optimal virtual topologies, and the number of grid points in the subdomain area are listed in table 5.1.

For large-scale simulations, where $P \geq 12$ it is thus an advantage to use a three-dimensional virtual topology, although it increases the programming complexity. The solver has been written to allow for the computational domain to be decomposed in arbitrary virtual topologies.

The possibility of using three-dimensional virtual topologies is the motivation for choosing both finite difference stencil and the criteria for adding and removing entries in the sparse matrix data structure to only use information from nearest neighbor grid points, as described in sections 5.4.1 and 5.4.2: In the current implementation, a subdomain communicates with its six nearest neighbors. Were information from second nearest neighbors also needed, this number would rise to 18, and again to 26 if third nearest neighbor information was needed. This would likely decrease the performance of the parallellization only slightly, since the number of grid points which must be shared with second and third nearest neighbors is low, but would be a programming challenge, with few obvious benefits for motivation.

5.4.4.2 Interlaced communication

The most easily manageable mode of internode communication using MPI is *blocking* communication. When node A is to send data to be received by node B, then node A must be issued a *blocking send* command at some time, while node B must be issued a *blocking receive* command at some time. The node issued its command first will halt execution and wait until the other node has been issued its conjugate command, hence the term *blocking*, which thus ensures

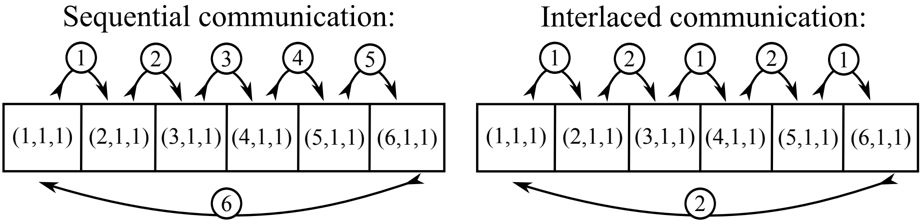

Figure 5.13: One-dimensional virtual topologies $(6, 1, 1)$, illustrating sequential and interlaced communication. Numbers on the arrows designate in which sequential step the transfer will occur.

synchronization.

Consider a one-dimensional virtual topology, $(P, 1, 1)$ with periodic boundary conditions for illustrative purposes. All subdomains must send some data to one nearest neighbor prior to iteration (for real simulations each node must obviously send data to two nodes), so node $(i, 1, 1)$ must send to node $(i + 1, 1, 1)$, etc. A simple albeit inefficient way to achieve this, is to issue following commands to all nodes

1. Receive data from one neighbor.
2. Send data to other neighbor.

except for e.g. node $(1, 1, 1)$, for which the order is reversed. This will have the effect that node $(1, 1, 1)$ will send data to node $(2, 1, 1)$, while all other nodes wait. Then node $(2, 1, 1)$ sends to node $(3, 1, 1)$, and so forth, until finally node $(P, 1, 1)$ sends to node $(1, 1, 1)$. This is illustrated as *sequential communication* in figure 5.13. The data transfer is thus performed in P sequential transfers.

This communication may be performed more effectively, provided P is even. Let i designate the position of a given node in the virtual topology $(i, 1, 1)$. Issuing the following commands

1. Receive data from neighbor if i is odd. Send data to neighbor if i is even.
2. Send data to neighbor if i is odd. Receive data from neighbor if i is even.

which means that while node $(1, 1, 1)$ is transferring data to node $(2, 1, 1)$, node $(3, 1, 1)$ will be transferring to node $(4, 1, 1)$, etc. This requires only two sequential transfers independently of P, and thus cuts down on the time spent on internodal communication when $P > 2$, while for $P = 2$ the communication time should be comparable to that taken by sequential communication. Interlaced communication was therefore implemented in the solver. If P is odd, the data transfer may be accomplished in 3 sequential steps rather than 2.

5.4.5 Comments on sparse data structure and boundary conditions

Straightforwardly implementing a solver of the kind described in present text, where the main loop is

1. Send and receive boundary conditions.
2. Add and remove entries into sparse data structure.
3. Iterate forward in time.

will result in the simulation output varying slightly with the virtual topology. More specifically, small numeric differences between output from simulations of different virtual topology are found to be related to interfaces crossing subdomain boundaries.

Careful consideration reveals that this is related to the removal of entries in the subdomain boundary area. Consider an entry with index $I = i$ and value $V < \eta$, with no nearest neighbors of $I = i$ and $V \geq \eta$, thus an entry which is to be removed when the algorithm to do so has been executed cf. section 5.4.2. If this entry is on the subdomain boundary, it will be copied to another node as a subdomain boundary condition, necessary for adding and removing entries from the sparse data structure. As that is done, the original entry will be removed prior to iteration, but unless the subdomain boundary conditions are updated, the entry will remain in the subdomain boundary conditions, and thus be used in the determination of the Laplacian, which would not have happened had the solver not been parallellized. This issue is illustrated in figure 5.14.

The solver therefore transfers boundary conditions twice, first for the algorithm to add and remove entries into the sparse data structure, and a second time before iteration, ensuring that simulation output is independent of the chosen virtual topology. Adding entries into the sparse data structure does not introduce comparable numeric problems, as these entries are initialized to a value of $V = 0$.

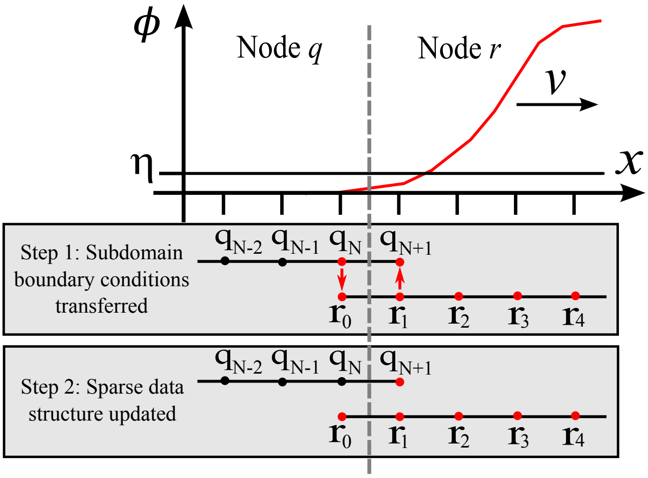

Figure 5.14: Illustration of the issue related to the sparse data structure and parallellization of section 5.4.5. An interface is passing though the subdomain boundary from node q to node r. The value of the phase-field variable at grid points q_N and r_1 are both below η, and so the entry at q_N should be removed when updating the sparse data structure. First, the subdomain boundary conditions are transferred, copying the values at q_N and r_1 to r_0 and q_{N+1} respectively. Second, the sparse matrix data structure is update, which removes the entry at q_N. However, this entry has been transferred to r_0, and if not removed before iteration forward in time will affect the determination of the Laplacian at grid point r_1 compared to simulations which are not parallellized.

5.5 Simulations of coupled grain growth and coarsening in dual-phase materials

The solver was compiled using the Intel Fortran compiler, and executed on the Thyra cluster, located at Risø DTU. Thyra is a 128 node cluster running CentOS 5.4 linux, each node containing two dual-core AMD Opteron 2218 CPUs running at 2.6 GHz, and so is will appear as a 512 node cluster to a user. Communication was enabled by OpenMPI over a high-speed InfiniBand interconnect.

The Intel Fortran compiler allows for certain high-level optimizations that are incompatible with CPUs from other vendors. However, tests of execution speed showed that the Intel compiler performed en par with the Pathscale compiler also available on Thyra, so the Intel compiler was chosen, as the solver had been developed using this.

The solver has been implemented in a manner such that iteration may be halted, and restarted later without any loss of information, so execution has been performed on a varying number of nodes, but at most 216, i.e. 54 physical nodes × 2 CPUs per node × 2 cores per CPU.

5.5.1 Initial conditions for simulations

A Voronoi tessellation with periodic boundaries was generated on a grid of 512^3 points as a rough approximation of a grain structure. This resulted in the grid being subdivided into 8331 Voronoi cells. A number of Voronoi cells were chosen without spatial correlation, and the volume of this subset determined, repeating the selection process until volume ratios of 50/50 and 40/60 were reached. The subset will be referred to as the α subset, while the remaining Voronoi cells will be referred to as the β subset. For the 50/50 volume ratio configuration, the α and β subsets consisted of $N_\alpha = 4189$ and $N_\beta = 4142$ Voronoi cells, respectively, while for the 40/60 volume ratio set these numbers were $N_\alpha = 3335$ and $N_\beta = 4996$.

These two configurations were used to generate four sets of initial conditions:

1. A 50/50 volume ratio microstructure where both phases were polycrystalline (which will sometimes be denoted 50PC)
2. A 50/50 volume ratio microstructure where both phases were liquid (50L)

3. A 40/60 volume ratio microstructure where both phases were polycrystalline (40PC)
4. A 40/60 volume ratio microstructure where both phases were liquid (50L)

The two liquid sets of initial conditions were employed mainly to be able to compare and contrast simulation output to that of the polycrystalline simulations.

For the two sets of polycrystalline initial conditions (50PC and 40PC), each Voronoi cell in the α subset were made to correspond to a unique α grain orientation by letting

$$\alpha_i(\mathbf{r}) = \left\{ \begin{array}{l} 1 \\ 0 \end{array} \right. \text{ for } \begin{array}{l} \mathbf{r} \in V_i^\alpha \\ \mathbf{r} \notin V_i^\alpha \end{array} \text{ and } i = 1, 2, \cdots, N_\alpha \tag{5.26}$$

where V_i^α designates the grid points belonging to the i^{th} Voronoi cell in the α subset. Vice versa for β.

For the liquid sets of initial conditions (50L and 40L), all Voronoi cells in the α subset were made to correspond to the same, single α orientation by letting

$$\alpha_1(\mathbf{r}) = \left\{ \begin{array}{l} 1 \\ 0 \end{array} \right. \text{ for } \begin{array}{l} \mathbf{r} \in V^\alpha \\ \mathbf{r} \notin V^\alpha \end{array} \text{ and } i = 1, 2, \cdots, N_\alpha \tag{5.27}$$

where V^α is the union of all V_i^α Voronoi cells.

For all four sets the initial composition was set to

$$C(\mathbf{r}) = \left\{ \begin{array}{l} C_\alpha \\ C_\beta \end{array} \right. \text{ for } \begin{array}{l} \mathbf{r} \in V^\alpha \\ \mathbf{r} \notin V^\alpha \end{array} \text{ and } i = 1, 2, \cdots, N_\alpha \tag{5.28}$$

Cross sections of the four sets of initial conditions are found in figure 5.15, which shows how the same Voronoi tessellation has been used to generate all initial conditions.

The reason for referring to the liquid sets of initial conditions as such, is that this setup does not allow for $\alpha\alpha$ and $\beta\beta$ boundaries to form, meaning that any two α regions coming in contact with each other will coalesce, rather than form a boundary, and vice versa for β. Note that the model employed is significantly more complicated than those usually employed to study liquid/liquid systems, e.g. [85]. Current model is employed for two reasons: Firstly that a solver has been implemented, and secondly to ease comparisons between liquid and polycrystalline simulations, since $\alpha\beta$ boundary width and energy is equal when using the same model and parameters for all simulations.

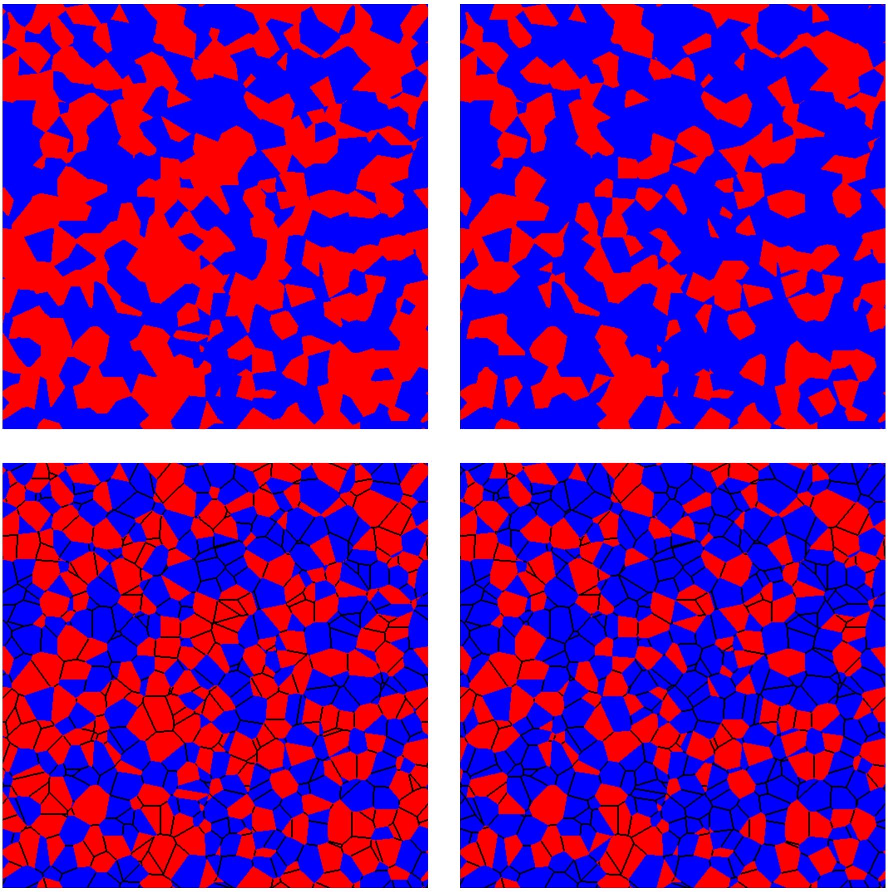

Figure 5.15: Cross sections of the four sets of initial conditions. Red: α phase, blue: β phase. Black marks $\alpha\alpha$ and $\beta\beta$ boundaries. α is minority phase for the 40/60 volume ratio initial conditions. Top left: 50/50 volume ratio liquid (50L), top right: 40/60 volume ratio liquid (40L), bottom left: 50/50 volume ratio polycrystalline (50PC), bottom right: 40/60 volume ratio polycrystalline (40PC).

5.5.2 Qualitative characterization

All four sets of initial conditions have been iterated up to a simulation time of $t = 300.000$, and output has been generated at intervals of $\Delta t = 1000$. An initial transient up to $t = 10.000$ will be omitted in the following. The first part of this transient is related to setting up of local equilibrium phase-field variable profiles. The second, longer, part is for the polycrystalline simulations (50PC and 40PC) found to be related to movement of triple junctions and migration of boundaries to achieve the local equilibrium triple junction angles stated in equation (5.21b). For the liquid simulations (50L and 40L) it is found to be related to a smoothing out of the non-smooth curvature at the triple junctions of Voronoi cells. For all sets of initial conditions, this transient is thus an uninteresting consequence of the initial conditions.

Visualization of output from large-scale simulations is difficult, so several different visualization types have been employed to allow qualitative insight into the simulated microstructure and its evolution. For all types, the microstructure is displayed at simulation times $t = 10.000$, $t = 50.000$ and $t = 300.000$. The time $t = 50.000$ is chosen, as it will be argued that the microstructural evolution becomes topologically self-similar around this time.

Cross sections of the microstructure of the two liquid simulations are shown in figure 5.16. These are simply cross sections of the compositional phase-field variable C. Equivalent cross sections of the grain structure of the two polycrystalline simulations are shown in figure 5.17. These are the same cross sections which were used to visualize the initial conditions in figure 5.15 to allow for some measure of comparison between initial conditions and simulation output. The grain structure of the polycrystalline simulations show $\alpha\alpha\alpha$ and $\beta\beta\beta$ triple junctions at all times.

The intraphase interfaces of the polycrystalline simulations are found to have definite curvature, meaning that these boundaries do not form a minimal surface, as is known to be the case for soap froths [114], which are often used as simple model systems for polycrystalline materials. The interphase interfaces of larger grains at late times sometimes exhibit peculiar ”sinusoidal-like” shapes, which will be explained in section 5.5.8. The $\alpha\alpha$ and $\beta\beta$ grain boundaries do not display such large variations in curvature.

The interphase interface of the two liquid simulations are shown in figure 5.18, which is the $C = 0.5$ isolevel. These show 1/8 of the computational domain, i.e. they are created from a 256^3 box out of the total 512^3 grid points, to show more detail. Same box of 256^3 grid points are used to show the grain structure of the polycrystalline simulations in figure 5.19.

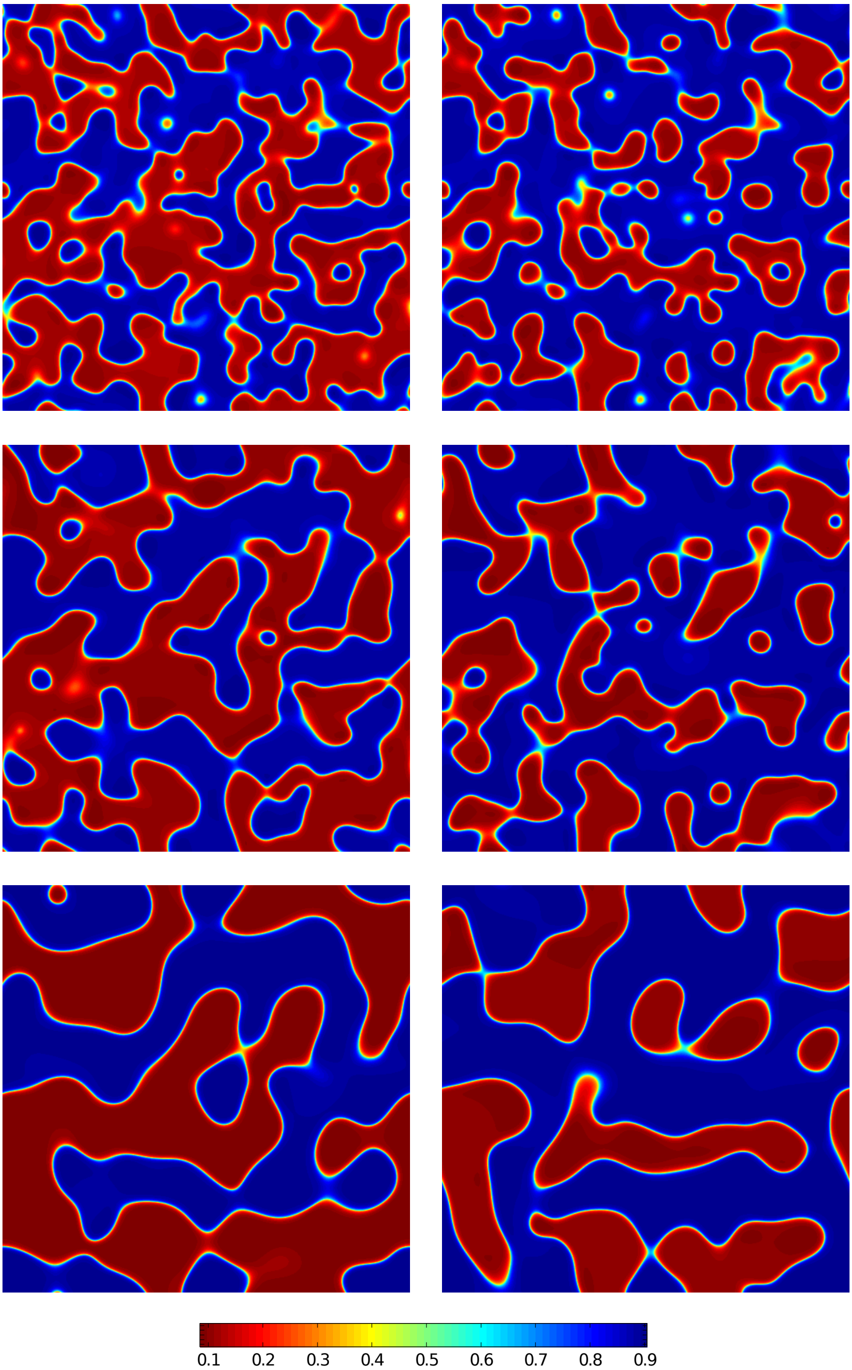

Figure 5.16: Cross sections of the compositional phase-field variable C of the two liquid simulations, where $C_\alpha = 0.1$ and $C_\beta = 0.9$ are the bulk equilibrium composition in α and β phase respectively. Left: 50/50 volume ratio. Right: 40/60 volume ratio. Top to bottom: Times $t = 10.000$, $t = 50.000$ and $t = 300.000$.

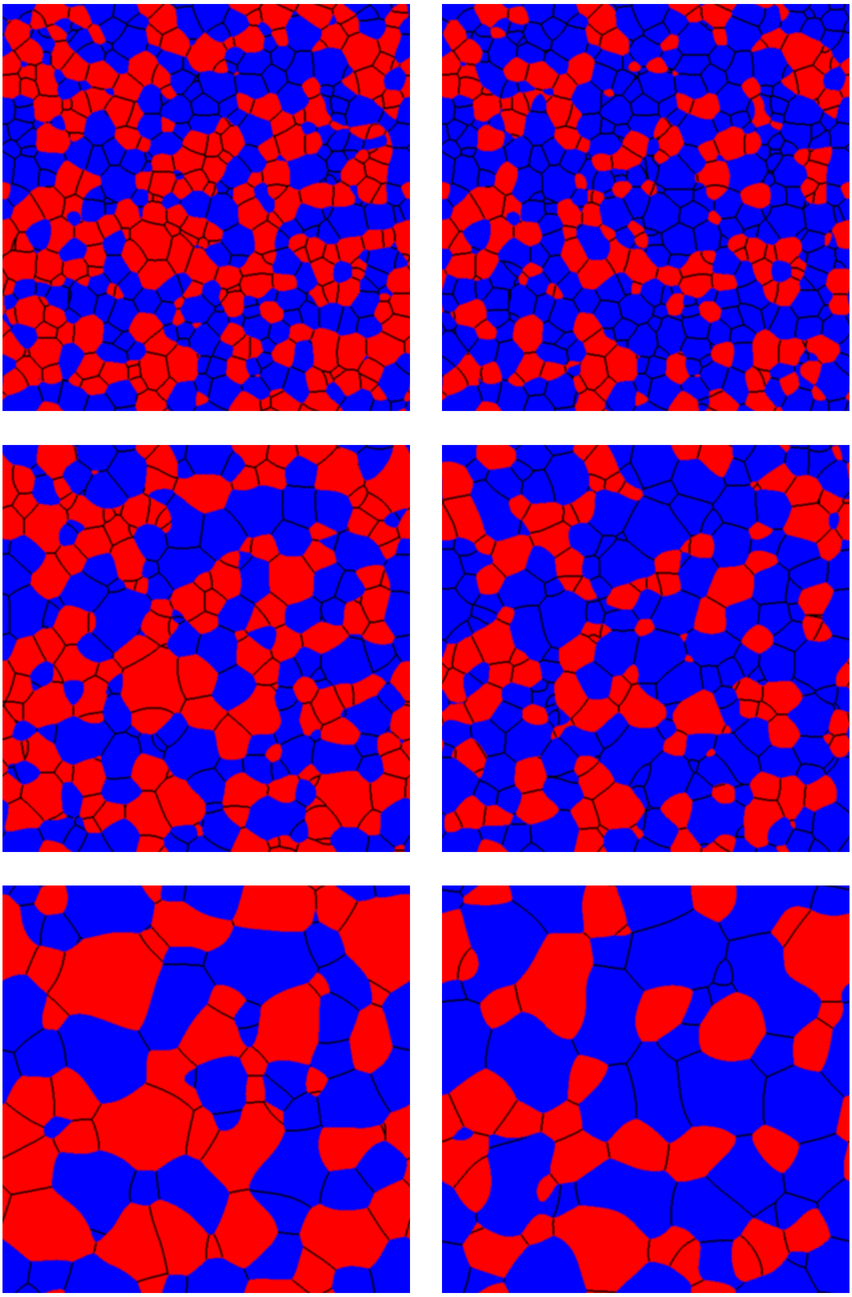

Figure 5.17: Cross sections of the grain structure of the two polycrystalline simulations. α phase grains are red, β phase grains are blue. Left: 50/50 volume ratio. Right: 40/60 volume ratio. Top to bottom: Times $t = 10.000$, $t = 50.000$ and $t = 300.000$.

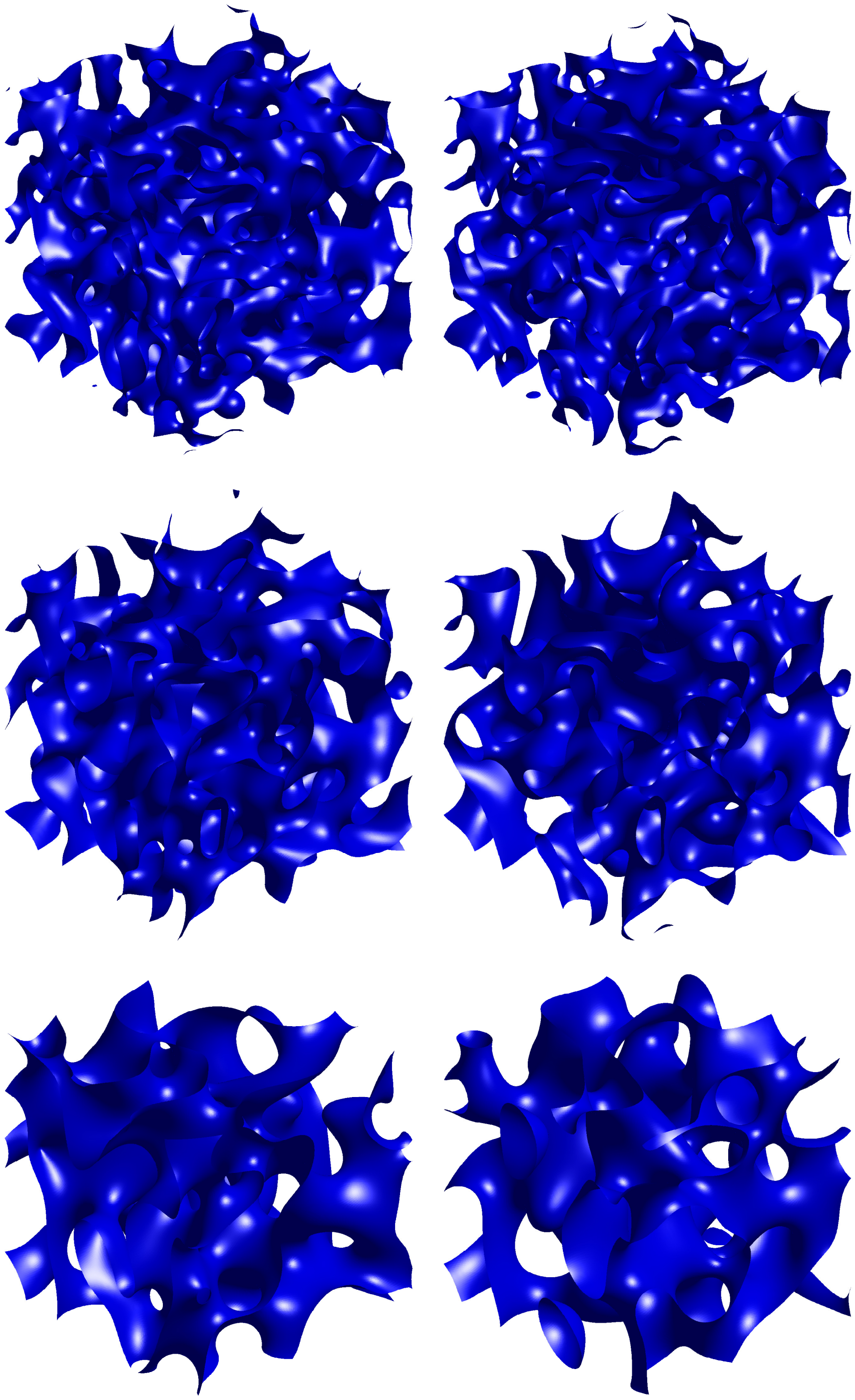

Figure 5.18: The interphase interface of the two liquid simulations (1/8 of the computational domain). Left: 50/50 volume ratio. Right: 40/60 volume ratio. Top to bottom: Times $t = 10.000$, $t = 50.000$ and $t = 300.000$.

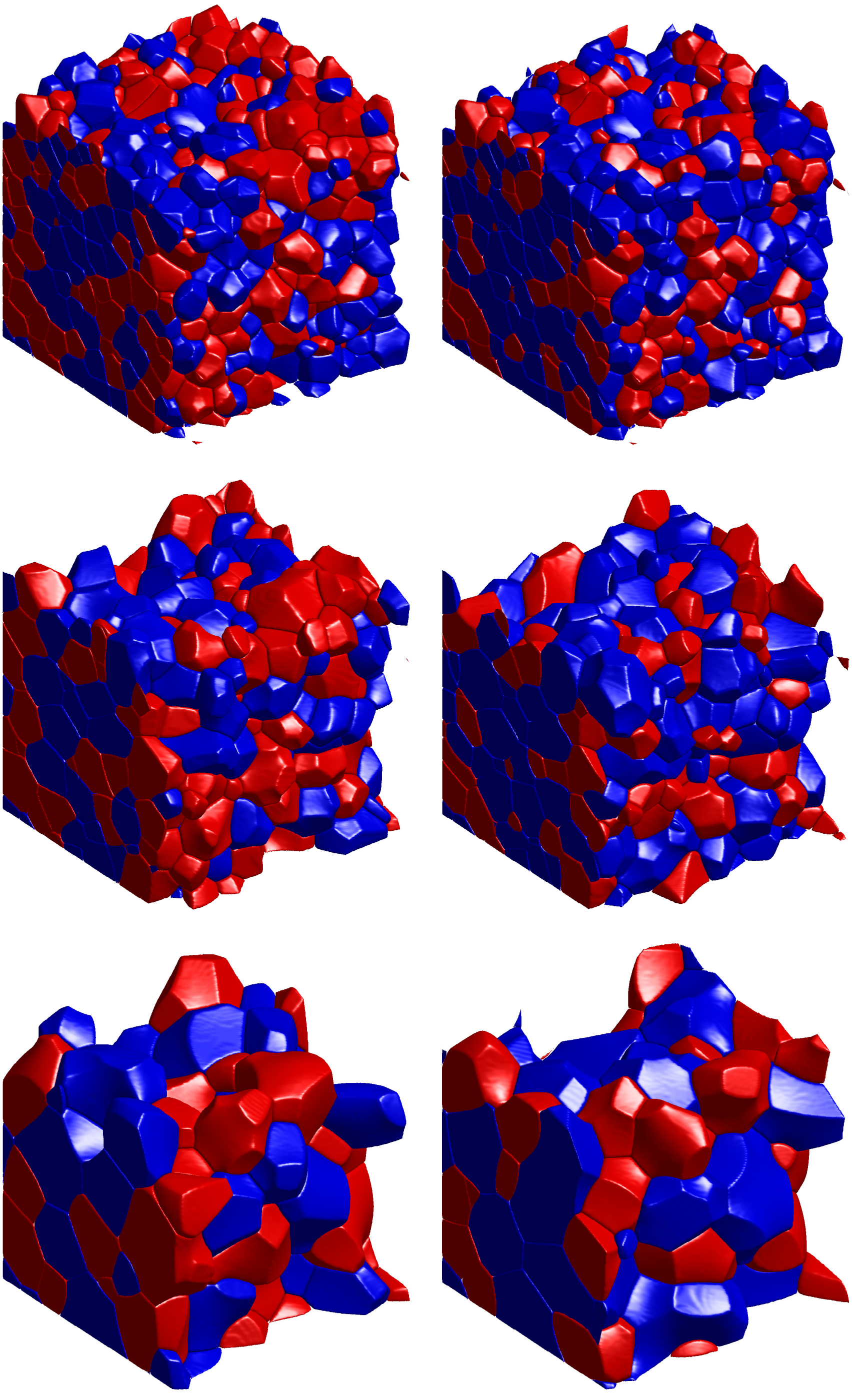

Figure 5.19: Grain structure of the two polycrystalline simulations (1/8 of the computational domain) with grains touching top and/or right side of box removed. α grains are red, β grains are blue. Left: 50/50 volume ratio. Right: 40/60 volume ratio. Top to bottom: Times $t = 10.000$, $t = 50.000$ and $t = 300.000$.

All simulated microstructures are found to be bicontinuous or nearly bicontinuous at all simulated times after the initial transient up to time $t = 10.000$. Bicontinuity is the property defined as the two phases being completely interconnected, i.e. that any two points within the volume of either phase may be connected by a curve which is wholly contained in said volume. By nearly bicontinuous is meant that bicontinuity may be lost briefly when small grains break off from the structure, but this is not a common phenomenon, and bicontinuity is reestablished fast as the small grain is eliminated by diffusion. This mainly occurs with grains the size of which is on the order of or less than the size required to sustain local equilibrium interface profiles. In [85] it was found through simulations resembling those of the liquid microstructures in present work, that structures at significantly lower phase fractions (down to at least 36%) were bicontinuous.

5.5.3 Characteristic length scales

Quantifying the magnitude of simulated microstructural evolution is difficult to do in terms of simulation time, as this may be normalized as seen fit, and parameters in a phenomenological model will typically be difficult to fit to measurable quantities for comparisons to experimental data. Comparisons may instead be conveniently performed through characteristic length scales.

It is well-known that the time dependence of characteristic length scales of a wide variety of physical systems during growth may be described by power law relationships:

$$\lambda^n - \lambda_0^n = kt \tag{5.29}$$

Here λ is the characteristic length scale at time t, λ_0 is the characteristic length scale at time $t = 0$, while n and k are positive constants. The characteristic length scales in physical systems described by this law thus increases smoothly, but slows down at "late" times. See e.g. [115] for a more comprehensive treatment. In the limit where $\lambda^n \gg \lambda_0^n$ this relationship becomes scale invariant, which is usually taken as a necessary (but not sufficient) condition for (asymptotically) self-similar microstructural evolution.

This relation has been found to hold for the mean grain size during normal grain growth in pure systems with $n = 2$, e.g. [116, 117], for mean radius of particles undergoing Ostwald ripening in dilute systems (LSW theory) [118, 119], and for systems with a higher fraction of coarsening particles, e.g. [120, 121] with $n = 3$. A growth exponent of $n = 3$ is generally observed in many structures late-stage coarsening through bulk diffusion [115], and $n = 3$ has also been found for mean grain size during grain growth with solute drag, e.g. [122]. The exponent of the

Data set		Simulation time (units of 1.000)			
		0	10	50	300
50PC	N_α	4.189	3.426	1.320	270
	N_β	4.142	3.405	1.353	263
	Σ	8.331	6.831	2.673	533
40PC	N_α	3.335	2.789	1.187	269
	N_β	4.996	4.011	1.460	247
	Σ	8.331	6.800	2.647	516

Table 5.2: The number of α and β grains and their sum at significant simulation times for the two polycrystalline simulations.

characteristic length scale is therefore often taken to be related to the physical mechanism controlling the growth.

For the polycrystalline simulations, the simplest characteristic measure is the time evolution of the number of grains in the system. This is shown in table 5.2 for the simulation times taken to be of special significance.

The number of grains may be used to define three characteristic length scales, since the mean grain volume can be determined from the number of grains through $\langle V_G \rangle = V/N$, where V and N may be the system volume and number of all grains, α volume and number of α grains, or β volume and number of β grains. A length scale may then be determined from the mean grain volume as e.g. $\left\langle \tilde{R} \right\rangle = \sqrt[3]{3 \langle V_G \rangle / 4\pi}$. This is, however, not the true mean grain radius, and so this characteristic length will not be used for the present investigation. Two other characteristic length scales are chosen: The mean grain radius, $\langle R \rangle$, as applicable to the two polycrystalline simulations (50PC and 40PC), and the system area V per interphase surface area S, so $S_V = V/S$, which is applicable to all four simulations, and provides a direct means of comparison.

Here, and in the remainder of this chapter, a grains volume was determined by counting the number of grid points where the corresponding α or β type phase-field variable attained a higher value than all other α and β type phase-field variables. The grain radius was then determined from this volume by the usual relation $R = \sqrt[3]{3V/4\pi}$.

Surfaces were extracted with an implementation of the standard marching cubes algorithm [64] on the phase-field variable in question. The implementation used linear interpolation to determine the location of the vertices. Surface areas were determined by summing the areas of the triangle faces output by the marching cubes algorithm. When speaking of $\alpha\beta$ surfaces, the compositional phase-field variable C was polygonized with a threshold of $(C_\alpha + C_\beta)/2 = 0.5$, i.e. the

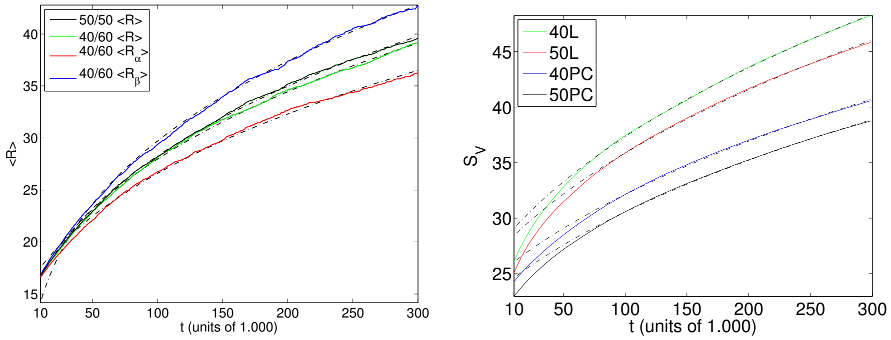

Figure 5.20: Time evolution of characteristic length scales. Left: Mean grain radii. Top to bottom: β (majority) phase of the 40/60 simulation, mean of both phases of the 50/50 simulation, mean of both phases of the 40/60 simulation, and α (minority) phase of the 40/60 simulation. Right: System volume per surface area, S_V. Top to bottom: 40/60 liquid, 50/50 liquid, 40/60 polycrystalline and 50/50 polycrystalline. Both characteristic length scales become consistent with power law growth with a growth exponent of $n = 3$ after $t \approx 50.000$. Before this time, the fits are poor.

interphase surface was taken to be given by the $C = 0.5$ isosurface.

Examinations of both $\langle R \rangle$ and S_V vs. time has revealed the time dependence to be consistent with a power law of the form of equation (5.29) with $n = 3$ after a simulation time of $t \approx 50.000$. The time evolution of the specific length scales are shown in figure 5.20 along with fitting curves of the form (5.29) with $n = 3$. It is seen that although the presence of the grain boundaries in the polycrystalline simulations seem to retard the evolution of the characteristic length scale as compared to the liquid simulations, they do not seem to affect the growth exponent significantly.

This kinetic exponent is clearly indicative of bulk diffusion controlled microstructural evolution in the cases of the two liquid simulations, as no other mechanisms are present in the model. This is also believed to be the controlling mechanism in the two polycrystalline simulations. As mentioned above, a growth exponent of $n = 3$ is also observed in systems undergoing grain growth with solute drag. However, it is argued in [122] that this is due to a non-linear relationship between grain boundary velocity and driving force caused by the impurity concentration on the grain boundaries, which is not observed for the present model cf. section 5.3.8.1.

The left part of figure 5.20 reveals that the mean grain radius of the α (minority)

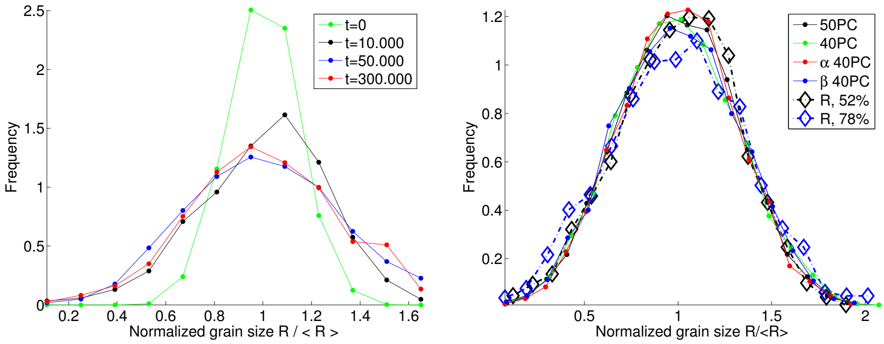

Figure 5.21: Normalized grain size distribution. Left: for 40/60 volume ratio polycrystalline simulation. Time $t = 0$ show the size distribution of the initial conditions. Right: Steady state grain size distributions. Black and green curves are for 50/50 and 40/60 volume ratio simulations respectively when grains of both phases are considered as a whole. Red and blue curves are for α (minority) and β (majority) phase grains of the 40/60 volume ratio simulation respectively. Data marked with diamonds are from Rowenhorst *et al.* [123] for particles coarsening in high volume fraction solid/liquid mixtures with 52% and 78% volume fractions. Size distributions are generated from 1818 individual particles for the 52% volume fraction experiment, and from 1138 individual particles for the 78% volume fraction experiment.

phase increases more slowly than the mean grain radius of the β (majority) phase for the polycrystalline simulation with the 40/60 volume ratio. This observation lends further credibility to the assumption that bulk diffusion is the mechanism controlling growth, when the distance necessary for growth by bulk diffusion is considered: Mass transport between two β regions by bulk diffusion through an intermediate α region in this case occurs over a distance, d_α, proportional to the characteristic length scale of the α phase, and equivalently for bulk diffusion through a β region

$$d_\alpha \propto \frac{V_\alpha}{S} = 0.4 S_V \quad \text{and} \quad d_\beta \propto \frac{V_\beta}{S} = 0.6 S_V$$

Here $V_\alpha = 0.4V$ and $V_\beta = 0.6V$ are the conserved volumes of α and β phase, and S is the interphase surface area. Thus, the smaller separation between β (majority) phase regions enables these to grow faster than α regions.

5.5.4 Grain size distributions

Examination of normalized grain size distributions reveal that there is little variation for times $t \geq 50.000$, as may be seen in the left part of figure 5.21, where the grain size distributions are extracted from the 40/60 volume ratio simulation. Equivalent distributions extracted from to 50/50 volume ratio simulations are qualitatively identical.

The grain size distributions taken at $t \geq 50.000$ are therefore assumed to be steady state distributions for these simulations. They are shown for both polycrystalline simulations in the right side of figure 5.21. These are generated by taking the mean of the normalized grain size distributions from time $t = 50.000$ to $t = 300.000$ in increments of 50.000 to gain better statistics. Note that the mean grain size used for normalization is the mean grain size of the species considered, i.e. the α grain size distribution is normalized to the mean size of the α grains, etc.

It is interesting to note that the distribution for the 40/60 volume ratio simulation and the distribution for the 50/50 volume ratio simulation are nearly identical when normalized by their respective mean grain sizes (the distribution for the 40/60 volume ratio simulation is only slightly wider). It is also interesting to note that the distribution of α (minority) grain sizes and the distribution of β (majority) grain sizes in the 40/60 volume ratio simulation are also near-identical when normalized by their mean size, i.e. the α distribution is normalized by the mean grain size of α grains, and vice versa. In this case, the α grains, having a lower mean grain size cf. figure 5.20 (left), will contribute preferentially to the lower-than-average part of the total grain size distribution, while the β grains conversely contribute preferentially to the larger-than-average part.

The steady state grain size distributions are found to be highly symmetrical about their average. Comparing these distributions to those found in the literature, it is found that these symmetrical distributions do not resemble the "log-normal-like" distributions that are usually observed both experimentally and during simulations of single-phase materials, an example of which is shown in figure 4.5. There is a clearer resemblance to those distributions observed during Ostwald ripening in high-volume fraction mixtures, which also tend to display this symmetry. Experimental data for solid tin-rich particles of 52% and 78% volume percent coarsening in a liquid lead-tin matrix published in [123] is shown alongside the simulation output, and seen to be similar to these. This hints that the growth kinetics of individual grains is also dominated by bulk diffusion. This is likely explainable by considering a curved $\alpha\alpha$ or $\beta\beta$ grain boundary as may be seen in the cross sections of figure 5.17. Such a boundary

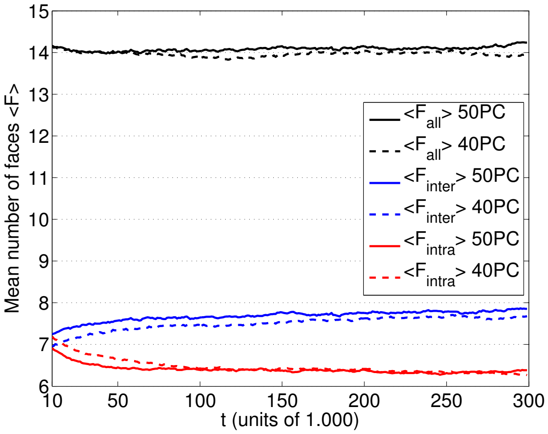

Figure 5.22: Temporal evolution of the mean number of faces for all grains, $\langle F \rangle$. Full lines are for the 50/50 volume ratio simulation, while dashed lines are for the 40/60 volume ratio simulation. Black: Mean number of faces. Blue: Mean number of intraphase faces. Red: Mean number of interphase faces.

is connected to other boundaries at its triple junctions, so moving the boundary in question also entails moving these boundaries to some extent, and a number of these will likely be $\alpha\beta$ boundaries, which are therefore dependent on bulk diffusion for their movement.

5.5.5 Distributions of grain faces

The number of faces of individual grains and the distribution of these has been a long-standing area of study in grain growth, due to their correlation to the growth kinetics of individual grains, as briefly discussed in chapter 4.

Figure 5.22 show the time evolution of the mean number of faces for both 50/50 and 40/60 volume ratio simulations. It is seen that the evolution is virtually identical when grains of both phases are considered as a whole. Both simulations tend to favor interphase faces slightly, $\langle F_{\text{inter}} \rangle \approx 7.8$ to intraphase faces, $\langle F_{\text{intra}} \rangle \approx 6.3$, and these values are nearly constant after a short initial transient.

The mean number of faces for the 40/60 volume ratio simulation is examined in more detail in figure 5.23. It is seen that the α (minority) phase grains on average form fewer faces than the β (majority) grains, and the difference

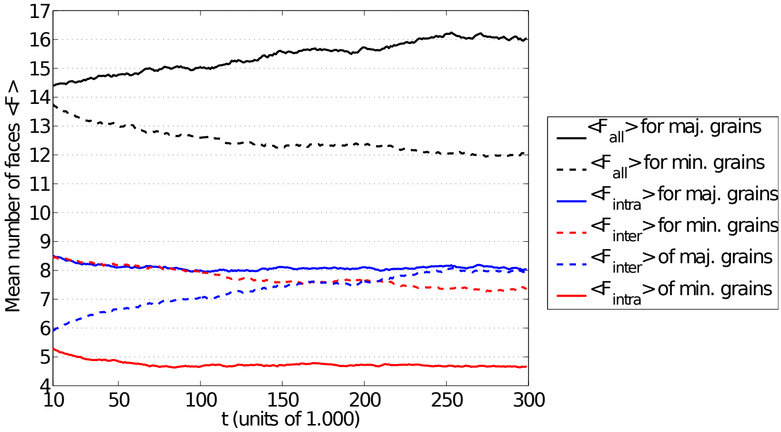

Figure 5.23: Temporal evolution of the mean number of faces, $\langle F \rangle$ for the $40/60$ volume ratio simulation. Solid black line: Mean number of faces for β (majority) phase grains. Dashed black line: Mean number of faces for α (minority) phase grains. Solid blue and dashed blue: Mean number of faces for β (majority) phase grains that are shared with grains of same - and other phase, respectively. Solid red and dashed red: Mean number of faces for α (minority) phase grains that are shared with grains of same - and other phase, respectively.

between these numbers increases over time. As both phases have a near constant average number of faces shared with neighbors of the same phase, this increasing difference is only related to the creation and elimination of interphase faces.

It may seem paradoxical that the α (minority) phase grains will form less faces shared with β (majority) phase grains over time, while β (majority) phase grains will form more faces shared with α (minority) phase grains. This is resolved by considering that the mean grain size is increasing slower for the α (minority) phase grains than for the β (majority) phase grains, cf. section 5.5.3. As the volumes of the two phases are conserved, this means that α (minority) phase grains are eliminated at a slower rate than β (majority) phase grains. Thus, the trend is for the α (minority) phase grains to evolve to be both smaller than, and to have fewer faces than the β grains, but to become relatively more numerous than these, i.e. the ratio of number of α grains to number of β grains increases above $40/60$ with time, as is evident in table 5.2.

As for the grain size distributions, it is found that a distribution of the number of faces that is approximately time invariant occurs after a time $t \geq 50.000$, which is illustrated in figure 5.24 (left) for the $40/60$ volume ratio simulation. The time invariant distributions are shown in figure 5.24 (right), where it is seen

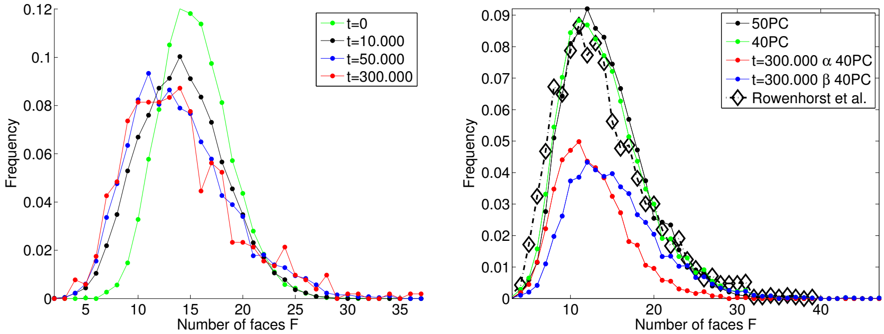

Figure 5.24: Distributions of the number of faces of individual grains. Left: Distribution of faces at various times for the 40/60 polycrystalline simulation. Right: Time invariant distributions of faces. Black and blue lines are steady state distributions for the 50/50 volume ratio and the 40/60 volume ratio simulations respectively, where grains of both phases are considered as a whole. Red and green curves are the distributions of number of faces of individual α (minority) grain, and β (majority) grains respectively, for the 40/60 volume ratio simulation at time $t = 300.000$. The distribution of faces for 2098 individual grains by Rowenhorst *et al.* [69] is shown for comparison. This is the same distribution as was shown in figure 4.5.

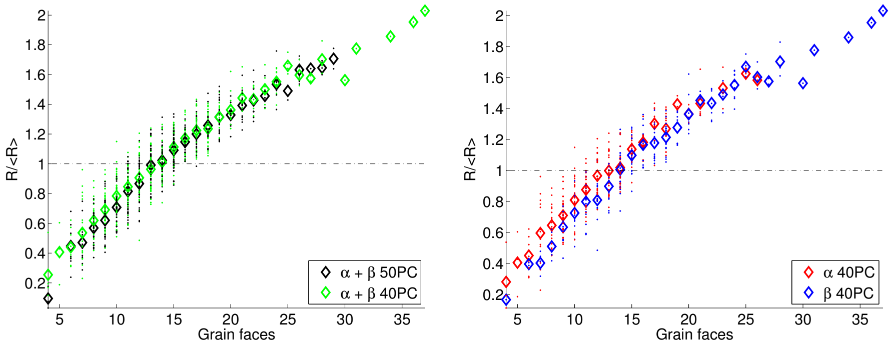

Figure 5.25: Normalized grain size as function of number of grain faces. Left: For all grains and both polycrystalline simulations. Black is 50/50 volume ratio, green is 40/60 volume ratio. Mean values are marked with diamonds. Right: Red is α (minority) phase grains, blue is β (majority) phase grains for the 40/60 volume ratio simulation. The corresponding distribution into topological class are shown in figure 5.24. The mean grain size used for normalization is for all grains.

that the 50/50 and 40/60 volume ratio simulations result in identical steady state distributions, which appear ”log-normal-like”, which may be seen by the reasonably good correspondence with experimental data by Rowenhorst *et al.* [69] for 2098 individual grains of a single-phase β titanium, as was also shown in figure 4.5. Also shown on figure 5.24 are the distribution of the number of faces for grains of the two phases individually, normalized to the total number of grains in the simulation. These two distributions are qualitatively similar to the distribution of all grains, but quantitatively different: The α (minority) phase grains on average have less faces than the β (majority) phase grains, and the α (minority) phase distribution is skewed towards the side of fewer faces compared to the β phase distribution.

Finally, the relationship between the size of a grain, and its topological class is shown in figure 5.25 for the simulation time $t = 300.000$ (see table 5.2 for the statistical basis). When all grains are considered as a whole (left figure), the relationship seems qualitatively similar to the equivalent result from a single-phase grain structure, see figure 4.6 or [69]. The mean grain sizes are identical, $\langle R_{50\mathrm{PC}} \rangle = \langle R_{40\mathrm{PC}} \rangle = 36.1$, so the shown results for the two simulations may be quantitatively compared. Only the 40/60 volume ratio simulation have grains with faces $F \geq 30$, and these grains are large, $R \geq 1.5 \langle R \rangle$, but at most one grain is in each of these topological classes, and so these do not contribute significantly to the mean grain size. The right side of figure 5.25 show the same relationship for the two phases of the 40/60 volume ratio simulation, and it is seen that the grains with faces $F \leq 30$ are β (majority) phase grains, and so their sizes are likely a simple consequence of the larger β domains. Comparing the α and β phases of the 40/60 volume ratio simulation, it is interesting to note that the mean grain size in a given topological class are fairly similar. For a low number of faces $F < 14$ the α (minority) phase grains are larger on average than the β (majority) phase grains, but the magnitude of the difference is fairly small. It thus seems like the relationship between grain size and faces is almost the same for the grains of the two phases, but as the distributions of topological class are different for the grains of the two phases, figure 5.24 (right), a lower mean grain size results for the α (minority) grains than for the β (majority) grains.

5.5.6 Characterization of interphase topology

The topology of the interphase surfaces will be quantified through its genus. This is a quantity that expressed the "interconnectedness" of a surface, in that it for a closed or periodic surface is equal to the number of cuts that may be made through the surface without thereby creating two disjoint objects, or alternatively the genus of a surface may be thought of as the number of holes in that surface. By these simple definitions, the genus is scale invariant, and equal for two homeomorphic surfaces, i.e. for two surfaces that may be made to coincide by continuous stretching and bending.

The genus may be determined as an integral over the Gaussian curvature K of the surface S, through the Gauss-Bonnet theorem, see for example [124].

$$g = 1 - \frac{1}{4\pi} \int_S K dS \tag{5.30}$$

The Gaussian curvature is a quantity that will be used for morphological characterization, so the method by which it is determined is described in detail in section 5.5.7. The genus evolves through topological events. The coming-together of regions raises the genus, while the pinching-off of necking regions lowers the genus [85, 125].

The evolution of the genus has been examined as a function of the characteristic length to enable direct comparisons between the four simulations. By log-log plotting and least squares fitting straight lines as shown in figure 5.26 (left), it is found that the genus with good approximation scales as

$$g \propto S_V^{-3} \propto t^{-1} \tag{5.31}$$

Specific values ~ -3 for the exponent on S_V is found in the figure caption. The genus is thus found to scale with approximately the same temporal exponent

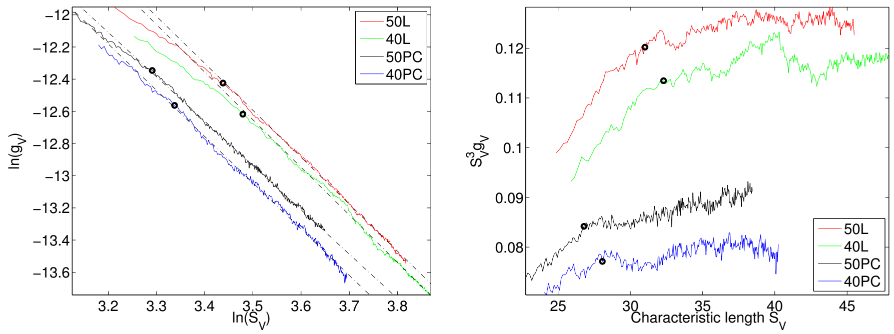

Figure 5.26: Genus vs. characteristic length. Left: Top to bottom: 50/50 volume ratio polycrystalline simulation, 40/60 volume ratio polycrystalline simulation, 50/50 liquid/liquid simulation, 40/60 liquid/liquid simulation. The slope of the fitting lines are given by (again top to bottom) $a = -2.92, a = -2.96, a = 2.76$ and $a = -2.88$. Markers signify the time $t = 50.000$. Right: The genus per system volume scaled by the cube of the characteristic length, $S_V^3 g/V$ vs. characteristic length. Markers signify the time $t = 50.000$.

as the characteristic length, which must be taken to be a necessary criterium for topologically self-similar evolution, as this implies that the genus scales such that the genus in a unit of characteristic volume $S_V^3 g$ is approximately constant. This quantity is found in the right side of figure 5.26. Comparing to the results in [85] (figure 8) it is found that there is quantitative agreement with the genus of the liquid simulations of present work. The polycrystalline simulations display a lower genus per specific volume than the liquid simulations, but the scaling with characteristic length is roughly equal. The presence of grain boundaries therefore seem to result in phase structures that are less topologically complex.

5.5.7 Characterization of interphase morphology

The morphology of surfaces is customarily quantified through their curvature. The curvature κ associated with a point on a surface is a function of the chosen direction in the normal plane, i.e. standing on a surface, one may see different curvatures depending on which direction one is facing.

The *principal curvatures*, κ_1 and κ_2, are defined as the extrema of the curvature as a function of the angle θ in the normal plane. The presently chosen definition is $\kappa_1 \equiv \max(\kappa(\theta))$ and $\kappa_2 \equiv \min(\kappa(\theta))$, and so $\kappa_1 \geq \kappa_2$.

The principal curvatures are the quantities of primary interest in this section. However, the direct determination of these is difficult. From the principal curvatures, two other types of curvature may be defined (or vice versa), which are of physical interest in their own right, but also allow for easy determination of the principal curvatures. Mean curvature, H, is defined as

$$H \equiv \frac{\kappa_1 + \kappa_2}{2} \tag{5.32}$$

and the Gaussian curvature, K, which in section 5.5.6 was used to determine the topological quantity genus, is defined as

$$K \equiv \kappa_1 \kappa_2 \tag{5.33}$$

Combining these, the principal curvatures may be expressed as

$$\kappa_1 = H + \sqrt{H^2 - K} \tag{5.34a}$$

$$\kappa_2 = H - \sqrt{H^2 - K} \tag{5.34b}$$

Prior to determining H and K for any surface contained in a phase-field variable, this phase-field variable is smoothed with a 5^3 grid point mean filter that respects the periodic boundary conditions, and the surface is extracted through the marching cubes algorithm, as described in section 5.5.3. The specific method chosen for determining H and K on the resulting polygonized surface is described in [126]:

For each vertex of the polygonized surface, V_i, for $i = 1, 2, \cdots, N_V$, where N_V is the total number of vertices, both mean curvature, H_i and Gaussian curvature, K_i and the quantity *mixed area*, A^i_M are determined. A^i_M is a measure of the amount of surface area "which belongs to" the vertex V_i. Thus the mixed area is necessary for numeric integration of quantities defined on a per vertex basis, such as for determining the genus via equation (5.30). From H_i and K_i, the principal curvatures at vertex V_i, κ^i_1 and κ^i_2 are determined trivially from equations (5.34).

Note that while mathematically $H^2 \geq K$ for any smooth surface by definition, this may not always be the case when H and K are determined numerically, therefore care must be taken where $H^2 \sim K$, i.e. flat or spherical-like surface patches where $\kappa_1 \sim \kappa_2$. For the present analysis, it was found that the total mixed area of vertices for which $H^2 < K$ were always less than 2% for the two polycrystalline simulations, and always less than 1% for the two liquid simulations, owing to the smoother nature of these surfaces. It was found by visual examination of surfaces extracted at various times from the four data

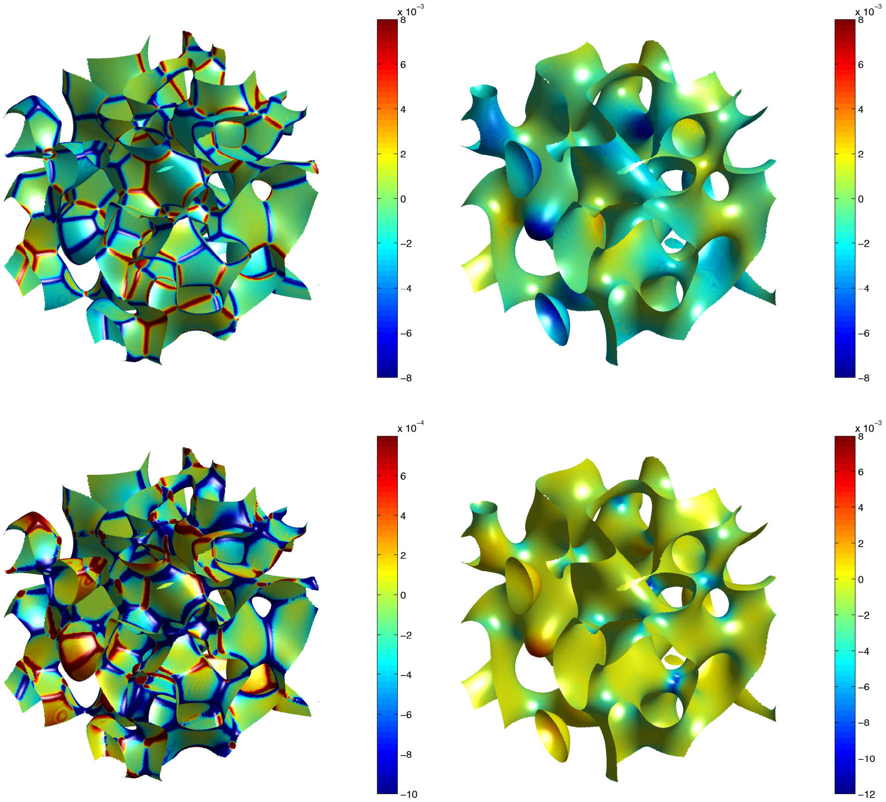

Figure 5.27: Interphase surfaces of the two 40/60 volume ratio simulations at time $t = 300.000$ colored according to curvature (1/8 of the computational domain). Left: Polycrystalline. Right: Liquid. Top: Mean curvature H. Bottom: Gaussian curvature K.

sets that the offending vertices were not spatially correlated. Furthermore, as distributions of principal curvature are of interest, and will be presented in next section, these offending surface patches were examined statistically. It was found that inclusion of these surface patches by setting $H_i^2 - K_i = 0$, thus $\kappa_1^i = \kappa_2^i = H_i$ did not affect distributions of the principal curvatures significantly, and so the author concluded that these surface patches could be excluded from further analysis without thereby introducing significant bias.

Examples of surfaces colored according to their mean curvature and Gaussian curvature is found in figure 5.27. The polycrystalline simulation show curvature on the grain faces, but the largest magnitudes of both kinds of curvature are found in the triple junction grooves. It must be noted that the curvature in the triple junction grooves to some extent is a function of the numeric grid size, and so can not be taken to have physical significance. It is seen that both mean curvature and Gaussian curvature is non-constant across grain faces. This will be discussed in section 5.5.8.

5.5.7.1 Interfacial shape distributions

A convenient way to visualize the statistical distribution of principal curvatures are through interfacial shape distributions (ISD) [85]. Given a set of principal curvatures, κ_1 and κ_2, an ISD represents the probability distribution of any randomly chosen surface patch having principal curvatures κ_1 and κ_2. In other words, an ISD may be thought of as containing the "building blocks" for constructing a surface.

As the principal curvatures determined in the previously described manner are necessarily discrete, constructing an ISD requires binning. In practice, this is done by defining a grid of bins $P(i,j)$, with centers (k_1^i, k_2^j), and a spacing between nearest neighbor bin centers of $\Delta\kappa$. The value of a given bin is then set to the sum of all mixed areas for which the principal curvatures are closer to the given bin center than any other, and the ISD is normalized, i.e.

$$P(i,j) = c\sum_n A_M^n \text{ for all } n \text{ where } \left\{ \begin{array}{l} k_1^i - \Delta\kappa/2 \leq \kappa_1^n < k_1^i + \Delta\kappa/2 \\ k_2^j - \Delta\kappa/2 \leq \kappa_2^n < k_2^j + \Delta\kappa/2 \end{array} \right. \tag{5.35}$$

where c is a normalization constant defined as

$$c = \frac{1}{\Delta\kappa^2 \sum_{ij} P(i,j)} \tag{5.36}$$

which ensures that numeric integration over all κ_1 and κ_2 gives one.

The ISDs may be divided into five regions by considering the sign and magnitude of the curvatures. These regions are indicated on figure 5.28, and the curvature characteristics are summed up in table 5.3. Region 5 contains no density by the definition $\kappa_1 \geq \kappa_2$, and is therefore excluded in the following. Region 1 contains convex surface patches, i.e. surface patches that curve away from the surface normal. Region 2-3 contains hyperbolic surface patches, i.e. saddle-like patches. Region 4 contains concave surface patches, i.e. surface patches that curve towards the surface normal. The surface normal is required to point out of α (minority) regions in present work. The line demarking regions 2 and 3 (marked in red on figure 5.28) is the line of vanishing mean curvature, $H = 0$, ($\kappa_1 = -\kappa_2$) and so all curvature of a minimal surface would be expected to

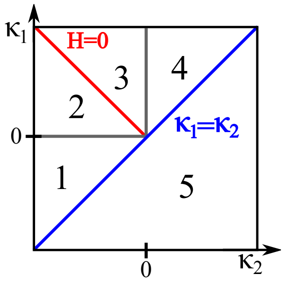

Figure 5.28: Sketch of the five regions of an interfacial shape distribution. The curvature characteristics of these may be found in table 5.3.

	Region 1	Region 2	Region 3	Region 4
H	$H < 0$	$H < 0$	$H > 0$	$H > 0$
K	$K > 0$	$K < 0$	$K < 0$	$K > 0$
κ_1, κ_2	$\kappa_2 < \kappa_1 < 0$	$\kappa_1 > 0 > \kappa_2$ $\kappa_1 < -\kappa_2$	$\kappa_1 > 0 > \kappa_2$ $\kappa_1 > -\kappa_2$	$\kappa_1 > \kappa_2 > 0$
Type	Convex	Hyperbolic	Hyperbolic	Concave

Table 5.3: Curvature characteristics of the five regions of an interfacial shape distribution. A sketch of these is seen in figure 5.28.

reside on this line. The iso-H surface patches are parallel to this, with positive towards the right. The line $\kappa_1 = \kappa_2$ contains spherical-like surface patches.

A necessary condition for morphologically self-similar microstructural evolution is that the ISDs should become invariant under correct scaling of the axes. As the curvature of the surface is defined as the inverse of the radius of curvature, $\kappa = 1/R$, "correct scaling" must mean scaling by the characteristic length scale, S_V. An example of the evolution of ISDs of the liquid 50/50 volume ratio simulation is shown in figure 5.29 with both unnormalized and normalized axes, and it shows that the scaling is reasonable, as the ISD is found to extend approximately the same distance along the $H = 0$ line at all the times shown.

Examination of the time evolution of the axes normalized ISDs reveals that the trend is for curvature to change is a manner such that the average mean curvature remains approximately constant, as may be seen in figure 5.29. That is, the ISDs appears increasingly "squeezed" along the direction of the $\kappa_1 = \kappa_2$ line about the line of average mean curvature $H = \langle H \rangle$. It is found that the average mean curvatures are approximately constant in time. These are found to be $\langle HS_V \rangle \approx 0.0$ for the 50/50 volume ratio simulations, and $\langle HS_V \rangle \approx 0.3$ for 40/60 volume ratio simulations.

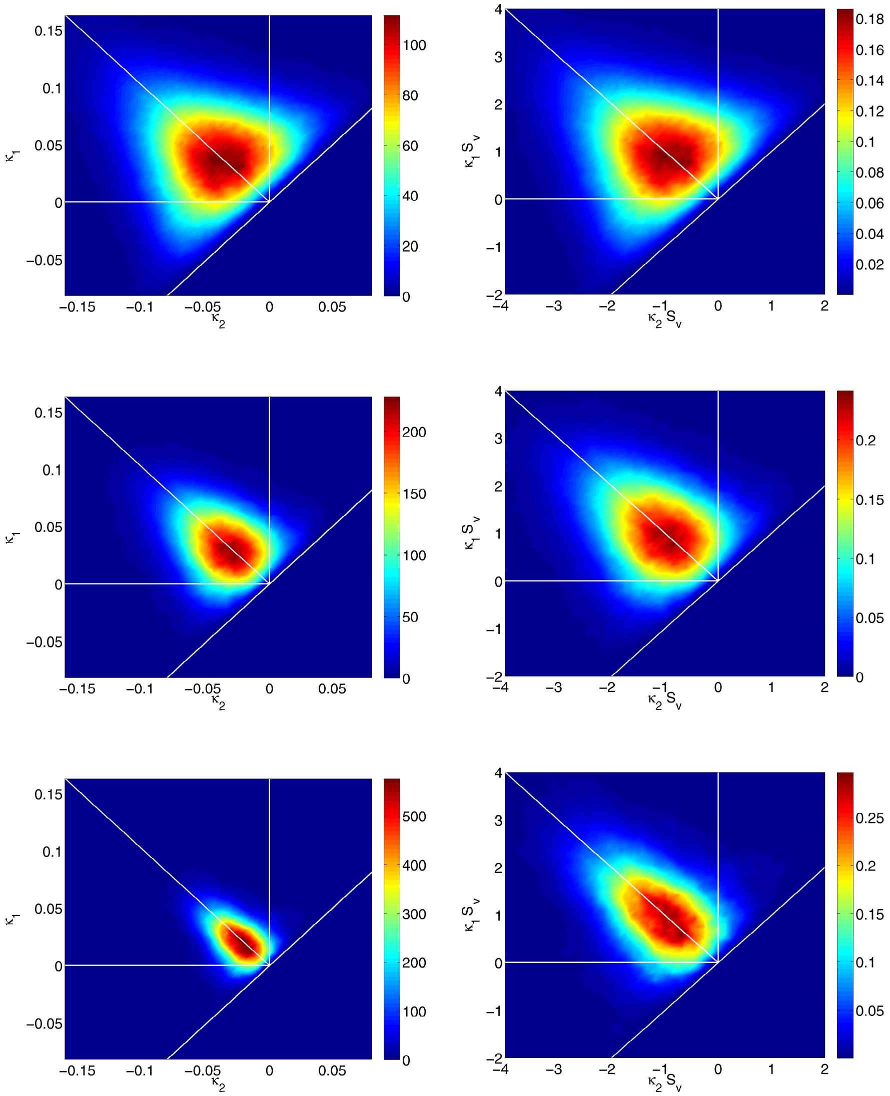

Figure 5.29: ISDs for the 50/50 volume ratio liquid simulation. From top to bottom: times $t = 10.000$, $t = 50.000$ and $t = 300.000$. Left side shows ISDs with unnormalized axes, (κ_1, κ_2), right side shows ISDs with normalized axes, $(\kappa_1 S_v, \kappa_2 S_V)$.

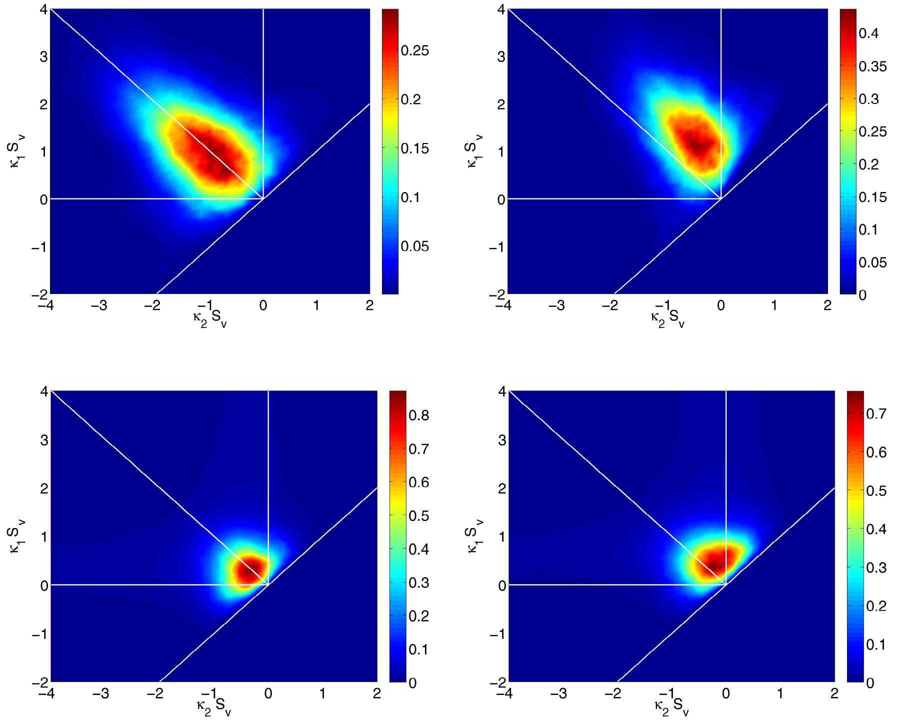

Figure 5.30: The configuration of the self-similar ISDs. Top left: 50/50 volume ratio liquid simulation. Top right: 40/60 volume ratio liquid simulation. Bottom left: 50/50 volume ratio polycrystalline simulation. Bottom right: 40/60 volume ratio polycrystalline simulation.

By examination of simulation output it is found that the ISDs tend to steady state configurations for all four simulations at late times under correct scaling. The self-similar ISDs are shown in figure 5.30. These are generated from data at time $t = 300.000$. The self-similar ISDs for the liquid simulations are in good correspondence to those presented in [85].

There is a high degree of symmetry about the $H = 0$ line for both 50/50 volume ratio simulations. This is expected: All materials parameters are the same for the two phases, which are present in equal amounts, so the direction of the surface normal can be set arbitrarily. However, changing the direction of the surface normal changes the sign of the mean curvature, wherefore symmetry about $H = 0$ is required. A similar symmetry about $\langle HS_V \rangle \approx 0.3$ is not observed for the 40/60 volume ratio simulations.

The self-similar ISDs of the liquid simulations are in good agreement with those presented in [85]. The ISDs of the polycrystalline simulations in figure 5.29 resemble their respective counterparts from the liquid simulations in that their width in the $\kappa_1 = \kappa_2$ directon are similar. They are, however, more "compressed" towards the point of origin, meaning that the normalized principal curvatures are numerically lower, i.e. the interfaces are flatter, than for the liquid simulations. This will be discussed in section 5.5.8. The axes normalized polycrystalline ISDs display smeared-out low-density "tails" on and near the axes. This is due to surface patches in the triple junction grooves: These have numerically low curvature along the direction of the triple junction, and numerically large curvature orthogonal to this direction, and so either $\kappa_1 \sim 0$ or $\kappa_2 \sim 0$. These cannot be taken as physical quantities, since the magnitude of the curvatures in the triple junction grooves are a function of the lattice parameter of the computational grid, as previously mentioned.

5.5.8 Discussion of interphase interface morphology

Grain faces in isotropic single-phase grain growth simulations may with approximation be taken as lying on the surface of a sphere. The surface patches are thus of near-constant mean and Gaussian curvatures. Inspection of the curvatures on figure 5.27 show that this is not the case for the simulations in the present work, as the magnitude of both curvatures varies across grain faces, and spherical-like surface patches would appear on the self-similar ISDs, figure 5.30, as density close to the $\kappa_1 = \kappa_2$ line. In comparing the self-similar ISDs of the liquid simulations to those of the polycrystalline simulations, it is seen that there is an increased density there, but it is not total. Furthermore, investigation of the cross sections of the grain structure of the polycrystalline simulations, 5.17, at late times reveal that while the interphase interfaces are observed to often

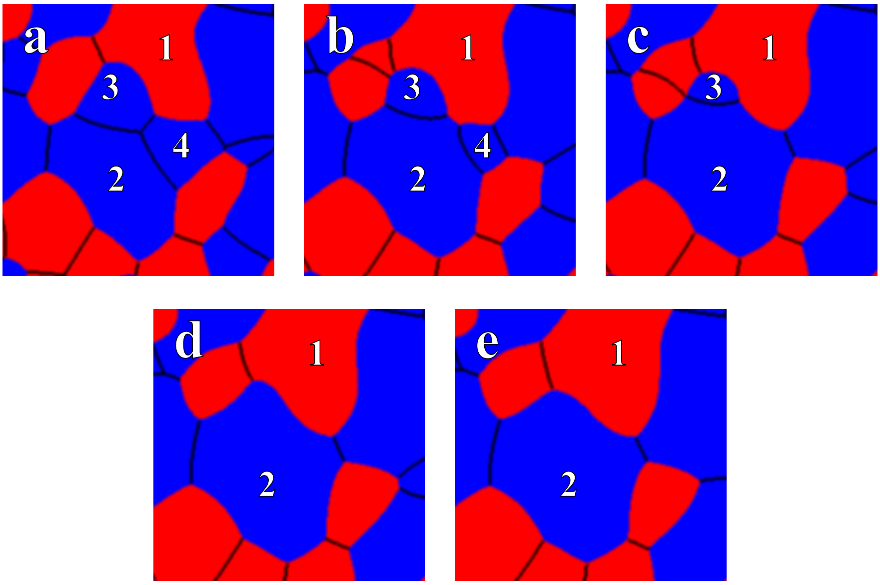

Figure 5.31: Five cross sections of simulation data illustrating the formation of a non-spherical interphase interface in the 40/60 volume ratio polycrystalline simulation. Red: α (minority) phase. Blue: β (majority) phase. a: $t = 172.000$. b: $t = 230.000$. c: $t = 255.000$. d: $t = 268.000$. e: $t = 300.000$.

have varying curvatures, the intraphase interfaces appear more as would be expected from single-phase grain growth. All triple junction dihedral angles are found to be approximately at their local equilibrium values, as given by (5.21). Deviations from spherical-like interphase interfaces raise the free energy of the system, thus there is a driving force for non-spherical-like interphase faces to evolve to a spherical-like morphology. However, if the magnitude of the curvature difference of the spherical-like and non-spherical-like interfaces are low, the driving force will be weak. Additionally, the movement of the interphase interface is dependent on bulk diffusion of mass, and so the migration of the boundary will be slow if the distance required for diffusion to or from the boundary is large. The triple junctions of the non-spherical-like face may also not move easily, since their movement in general is dependent on bulk diffusion of mass, in order to preserve equilibrium triple junction angles and low curvatures on the neighboring grain faces. By visual inspection of the simulation data it is found that these non-spherical-like boundaries have a tendency to evolve towards spherical-like, but that this may require long times.

Attention will now be switched to the generation of these non-spherical-like interfaces. They are observed to be transient phenomena, albeit slowly so. To maintain the observed morphological self-similarity, these interface morphologies must thus be formed with regularity. Such an interface morphology could conceivably be reached by rotation of one or more of the triple junctions of a spherical-like face, but this is not supported by the simulation data. Rather, it is found that these interfaces occur through grain growth, as shown in figure 5.31: Grain 2 grows at the expense of grains 3 and 4. When grains 3 and 4 are eliminated, a non-spherical interphase interface has been formed, the shape of which is largely given by the shapes of the interfaces of the two grains that were eliminated. This interface then goes to reduce its mean curvature slowly.

The numerically lower principal curvatures of the polycrystalline simulations, as compared to the liquid simulations (the "compression" towards the point of origin) seems to be a simple combination of the need for sustaining equilibrium triple junction angles at all the edges of a given grain face, while the curvatures on the face, and the triple junctions are smooth. If the principal curvatures on the grain face somewhere are numerically "large" and $\kappa_1 \sim -\kappa_2$, so that a strongly "saddle-like" morphology results, it seems that smooth curves along the grain edges are impossible, however the author is currently unable to substantiate this assertion further.

5.6 Outlook

The limiting factor for the work presented in this chapter has been the lack of experimental data. Acquisition and segmentation of data sets before and after an annealing stage is the first priority, as the direction of the research and development of the phase-field model would be determined by this data.

First, examination of triple junction angles in the experimental data would allow determination of grain boundary energies. If sufficient variation were found in the triple junction angles, anisotropic interface energies would be sought incorporated into the model.

Large-scale simulations would then be carried out, and the output compared to the microstructure characterized after the annealing step. This would help estimate the ratio between grain boundary mobilities and the diffusive mobility. If the experimental data showed signs of significantly enhanced diffusion at grain boundaries, this would be sought incorporated into the phase-field model. Simulations would then be performed again, in an effort to maximize the correspondence between the simulation output and the experimentally characterized microstructure.

CHAPTER 6

Conclusions

Synchrotron X-ray radiation for non-destructive microstructural characterization has become an invaluable tool for the study of kinetic phenomena in three-dimensional, bulk microstructures in recent years. The strength of these methods is the novel possibility to directly probe the evolution of *specific* microstructural features, rather than having to infer kinetics from destructive characterizations of different microstructures. In recent years, large-scale three-dimensional simulations of microstructural evolution have become possible, due to the increase in computer power available, affording alternative insight into the evolution of specific microstructural features. The three main parts of this work has focused on microstructural evolution during annealing. First, experimentally during recrystallization, where the driving force is the energy stored plastically in the deformed matrix. Second, experimentally during grain growth, where the driving force is the energy stored in the grain boundaries. Third, by simulation during coupled grain growth and coarsening in dual-phase materials under phase ratio conserving conditions, where the driving force is the energy associated with the grain boundaries between grains of the same phase, and the energy associated with the interfaces between the two phases. In the following, the conclusions of these three main parts are drawn.

6.1 Recrystallization kinetics in cold-rolled aluminium

3DXRD has been employed to study the recrystallization kinetics and grain-averaged activation energy of a large number of individual grains during recrystallization in 50% cold-rolled aluminium.

The recrystallization kinetics of 1406 individual grains were examined. The recrystallization kinetics of individual grains was found to deviate significantly from mean kinetics. The diameters of the recrystallizing grains could in many cases be described as piecewise linear, and an explanation related to the cell block microstructure of cold-rolled aluminium was proposed.

Grain-averaged activation energies for recrystallization were determined for 793 individual grains, and forms a wide distribution, the mean of which was found to correspond well with values for the activation energy of recrystallization found in the literature. This distribution is significantly wider than is predicted by experimental observations of migration of large boundaries of well-defined misorientation [48], which is taken as evidence that recrystallization occurs in a more complicated manner.

6.2 Grain topology and grain growth in β titanium

Edge enhanced tomography has been employed to visualize the grain structure of a sample of Ti-21S β titanium with high resolution before and after undergoing grain growth.

A static analysis of 556 bulk grains of the first data set predicted the sign of the growth rate to change at an average number of grain faces of $F = 15.65$ by an application of the three-dimensional Von Neumann-Mullins equation, which was in good agreement with experimental results by Rowenhorst *et al.* [69]. The predicted rate of shrinkage for grains with few faces, $F \leq 10$ seemed to tend to a constant value. As a minimal rate of shrinkage was predicted by Glicksman to occur at $F = 6$ [66], better statistics might have shown the present results to be compatible with that assertion. The sign change of the predicted growth rate is found to be at a grain size of $R = 1.3\,\langle R\rangle$, while a minimal rate of shrinkage is found to occur for grains of size $R = 0.7\,\langle R\rangle$.

The growth of 31 grains were investigated. The sign of the growth of 22 grains seems to be correctly predicted by the three-dimensional Von Neumann-Mullins equation (4.3). Furthermore, the growth of 5 additional grains may arguably have been predicted correctly, to a total maximum of $71-87\%$ correct predictions. The growth of four grains were predicted incorrectly. It must be kept in mind, that there has been considerable growth between the two characterizations, that the three-dimensional Von Neumann-Mullins equation is derived under assumption of isotropy, and neglects surface effects.

6.3 Coupled grain growth and coarsening of dual-phase materials

Three-dimensional phase-field simulations of the microstructural evolution in dual-phase materials with conserved phase ratio have been performed. Four sets of initial conditions were employed: liquid/liquid and polycrystalline/polycrystalline in 50/50 and 40/60 volume ratio.

The characteristic length scales were found to be compatible with power-law growth with an exponent of 3, which is argued to be indicative of bulk diffusion limited growth.

For the 40/60 volume ratio polycrystalline simulation, the mean grain size increased at a slower rate for the minority phase than for the majority phase, which is argued to be due to the larger distance mass must be transported diffusively between minority regions than between majority regions. It was found that the minority phase grains tended to form less faces than the majority phase grains over time.

Topologically self similar evolution was found to set in after a transient caused by the initial conditions. Steady state grain size distributions were found to be approximately consistent with size distributions of solid particles of high volume fraction in a liquid matrix e.g. determined experimentally by Rowenhorst *et al.* [123]. These were identical for the 50/50 and the 40/60 volume ratio simulations when all grains were considered collectively, and the distributions of minority and majority phases in the 40/60 volume ratio simulation were found to be identical when normalized by their respective mean grain sizes. The grains in both simulations during self similar evolution favored interphase faces, $\langle F_{\text{inter}} \rangle \approx 7.8$ and $\langle F_{\text{intra}} \rangle \approx 6.3$. No qualitative difference between the distribution of number of faces for the 50/50 and the 40/60 volume ratio simulations was found when all grains were considered collectively. This distribution was found to be consistent with experimental data by Rowenhorst *et al.* [69] for single-phase grain topology. The genus of the interphase interface was found to evolve with the same growth exponent with good approximation for both liquid/liquid and polycrystalline/polycrystalline simulations, but the genus of the latter was found to be lower, meaning that the interphase surface of the polycrystalline/polycrystalline simulations were less topologically complex than for the liquid/liquid simulations.

Morphologically self similar evolution was found to set in at a later time than the topologically self similar evolution. The morphology was quantified with interfacial shape distributions (ISDs). The self similar ISDs for the polycrystalline/polycrystalline simulations were found to appear ”squeezed” towards the direction of vanishing principal curvatures. The self similar ISDs of the polycrystalline/polycrystalline simulations as compared to the self similar ISDs of the liquid/liquid simulations thus showed an increased, but not total preference for spherical-like surface patches. That the preference is not total is argued to be due to the dependence of the movement of interphase surface patches on bulk diffusion of mass, and the need for preservation of local equilibrium triple junction angles. Non-spherical-like surface patches are observed to be a transient, but long-lived phenomenon which occurs as a result of migration of intraphase interfaces.

References

[1] R.T. DeHoff. Quantitative serial sectioning analysis - preview. *Journal of Microscopy - Oxford*, 131:259–263, 1983.

[2] C.A. Volkert and A.M. Minor. Focused ion beam microscopy and micromachining. *MRS Bulletin*, 32(5):389–395, 2007.

[3] J.E. Spowart. Automated serial sectioning for 3-D analysis of microstructures. *Scripta Materialia*, 55(1):5 – 10, 2006.

[4] T. Chatterji. *Neutron Scattering from Magnetic Materials. 1st Edition.* Elsevier Science, 2005.

[5] J. Fitter, T. Gutberlet, and J. Katsaras. *Neutron Scattering In Biology: Techniques And Applications. 1st Edition.* Springer, 2006.

[6] H.F. Poulsen. 3DXRD microscopy - a comparison with neutron diffraction. *Applied Physics A - Materials Science & Processing*, 74(Part 2, S):S1673–S1675, 2002.

[7] K. Thornton and H.F. Poulsen. Three-dimensional materials science: An intersection of three-dimensional reconstructions and simulations. *MRS Bulletin*, 33(6):587–595, 2008.

[8] H.F. Poulsen. *Three-Dimensional X-ray Diffraction Microscopy: Mapping Polycrystals and their Dynamics. 1st Edition.* Springer, 2004.

[9] G.T. Herman. *Fundamentals of Computerized Tomography. 2nd Edition.* Springer, 2009.

[10] F. J. Humphreys and M. Hatherly. *Recrystallization and Related Annealing Phenomena. 2nd Edition.* Elsevier, 2004.

[11] H.V. Atkinson. Theories of normal grain-growth in pure single-phase systems. *Acta Metallurgica*, 36(3):469–491, 1988.

[12] R.D. MacPherson and D.J. Srolovitz. The von Neumann relation generalized to coarsening of three-dimensional microstructures. *Nature*, 446(7139):1053–1055, 2007.

[13] J. Als-Nielsen and D. McMorrow. *Elements of Modern X-Ray Physics. 1st Edition.* John Wiley & Sons, Ltd., 2001.

[14] ID11. ID11 - Materials Science Beamline – ESRF. `http://www.esrf.eu/UsersAndScience/Experiments/StructMaterials/ID11/`, 2011.

[15] B. E. Warren. *X-ray Diffraction. Reprint of 1st Edition.* Dover Publications, Inc., New York, 1990.

[16] A. Guinier. *X-Ray Diffraction in Crystals, Imperfect Crystals and Amorphous Bodies. 1st Edition.* W.H. Freeman and Company, 1963.

[17] B.E.A. Saleh and M.C. Teich. *Fundamentals of Photonics. 1st Edition.* John Wiley & Sons, Inc., 1991.

[18] P. Cloetens. *Contribution to Phase Contrast Imaging, Reconstruction and Tomography with Hard Synchrotron Radiation.* Ph.D. thesis, Vrije Universiteit Brussel, 1999.

[19] A. Momose, T. Takeda, Y. Itai, and K. Hirano. Phase-contrast X-ray computed tomography for observing biological soft tissues. *Nature Medicine*, 2(4):473–475, 1996.

[20] U. Bonse and M. Hart. An X-ray interferometer. *Applied Physics Letters*, 6(8):155–&, 1965.

[21] S.C. Mayo, P.R. Miller, S.W. Wilkins, T.J. Davis, D. Gao, T.E. Gureyev, D. Paganin, D.J. Parry, A. Pogany, and A.W. Stevenson. Quantitative X-ray projection microscopy: phase-contrast and multi-spectral imaging. *Journal Of Microscopy - Oxford*, 207(Part 2):79–96, 2002.

[22] D. Gabor. A new microscopic principle. *Nature*, 161(4098):777–778, 1948.

[23] G.B. Arfken and H.J. Weber. *Mathematical Methods for Physicists. 5th Edition.* Academic Press, 2000.

[24] A.V. Bronnikov. Theory of quantitative phase-contrast computed tomography. *Journal of the Optical Society of America A - Optics Image Science and Vision*, 19(3):472–480, 2002.

[25] M. Stampanoni, A. Groso, A. Isenegger, G. Mikuljan, Q. Chen, A. Bertrand, S. Henein, R. Betemps, U. Frommherz, P. Boehler, D. Meister, M. Lange, and R. Abela. Trends in synchrotron-based tomographic imaging: the SLS experience. In U. Bonse, editor, *Developments in X-Ray Tomography V*, volume 6318 of *Proceedings Of The Society Of Photo-Optical Instrumentation Engineers (SPIE)*, pages U199–U212, 2006.

[26] A.V. Bronnikov. Phase-contrast CT: Fundamental theorem and fast image reconstruction algorithms. In U. Bonse, editor, *Developments in X-Ray Tomography V*, volume 6318 of *Proceedings of the Society of Photo-Optical Instrumentation Engineers (SPIE)*, page Q3180, 2006.

[27] P. Cloetens, W. Ludwig, J. Baruchel, D. Van Dyck, J. Van Landuyt, J.P. Guigay, and M. Schlenker. Holotomography: Quantitative phase tomography with micrometer resolution using hard synchrotron radiation X-rays. *Applied Physics Letters*, 75(19):2912–2914, 1999.

[28] M.O. de Beeck, D. Van Dyck, and W. Coene. Wave function reconstruction in HRTEM: The parabola method. *Ultramicroscopy*, 64(1-4):167–183, 1996.

[29] J. Earl and E.J. Kirkland. Improved high resolution image processing of bright field electron micrographs: I. Theory. *Ultramicroscopy*, 15(3):151 – 172, 1984.

[30] W. Ludwig, A. King, P. Reischig, M. Herbig, E.M. Lauridsen, S. Schmidt, H. Proudhon, S. Forest, P. Cloetens, S.R. du Roscoat, J.Y. Buffiere, T.J. Marrow, and H.F. Poulsen. New opportunities for 3D materials science of polycrystalline materials at the micrometre lengthscale by combined use of X-ray diffraction and X-ray imaging. *Materials Science and Engineering A - Structural Materials Properties, Microstructure and Processing*, 524(1-2):69–76, 2009.

[31] H.F. Poulsen, D. Juul Jensen, and G.B.M. Vaughan. Three-dimensional X-ray diffraction microscopy using high-energy X-rays. *MRS Bulletin*, 29(3):166–169, 2004.

[32] E.M. Lauridsen. *The 3D X-Ray Diffraction Microscope and its Application to the Study of Recrystallization Kinetics.* Ph.D. thesis, Risø National Laboratory, 2001.

[33] S. Schmidt. Grainspotter v. 0.82. `http://sourceforge.net/apps/trac/fable/wiki/grainspotter`, 2010.

[34] A. Lyckegaard, E.M. Lauridsen, W. Ludwig, R.W. Fonda, and H.F. Poulsen. On the use of Laguerre tessellations for representations of 3D

grain structures. *Advanced Engineering Materials*, 13(3, SI):165–170, 2011.

[35] H.F. Poulsen and X. Fu. Generation of grain maps by an algebraic reconstruction technique. *Journal of Applied Crystallography*, 36(4):1062–1068, 2003.

[36] W. Ludwig, S. Schmidt, E.M. Lauridsen, and H.F. Poulsen. X-ray diffraction contrast tomography: a novel technique for three-dimensional grain mapping of polycrystals. I. Direct beam case. *Journal Of Applied Crystallography*, 41(Part 2):302–309, 2008.

[37] G. Johnson, A. King, M.G. Honnicke, J. Marrow, and W. Ludwig. X-ray diffraction contrast tomography: a novel technique for three-dimensional grain mapping of polycrystals. II. The combined case. *Journal Of Applied Crystallography*, 41(Part 2):310–318, 2008.

[38] W. Ludwig, P. Reischig, A. King, M. Herbig, E.M. Lauridsen, G. Johnson, T.J. Marrow, and J.Y. Buffiere. Three-dimensional grain mapping by X-ray diffraction contrast tomography and the use of Friedel pairs in diffraction data analysis. *Review Of Scientific Instruments*, 80(3), 2009.

[39] J.W. Cahn and W.G Hagel. Divergent pearlite in a manganese eutectoid steel. *Acta Metallurgica*, 11(6):561 – 574, 1963.

[40] D. Juul Jensen. Growth of nuclei with different crystallographic orientations during recrystallization. *Scripta Metallurgica et Materialia*, 27(5):533 – 538, 1992.

[41] W.A. Johnson and R.F. Mehl. Reaction kinetics in processes of nucleation and growth. *Transactions of the American Institute of Mining and Metallurgical Engineers (Trans AIME)*, 135:416–442, 1939.

[42] M. Avrami. Kinetics of phase change I - General theory. *Journal of Chemical Physics*, 7(12):1103–1112, 1939.

[43] A.N. Kolmogorov. *Selected Works of A.N. Kolmogorov: Probability Theory and Mathematical Statistics, Volume 2. 1st Edition.* Springer, 1992.

[44] R.A. Vandermeer and B.B. Rath. Microstructural modeling of recrystallization in deformed iron single-crystals. *Metallurgical Transactions A - Physical Metallurgy and Materials Science*, 20(10):1933–1942, 1989.

[45] E.M. Lauridsen, D. Juul Jensen, H.F. Poulsen, and U. Lienert. Kinetics of individual grains during recrystallization. *Scripta Materialia*, 43(9):561–566, 2000.

[46] E.M. Lauridsen, H.F. Poulsen, S.F. Nielsen, and D. Juul Jensen. Recrystallization kinetics of individual bulk grains in 90% cold-rolled aluminium. *Acta Materialia*, 51:4423–4435, 2003.

[47] S. Schmidt, S.F. Nielsen, C. Gundlach, L. Margulies, X. Huang, and D. Juul Jensen. Watching the growth of bulk grains during recrystallization of deformed metals. *Science*, 305(5681):229–232, 2004.

[48] G. Gottstein and L.S. Shvindlerman. *Grain Boundary Migration in Metals. 1st Edition.* CRC Press, 1999.

[49] D.A. Porter and K.E. Easterling. *Phase Transformation in Metals and Alloys. 2nd Edition.* CRC Press, 2004.

[50] R.A. Vandermeer. Kinetic aspects of nucleation and growth in recrystallization. In N. Hansen, X. Huang, D. Juul Jensen, E.M. Lauridsen, T. Leffers, W. Pantleon, T.J. Sabin, and J.A. Wert, editors, *21st Risø International Symposium on Materials Science*, pages 179–200, 2000.

[51] R.A. Vandermeer, E.M. Lauridsen, and D. Juul Jensen. Growth rate distribution during recrystallization of copper. In B. Bacroix, J.H. Driver, R. LeGall, C. Maurice, R. Penelle, H. Regle, and L. Tabourot, editors, *2nd Joint International Conference on Recrystallization and Grain Growth*, pages 467–470, 2004.

[52] C. Zener quoted by C.S. Smith. Grains, phases, and interfaces - an interpretation of microstructure. *Transactions of the American Institute of Mining and Metallurgical Engineers (Trans AIME)*, 175:15–51, 1948.

[53] A. Hammersley. FIT2D.
`http://www.esrf.eu/computing/scientific/FIT2D`, 2011.

[54] N. Hansen. New discoveries in deformed metals. *Metallurgical Transactions A*, 32(12):2917–2935, 2001.

[55] D.A. Hughes and N. Hansen. *ASM Handbook, Volume 9, Metallography and Microstructures*, chapter Plastic Deformation Structures, pages 192–206. ASM International, 2004.

[56] Y.B. Zhang, A. Godfrey, Q. Liu, W. Liu, and D. Juul Jensen. Analysis of the growth of individual grains during recrystallization in pure nickel. *Acta Materialia*, 57:2631–2639, 2009.

[57] D.L. Olmsted, E.A. Holm, and S.M. Foiles. Survey of computed grain boundary properties in face-centered cubic metals-II: Grain boundary mobility. *Acta Materialia*, 57(13):3704–3713, 2009.

[58] J.W. Cahn, Y. Mishin, and A. Suzuki. Coupling grain boundary motion to shear deformation. *Acta Materialia*, 54(19):4953–4975, 2006.

[59] J.W. Cahn, Y. Mishin, and A. Suzuki. Duality of dislocation content of grain boundaries. *Philosophical Magazine A*, 86(25):3965–3980, 2006.

[60] H.H. Liu, S. Schmidt, H.F. Poulsen, A. Godfrey, Z.Q. Liu, J.A. Sharon, and X. Huang. Three-dimensional orientation mapping in the transmission electron microscope. *Science*, 332(6031):833–834, 2011.

[61] C.S. Smith. Grains, phases, and interfaces - an interpretation of microstructure. *Transactions of the American Institute of Mining and Metallurgical Engineers (Trans AIME)*, 175:15–51, 1948.

[62] J. Von Neumann. *Metal Interfaces*, pages 108–111. American Society for Metals, 1952.

[63] W.W. Mullins. Two-dimensional motion of idealized grain boundaries. *Journal of Applied Physics*, 27(8):900–904, 1956.

[64] W.E. Lorensen and H.E. Cline. Marching cubes: A high resolution 3D surface construction algorithm. *SIGGRAPH Computer Graphics*, 21:163–169, 1987.

[65] S. Hilgenfeldt, A.M. Kraynik, S.A. Koehler, and H.A. Stone. An accurate von Neumann's law for three-dimensional foams. *Physical Review Letters*, 86(12):2685–2688, 2001.

[66] M.E. Glicksman. Analysis of 3-D network structures. *Philosophical Magazine*, 85(1):3–31, 2005.

[67] K. Brakke. The Surface Evolver. *Experimental Mathematics*, 1:141–165, 1992.

[68] F. Wakai, N. Enomoto, and H. Ogawa. Three-dimensional microstructural evolution in ideal grain growth - general statistics. *Acta Materialia*, 48(6):1297–1311, 2000.

[69] D.J. Rowenhorst, A.C. Lewis, and G. Spanos. Three-dimensional analysis of grain topology and interface curvature in a beta-titanium alloy. *Acta Materialia*, 58(16):5511–5519, 2010.

[70] TIMET. TIMETAL 21S data sheet. `http://www.timet.com/pdfs/21s.pdf`, 2000.

[71] A. Lyckegaard. *Development of tomographic reconstruction methods in materials science with focus on advanced scanning methods.* Ph.D. thesis, Risø DTU, 2011.

[72] M. Couprie and G. Bertrand. Topological grayscale watershed transformation. In R.A. Melter, A.Y. Wu, and L.J. Latecki, editors, *Vision Geometry VI*, volume 3168 of *Proceedings of the Society of Photo-Optical Instumentation Engineers (SPIE)*, pages 136–146, 1997.

[73] Z. Wu and J.M. Sullivan. Multiple material marching Cubes algorithm. *International Journal For Numerical Methods In Engineering*, 58(2):189–207, 2003.

[74] I. M. McKenna. *Three-Dimensional Anisotropic and Isotropic Grain Growth Simulations with Comparisons to Experiment.* Ph.D. thesis, Northwestern University, 2010.

[75] L.-Q. Chen and W. Yang. Computer simulation of the domain dynamics of a quenched system with a large number of nonconserved order parameters: The grain-growth kinetics. *Physical Review B*, 50(21):15752–15756, 1994.

[76] C.E. Krill and L.-Q. Chen. Computer simulation of 3-D grain growth using a phase-field model. *Acta Materialia*, 50(12):3057–3073, 2002.

[77] S.G. Kim, D.I. Kim, W.T. Kim, and Y.B. Park. Computer simulations of two-dimensional and three-dimensional ideal grain growth. *Physical Review E*, 74(6):061605, 2006.

[78] A. Kazaryan, Y. Wang, S.A. Dregia, and B.R. Patton. Generalized phase-field model for computer simulation of grain growth in anisotropic systems. *Physical Review B*, 61(21):14275–14278, 2000.

[79] N. Moelans, B. Blanpain, and P. Wollants. Quantitative phase-field approach for simulating grain growth in anisotropic systems with arbitrary inclination and misorientation dependence. *Physical Review Letters*, 101(2):025502, 2008.

[80] R. Kobayashi. A numerical approach to three-dimensional dendritic solidification. *Experimental Mathematics*, 3:59–81, 1994.

[81] A. Karma and W.-J. Rappel. Phase-field method for computationally efficient modeling of solidification with arbitrary interface kinetics. *Physical Review E*, 53(4):R3017–R3020, 1996.

[82] W.J. Boettinger, J.A. Warren, C. Beckermann, and A. Karma. Phase-field simulation of solidification. *Annual Review of Materials Research*, 32:163–194, 2002.

[83] D. Fan, L.-Q. Chen, S.P. Chen, and P.W. Voorhees. Phase field formulations for modeling the Ostwald ripening in two-phase systems. *Computational Materials Science*, 9(3-4):329–336, 1998.

[84] I.S. Aranson, V.A. Kalatsky, and V.M. Vinokur. Continuum field description of crack propagation. *Physical Review Letters*, 85(1):118–121, 2000.

[85] Y. Kwon, K. Thornton, and P.W. Voorhees. Morphology and topology in coarsening of domains via non-conserved and conserved dynamics. *Philosophical Magazine*, 90(5):317–335, 2010.

[86] J.W. Cahn and J.E. Hilliard. Free energy of a nonuniform system. I. interfacial free energy. *Journal of Chemical Physics*, 28(2):258–267, 1958.

[87] J.W. Cahn. On spinodal decomposition in cubic crystals. *Acta Metallurgica*, 10(3):179–183, 1962.

[88] S.M. Allen and J.W. Cahn. A microscopic theory for antiphase boundary motion and its application to antiphase domain coarsening. *Acta Metallurgica*, 27:1085–1095, 1979.

[89] L.-Q. Chen and Y.Z. Wang. The continuum field approach to modeling microstructural evolution. *JOM - Journal Of The Minerals Metals & Materials Society*, 48(12):13–18, 1996.

[90] N. Moelans, B. Blanpain, and P. Wollants. An introtroduction to phase-field modeling of microstructure evolution. *Computer Coupling of Phase Diagrams and Thermochemistry*, 32:268–294, 2008.

[91] I. Steinbach. Phase-field models in materials science. *Modelling and Simulation in Materials Science and Engineering*, 17(7):073001, 2009.

[92] J.D. van der Waals. The equation of state for gases and liquids. Reprinted from Nobel lecture, December, 1910. *Journal of Supercritical Fluids*, 55(2, SI):403–414, 2010.

[93] L.D. Landau and E.M. Lifshitz. *Statistical Physics, Part 1, Volume 5. 3rd Edition.* Pergamon Press, 1994.

[94] W.F. Ames. *Numerical Methods for Partial Differential Equations. 3rd Edition.* Academic Press, 1992.

[95] A.W. Bush. *Perturbation Methods for Engineers and Scientists. 1st Edition.* CRC Press, 1992.

[96] E.A. Holm and C.C. Battaile. The computer simulation of microstructural evolution. *JOM - Journal of the Minerals Metals & Materials Society*, 53(9):20–23, 2001.

[97] L.I. Rubinstein. *The Stefan Problem, Translations of Mathematical Monographs, Vol. 27. 1st Edition.* American Mathematical Society, 1971.

[98] D. Fan, L.-Q Chen, and S.P. Chen. Effect of grain boundary width on grain growth in a diffuse-interface field model. *Materials Science and Engineering A*, 238:78–84, 1997.

[99] S.J. Osher and R.P. Fedkiw. Level set methods: An overview and some recent results. *Journal of Computational Physics*, 169(2):463–502, 2001.

[100] S.J. Osher and R.P. Fedkiw. *Level Set Methods and Dynamic Implicit Surfaces. 1st Edition.* Springer, 2002.

[101] G. Russo and P. Smereka. A level set method for the evolution of faceted crystals. *SIAM Journal on Scientific Computing (SCIC)*, 2000:2073–2095, 2000.

[102] L.-Q. Chen and D. Fan. Computer simulation model for coupled grain growth and Ostwald ripening - application to Al2O3-ZrO2 two-phase systems. *Journal of the American Ceramical Society*, 79(5):1163–1168, 1996.

[103] D. Fan and L.-Q. Chen. Diffusion-controlled grain growth in two-phase solids. *Acta Materialia*, 45(8):3297–3310, 1997.

[104] D. Fan and L.-Q. Chen. Topological evolution during coupled grain growth and Ostwald ripening in volume-conserved 2-D two-phase polycrystals. *Acta Materialia*, 45(10):4145–4154, 1997.

[105] D. Fan and L.-Q. Chen. Grain growth and microstructural evolution in a two-dimensional two-phase solid containing only quadrijunctions. *Scripta Materialia*, 37(2):233–238, 1997.

[106] J.W. Cahn. Stability, microstructural evolution, grain-growth, and coarsening in a 2-dimensional 2-phase microstructure. *Acta Metallurgica et Materialia*, 39(10):2189–2199, 1991.

[107] High Performance Fortran Forum. High Performance Fortran.
`http://hpff.rice.edu/index.htm`, 2011.

[108] MPI Forum. Message Passing Interface Forum.
`http://www.mpi-forum.org/index.html`, 2011.

[109] L.-Q. Chen and J. Shen. Applications of semi-implicit Fourier-spectral method to phase field equations. *Computer Physics Communications*, 108(2-3):147–158, 1998.

[110] M. Frigo and S.G. Johnson. FFTW. `http://www.fftw.org`, 2011.

[111] L. Vanherpe, N. Moelans, B. Blanpain, and S. Vandewalle. Bounding box algorithm for three-dimensional phase-field simulations of microstructural evolution in polycrystalline materials. *Physical Review E*, 76(5):056702–1–11, 2007.

[112] J. Gruber, N. Ma, Y. Wang, A.D. Rollett, and G.S. Rohrer. Sparse data structure and algorithm for the phase field method. *Modelling and Simulation in Materials Science and Engineering*, 14(7):1189–1195, 2006.

[113] W. Gropp, E. Lusk, and R. Thakur. *Using MPI-2: Advanced Features of the Message-Passing Interface. 1st Edition.* MIT Press, 1999.

[114] C. Isenberg. *The Science of Soap Films and Soap Bubbles. 2nd Edition.* Dover Publications, 1992.

[115] L. Ratke and P.W. Voorhees. *Growth and Coarsening, Ripening in Material Processing. 1st Edition.* Springer, 2002.

[116] J.E. Burke and D. Turnbull. Recrystallization and grain growth. *Progress in Metal Physics*, 3:220–292, 1952.

[117] R.A. Vandermeer and H. Hu. On the grain growth exponent of pure iron. *Acta Metallurgica et Materialia*, 42(9):3071–3075, 1994.

[118] I.M. Lifshitz and V.V. Slyozov. The kinetics of precipitation from supersaturated solid solutions. *Journal of Physics and Chemistry of Solids*, 19(1-2):35 – 50, 1961.

[119] C. Wagner. Theorie der Alterung von Niederschlagen durch Umlösen (Ostwald-reifung). *Zeitschrift Für Elektrochemie*, 65(7-8):581–591, 1961.

[120] N. Akaiwa and P.W. Voorhees. Late-stage phase separation: Dynamics, spatial correlations, and structure functions. *Physical Review E*, 49:3860–3880, 1994.

[121] S. Hardy and P.W. Voorhees. Ostwald ripening in a system with a high volume fraction of coarsening phase. *Metallurgical and Materials Transactions A*, 19:2713–2721, 1988. 10.1007/BF02645806.

[122] J.W. Martin, R.D. Doherty, and B. Cantor. *Stability of Microstructure in Metallic Systems. 2nd Edition.* Cambridge University Press, 1997.

[123] D.J. Rowenhorst, J.P. Kuang, K. Thornton, and P.W. Voorhees. Three-dimensional analysis of particle coarsening in high volume fraction solid-liquid mixtures. *Acta Materialia*, 54(8):2027–2039, 2006.

[124] E.W. Weisstein. "Gauss-Bonnet Formula" from MathWorld - A Wolfram Web Resource.
`http://mathworld.wolfram.com/Gauss-BonnetFormula.html`, 2011.

[125] L.K. Aagesen, A.E. Johnson, J.L. Fife, P.W. Voorhees, M.J. Miksis, S.O. Poulsen, E.M. Lauridsen, F. Marone, and M. Stampanoni. Universality and self-similarity in pinch-off of rods by bulk diffusion. *Nature Physics*, 6(10):796–800, 2010.

[126] N. Meyer, M. Desbrun, P. Schroder, and A.H. Barr. Discrete differential-geometry operators for triangulated 2-manifolds. In H.C. Hege and K. Polthier, editors, *Visualization and Mathematics III*, pages 35–57, 2003. 3rd International Workshop on Visualization and Mathematics, Berlin, Germany, May 22-25, 2002.

Appendix A

A.1 Asymptotic solutions for planar grain boundaries

We consider two phase-field variables, ϕ_+ and ϕ_-, which may be any combination of α and β type phase-field variables. Introducing the constraint $\phi_+ + \phi_- = 1$ leads to the approximate solutions to the equations (5.14b) and (5.14c) to be given by the functions

$$\phi_\pm = \frac{1}{2}\left(1 \pm \tanh\left(\sqrt{\xi}\frac{x}{2}\right)\right) \tag{A.1}$$

where the quantity ξ may vary with the interface type in question, and is defined as

$$\xi = \begin{cases} \epsilon_{\alpha\alpha} - X^2\gamma_\alpha \text{ for } \alpha\alpha \\ \epsilon_{\beta\beta} - X^2\gamma_\beta \text{ for } \beta\beta \\ \epsilon_{\alpha\beta} - X^2\gamma_\alpha \text{ for } \alpha\beta \text{ if and only if } D_\alpha = D_\beta \end{cases} \tag{A.2}$$

For the $\alpha\beta$ interface, the requirement of $D_\alpha = D_\beta$ is equivalent to requiring $\gamma_\alpha = \gamma_\beta$ cf. the defining equation (5.16), and so either may be used in ξ.

The above solutions are dependent on specific composition profiles, C, which are not consistent with the full steady state equation governing C, equation

(5.14a), however, they become solutions to first order in $C - C_\alpha$ and $C - C_\beta$, with the choice

$$\epsilon_{\alpha\alpha} = \epsilon_{\beta\beta} = \epsilon_{\alpha\beta} = 3X^2\gamma_\alpha - \frac{16X^2\gamma_\alpha^2}{3BX^2 + 12D_\beta X^2 - 4A} \tag{A.3}$$

where it is again necessary to choose $D_\alpha = D_\beta$ and so $\gamma_\alpha = \gamma_\beta$ cf. equation (A.1)

The approximated equilibrium compositional profiles through an $\alpha\alpha$ - or a $\beta\beta$ interface are given by

$$\bar{C} = \frac{2X\gamma_\alpha}{3BX^2 - 4A + 12D_\beta X^2} \operatorname{sech}^2\left(\sqrt{\xi}\frac{x}{2}\right) \tag{A.4}$$

where $\bar{C}$ is defined as

$$\bar{C} = \begin{cases} C - C_\alpha \text{ for } \alpha\alpha \\ \bar{C}_\beta - C \text{ for } \beta\beta \end{cases} \tag{A.5}$$

ξ is defined as in equation (A.1). For the $\alpha\beta$ interface, the approximated profile is found to be a poor approximation to that found by numeric solution. This is since approximations by expansion in C fails due to the large magnitude of the change in composition across an interphase interface, and so it is not shown. Numeric solutions are shown alongside the approximate solutions in figure A.1 Inspection reveals that the approximated solutions may accurately predict the width of all planar grain boundaries, as the approximated solutions follow the numeric solutions closely where the phase-field variable $\phi \approx 1$. The analytical expressions for $\alpha\alpha$- and $\beta\beta$ interfaces show better correspondence to the numeric solutions than the analytical expression for the $\alpha\beta$ interface. This is again due to the large magnitude of the change in composition occurring across the interphase boundary, which invalidates the first-order in C expansion that equation (A.1) solves. This in turn invalidates the assumption of $\phi_+ + \phi_- = 1$, as can clearly be seen at the crossing $\phi_+ = \phi_-$.

If we take for the interface width the somewhat arbitrary distance between the points where the α and/or β-type phase-field variables forming the interface attain values of $\phi_\pm \approx 0.98$, then we get the simple expression for the boundary width

$$W = \frac{8}{\sqrt{\xi}} \tag{A.6}$$

which is valid for all planar grain boundaries in the system, provided we have chosen $D_\alpha = D_\beta$, since ξ will then have the same value for all interface types. Other definitions of the interface width would change the constant of proportionality in equation (A.6), however the specific values the phase-field variables should attain should be sufficiently close to 1 for correspondence between

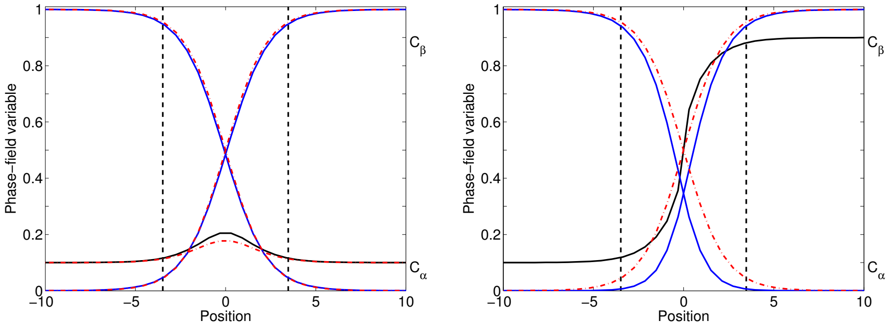

Figure A.1: Numerically determined equilibrium planar grain boundary profiles and approximate analytical solutions. Black lines are composition, C, blue lines are α and β-type phase-field variables. Red dash-dotted lines are approximate analytical solutions. Interface widths according to equation (A.6) are indicated by vertical lines. The remaining model parameters are chosen according to section 5.3.8. Left: $\alpha\alpha$ interface. Right: $\alpha\beta$ interface. Here, the approximate solution for the composition, C, is not shown, as it is found to be a poor approximation.

asymptotic and numeric solutions to be guaranteed. The interface width for the illustration of the correspondence between asymptotic solutions and numeric solutions in figure A.1 is $W \approx 6.95$, and the interface is indicated by vertical lines.

APPENDIX B

Papers

B.1 In situ measurements of growth rates and grain-averaged activation energies of individual grains during recrystallization of 50% cold-rolled aluminium

Available online at www.sciencedirect.com

ScienceDirect

Scripta Materialia 64 (2011) 1003–1006

Scripta MATERIALIA

www.elsevier.com/locate/scriptamat

In situ measurements of growth rates and grain-averaged activation energies of individual grains during recrystallization of 50% cold-rolled aluminium

S.O. Poulsen,[a,*] E.M. Lauridsen,[a] A. Lyckegaard,[b] J. Oddershede,[a] C. Gundlach,[c]
C. Curfs[d] and D. Juul Jensen[e]

[a] *Center for Fundamental Research: Metal Structures in Four Dimensions, Risø DTU, Frederiksborgvej 399, 4000 Roskilde, Denmark*
[b] *DTU Transport, Technical University of Denmark, Bygningstorvet 116, 2800 Kgs. Lyngby, Denmark*
[c] *MAX-lab, Lund University, P.O. Box 118, SE-22100 Lund, Sweden*
[d] *European Synchrotron Radiation Facility, 6 Rue Jules Horowitz, 38043 Grenoble Cedex 9, France*
[e] *Danish Chinese Center for Nanometals, Risø DTU, Frederiksborgvej 399, 4000 Roskilde, Denmark*

Received 2 December 2010; revised 28 January 2011; accepted 31 January 2011
Available online 21 February 2011

Three-dimensional X-ray diffraction has been used to study the growth kinetics of 1406 individual grains recrystallizing in 50% cold-rolled aluminium. It is found that each grain follows its own kinetics. The radial growth of individual grains is found to often be piecewise linear, and an explanation based on the cell block microstructure of cold-rolled aluminium is proposed. Grain-averaged activation energies of 793 individual grains are determined, and found to constitute a broad distribution. Reasons and implications of these findings are discussed.

Keywords: Static recrystallization; Recrystallization kinetics; Aluminum; Grain-averaged activation energy; X-ray diffraction (XRD)

When a metal or alloy is deformed plastically, a part of the work expended is stored in the form of crystal defects. A reduction in this stored energy is the driving force for recrystallization, during which almost defect-free grains are nucleated and subsequently grow by grain boundary migration.

Until recently, most investigations of recrystallization kinetics have focussed on average kinetics. The reason for this focus has mainly been due to lack of non-destructive, in situ experimental methods, making it impossible to follow recrystallization in local bulk microstructures.

Following the introduction of three-dimensional X-ray diffraction (3DXRD) microscopy [1], it has been shown that there is considerable variation between the recrystallization kinetics of different grains in the same recrystallizing sample, thus contradicting the assumptions of mean microstructural models.

This paper describes a quantitative 3DXRD investigation of the recrystallization kinetics of a large number of individual grains in 50% cold-rolled aluminium AA 1050. Growth rates of individual grains have been determined, and are compared to those found in the more heavily subdivided matrix of 90% cold-rolled aluminium [2]. Furthermore, the measurements allow for the determination of the activation energies for recrystallization of the individual grains. This has previously only been done in a preliminary study of eight grains during recrystallization of pure copper [3].

During grain boundary migration, the velocity of a grain boundary is considered to be the product of a boundary mobility and a driving force (e.g. [4]):

$$v = MF \tag{1}$$

As the driving force for recrystallization is taken to be the reduction in stored energy, it is only a function of the local deformed microstructure. The grain boundary mobility, however, has been found to be a thermally activated parameter, and so follows an Arrhenius relationship. Thus, the grain boundary velocity may be written as:

$$v = m_0 \exp\left(-\frac{Q}{RT}\right)F \tag{2}$$

---

[*] Corresponding author. E-mail: spou@risoe.dtu.dk

1359-6462/$ - see front matter © 2011 Acta Materialia Inc. Published by Elsevier Ltd. All rights reserved.
doi:10.1016/j.scriptamat.2011.01.046

where m_0 is a quantity with dimensions of time per mass (reflecting the choice of F as a driving force, rather than a pressure), R is the universal gas constant, T is the absolute temperature and Q is the activation energy of the migration of the specific grain boundary in question. When activation energies of recrystallization of bulk structures are reported (e.g. [5]) it is an average of the migration activation energies of all boundaries in the system weighted by their area.

3DXRD allows for the tracking of the individual volumes of a large number of bulk grains in situ. Determining the radial growth rates v_1 and v_2 at temperatures T_1 and T_2 with a time resolution in which the local surroundings of a recrystallizing grain may be assumed nearly constant allows for the "grain-averaged activation energy" to be expressed by application of Eq. (2) as:

$$Q = R\left(\frac{1}{T_1} - \frac{1}{T_2}\right)\ln\frac{v_2}{v_1} \tag{3}$$

These are termed grain-averaged activation energies to underline that they are not a weighted average over all boundaries in the bulk system, but rather a weighted average of the boundaries of an individual grain. The link to the well-known activation energy of recrystallization is that an average over a large number of representative grain-averaged activation energies must reduce to the bulk value.

Three box-shaped samples of similar dimensions were cut from the centre of a sheet of 50% cold-rolled aluminium AA 1050 for the experimental investigation. This was the same material as previously investigated at larger strain (90% cold-rolling) in Ref. [2].

These samples were electropolished to remove preferred nucleation sites introduced on the surface when cutting. In turn, samples were mounted in a hot finger furnace in an inert gas athmosphere at the ID11 beamline at the European Synchrotron Radiation Facility (ESRF). The 3DXRD experimental set-up can be seen in Supplementary information. The rotation around the vertical axis of the sample was denoted ω, and the sample was mounted so that the (x, y, z) directions coincided with the (ND, TD, RD) directions of the sample for $\omega = 0$.

A wide rectangular beam profile of height $h_0 = 400$ μm was defined by slits, and a box-shaped part of the sample was illuminated by 65 keV X-rays. The gauge volume, V_{gauge}, was given by the product of the slit height and the sample cross-section, $V_{gauge} \simeq 400 \times 850 \times 850$ μm^3.

The furnace temperature was set to $T_1 = 310$ °C, and the sample was rotated in increments of $\Delta\omega = 0.5°$ from $\omega = -15°$ to $\omega = +15°$, each individual rotation taking 2 s. Restricting ω to a 30° window does not cause significant textural bias due to the high symmetry of the cubic lattice. Images of the diffracted beam were acquired with a 14-bit FReLoN camera during rotation, resulting in a time resolution of 3.2 min between images at the same ω.

This was repeated for 120 min. This duration was chosen to result in ~20% recrystallization, as determined by hardness tests following a series of ex situ annealing experiments performed before the 3DXRD experiment. The furnace temperature was then swiftly raised to $T_2 = 325$ °C for two of the samples and to $T_2 = 320$ °C for the last sample. Rotation and image acquisition proceeded in the manner previously described for 90 min. During acquisition the recorded images were continually monitored, and the beam attenuation set so as to minimize detector saturation.

Periodically, the distance between the slits defining the vertical beam profile was increased. Grains growing partly outside the original gauge volume would then be revealed by a discontinous spike of the intensity of its corresponding diffraction spots, as the diffracted intensity is proportional to the illuminated volume of the grain [6]. These grains were left out of further analysis, as described in Ref. [7].

It must here be noted that the experimental set-up did not allow for direct, reliable determination of the degree of impingement of the recrystallizing grains on other recrystallizing grains, or the sample surface. Therefore, the temperature was changed early in the experiment to determine grain-averaged activation energies, since data taken at late times will be strongly affected by impingement effects.

Details regarding data processing, diffraction spot indexing and conversion from integrated intensities to physical grain volumes may be found in Supplementary information. The grain volumes were converted to equivalent sphere diameters as $d = \sqrt[3]{6V_{grain}/\pi}$. The time evolution of the volumes and equivalent sphere diameters of six individual grains out of the total of 1406 can be seen in Figure 1.

It is found that there are large variations in the growth kinetics when comparing individual grains. The radial growth rate of most grains may be characterized as being composed of approximately linear stretches of varying lengths, i.e. linear radial growth at one rate changing to linear growth at another rate on the timescale of measurements, i.e. 3.2 min.

Focusing on the six grains of Figure 1, at late times grains 2–5 show a kinetic slow-down which is assumed to be due to impingement with other recrystallized grains and/or the sample surface. This impingement may manifest itself as an abrupt kinetic slow-down (e.g. grain 2), but is more often observed as a gradual slow-down (e.g. grains 4 and 5). This is assumed to be both due to a gradually increasing degree of impingement, and a lower recrystallization rate of matrix in proximity to several recrystallizing grains.

While impingement is difficult to exclude as the mechanism responsible for "slow-downs", sudden kinetic "speed-ups" are also observed. Quantified as change in equivalent spherical diameter per change in time, we find, for example, grain 2 going from 0.10 to 0.54 μm min^{-1} at $t = 160$ min, grain 3 going from 0.50 to 0.71 μm min^{-1} at $t = 141$ min, grain 5 going from 0.42 to 0.62 μm min^{-1} and grain 6 going from 0.24 to 0.40 μm min^{-1} at $t = 195$ min. Note that the relative magnitude of speed-up for grain 2 is the largest observed during this analysis.

A sudden change in the boundary migration rate could conceivably be due to particle pinning/depinning of one or more boundaries, but it is an unlikely explanation for the present alloy: as f/r, where f is the volume fraction of particles, and r is their radius, is not large in the present alloy, the Zener pinning force [8] is significantly less than the driving force for recrystallization, this explanation would not hold for all observations of sudden changes.

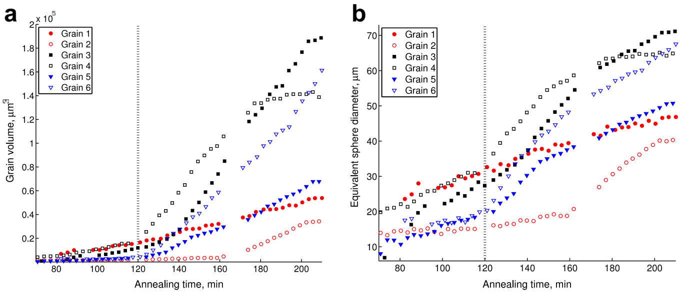

Figure 1. The recrystallization kinetics of six individual grains. (a) Grain volume. (b) Equivalent sphere diameter. The dashed lines indicate when the temperature was increased from 310 °C. For grains 1 and 6 the temperature was increased to 320 °C, for all others to 325 °C.

As these changes are observed fairly often (i.e. for many individual grains, ~1/3 of the individual grains; note that the grains shown in Figure 1 overrepresent this phenomenon somewhat as four out of six grains show a sudden change in growth rate), it is also unlikely that they are due to a surface effect.

Thus, the observed changes in growth rate are much more likely to relate to the deformed microstructure. Aluminium is known to form a cell block structure during cold-rolling, which may be characterized as cells surrounded by low-angle (incidental dislocation) boundaries, grouped into cell blocks delineated by higher-angle (geometrically necessary) boundaries [9,10]. For 50% cold-rolled aluminium, the characteristic cell block width is known to be of the order of 4 μm.

This means that recrystallizing grains generally form boundaries with cell blocks of many different orientations. The volume change of an individual grain is then effectively a sum over the volume change caused by the migration of the grains boundaries into its surrounding cell blocks. A recrystallizing grain forming relatively low-mobility boundaries with its surrounding dislocation cells could possibly see an abrupt increase in boundary mobility, if a significant part of the grain boundary cross into new cell blocks forming higher-mobility boundaries and vice versa.

A simple cellular automaton model has been implemented to examine this hypothesis, the details of which may be found in Supplementary information. Recrystallization in a cell block structure is simulated by introducing a matrix divided into cubes of equal size. The boundary mobility is constant inside these cubes, but varies abruptly between cubes. Note that no orientational correlation between cell blocks has been assumed, which is known to be a crude approximation [9].

Such a set-up results in radial growth rates that appear piecewise linear. Abrupt changes in radial growth rate are observed once or twice in most individual simulations when the grain diameter is less than 3–4 cell block diameters. Above this approximate value, the grain grows into sufficiently many cell blocks that the radial growth rate tends towards a value given by the average boundary mobility of the set-up. This lends credibility to the suggestion that the experimentally observed recrystallization kinetics are strongly influenced by the cell block structure of the deformed matrix.

In comparing the present work with the previous work on 90% cold-rolled aluminium, it is found that the statement "Inspection of the growth curves reveals that every grain has its own kinetics; no two growth curves are alike" of Ref. [2] equally well describes the present findings, and thus was not a result of the more severely deformed matrix.

In order to gain quantitative information about the grain-averaged activation energy of recrystallization, the recrystallization kinetics curves were inspected, and straight lines were least-squares fitted to M grain diameters immediately before, and N diameters immediately after, the temperature change. M and N were chosen individually for each diffraction spot (but were always at least 3), so as to best capture the trend in the data. The diffraction spot was left out of further analysis if no approximately linear trend was seen, as the data was deemed too noisy. With these strict criteria for a good fit, about half of the diffraction spots were excluded. This exclusion procedure is not believed to cause significant bias in the results. The grain-averaged activation energies were then determined by Eq. (3).

The radial growth rates of a total of 793 individual grains were used to determine grain-averaged activation energies in this manner. No qualitative differences were found between the grain-averaged activation energies determined in the three different samples, so they are presented together.

The distribution of all grain-averaged activation energies is shown in Figure 2. It should be noted that the mean value $\langle Q \rangle = 187\ \mathrm{kJ\ mol^{-1}}$ is consistent with the values reported in Ref. [5] for impurity-controlled recrystallization of aluminium. The grain-averaged activation energies determined for the six grains shown in Figure 1 are 0, 98, 182, 199, 279 and 547 kJ mol^{-1} for grains 1–6, respectively, so it can be seen that the six grains were chosen to display the width of the distribution of grain-averaged activation energies. The eight grains in pure copper analyzed in Ref. [3] also showed substantial deviations of the grain-averaged activation energy of the individual grains from its mean.

The distribution of grain-averaged activation energies, Figure 2, is quite wide. Measurements of the activation energy of the boundary mobility for different alloys during grain growth (e.g. those presented in Ref. [4]) show substantial variations (a factor of ~2) as a function of misorientation. However, interpreting grain-averaged activation energies as a mean over the activation energies of the boundaries of an individual grain would entail variations of grain-averaged activation energies of at most a factor of ~2. The finding that the present variations in

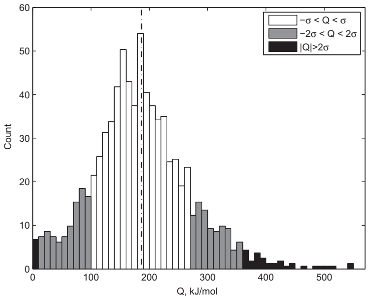

Figure 2. Distribution of grain-averaged activation energies. The mean of the distribution, $\langle Q\rangle = 187\ \text{kJ mol}^{-1}$, is indicated by the vertical line. The standard deviation is $\sigma = 82.9\ \text{kJ mol}^{-1}$, and the 1σ and 2σ confidence intervals are indicated by the colour of the bars.

grain-averaged energies are much more substantial hints that the boundary migration occuring in recrystallization is more complicated than migration of single boundaries of well-defined misorientation, as has also been argued, for example, for the case of recrystallization in 96% cold-rolled nickel in Ref. [11]. There, observations of stepwise boundary migration during recrystallization were reported on timescales similar to that used in this experiment. These were argued to be related to complex atomic rearrangement processes occuring in the deformed matrix near the grain boundary.

Focusing again on the six grains of Figure 1, grains 2–6 show a radial growth rate increasing at different magnitudes with temperature, consistent with it being a thermally activated process. However, grain 1 displays constant, linear radial growth for the duration of the experiment, independent of temperature. Grain 1 therefore has a grain-averaged activation energy of 0 (a similar finding was reported for recrystallization in pure copper [3]). Such a seemingly temperature-independent recrystallization rate is puzzling. However, in Ref. [12] where molecular dynamics simulations are used to compute absolute grain boundary mobilities for 388 boundaries driven by a synthetic driving force, it is found that for 117 boundaries the mobility decreases when the temperature is increased, at least over some temperature range. This implies a non-activated motion, which in Ref. [12] is substantiated by the observation of diffusionless boundary motion in Ref. [13,14]. Such non-activated boundary migration could explain our observation of the grain-averaged activation energy of 0 for grain 1. Another explanation may be that a thermally dependent increase in migration rate of the grain boundary was counterbalanced by a decrease in the local driving force for recrystallization. It must be noted that very low grain-averaged activation energies ($Q < 10\ \text{kJ mol}^{-1}$) are rare, accounting for less than 1% of total occurences in the present dataset.

In summary, it has been shown that 3DXRD allows for in situ characterization of the growth rates of individual bulk grains undergoing recrystallization.

It has been shown that recrystallization kinetics of individual bulk grains deviate significantly from mean kinetics, each grain having its own kinetics. This finding agrees with similar findings for the same material cold-rolled 90% [2]. The radial growth rates of individual grains were found to show approximately linear stretches, and an explanation for this observation related to the cell block microstructure of cold-rolled aluminium has been proposed.

A total of 793 grain-averaged activation energies have been determined, the mean value of which agrees well with values for bulk recrystallization found in the literature. The width of the distribution of grain-averaged activation energies is significant, showing a generally complicated dependence of the rate of recrystallization of individual grains on temperature. Non-activated boundary motion as simulated in Ref. [12] as well as the subdivision of the deformed microstructure may explain this complexity.

A detailed model of recrystallization would have to take the complicated dependence of the recrystallization rate of individual grains on both microstructure and temperature, and thus the wide distribution of grain-averaged activation energies, into account.

The authors gratefully acknowledge the Danish National Research Foundation for supporting the Center for Fundamental Research: Metal Structures in Four Dimensions and the Danish Chinese Center for Nanometals. The ESRF is acknowledged for provision of beam time. Additional support for this work was provided by the Danish research council SNF (via DanScatt). The authors also thank R.A. Vandermeer for useful comments.

Supplementary data associated with this article can be found, in the online version, at doi:10.1016/j.scriptamat.2011.01.046.

[1] H.F. Poulsen, Three-Dimensional X-ray Diffraction Microscopy: Mapping Polycrystals and their Dynamics, Springer, 2004.
[2] E.M. Lauridsen, H.F. Poulsen, S.F. Nielsen, D. Juul Jensen, Acta Mater. 51 (2003) 4423–4435.
[3] R.A. Vandermeer, E.M. Lauridsen, D. Juul Jensen, in: B. Bacroix, J. H. Driver, R. LeGall, C. Maurice, R. Penelle, H. Regle, L. Tabourot (Eds.), 2nd Joint International Conference on Recrystallization and Grain Growth, (2004), pp. 467–470.
[4] G. Gottstein, L.S. Shvindlerman, Grain Boundary Migration in Metals, CRC Press LLC, Boca Raton, 1999.
[5] R.A. Vandermeer, in: N. Hansen, X. Huang, D. Juul Jensen, E.M. Lauridsen, T. Leffers, W. Pantleon, T.J. Sabin, J.A. Wert (Eds.), 21st Risø International Symposium on Materials Science, (2000), pp. 179–200.
[6] B.E. Warren, X-ray Diffraction, Dover Publications, Inc., New York, 1990.
[7] E.M. Lauridsen, The 3 D X-ray Diffraction Microscope and its Application to the Study of Recrystallization Kinetics, Ph.D. thesis, Risø National Laboratory, 2001.
[8] C. Zener, quoted by C.S. Smith, Trans. AIME 175 (1948) 15–51.
[9] N. Hansen, Metall. Trans. A 32 (2001) 2917–2935.
[10] D.A. Hughes, N. Hansen, ASM HandbookMetallography and Microstructures, vol. 9, ASM International, 2004.
[11] Y.B. Zhang, A. Godfrey, Q. Liu, W. Liu, D. Juul Jensen, Acta Mater. 57 (2009) 2631–2639.
[12] D.L. Olmsted, E.A. Holm, S.M. Foiles, Acta Mater. 57 (2009) 3704–3713.
[13] J.W. Cahn, Y. Mishin, A. Suzuki, Acta Mater. 54 (2006) 4953–4975.
[14] J.W. Cahn, Y. Mishin, A. Suzuki, Philos. Mag. A 86 (2006) 3965–3980.

B.2 Recrystallization kinetics of 50% cold-rolled aluminium

RECRYSTALLIZATION KINETICS OF 50% COLD-ROLLED ALUMINIUM

S. O. Poulsen*, A. Lyckegaard*, J. Oddershede*, E. M. Lauridsen*, C. Gundlach†, C. Curfs‡ and D. Juul Jensen*

* Center for Fundamental Research: Metal Structures in Four Dimensions, Risø DTU, Frederiksborgvej 399, 4000 Roskilde, Denmark
† MAX-lab, Lund University, P.O. Box 118, SE-221 00 Lund, Sweden
‡ European Synchrotron Radiation Facility, 6 Rue Jules Horowitz, 38043 Grenoble, France

ABSTRACT

A three-dimensional X-ray diffraction microscopy (3DXRD) experiment has been performed on 50% cold-rolled aluminium AA1050 to investigate *in situ* the growth rate of individual recrystallizing grains at 310°C and 325°C. Growth rates and apparent activation energies are determined for seven individual grains. It is found that the recrystallization kinetics of the individual grains show large deviations, in good agreement with earlier 3DXRD experiments. It is also found that the recrystallization kinetics at 50% deformation vary less in time than what has been found in similar studies of 90% deformed aluminium.

1. INTRODUCTION

Recrystallization is the process by which largely strain free grains nucleate and grow in a deformed matrix, thus reducing the stored energy of the sample. Experimental examinations of recrystallizing bulk structures have until recently relied on destructive microscopical characterization techniques, where microstructures at different stages of recrystallization are characterized and compared. These experiments can give precise insight into the average recrystallization kinetics, see e.g. (Vandermeer 1995).

The 3D kinetics of individual recrystallizing grains has been accessible by the development of 3DXRD microscopy (Poulsen 2004). Using this technique, it has been found that the kinetics vary substantially between grains in the same recrystallizing sample. Thus, the kinetics of individual grains are poorly described by average models (Lauridsen, Poulsen, Nielsen, and Juul Jensen 2003; Lauridsen, Juul Jensen, Poulsen, and Lienert 2000; Vandermeer, Lauridsen and Juul Jensen 2004).

This paper describes a 3DXRD investigation of the recrystallization kinetics of 50% cold-rolled aluminium AA1050, which is the same material as previously examined with 3DXRD after 90% deformation (Lauridsen, *et al.* 2000; Lauridsen, *et al.* 2003). A number of grains are examined to qualitatively investigate the effect of the lower degree of deformation.

Following e.g. (Vandermeer, *et al.* 2004), the radial (equivalent spherical) growth rate is assumed to follow an Arrhenius equation:

$$v = v_0 \exp\left(-\frac{Q}{RT}\right) \tag{1}$$

Here v is the radial growth rate ($\partial r/\partial t$), v_0 is a constant with dimension of length per time, Q is the apparent activation energy, R is the universal gas constant and T is the absolute temperature. Thus, equation (1) predicts a constant radial growth rate, hence radial growth that is linear in time.

By determining the radial growth rate of individual grains during isothermal annealing at two different temperatures, the apparent activation energy can be estimated for the individual grains as:

$$Q = R\left(\frac{1}{T_1} - \frac{1}{T_2}\right)^{-1} \ln\frac{v_2}{v_1} \tag{2}$$

where v_1 and v_2 are the radial growth rates determined at temperatures T_1 and T_2, respectively.

2. EXPERIMENTAL DETAILS

Commercial purity aluminium AA1050 was cold-rolled 50%, and a rectangular box-shaped sample was cut from the center. This sample was electropolished to remove preferred nucleation sites along the sample surface caused by cutting. After polishing, the sample measured approximately (3x0.75x0.75) mm in the (RD,TD,ND) directions. The sample was then mounted in a hot finger furnace, enclosed in an argon-filled glass chamber, and the furnace was mounted on the sample stage at the ID11 beamline at the European Synchrotron Radiation Facility (ESRF) in Grenoble, France. A (1800x400) μm rectangular beam profile was defined in the (z,y) directions by two pairs of slits, and the sample was illuminated with 65 keV (high energy) X-rays. The experimental setup was identical to the one used by (Lauridsen, *et al.* 2003), which can be seen on figure 1, where the coordinate system is indicated. The sample was oriented so (RD,TD,ND) are directed along (z,y,x) for a sample rotation of $\omega = 0$.

The experiment was performed by isothermally annealing at 310°C while rotating the sample from $\omega = -15^\circ$ to $\omega = 15^\circ$ in steps of $\Delta\omega = 0.5^\circ$. Images of the diffracted beam were recorded with a 14-bit FReLoN camera during the individual rotations, to provide an ω-integrated intensity. This was repeated several times to provide a time series. The restriction of ω to a 30° window was to increase the temporal resolution.

After annealing for 120 minutes, the temperature was swiftly ramped up to 325°C. When the temperature was stabilized after about 1 minute, image acquisition proceeded for 90 minutes in the same manner as described above.

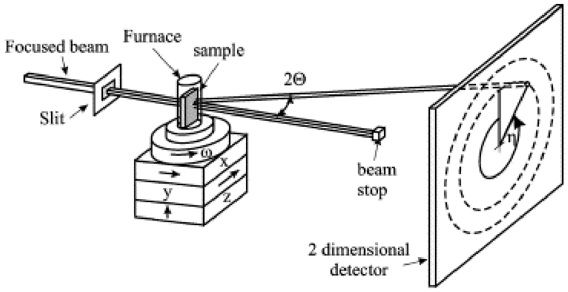

Fig. 1: Experimental setup. Reproduced after (Lauridsen, *et.al.* 2003).

The slits defining the beam profile were periodically widened for an entire ω-cycle during the whole experiment. Grains not fully contained in the smaller gauge volume are then revealed by a discontinuous spike of the intensity of their diffraction spots (Lauridsen 2001). Such grains are left out of further analysis.

3. DATA ANALYSIS

The images obtained are corrected for dark current, spatial (camera) distortion, time dependent synchrotron current, and the Debye-Scherrer rings of interest are integrated over their 2θ spread to produce time series intensity profiles, $I_{2\theta}(\omega, \eta, t)$. At early times, before the visible onset of recrystallization, $I_{2\theta}$ consists of a slowly varying background given by the relatively weak texture of the deformed matrix. As recrystallization progresses, the background is gradually replaced by sharp diffraction spots as the deformed matrix is consumed by the recrystallizing grains.

All diffraction spots in $I_{2\theta}$ are initially identified by their (ω, η) position. As η is given by the orientation of the diffracting plane, and ω relates this orientation to the sample frame of reference, these values are time invariant during this experiment. A specific diffraction spot characterized by $(\omega, \eta) = (\omega_0, \eta_0)$ is then discarded if

a) An η-region, $\Delta\eta = [\eta_0 - x, \eta_0 + x]$ cannot be defined so $I_{2\theta}(\omega_0, \Delta\eta, t)$ shows only the diffraction spot and background for all t.

b) $I_{2\theta}(\omega_{0\pm1}, \Delta\eta, t)$ does not only contain background for all t.

c) The grain giving the diffraction spot is found to not be fully contained in the gauge volume by significant intensity increase upon widening the slits.

If a) is true, then two or more diffraction spots are overlapping, and cannot be separated without making assumptions on their shapes. If b) is true, then the background cannot be determined from $I_{2\theta}(\omega_{0\pm1}, \Delta\eta, t)$. As the ω range in this experiment is not the full 360°, this criterion excludes all diffraction spots in the first and last measured ω ($\omega = \pm 15^\circ$).

Background is estimated as $BG_{2\theta}^{\omega_0}(\eta, t) = I_{2\theta}(\omega_{0\pm1}, \eta, t)/2$, and the normalized grain volumes are determined as $V_{2\theta}^{\omega_0\eta_0}(t) = \int_{\Delta\eta} [I_{2\theta}(\omega_0, \eta, t) - BG_{2\theta}^{\omega_0}(\eta, t)]\, \mathrm{d}\eta$. The equivalent spherical radii are determined as $r_{2\theta}^{\omega_0\eta_0}(t) = \sqrt[3]{3V_{2\theta}^{\omega_0\eta_0}(t)/4\pi}$. In order to determine activation energies, straight lines are least-squares fitted to a section of the curves immediately before and after the temperature increase, the slopes of which give the radial rate of growth, see equation (1). For the grains shown here, these slopes were found to be robust with respect to the selected number of points used in the fit. When the radial rates of growth are determined at the two different temperatures, the apparent activation energy of recrystallization is determined with equation (2).

4. EXPERIMENTAL RESULTS AND DISCUSSION

A total of 471 diffraction spots were identified in the inner six Debye-Scherrer rings. Of these, seven from the {111} ring were chosen for the present analysis. Their volumes and equivalent sphere radii are shown in figures 2(a) and 2(b) respectively.

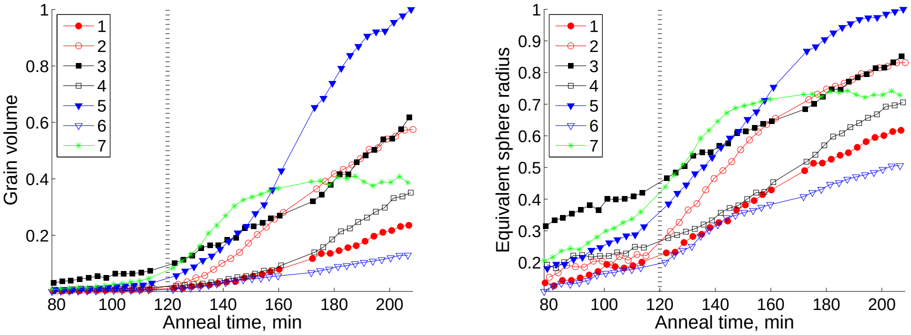

(a)   (b)

Fig. 2: (a): Grain volume (arbitrary normalization), (b): Equivalent sphere radii (arbitrary normalization). The dashed lines indicate when the temperature was increased from 310°C to 325°C. The data has not been smoothened, but the measured intensity have been corrected for the beam polarization, so the data for different grains are directly comparable. The equivalent sphere radii are seen to have long stretches of linear growth.

The decrease in growth rate occuring for crystallites 5 and 7 around $t = 160$ min and 140 min respectively may well be attributed to impingement by other recrystallizing nuclei. It is found that the linear growth for all seven crystallites before impingement becomes severe are reasonably well described by a piecewise linear relationship. The radial growth rate vary only little on the timescale of consecutive measurements (3.2 min). Large differences in growth rate and apparent activation energies from grain to grain, see table 1, are observed. This cannot be explained by early size advantages, rather, it seems that each grain has its own kinetic parameters during recrystallization, as is also the conclusion in (Lauridsen, *et al.* 2000; Lauridsen, *et al.* 2003; Vandermeer, *et al.* 2004).

Table 1: Apparent activation energies

Grain #	1	2	3	4	5	6	7
Q [kJ/mole]	181	281	104	193	211	180	183

The largest abrupt change of radial growth rate occurs at the change of temperature as expected, but smaller abrupt changes are also observed, see e.g. curve 6. This shows that the recrystallization does not progress completely smoothly. However, only a few significant changes in growth rate are observed for the seven grains during the recrystallization process. This seems to be in contrast with the findings by (Lauridsen, *et al.* 2000; Lauridsen, *et. al.* 2003), where variations in the growth rates of individual crystallites are observed on the timescale of consecutive measurements. This may be related to the difference in the cold-rolled microstructure for 90% - and 50% deformation. It should be noted, however, that the timescale in the previous measurements is 50 s, whereas the timescale of consecutive measurements in this experiment is 3.2 min

The apparent activation energies are listed in table 1. The average value here, $\langle Q \rangle \approx$ 190 kJ/mole lies between the values reported in (Vandermeer 2000) for iron and silicon impurity-controlled boundary migration, $Q = 172$ kJ/mole and $Q = 217$ kJ/mole. It must however be noted, that seven grains are not enough to generate reliable statistics.

The large relative differences in activation energies are akin to those found by (Vandermeer, *et al.* 2004) investigating recrystallization in 92% cold-rolled copper. These results indicate that activation energy based modelling of the recrystallization kinetics of individual grains will need to take a wide distribution of kinetic parameters into account. Such a procedure may give accurate grain size distributions, but as the experimentally determined growth rate of the recrystallizing grains appear to be varying in time, such an approach would likely only predict the recrystallization kinetics of individual grains poorly.

5. CONCLUSIONS

Investigations of the recrystallization of individual grains in 50% cold-rolled aluminium AA1050 has been performed *in situ* using 3DXRD. The recrystallization kinetics vary not only between grains, but also in time. For the individual grains, the radial growth rates are found to be best described as approximately piecewise linear. Apparent activation energies have been determined displaying considerable variations between grains.

ACKNOWLEDGEMENT

The authors gratefully acknowledge the Danish National Research Foundation for supporting the Center for Fundamental Research: Metal Structures in Four Dimensions. The ESRF is acknowledged for provision of beam time. Additional support for this work was provided by the Danish research council SNF (via DanScatt). Fengxian Lin is thanked for EBSD microscopy.

REFERENCES

Lauridsen, E.M. (2001). Ph.D. thesis: The 3D X-ray diffraction microscope and its applications to the study of recrystallization kinetics. Risø-R-1266(EN): Risø National Laboratory

Lauridsen, E.M., Juul Jensen, D., Poulsen, H.F. and Lienert, U. (2000). Kinetics of individual grains during recrystallization. Scripta mater. 43, 561-566

Lauridsen, E.M., Poulsen, H.F., Nielsen, S.F. and Juul Jensen, D. (2003). Recrystallization kinetics of individual bulk grains in 90% cold-rolled aluminium. Acta mat. 51, 4423-4435

Poulsen, H.F. (2004). Three-Dimensional X-ray Diffraction Microscopy: Mapping Polycrystals and their Dynamics. Springer

Vandermeer, R.A. (1995). Analytical modeling of the kinetics of recrystallization. In: Microstructural and Crystallographic Aspects of Recrystallization. Risø National Laboratory. Editors: Hansen, N. Juul Jensen, D., Liu, Y. and Ralph, B. 193-213

Vandermeer, R.A. (2000). Kinetic aspects of nucleation and growth in recrystallization. In: Recrystallization - Fundamental aspects and relations to deformation microstructure. Risø National Laboratory. Editors: Hansen, N., Huang, X., Juul Jensen, D., Lauridsen, E.M., Leffers, T. Pantleon, W., Sabin, T.J. and Wert, J.A., 179-200

Vandermeer, R.A., Lauridsen, E.M. and Juul Jensen, D. (2004). Growth rate distributions during recrystallization of copper. In: Recrystallization and grain growth. Editors: Bacroix, B., Driver, J.H., LeGall, R., Maurice, C., Penelle, R., Regle, H. and Tabourot, L., 467-470

B.3 Towards a phase field model of the microstructural evolution of duplex steel with experimental verification

The oral presentation of this paper was awarded the ”Young Scientist Prize” at Rex&GG IV - 4th International Conference on Recrystallization and Grain Growth, 4-9 July, 2010, Sheffield, UK.

Important errata:

Equation (16) and the preceding text states that the time evolution of the mean grain size follows a parabolic power law at early times. This is shown in figure 2. While this is true at the earliest time, it has later been found that a cubic power law describes this evolution better, in agreement with the findings for three-dimensional simulations of chapter 5 of the present work. The parabolic power law approximated the early time behaviour of the cubic power law well, which led to the premature conclusion stated in this paper.

Towards a phase field model of the microstructural evolution of duplex steel with experimental verification

S. O. Poulsen[1, a], P. W. Voorhees[2,b] and E. M. Lauridsen[1,c]

[1]Center for Fundamental Research: Metal Structures in Four Dimensions, Risø National Laboratory for Sustainable Energy at the Technical University of Denmark, Frederiksborgvej 399, 4000 Roskilde, Denmark

[2]Department of Materials Science and Engineering, Northwestern University, Evanston, IL, 60208 USA

[a]spou@risoe.dtu.dk, [b]p-voorhees@northwestern.edu, [c]emla@risoe.dtu.dk

Keywords: Phase field modelling, coupled growth and coarsening, dual-phase, conserved phase fraction

Abstract. A phase field model to study the microstructural evolution of a polycrystalline dual-phase material with conserved phase fraction has been implemented, and 2D simulation runs has been performed. For 2D simulations, the model predicts the parabolic growth well-known from single phase systems. Some interphase boundaries are found to show a persistent non-constant curvature, which seems to be a feature of multi-phase materials. Finally, it is briefly outlined how this model is to be applied to investigate microstructural evolution of duplex steel.

Introduction

The existence of boundaries between grains or phases cause an excess of free energy, which gives rise to a driving force for microstructural evolution when thermally activated. Thus, in a polycrystalline material, some grains may grow at the expense of others, in such a manner that the total boundary energy is lowered. This process, *grain growth*, requires short-range transfer of atoms across the grain boundary. In a dual-phase system the smaller particles will typically transfer mass to the larger particles by diffusion, with a reduction in interphase boundary energy as result. This is termed *Ostwald ripening* or *coarsening*, and is a process requiring long-range mass transfer. Both grain growth and coarsening have been studied extensively (see e.g. [1,2]).

The microstructural evolution of a dual-phase polycrystalline material under conditions conserving phase fractions can be thought of as a coupling of these two phenomena, but has been studied less due to the added complexity [3].

In the following, a phase field model of a dual-phase polycrystalline material is presented, and it is outlined how it will be used to simulate the morphological evolution of duplex steel during an isothermal anneal, using X-ray tomographic data for both initial conditions, as well as later comparison with the output of the simulation.

The Phase Field Method

On The Technique. In the phase field framework, all dynamic materials parameters are represented as field variables, which are continuous in space and time. The most conceptually simple field variable is a compositional variable, which will attain one equilibrium value in the bulk of one (physical) phase, and another equilibrium value in the bulk of another phase. An interface of two such regions is represented by the smooth variation of the field variable between these two equilibrium values. The phase field technique is a diffuse-interface technique, since all interfaces will have a finite width, characteristic of the interface type. These are handled implicitly, and so no explicit interface tracking is necessary.

In the phase field method, the free energy of the system is approximated as an integral over a bulk free energy term written as a function of the underlying field variables and a term for each field variable proportional to the square of the gradient of that field variable. So the problem of determining a free energy of the system is reduced to the much simpler determining of a local bulk free energy function, which can either be derived from physical principles, be phenomenological or calculated from thermodynamic databases.

A distinction is made between conserved quantities, such as composition in a closed system, and non-conserved quantities such as crystallographic orientation or the (solid/liquid) state in a solidification problem. The rate of change of the two kinds of field variables are required to fulfill different equations, which results in a set of non-linear partial differential equations that are coupled through the bulk free energy function. The derivation is performed with the calculus of variations, and ensures that the system will evolve in time so as to monotonically decrease the total free energy of the system. For a comprehensive introduction to the method, see e.g. [4,5].

The phase field technique has been successfully applied to a multitude of problems in materials science, including growth and coarsening, phase transformations, crack propagation, etc. and the range of applicability is increasing with increasing computing power.

On The Model Used. We employ the phase field technique to model a binary dual-phase material. A binary material is chosen for modelling convenience. Correspondence to a many-component system may be found under the assumption that the coarsening kinetics in the many-component system is controlled by the slowest diffusing element. This material is taken to be polycrystalline in both phases, which we denote α and β. The model used is a variation on the model presented in [3], and so the symbols are chosen to conform when possible. We introduce a compositional field, *C*, which attains its equilibrium value of C_α in the bulk of an α-region, and likewise C_β in a β-region. The crystallography is represented by two vectors of field variables

$$\vec{\phi}_\alpha=(\phi_{\alpha 1},\phi_{\alpha 2},\cdots,\phi_{\alpha N\alpha}). \tag{1}$$

$$\vec{\phi}_\beta=(\phi_{\beta 1},\phi_{\beta 2},\cdots,\phi_{\beta N\beta}). \tag{2}$$

Here N_α and N_β are the number of unique crystallographic orientations in the α- and β-phase respectively and the dependence of Φ_α and Φ_β on space and time is suppressed as shorthand. As implied by the notation, Φ_α represents the grains that can be in equilibrium at or near the concentration C_α and likewise for Φ_β. This coupling is achieved through the bulk free energy function, and will be elaborated upon.

The microstructural evolution is considered isotropic, and each of the three different types of interfaces possible in the system (αα, ββ and αβ) has a single grain boundary energy for all interfaces of the corresponding type. Both grain-boundary and compositional mobilities are considered constant.

With these assumptions, the free energy of the system is written as

$$F=\int d\vec{r}\left(f(C,\vec{\phi}_\alpha,\vec{\phi}_\beta)+\frac{\epsilon_C}{2}\left|\nabla C\right|^2+\frac{\epsilon_\alpha}{2}\sum_{i=1}^{N\alpha}\left|\nabla\phi_{\alpha i}\right|^2+\frac{\epsilon_\beta}{2}\sum_{i=1}^{N\beta}\left|\nabla\phi_{\beta i}\right|^2\right). \tag{3}$$

$f(C,\Phi_\alpha,\Phi_\beta)$ is the bulk free energy function specified below, and ε_C, ε_α and ε_β are termed the gradient energy coefficients for composition, α- and β-fields, respectively. The gradient energy coefficients raise the free energy whenever gradients in the phase fields are present. Higher gradient energy coefficients will thus smoothen the corresponding interfaces by widening them.

The bulk free energy function is chosen as a phenomenological function, and is defined as

$$\begin{aligned} f=f_1(C)&+\sum_{i=1}^{N\alpha}f_{2\alpha}\left(C,\phi_{\alpha i}\right)+\sum_{i=1}^{N\beta}f_{2\beta}\left(C,\phi_{\beta i}\right)\\ &+\sum_{i=1}^{N\alpha}\sum_{\substack{j=1\\ j\neq i}}^{N\alpha}f_{3\alpha}\left(\phi_{\alpha i},\phi_{\alpha j}\right)+\sum_{i=1}^{N\beta}\sum_{\substack{j=1\\ j\neq i}}^{N\beta}f_{3\beta}\left(\phi_{\beta i},\phi_{\beta j}\right)\end{aligned}$$

$$+\sum_{i=1}^{N\alpha}\sum_{j=1}^{N\beta} f_4(\phi_{\alpha i},\phi_{\beta j}). \quad (4)$$

f_1 is a function strictly of composition, given by

$$f_1(C)=-\frac{A}{2}(C-C_m)^2+\frac{B}{4}(C-C_m)^4+\frac{D_\alpha}{4}(C-C_\alpha)^4+\frac{D_\beta}{4}(C-C_\beta)^4. \quad (5)$$

Here we have defined $C_m = (C_\alpha + C_\beta) / 2$. The functions $f_{2\alpha}$ and $f_{2\beta}$ are given by

$$f_{2\alpha}(C,\phi_{\alpha i})=\frac{\gamma_\alpha}{2}\left([C-C_\alpha]^2-[C-C_\beta]^2\right)\phi_{\alpha i}^2+\frac{\delta_\alpha}{4}\phi_{\alpha i}^4. \quad (6)$$

$$f_{2\beta}(C,\phi_{\beta i})=\frac{\gamma_\beta}{2}\left([C-C_\beta]^2-[C-C_\alpha]^2\right)\phi_{\beta i}^2+\frac{\delta_\beta}{4}\phi_{\beta i}^4. \quad (7)$$

These are responsible for the coupling between composition and crystallography. The form of these coupling-terms result in a tighter coupling than with those found in [3], where a compositional interface is considerably wider than the two crystallographic interfaces it is coupled to, which allows for unintended fast diffusion through small grains.
The functions $f_{3\alpha}$, $f_{3\beta}$ and f_4 are defined as

$$f_{3\alpha}(\phi_{\alpha i},\phi_{\alpha j})=\frac{\epsilon_{\alpha\alpha}}{2}\phi_{\alpha i}^2\phi_{\alpha j}^2. \quad (8)$$

$$f_{3\beta}(\phi_{\beta i},\phi_{\beta j})=\frac{\epsilon_{\beta\beta}}{2}\phi_{\beta i}^2\phi_{\beta j}^2. \quad (9)$$

$$f_4(\phi_{\alpha i},\phi_{\beta j})=\frac{\epsilon_{\alpha\beta}}{2}\phi_{\alpha i}^2\phi_{\beta j}^2. \quad (10)$$

A, B, D_α, D_β, γ_α, γ_β, δ_α, δ_β, $\varepsilon_{\alpha\alpha}$, $\varepsilon_{\alpha\beta}$ and $\varepsilon_{\beta\beta}$ are positive model parameters. The functions $f_{3\alpha}$, $f_{3\beta}$ and f_4 create repulsion between α- and α-fields, β- and β-field, and α- and β-fields respectively and so ensure that the free energy of the system is raised if space is occupied by more than one crystallographic orientation. The crossterm-function f_4 which is not found in [3] allows for some measure of control of the αβ-interface energies without varying the compositional gradient energy coefficient, ε_C.
The bulk free energy function, f, has sufficient degrees of freedom so its' minima can be placed at $C=C_\alpha$, $\Phi_{\alpha i}=1$ for any one i, and $\Phi_{\alpha j}=0$ for $j\neq i$, and likewise when interchanging α and β. This requirement, along with the common tangent assumption across an αβ-interface fixes most parameters in the model as functions of the remaining free parameters.

Governing Equations. With the calculus of variations [6] and the assumptions stated in previous section, the Cahn-Hilliard (diffusion) equation governing the rate of change of the composition can be written

$$\frac{\partial C}{\partial t}=M_C\nabla^2\left(\frac{\partial f(C,\vec{\phi}_\alpha,\vec{\phi}_\beta)}{\partial C}-\epsilon_C\nabla^2 C\right). \quad (11)$$

while the rate of change of the crystallographic phase fields is given by the simpler Allen-Cahn equation (for i=1, 2, ..., N_α and j=1, 2, ..., N_β)

$$\frac{\partial \phi_{\alpha i}}{\partial t} = -L_\alpha \left(\frac{\partial f\left(C, \vec{\phi}_\alpha, \vec{\phi}_\beta\right)}{\partial \phi_{\alpha i}} - \epsilon_\alpha \nabla^2 \phi_{\alpha i} \right). \tag{12}$$

$$\frac{\partial \phi_{\beta j}}{\partial t} = -L_\beta \left(\frac{\partial f\left(C, \vec{\phi}_\alpha, \vec{\phi}_\beta\right)}{\partial \phi_{\beta j}} - \epsilon_\beta \nabla^2 \phi_{\beta j} \right). \tag{13}$$

Here the explicit dependence of the bulk free energy functional has been kept to emphasize the coupling between all $N_\alpha + N_\beta + 1$ phase fields defining the system. M_C, L_α and L_β are parameters setting the timescale for diffusion and grain boundary movement in the α - and β phase respectively.

Numeric Methods. The second - and fourth order gradient operators are approximated for a computational grid by compact nearest-neighbor and next-nearest-neighbor finite-difference stencils, shown for one dimension below

$$\delta^2 x_i = \frac{1}{\Delta h^2}\left(x_{i+1} + x_{i-1} - 2\mathrm{x}_i\right). \tag{14}$$

$$\delta^4 x_i = \frac{1}{\Delta h^4}\left(x_{i+2} + x_{i-2} - 4\mathrm{x}_{i+1} - 4\mathrm{x}_{i-1} + 6\mathrm{x}_i\right). \tag{15}$$

where Δh is the grid spacing. Time is discretized with the simple forward Euler method. The fixed time step, Δt, is severely limited by the fourth spatial derivative in the compositional equation, Eq. 11. To get around this we set ϵ_C=0. This limits the range of possible αβ-interface energies, and couples this to the energies of αα- and ββ-interfaces, but this is not a problem for the current application. If the fourth order derivative term must be kept, then an implicit time scheme can be used with advantage for the composition, while still solving the crystallographic equations with an explicit scheme to overcome the bottlenecking of the solution by the single compositional equation out of a total of $N_\alpha + N_\beta + 1$ equations.

The crystallographic phase fields are stored in sparse arrays as described in [7], so that values less than η = 0.0001 are considered mathematically zero and thus discarded. The reason is two-fold: First to conserve memory when doing many-grain simulations, and second to speed up computations, since the sparse matrix approach reduces the problem from solving $N_\alpha + N_\beta + 1$ equations per grid point to solving ~ 1 - 4 equations per grid point.

The solver is fully parallelized, and scales well when adding compute nodes.

Proof-of-concept Simulations

Five 2D simulation run has been performed on a 1024x1024 grid with periodic boundary conditions. Four were with 500 α-, 500 β-grains and one was with 150 periodic boundary conditions. The four 1000 grain simulations used the same initial conditions, so only two distinct sets of initial conditions were used. Both sets were generated with a Voronoi tessellation with randomly distributed phases, which in the cases chosen resulted in equal phase fractions. The only parameter varied in the four 1000 grain simulations is M_C, the compositional mobility, and the 300 grain simulation was done with M_C=1. All model parameters can be found in table 1. There is complete symmetry between the parameters of the two phases.

C_α=0.1	C_β=0.9	A=5	B=4.5	D_α=D_β=6	M_C= ¼,½,1,2	L_α=L_β=1	ϵ_C=0	$\epsilon_{\alpha\alpha}$=$\epsilon_{\beta\beta}$=2	$\epsilon_{\alpha\beta}$=0	Δt=0.012	Δh=0.6

Table 1: Model parameters chosen for the simulation

The evolution of the mean grain sizes can be found on figure 1, where it can be seen that the growth at early times follows the parabolic growth well-known for single phase systems:

$$\frac{\langle d(t)\rangle^2}{\langle d(0)\rangle^2}-1=k\,t. \tag{16}$$

The $M_C=1$ and $M_C=2$ systems depart from parabolic growth around where the mean particle size has increased by a factor of two by increasing the growth rate. For the $M_C=1/2$ system, parabolic growth provides a reasonable fit in the entire range, while the $M_C=1/4$ system apparently sees an decreasing growth rate at late times.

Figure 2 shows the grain size distribution at three different times for the $M_C=2$ simulation. normalized to the average grain size at the given time. It is seen that the size distribution does not change qualitatively from a log-normal distribution, even at times outside the parabolic growth region.

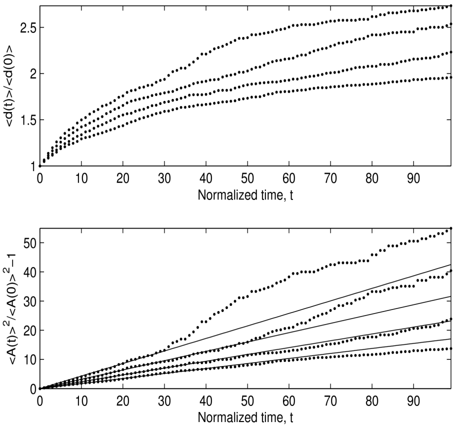

Figure 2: Grain size evolution. For both plots we have that the curves from top to bottom are for Mc={2,1,1/2,1/4}, respectively.

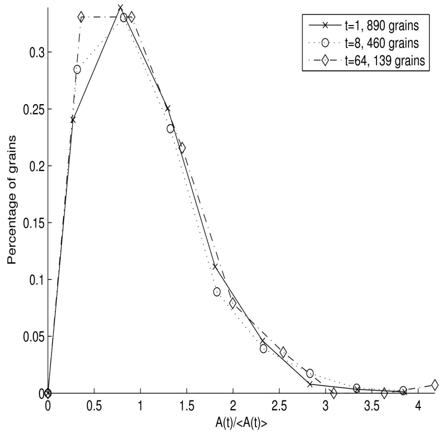

Figure 1: Normalized grain size distribution for the 1000 grain simulation with Mc=2

Figures 3 and 4 show the 300 grain-simulated microstructure at two different times. Note that both times are to be considered late times, there are 61 and 24 of the original 300 grains remaining at $t=20$ and $t=138$ respectively.

The white areas are α-phase, while the gray areas are β-phase. The white arrow on figure 3 points to an α-island surrounded by β-grains, which pins the grain boundaries in its' contact. This α-grain diffuses through its' neighbors, and when it disappears, the grain boundaries are depinned.

The black arrows on figures 3 and 4 point to the S-curved αβ-boundary, which is seen to be persistent. This non-equilibrium boundary shape can be attributed to a pinning of the boundaries ααβ- and αββ-trijunctions, the movement of which is dependent on bulk diffusion.

The white arrows on figure 4 point to two grains which have followed the qualitatively same evolution. The lower grain is five-sided, but evolves slowly so the top-facing side becomes smaller, and is finally pinched off, becoming a trijunction whose movement is not dependent on bulk diffusion, as is the case for the upper grain. When this topological change occurs, the local evolution occurs fast, even at late times where the evolution has almost stagnated.

Outlook

The future goal with this research project is to employ this idealized model to investigate microstructural evolution in duplex steel during an isothermal anneal, conserving the ratio of the two phases present. Recent advances in synchrotron X-ray tomography [8] has made it possible to non-destructively acquire 3D maps of the phase distribution as well as full grain maps - both crystallography, center of mass and volume, and to some extent the morphology of the individual grains. This gives the unique possibility of comparing the output of a simulation to an evolution observed in a specific microstructure. Such a comparison is expected to shed light on which processes are most important for the microstructural evolution of the duplex steel, so the model may be refined and extended to achieve better correspondence with experiment.

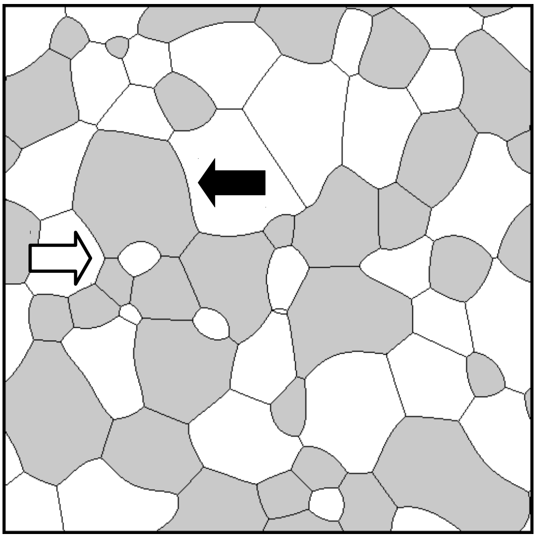

Figure 3: The simulated microstructure at time t=20

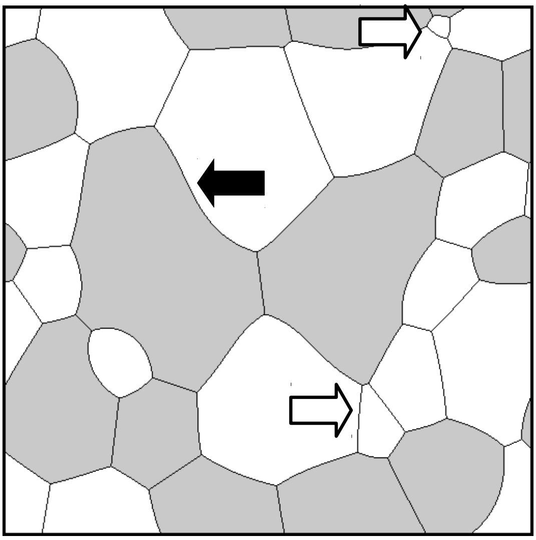

Figure 4: The simulated microstructure at time t=138

Acknowledgements

S. O. Poulsen would like to thank Ian M. McKenna for useful discussions regarding sparse data storage and scientific computing in general, and Dorte Juul Jensen for general input and discussions.

S. O. Poulsen and E. M. Lauridsen gratefully acknowledge the Danish Research Foundation for supporting the Center for Fundamental Research: Metal Structures in Four Dimensions.

References

[1] H.V. Atkinson, Acta metall., 36, 3 (1988)

[2] P.W. Voorhees, J. Stat. Phys., 38, 1-2 (1985)

[3] D. Fan, L.-Q. Chen, Acta mater., 45 (10) (1997)

[4] N. Moelans et al., CALPHAD - Computer coupling of phase diagrams and thermochemistry, 32 (2), (2008)

[5] L.-Q. Chen, Annu. Rev. Mater. Res., 32 (2002)

[6] S.M. Allen, J. W. Cahn, Acta metall., 27 (1979)

[7] J. Gruber et al., Modelling Simul. Mater. Sci. Eng. 14, 1189 (2006)

[8] W. Ludwig et al., Mat. Sci. Eng. A, 524,1-2 (2009)

B.4 Universality and self-similarity in pinch-off of rods by bulk diffusion

LETTERS
nature physics

Universality and self-similarity in pinch-off of rods by bulk diffusion

Larry K. Aagesen[1], Anthony E. Johnson[1], Julie L. Fife[1,2], Peter W. Voorhees[1,3]★, Michael J. Miksis[3], Stefan O. Poulsen[4], Erik M. Lauridsen[4], Federica Marone[2] and Marco Stampanoni[2,5]

As rodlike domains pinch off owing to Rayleigh instabilities, a finite-time singularity occurs as the interfacial curvature at the point of pinch-off becomes infinite. The dynamics controlling the interface become independent of initial conditions and, in some cases, the interface attains a universal shape[1]. Such behaviour occurs in the pinching of liquid jets and bridges[2–9] and when pinching occurs by surface diffusion[10–12]. Here we examine an unexplored class of topological singularities where interface motion is controlled by the diffusion of mass through a bulk phase. We show theoretically that the dynamics are determined by a universal solution to the interface shape (which depends only on whether the high-diffusivity phase is the rod or the matrix) and materials parameters. We find good agreement between theory and experimental observations of pinching liquid rods in an Al–Cu alloy. The universal solution applies to any physical system in which interfacial motion is controlled by bulk diffusion, from the break-up of rodlike reinforcing phases in eutectic composites[13–16] to topological singularities that occur during coarsening of interconnected bicontinuous structures[17–20], thus enabling the rate of topological change to be determined in a broad variety of multiphase systems.

As pinch-off is approached, the length and timescales near the singularity become much smaller than the scale of the initial conditions that caused the singularity to form. In this regime the interfacial morphology can be written in scale-independent self-similar coordinates[2]. Experimental investigations of self-similar evolution that determine both the interfacial morphology and dynamics near topological singularities have largely been confined to multiphase fluids. In some cases, the interface asymptotically approaches a symmetric cone shape as the time of pinch-off is approached. For pinching by surface diffusion, a countable set of solutions can be identified, each with a different cone angle. A stable solution is found for only the largest cone angle, and thus the geometry of the system close to pinching is universal[12]. This universality has not been observed experimentally. There is no corresponding analysis for pinching through mass diffusion in the bulk phases.

We examine the evolution of interfacial morphology of liquid rods in a solid matrix. An Al–15 wt.% Cu alloy is employed along with 4D synchrotron radiation-based tomographic microscopy. The interfaces evolve by bulk diffusion of solute through the high-diffusivity liquid[21]. The rods were created by holding a 1-mm-diameter sample isothermally 5 °C above the eutectic temperature to form a solid–liquid mixture. The interfacial morphology of liquid rods was observed *in situ* using tomographic microscopy at the TOMCAT beamline of the Swiss Light Source over a 12 h period[22,23] (see Methods for details). Hundreds of pinching events were observed during this time. Figure 1 shows one such pinching event.

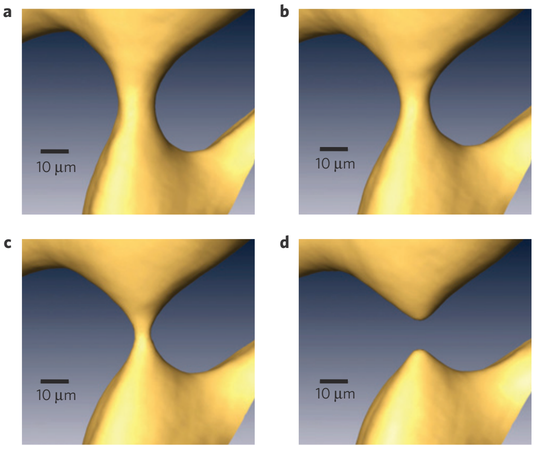

Figure 1 | Time sequence of a liquid rod pinching owing to interfacial-energy-driven bulk diffusion. **a**, 142.5 min; **b**, 155 min; **c**, 165 min; **d**, 170 min.

To determine whether a self-similar solution exists near pinch-off, we define a set of self-similar variables in cylindrical coordinates:

$$\eta = \frac{rB}{(t_s - t)^{\alpha}}, \quad \xi = \frac{zB}{(t_s - t)^{\alpha}} \qquad (1)$$

where r is the radial coordinate of the interface position, t is time, z is the axial coordinate, t_s is the time of the singularity, η and ξ are the radial and axial coordinates in the time-independent similarity variables, B is a scaling constant dependent on material properties and α is an exponent specific to the process. The system is assumed to be symmetric about the z and ξ axes.

We assume that the diffusion coefficient of solute in the solid, $D_S = 0$ in the surrounding solid, and that interface motion is slow compared with the time required for the diffusion field to relax.

---

[1]Department of Materials Science and Engineering, Northwestern University, Evanston, Illinois 60208-3108, USA, [2]Swiss Light Source, Paul Scherrer Institut, CH-5232 Villigen, Switzerland, [3]Department of Engineering Sciences and Applied Mathematics, Northwestern University, Evanston, Illinois 60208-3108, USA, [4]Risø National Laboratory for Sustainable Energy, Technical University of Denmark, P.O. Box 49, DK-4000 Roskilde, Denmark, [5]Institute for Biomedical Engineering, University and ETH Zürich, 8092 Zürich, Switzerland. *e-mail: p-voorhees@northwestern.edu.

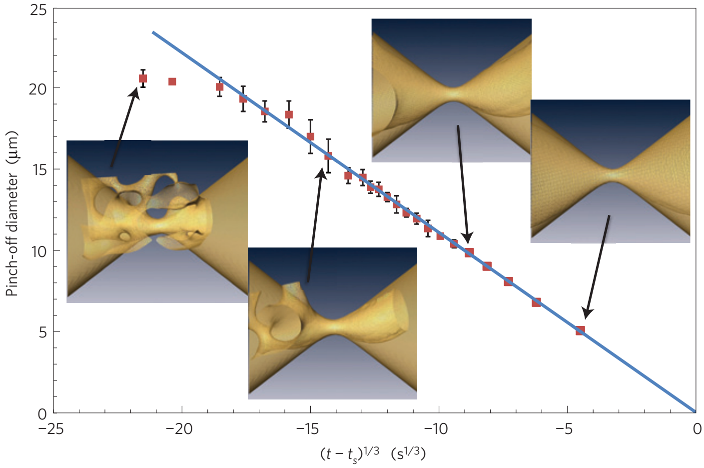

Figure 2 | Rod diameter follows a power law before singularity. The diameter of a single pinching rod as a function of $(t-t_s)^{1/3}$ along with the experimentally measured and theoretically predicted interface shapes at various times and a line showing the least-squares fit to the experimental data. Error bars show the standard deviation in the measured diameters of the single rod, which is not circular at all times. Experimental error in each measurement is one half-voxel in size or 0.74 µm. It is clear that, even when the interfacial morphology is far from the self-similar shape, the kinetics of the pinching process are still well described by $(t-t_s)^{1/3}$.

Thus the diffusion field in the liquid is given by a solution to Laplace's equation:

$$\nabla^2 C_L = 0 \tag{2}$$

where C_L is the solute concentration in the liquid. We seek a solution to (2) consistent with the boundary conditions. The first is the Gibbs–Thomson equation

$$C_L = {C_L}^0 + ({C_L}^0 - {C_S}^0) d_0 H \tag{3}$$

where C_L is the solute concentration on the liquid side of the interface, ${C_L}^0$ and ${C_S}^0$ are the equilibrium solute concentrations at a flat interface, d_0 is the capillary length and H is the mean interfacial curvature. The other boundary condition is the interfacial mass balance,

$$({C_L}^0 - {C_S}^0) v = -D_L \frac{\partial C_L}{\partial n} \tag{4}$$

where v is the interfacial velocity in the direction normal to the interface, D_L is the diffusion coefficient in liquid and $\partial C_L / \partial n$ is the derivative of the concentration field in the normal direction.

We seek a similarity solution to (2) consistent with the boundary conditions by defining the difference between the solute concentration in the liquid and the equilibrium concentration in terms of a scaled concentration in similarity variables, $K(\xi,\eta)$:

$$C_L(r,z,t) - {C_L}^0 = (t_s - t)^{\beta} A K(\xi,\eta) \tag{5}$$

where A is a scaling constant dependent on materials properties. Substituting (5) into (3) and (4) and using (1), we find that $\alpha = -\beta = 1/3$ is required for a self-similar solution consistent with the boundary conditions and Laplace's equation. From (3) and (4), a similarity solution also requires that $B = (D_L d_0)^{-1/3}$ and $A = ({C_L}^0 - {C_S}^0)({d_0}^2/D_L)^{1/3}$. The interfacial coordinates thus scale as $r \sim z \sim [D_L d_0 (t_s - t)]^{1/3}$.

If the pinching process is self-similar, the diameter of the rod should decrease as $(t-t_s)^{1/3}$. Using data such as those shown in Fig. 1, we can determine whether this is the case in the experiment. As the data are obtained in three dimensions, it is possible to view the rod along its axis to measure accurately its smallest cross-section or diameter. Figure 2 shows that the diameter decreases linearly as $(t-t_s)^{1/3}$ for a single pinching rod. This behaviour was also observed in the 19 other pinching events investigated. These data suggest the presence of self-similar interfacial evolution, and we thus proceed to examine theoretically the interfacial morphology near the topological singularity.

Using the similarity variables of (1), the interfacial morphology, both before and after pinching, was determined numerically using a boundary-integral method (see Methods for details). The solid–liquid interface position is given by the function $\eta = f(\xi)$, along which $K(\xi,\eta)$ is equal to the interfacial curvature. After pinch-off, solutions were found for the shape of the two receding tips at any cone angle, consistent with previous findings for the pinch-off of rods by surface diffusion[10]. Before pinch-off, we find a discrete set of solutions for various cone angles, where the cone angle is defined as twice the angle of the interface from the ξ axis as $\xi \to \infty$. For diffusion inside the rod, we find solutions for cone angles of 30° and 76°; see Fig. 3. Further solutions are expected at cone angles smaller than 30°. However, as in the surface-diffusion-limited case[12], we expect that only the solution with the largest cone angle is stable and thus observable experimentally.

Additionally, we find that, for pinching by bulk diffusion outside the rod, the stable solution has a cone angle of 80° (with unstable solutions also expected but not identified). Examples where this shape would be found include the pinch-off of solid rods surrounded by liquid in Al–Cu at lower volume fractions of solid[24] and the pinching of atomically ordered eutectic intermetallic rods embedded in an atomically disordered intermetallic matrix[25].

The similarity solution for the interface shape $\eta = f(\xi)$ determines the prefactor of the temporal power law of the pinching event. Using (1), the radius at the centre ($\xi = 0$) of a pinching liquid rod, $R(t)$, evolves as

$$R(t) = f(0)[D_L d_0 (t_s - t)]^{1/3} \tag{6}$$

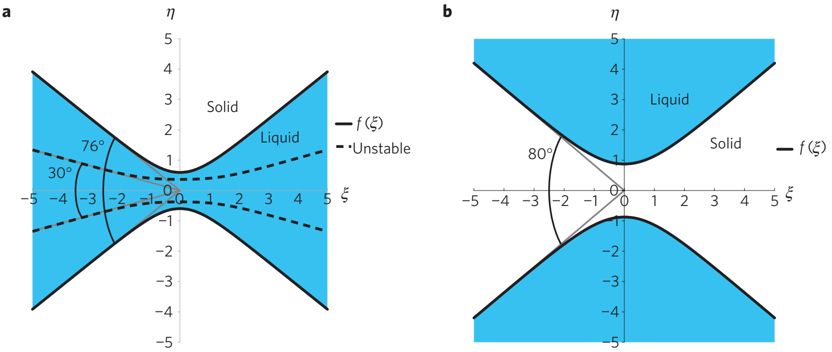

Figure 3 | Theoretically predicted interface shapes before the singularity. **a**, Diffusion inside the rod. **b**, Diffusion in the matrix outside the rod. Axes and interfaces are in the self-similar coordinates of equation (1). The shapes approach a cone with angle 76°, solid line, and 30°, dashed line (**a**), and 80° (**b**), far from the singularity at $\xi = 0$.

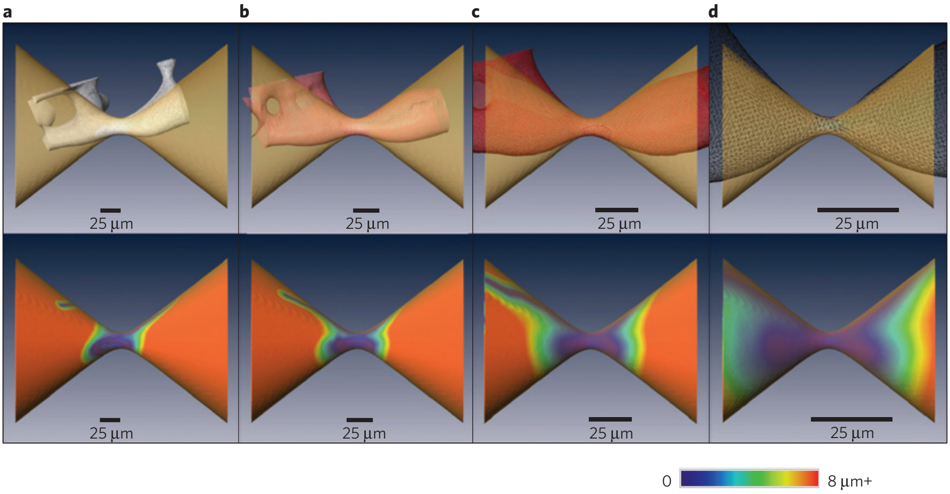

Figure 4 | Quantifying agreement between theoretically predicted and experimentally measured interface shapes. Top, the experimentally determined microstructure is superimposed on the theoretically predicted shape for the solution with a cone angle of 76° for several times leading up to pinch-off. The theoretical shapes are scaled to the same diameter as the experimental microstructures. Bottom, the theoretical shape is shown coloured by the distance from each point to the closest point on the experimentally measured shape. The mean deviation between experiment and theory decreases as the system approaches the time of pinch-off. In the case of the final time step, the mean deviation is less than the experimental resolution of the X-ray tomographic microscopy scan (1.48 µm). **a**, 85 min; **b**, 142.5 min; **c**, 180 min; **d**, 190 min.

where $f(0) = 0.60$ and 0.37 for the solutions with cone angles of 76°, and 30°, respectively; see Fig. 3. Thus, sufficiently close to the singularity, the time dependence of the radius is independent of initial conditions and is a function of only $f(0)$ and materials parameters.

Theory thus suggests that, as the topological singularity is approached, the interfacial shape may be universal; it does not depend on the initial conditions of the rod and materials system, and the kinetics of the pinching process are described by a simple temporal power law. This unique solution will also determine the shape before and after the pinching event. However, two issues remain to be addressed before we can conclude that the pinching process is universal: most importantly, whether the quasistationary approximation will hold sufficiently close to the pinch-off for universality to be observed, and second, whether there is evidence for similarity shapes with cone angles other than 76°.

To assess the validity of the quasistationary approximation, we define the characteristic length scale l as the diameter of the pinching rod, and the characteristic timescale τ as

$$\tau = \frac{l^3}{[2f(0)]^3 D_L d_0}$$

Writing the diffusion equation in dimensionless form after scaling by these characteristic length and timescales, we obtain

$$\epsilon \frac{\partial c}{\partial \tilde{t}} = \tilde{\nabla}^2 c$$

where $\tilde{t}$ is the dimensionless time, c is concentration, $\tilde{\nabla}^2$ is the dimensionless Laplacian and $\epsilon = [2f(0)]^3 d_0/l$. The quasistationary approximation is valid as long as $\epsilon \ll 1$. Using $f(0) = 0.60$ and the capillary length for the solid–liquid interface in Al–Cu, $d_0 = 2.27$ nm (ref. 27), the quasistationary approximation holds as long as the rod diameter is much greater than 3.9 nm, well below the 1.48 µm resolution of the tomography.

We test the theory by comparing the kinetics predicted by the similarity solution with experimental data on the evolution of rod diameter. From (6), the slope of the line shown in Fig. 2 is related to the materials parameters and $f(0)$, the interface location in similarity variables at $\xi=0$. Linear slopes were determined for 19 pinching events on the basis of diameters measured for at least three time steps before t_s. The average slope was 1.35 µm s$^{-1/3}$ with a standard deviation of 0.211 µm s$^{-1/3}$. From (6), the predicted slope, or prefactor, is given by $2f(0)(D_L d_0)^{1/3}$ (the factor of two converts radius to diameter). Using $D_L=8.3\times10^{-10}$ m^2 s^{-1} (ref. 26), $d_0=2.27$ nm (ref. 27) and $f(0)=0.60$, the theoretically predicted prefactor is 1.47 µm s$^{-1/3}$. This is within 0.57σ of the experimentally measured prefactor, indicating an excellent agreement between theory and experiment, given the uncertainties in the materials parameters. If we had used, instead, $f(0)$ for the solution with a cone angle of 30°, the predicted prefactor would be 0.91 µm s$^{-1/3}$, or 2.1σ below the value measured experimentally. Any other possible solutions will have cone angle smaller than 30° and a smaller $f(0)$ (ref. 12), so the predicted prefactor would be even smaller. This suggests that only the solution with a cone angle of 76° is observable experimentally. Moreover, the agreement between theory and experiment is excellent from very early in the pinching process.

As a further test of the theory, a three-dimensional representation of the theoretically predicted interface shape was created. We aligned the experimental data to the theoretically predicted shape for the solution with a cone angle of 76°, and linearly scaled the predicted shape such that the diameter at the centre of the pinching rod was the same as that measured experimentally (see Methods for details). The distance from the theoretically predicted shape to the closest point on the experimentally measured shape was calculated; see Fig. 4. As expected, the agreement between theory and experiment improved as the singularity is approached, because initial conditions have less influence and the shape becomes locally determined. Just before pinch-off, the mean deviation between shapes is less than the 1.48 µm resolution of the X-ray tomographic microscopy scan, indicating excellent agreement between theory and experiment. Even in the region where the experimentally measured shape differs most from the theory (lower right of Fig. 4d), the measured cone angle is 66°–71° (using the experimental error of 0.74 µm). Very similar diagrams result if we plot the distance between the experimentally measured and theoretically predicted shapes in similarity variables, confirming that the improved agreement as t_s is approached is not just a result of the changing length scale. In some cases, the initial shapes of the rods were asymmetric about the pinching axis, but still decayed at the rate predicted by the symmetric solution. In all 19 cases examined the agreement between theory and experiment improved as the singularity was approached. Thus, to the resolution of the tomography, the experiments confirm that, some distance from the pinching point, the shape approaches a cone with the predicted cone angle of 76°.

Both the interfacial morphology and dynamics of the pinching process measured experimentally agree with the predictions of theory for the solution with a cone angle of 76°, implying that the shape with the highest cone angle is the only stable shape. We therefore conclude that the pinching process under interfacial-energy-driven bulk diffusion is governed by a unique self-similar solution.

We find that topological singularities in a system evolving by a previously unexplored class of dynamics exhibit universal behaviour. Furthermore, the dynamics of the pinching process by capillarity-induced bulk diffusion agree very well with those predicted theoretically, even early in the pinching process, when the interfacial morphology is not precisely that given by theory. The theory also shows that self-similar shapes exist when pinching occurs by diffusion outside the rod, and we conjecture that the shape with the largest cone angle is also universal. As the prefactor of the temporal power law is in agreement with theory from very early in the evolution of the morphological instability, the universal behaviour caused by the approaching singularity exhibits itself far before the singularity occurs. These results are applicable to a variety of systems that exhibit topological singularities, such as eutectic and bicontinuous two-phase mixtures, and could be used, for example, to calculate the time required for a non-symmetric bicontinuous mixture to lose continuity in one phase, which results in a dramatic change in properties of the material.

Methods

Numerical solution for shape. We seek a solution for the shape of the solid–liquid interface in similarity variables, $\eta=f(\xi)$, or defined parametrically $F=\eta-f(\xi)=0$, assuming axial symmetry about ξ. Laplace's equation and the boundary conditions (3), (4) were transformed into the self-similar coordinate system. Green's third identity was used along with the free-space Green's function for Laplace's equation to yield an integrodifferential equation for the scaled concentration $K(\xi,\eta)$ on the interface:

$$\frac{1}{2}K(\xi_0,\eta_0)=\int_S\left(K(\xi,\eta)\frac{\partial g}{\partial n}-g\frac{\partial K}{\partial n}\right)\mathrm{d}S \qquad (7)$$

where g is the free-space Green's function for Laplace's equation, $g=1/|\mathbf{r}(\xi_0,\eta_0)-\mathbf{r}_i(\xi,\eta)|$, n is the unit normal vector to the interface and $\mathbf{r}(\xi_0,\eta_0)$ and $\mathbf{r}_i(\xi,\eta)$ are the field and source points, respectively. On the boundary, the concentration difference from equilibrium can be written in terms of the Gibbs–Thomson condition in similarity variables

$$K(\xi,\eta)=\nabla_{\xi,\eta}\cdot\hat{n}=\nabla_{\xi,\eta}\cdot\left(\frac{\nabla F}{|\nabla F|}\right) \qquad (8)$$

because $H=\nabla\cdot\hat{n}$. The solute-conservation boundary condition can used in combination with the material derivative for the interface to find $\partial K/\partial n$ on the boundary

$$\frac{\partial K}{\partial n}=\hat{n}\cdot\nabla K=\frac{1}{3}\frac{F_\xi\xi+F_\eta\eta}{\sqrt{{F_\xi}^2+{F_\eta}^2}} \qquad (9)$$

where the subscripts denote partial differentation. Substituting (8) and (9) into (7) gives a set of integrodifferential equations for $f(\xi)$. Boundary conditions on $f(\xi)$ are that $f(\xi)$ approaches a straight line with angle $\theta_c/2$ (where θ_c is the cone angle) from the ξ axis as $\xi\to\infty$ and $f'(0)=0$, which ensures finite curvature at the origin.

The integrodifferential equations were discretized, and the angular integral was rewritten as a complete elliptic integral of the first kind and approximated using the polynomial approximation of ref. 28. The integration was carried out numerically using the trapezoidal rule on a truncated domain along ξ. A Taylor expansion was used to approximate integrable singularities when $\xi=\xi_0$. Newton's method was then used to iteratively solve for $f(\xi)$. A coarse grid spacing along ξ was used to search for solutions as θ_c was varied. The grid spacing was refined using solutions from the coarse mesh as an initial guess to narrow down the exact cone half-angle to ±1°. Convergence was tested by varying the grid spacing and by varying truncation length in the ξ-direction; second-order convergence was obtained.

Experiment. Al–15 wt% Cu was directionally solidified to form Al-rich dendrites. In preparation for X-ray tomographic microscopy, 1-mm-diameter samples were cut from the original ingot and mounted in a custom-made sample furnace. The samples were coarsened *in situ* at 565 °C, and data were collected in real time using X-ray tomographic microscopy at the TOMCAT beamline located at the X02DA port of the Swiss Light Source at the Paul Scherrer Institut (Villigen, Switzerland). An energy of 20 keV was used with 80 ms exposure time, and 721 projections were captured over the 180° of rotation. A total of 1,024 slices, with a spatial resolution of 1.48 µm^3 per voxel, were collected at 150 s intervals for the first 4.5 h and at 450 s for the remaining 7.5 h. The tomograms were then converted to binary using sample-specific algorithms created in the IDL software package. Further information about the TOMCAT beamline and the details of the experiment can be found in refs 22 and 23, respectively.

Data analysis. In preparation for analysis, three-dimensional arrays from the experiment were smoothed to remove alignment and reconstruction artefacts from the interface. The arrays were then imported into the visualization program Amira, and the arrays were cropped to an individual pinching event. The pinch-off diameters (that is, the minimum diameters at the centre) were measured using

Amira. The theoretically predicted shape was also imported into Amira and the principal (or longitudinal) axes of the experimental shapes were then aligned with the theoretically predicted shape by aligning the two shapes to the axes with the lowest moment of inertia.

The pinch-offs at each time-step were scaled such that the cone diameter matched that of the theoretical shape. Scaling the pinch-offs to the theoretical shape provided a way to quantitatively observe the self-similarity and interface agreement with the theory over time. By plotting the diameter cubed versus time, the critical pinching time, t_s, was measured on the basis of a linear fit. The deviation between theory and experiment at a given vertex was determined as the distance to the closest point on the other surface.

Received 12 March 2010; accepted 24 June 2010; published online 1 August 2010

References

1. Eggers, J. Nonlinear dynamics and breakup of free-surface flows. *Rev. Mod. Phys.* **69,** 865–929 (1997).
2. Keller, J. B. & Miksis, M. J. Surface-tension driven flows. *SIAM J. Appl. Math.* **43,** 268–277 (1983).
3. Eggers, J. Universal pinching of 3D axisymmetrical free-surface flow. *Phys. Rev. Lett.* **71,** 3458–3460 (1993).
4. Chen, Y. J. & Steen, P. H. Dynamics of inviscid capillary breakup: Collapse and pinchoff of a film bridge. *J. Fluid Mech.* **341,** 245–267 (1997).
5. Day, R. F., Hinch, E. J. & Lister, J. R. Self-similar capillary pinchoff of an inviscid fluid. *Phys. Rev. Lett.* **80,** 704–707 (1998).
6. Zhang, W. W. & Lister, J. R. Similarity solutions for capillary pinch-off in fluids of differing viscosity. *Phys. Rev. Lett.* **83,** 1151–1154 (1999).
7. Cohen, I., Brenner, M. P., Eggers, J. & Nagel, S. R. Two fluid drop snap-off problem: Experiments and theory. *Phys. Rev. Lett.* **83,** 1147–1150 (1999).
8. Leppinen, D. & Lister, J. R. Capillary pinch-off in inviscid fluids. *Phys. Fluids* **15,** 568–578 (2003).
9. Sierou, A. & Lister, J. R. Self-similar recoil of inviscid drops. *Phys. Fluids* **16,** 1379–1394 (2004).
10. Wong, H., Miksis, M. J., Voorhees, P. W. & Davis, S. H. Capillarity driven motion of solid film wedges. *Acta Mater.* **45,** 2477–2484 (1997).
11. Wong, H., Miksis, M. J., Voorhees, P. W. & Davis, S. H. Universal pinch off of rods by capillarity-driven surface diffusion. *Scr. Mater.* **39,** 55–60 (1998).
12. Bernoff, A. J., Bertozzi, A. L. & Witelski, T. P. Axisymmetric surface diffusion: Dynamics and stability of self-similar pinchoff. *J. Stat. Phys.* **93,** 725–776 (1998).
13. Cline, H. E. Shape instabilities of eutectic composites at elevated temperatures. *Acta Metall.* **19,** 481–490 (1971).
14. Nakagawa, Y. G. & Weatherly, G. C. Thermal-stability of rod Al_3Ni–Al eutectic. *Acta Metall.* **20,** 345–350 (1972).
15. Majumdar, B. & Chattopadhyay, K. The Rayleigh instability and the origin of rows of droplets in the monotectic microstructure of zinc–bismuth alloys. *Metall. Mater. Trans. A* **27,** 2053–2057 (1996).
16. Liu, H. Y., Li, Y. & Jones, H. Thermal stability of the α-Zn–Mg_2Zn_{11} and α-Zn–β-Al eutectics obtained by Bridgman growth. *J. Mater. Sci.* **33,** 1159–1164 (1998).
17. Kwon, Y., Thornton, K. & Voorhees, P. W. Coarsening of bicontinuous structures via nonconserved and conserved dynamics. *Phys. Rev. E* **75,** 021120 (2007).
18. Kwon, Y., Thornton, K. & Voorhees, P. W. The topology and morphology of bicontinuous interfaces during coarsening. *Europhys. Lett.* **86,** 46005 (2009).
19. Jain, S. & Bates, F. S. On the origins of morphological complexity in block copolymer surfactants. *Science* **300,** 460–464 (2003).
20. Davidovitch, B., Ertas, D. & Halsey, T. C. Ripening of porous media. *Phys. Rev. E* **70,** 031609 (2004).
21. Kurz, W. & Fisher, D. J. *Fundamentals of Solidification* 3rd edn (Trans Tech Publications, 1992).
22. Stampanoni, M. *et al.* Trends in synchrotron-based tomographic imaging: The SLS experience. *Dev. X-ray Tomogr. V* **6318,** U199–U212 (2006).
23. Fife, J. L. *Three-dimensional Characterization and Real-time Interface Dynamics in Aluminum–Copper Dendritic Microstructures.* PhD thesis, Northwestern Univ. (2009).
24. Kammer, D., Mendoza, R. & Voorhees, P. W. Cylindrical domain formation in topologically complex structures. *Scr. Mater.* **55,** 17–22 (2006).
25. Louzguine-Luzgin, D. V., Louzguina-Luzgina, L. V. & Inoue, A. Deformation behavior of high strength metastable hypereutectic Ti–Fe–Co alloys. *Intermetallics* **15,** 181–186 (2007).
26. Aagesen, L. K. *Phase-Field Simulation of Solidification and Coarsening in Dendritic Microstructures.* PhD thesis, Northwestern Univ. (2010).
27. Gunduz, M. & Hunt, J. D. The measurement of solid–liquid surface energies in the Al–Cu, Al–Si and Pb–Sn systems. *Acta Metall.* **33,** 1651–1672 (1985).
28. Abramowitz, M. & Stegun, I. A. *Handbook of Mathematical Functions with Formulas, Graphs, and Mathematical Tables* (National Bureau of Standards Applied Mathematics Series, 55, US Dept. of Commerce : US G.P.O., 1972).

Acknowledgements

This work was partially supported by NSF RTG grant DMS-0636574 (L.K.A.). M.J.M. acknowledges support from US National Science Foundation RTG grant DMS-0636574 and NSF grant DMS-0616468. A.E.J., J.L.F. and P.W.V. acknowledge the US Department of Energy, grant DE-FG02-99ER45782, for financial support. E.M.L. and S.O.P. acknowledge the Danish National Research Foundation for supporting the Center for Fundamental Research: Metal Structures in 4D, within which part of this work was carried out. The authors thank the Paul Scherrer Institut for beam time at the TOMCAT beamlines of the Swiss Light Source. We would also like to thank G. Mikuljan from the TOMCAT team for his support in setting up the experiment at the beamline.

Author contributions

L.K.A. carried out the theoretical analysis and prepared the manuscript. M.J.M. and P.W.V. were involved with the theoretical calculations. P.W.V. and E.M.L. conceived the experiments. J.L.F., S.O.P. and E.M.L. conducted the experiments. A.E.J. and J.L.F. analysed the experimental data. F.M. and M.S. provided technical guidance for the experiments.

Additional information

The authors declare no competing financial interests. Reprints and permissions information is available online at http://npg.nature.com/reprintsandpermissions. Correspondence and requests for materials should be addressed to P.W.V.

B.5 Pinch-off of rods by bulk diffusion

Available online at www.sciencedirect.com
ScienceDirect
Acta Materialia 59 (2011) 4922–4932
Acta MATERIALIA
www.elsevier.com/locate/actamat

Pinch-off of rods by bulk diffusion

L.K. Aagesen [a,1], A.E. Johnson [a], J.L. Fife [a,2], P.W. Voorhees [a,c,*], M.J. Miksis [c], S.O. Poulsen [d], E.M. Lauridsen [d], F. Marone [b], M. Stampanoni [b,e]

[a] Department of Materials Science and Engineering, Northwestern University, Evanston, IL 60208-3108, USA
[b] Swiss Light Source, Paul Scherrer Institut, CH-5232 Villigen, Switzerland
[c] Department of Engineering Sciences and Applied Mathematics, Northwestern University, Evanston, IL 60208-3108, USA
[d] Risø National Laboratory for Sustainable Energy, Technical University of Denmark, P.O. Box 49, DK-4000 Roskilde, Denmark
[e] Institute for Biomedical Engineering, University and ETH Zürich, 8092 Zürich, Switzerland

Received 10 December 2010; received in revised form 13 April 2011; accepted 17 April 2011

Abstract

The morphology of a rod embedded in a matrix undergoing pinching by interfacial-energy-driven bulk diffusion is determined near the point of pinching. We find a self-similar solution that gives a unique temporal power law and interfacial shape prior to pinching and self-similar solutions after pinching. The theory is compared to experiments that employ in situ four-dimensional X-ray tomographic microscopy for rods of liquid or solid pinching by solute diffusion in the high-diffusivity liquid phase. The excellent agreement between experiment and theory confirms that the interfacial morphology near the singularity is universal both before and after pinching; the shape holds regardless of the material system and initial condition. This also implies that the predictions of the time-dependence of the process can be used to determine the time to pinching for a wide variety of physical systems, and thus provide estimates of the time required for capillarity-driven break-up of microstructures from the detachment of secondary dendrite arms to polymer blends.

Keywords: Bulk diffusion; Coarsening; Self-organization and patterning; Capillary phenomena; X-ray and neutron techniques

1. Introduction

Rod-like morphologies of one phase embedded in a matrix of another phase are unstable to infinitesimal axial perturbations with a wavelength greater than $2\pi R$, where R is the radius of the rod. This morphological instability, known as a Rayleigh instability, is driven by the reduction of interfacial energy. Unstable perturbations increase in amplitude until only a thin neck remains that finally pinches off. Rayleigh instabilities can have a significant effect on the behavior of materials. For example, the cylindrical phase found in eutectic and monotectic in situ composites can break-up into a row of droplets due to Rayleigh instabilities, leading to degradation in mechanical properties [1–4]. Recently, metal nanowires have been shown to break-up due to Rayleigh instabilities [5,6], which could affect their stability in proposed device applications. Rayleigh instabilities were used to produce chains of metal nanoparticles encased in a ceramic tube [7], suggesting a route to making structures for plasmonic applications. In some cases, Rayleigh instabilities can induce secondary dendrite arms to detach from the dendrite stem [8,9] or lead to grain refinement in highly undercooled melts [10]. Recent three-dimensional analysis of the coarsening of liquid domains in a solid has illustrated the importance of the pinching of the liquid domains in the coarsening process of these two-phase systems [11]. Because Rayleigh instabilities affect the properties of such a wide variety of

---

* Corresponding author at: Department of Materials Science and Engineering, Northwestern University, Evanston, IL 60208-3108, USA. Tel.: +1 847 491 7820.

E-mail address: p-voorhees@northwestern.edu (P.W. Voorhees).

[1] Present address: Department of Materials Science and Engineering, University of Michigan, Ann Arbor, MI 48109, USA.

[2] Present address: Swiss Light Source, Paul Scherrer Institut, CH-5232 Villigen, Switzerland.

1359-6454/$36.00 © 2011 Acta Materialia Inc. Published by Elsevier Ltd. All rights reserved.
doi:10.1016/j.actamat.2011.04.036

materials systems, it is important to understand their evolution.

Nichols and Mullins [12] examined the stability of a rod subject to morphological perturbations and found the amplification rate of perturbations evolving by bulk diffusion inside or outside the rod. However, this analysis only holds when the perturbation's amplitude is small compared to the rod's radius. As the perturbation's amplitude grows and the radius of the pinching neck approaches zero, a finite-time singularity occurs as the curvature of the interface becomes infinite. This singularity introduces strong nonlinearities into the governing equations. However, the effect of the initial conditions may become less and less important, and the interface shape may thus become locally determined. In such cases, the interface may attain a self-similar shape which is time-independent when scaled by the appropriate characteristic length. The characteristic length scales as $(t_s - t)^{\delta}$, where t is time, t_s is the time of the singularity and δ is an exponent that depends on the equations governing the interface evolution. Such behavior has been observed in a variety of physical systems, such as solid rods pinching by surface diffusion [13,14], liquid jets or bridges pinching off via fluid flow driven by surface tension [15–22], and interface motion by mean curvature, such as occurs in grain growth [23,24].

Previously, we showed that self-similar pinching can also occur when rods pinch-off by bulk diffusion inside the rods [25]. The theoretically predicted interface shape was found in self-similar variables and the predicted interface shape and time-dependence were compared to pinching liquid rods embedded in a solid in an Al–Cu alloy. We found that the shape for liquid rods pinching, where there is diffusion only inside the rod, agreed very well with that predicted by theory. The dynamics of the pinching process was described well by a temporal power law, with the materials–parameter-dependent prefactor very close to that predicted by theory. Thus, we concluded that the shape of the interface undergoing pinching when diffusion occurs inside the rod is universal and that the time required for the rod to break-up can be described well by theory. The other limit, where a low-diffusivity phase rod is embedded in a high-diffusivity matrix, was not examined experimentally, although a self-similar solution for the pinching process was found.

Here we review the theoretical development of self-similar pinching of rods by interfacial-energy-driven bulk diffusion, assuming isotropic surface energy and an isothermal system with no convection. We then compare the theoretical predictions of the interface shape and kinetics to experimental data for pinching solid rods surrounded by a high-diffusivity liquid in an Al–Cu alloy. To determine if the kinetics of pinching liquid and solid rods are different, we present a more extensive analysis of the kinetics of the pinching process of liquid rods than in Ref. [25] and compare the results with data on solid cylinders. We also address the issue of whether self-similarity can be observed after pinching by comparing the theoretical prediction of the kinetics of the interface with experimental data of post-pinching liquid rods. In Section 2 we detail the theoretical formulation of the problem. The interface shapes are shown in Sections 2.1 and 2.2, and the theoretical predictions for the interface shape and the time-dependence of pinching are compared with experimental data for solid rods and post-pinching liquid rods in Section 3.

2. Theory

We consider the case of a rod of one phase embedded in another, where the diffusivity of the solute is high in one phase and very low in the other. This high-diffusivity phase, α, can be either the rod or the matrix. The diffusivity of the other phase, β, is taken to be zero. Pinching is caused by the diffusional motion of solute atoms through the high-diffusivity α-phase driven by the interfacial energy between the two phases. The diffusion field in the α-phase is given by

$$\frac{\partial C_\alpha}{\partial t} = D_\alpha \nabla^2 C_\alpha \tag{1}$$

where C_α is the concentration of the solute and D_α is the diffusion coefficient of the solute in the noted phase. When the diffusion field relaxes much faster than the interface moves, the diffusion field is quasi-stationary, and the diffusion equation can be approximated by Laplace's equation:

$$\nabla^2 C_\alpha = 0 \tag{2}$$

The validity of this approximation will be addressed in Section 3.3.1.

The first boundary condition at the interface is the Gibbs–Thomson equation:

$$C_\alpha = C_\alpha^0 + \left(C_\beta^0 - C_\alpha^0\right) d_0 H \tag{3}$$

where C_α is the solute concentration on the α side of the interface, C_α^0 and C_β^0 are the equilibrium solute concentrations in the noted phases at a flat interface, d_0 is the capillary length and H is the mean interfacial curvature. The other boundary condition is the interfacial mass balance,

$$\left(C_\alpha^0 - C_\beta^0\right) v = -D_\alpha \frac{\partial C_\alpha}{\partial n} \tag{4}$$

where v is the interfacial velocity in the normal direction and $\partial C_\alpha / \partial n$ is the derivative of the concentration field in the normal direction, where a positive normal is pointing from the α phase to the β phase.

We assume that the interface is axially symmetric, and thus the position of the two-phase interface as a function of time is given in cylindrical coordinates (r, z). The interface before and after pinching is symmetric about the axial, z-axis (see Fig. 1). Near the point of pinching, the interface

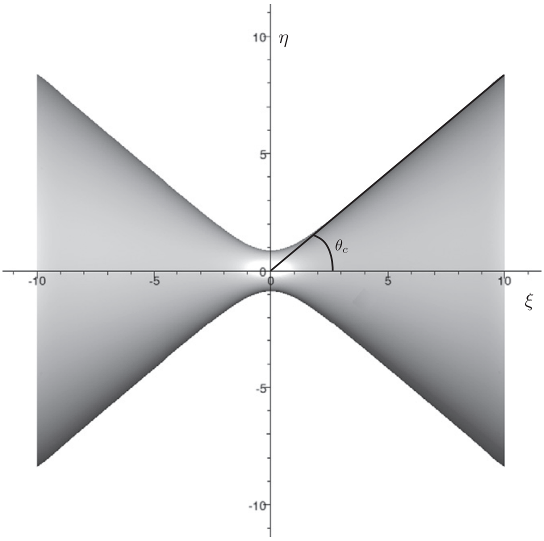

Fig. 1. The theoretically predicted shape of a zero-diffusivity β-phase rod pinching off in a high-diffusivity α-phase. The interface asymptotically approaches two opposing cones with angle $2\theta_c$ as the time of pinching is approached. Interface coordinates are in the self-similar variables of Eq. (5).

asymptotically approaches two opposing cones, each with cone angle $2\theta_c$.

If a valid similarity coordinate system can be found, the interface coordinates can be written in terms of self-similar variables as:

$$\eta = \frac{rB}{(t_s - t)^\delta}, \quad \xi = \frac{zB}{(t_s - t)^\delta} \tag{5}$$

where η and ξ are the radial and axial coordinates in the time-independent similarity variables and B is a scaling constant dependent on material properties. In the similarity variables, the position of the interface is given by the function $\eta = f(\xi)$, or defined parametrically, $F = \eta - f(\xi) = 0$.

We determine if a valid similarity coordinate system exists by finding the exponent δ of the similarity variables required to eliminate the time-dependence in the boundary conditions. We define the difference between the solute concentration in the high-diffusivity α phase and the equilibrium concentration in terms of a scaled concentration in similarity variables, $\widetilde{C}(\xi, \eta)$:

$$C_\alpha(r, z, t) - C_\alpha^0 = (t_s - t)^\gamma A \widetilde{C}(\xi, \eta) \tag{6}$$

where γ is a constant and A is a scaling constant dependent on material properties. Substituting Eq. (6) into Eq. (3) and using the fact that real-space derivatives give $B/(t_s - t)^\delta$ times derivatives in the similarity variables, we obtain

$$(t_s - t)^\gamma A \widetilde{C}(\xi, \eta) = \left(C_\beta^0 - C_\alpha^0\right) d_0 \frac{B}{(t_s - t)^\delta} \left(\nabla_{\xi,\eta} \cdot \hat{n}\right) \tag{7}$$

where $\nabla_{\xi,\eta}$ is in the similarity coordinate system. In order for a valid similarity solution for the concentration and interface shape to exist, the time-dependence on the left- and right-hand sides of the equation must cancel, meaning that $\gamma = -\delta$.

The solute conservation boundary condition (4) is also transformed into similarity variables. To find the normal velocity of the interface in similarity variables, we use the material derivative at the interface. Dividing by $|\nabla F|$ and using the chain rule for $\partial F/\partial t$, we find

$$\begin{aligned}(C_\alpha^0 - C_\beta^0)\delta(t_s - t)^{\delta-1} \frac{F_\xi \xi + F_\eta \eta}{\sqrt{F_\xi^2 + F_\eta^2}} \\ = D_\alpha \frac{(t_s - t)^\gamma}{(t_s - t)^\delta} AB^2 \left(\hat{n} \cdot \nabla_{\xi,\eta} \widetilde{C}\right)\end{aligned} \tag{8}$$

where subscripts of ξ, η denote partial differentiation with respect to the similarity variables. Comparing the time-dependence on the left and right sides yields $\delta - 1 = \gamma - \delta$. Substituting $\gamma = -\delta$ from Eq. (7), the required exponents for a similarity solution consistent with the boundary conditions are

$$\gamma = \frac{1}{3}, \quad \delta = -\frac{1}{3} \tag{9}$$

Thus the problem is reduced to solving Laplace's equation in similarity variables on the boundary. A similarity solution also requires (equating dimensional coefficients in Eqs. (8) and (7)) that $B = (D_\alpha d_0)^{-1/3}$ and $A = \left(C_\alpha^0 - C_\beta^0\right)\left(d_0^2/D_\alpha\right)^{1/3}$.

After transforming to the self-similar coordinate system of Eq. (5), the shape of the interface was determined by solving Laplace's equation $\nabla_{\xi,\eta}^2 \widetilde{C} = 0$ numerically using a boundary-integral method. Green's third identity can be used along with the free-space Green's function for Laplace's equation to yield an integrodifferential equation for the scaled concentration $\widetilde{C}(\xi, \eta)$ on the interface:

$$\frac{1}{2}\widetilde{C}(\xi_0, \eta_0) = \int_S \left(\widetilde{C}(\xi, \eta)\frac{\partial g}{\partial n} - g\frac{\partial \widetilde{C}}{\partial n}\right) dS \tag{10}$$

where g is the free-space Green's function for Laplace's equation:

$$g = \frac{-1}{4\pi\left|\mathbf{r}(\xi_{\mathbf{0},\eta_{\mathbf{0}})-\mathbf{r}_i(\xi,\eta)}\right|} \tag{11}$$

$$= \frac{-1}{4\pi\left[(\xi\cos\theta - \xi_0\cos\theta_0)^2 + (\xi\sin\theta - \xi_0\sin\theta_0)^2 + (\eta - \eta_0)^2\right]^{1/2}} \tag{12}$$

where $\mathbf{r}(\xi_\mathbf{0}, \eta_\mathbf{0})$ and $\mathbf{r}_i(\xi, \eta)$ are the field and source point, respectively, and θ is the angular coordinate in the cylindrical coordinate system.

The integration of Eq. (10) is performed along the ξ-axis, with the function $\eta = f(\xi)$ used for the position of the boundary. The angular portion of the integral is rewritten as a complete elliptic integral of the first kind and approximated using the polynomial approximation of Ref. [26]. Depending on whether the high-diffusivity phase is the matrix or rod, we obtain two different formulations for the integrodifferential equation, differing only in the direction of the normal vector. For the case of a rod with zero diffusivity embedded in a matrix with nonzero diffusivity, substituting for Green's function and using the solute conservation boundary condition (4) to substitute for $\frac{\partial C}{\partial n}$, the following integrodifferential equation for $\widetilde{C}[\xi,f(\xi)]$ is obtained:

$$\begin{aligned}2\pi\widetilde{C}[\xi_0,f(\xi_0)]=\int_0^\infty \mathrm{d}\xi f(\xi)\Bigg\{&\widetilde{C}[\xi,f(\xi)]\\
&\times\Bigg[\left(\frac{4f'(\xi)(\xi-\xi_0)}{(l_-^2+k^2)^{3/2}}-\frac{4(\eta+\eta_0)}{(l_-^2+k^2)^{3/2}}\right)\\
&\times M\left(\frac{k^2}{l_-^2+k^2}\right)-\left(\frac{32\eta\eta_0(\xi-\xi_0)f'(\xi)}{(l_-^2+k^2)^{5/2}}\right.\\
&\left.-\frac{16\eta_0\left[\eta^2-\eta_0^2-(\xi-\xi_0)^2\right]}{(l_-^2+k^2)^{5/2}}\right)M_\xi\left(\frac{k^2}{l_-^2+k^2}\right)\Bigg]\\
&-\frac{4}{3}\frac{[f'(\xi)\xi-f(\xi)]}{\sqrt{l_-^2+k^2}}M\left(\frac{k^2}{l_-^2+k^2}\right)\\
&+\widetilde{C}[\xi,f(\xi)]\Bigg[\left(\frac{4f'(\xi)(\xi+\xi_0)}{(l_+^2+k^2)^{3/2}}-\frac{4(\eta+\eta_0)}{(l_+^2+k^2)^{3/2}}\right)\\
&\times M\left(\frac{k^2}{l_+^2+k^2}\right)-\left(\frac{32\eta\eta_0(\xi+\xi_0)f'(\xi)}{(l_+^2+k^2)^{5/2}}\right.\\
&\left.-\frac{16\eta_0\left[\eta^2-\eta_0^2-(\xi+\xi_0)^2\right]}{(l_+^2+k^2)^{5/2}}\right)M_\xi\left(\frac{k^2}{l_+^2+k^2}\right)\Bigg]\\
&-\frac{4}{3}\frac{[f'(\xi)\xi-f(\xi)]}{\sqrt{l_+^2+k^2}}M\left(\frac{k^2}{l_+^2+k^2}\right)\Bigg\}\end{aligned}\tag{13}$$

where M is the polynomial approximation for a complete elliptical integral of the first kind defined in Ref. [26], M_ξ is the polynomial approximation differentiated with respect to ξ, $l_-\equiv(\xi-\xi_0)^2+[f(\xi)-f(\xi_0)]^2$, $l_+\equiv(\xi-\xi_0)^2+[f(\xi)+f(\xi_0)]^2$ and $k^2\equiv 4\xi\xi_0$. In this coordinate system, $\widetilde{C}$ is equivalent to curvature, which can be written in terms of the interface shape $f(\xi)$ as

$$\widetilde{C}=\nabla\cdot\hat{n}=-\frac{1}{f(\xi)\sqrt{1+[f'(\xi)]^2}}+\frac{f''(\xi)}{(1+[f'(\xi)]^2)^{3/2}}\tag{14}$$

Eq. (14) is substituted into Eq. (13) and an integrodifferential equation for $f(\xi)$ is obtained. The boundary conditions are that $f(\xi)$ approaches a straight line with angle θ_c far from the ξ-axis and $f'(0)=0$, which ensures finite curvature at the origin.

For the case of a rod with a nonzero diffusivity embedded in a matrix with zero diffusivity, the direction of the normal vector is reversed, leading to a change in sign of derivatives in the normal direction. This changes the integrodifferential equation for $\widetilde{C}[\xi,f(\xi)]$ to

$$\begin{aligned}2\pi\widetilde{C}[\xi_0,f(\xi_0)]=\int_0^\infty \mathrm{d}\xi f(\xi)\Bigg\{&\widetilde{C}[\xi,f(\xi)]\\
&\times\Bigg[\left(-\frac{4f'(\xi)(\xi-\xi_0)}{(l_-^2+k^2)^{3/2}}+\frac{4(\eta+\eta_0)}{(l_-^2+k^2)^{3/2}}\right)\\
&\times M\left(\frac{k^2}{l_-^2+k^2}\right)+\left(\frac{32\eta\eta_0(\xi-\xi_0)f'(\xi)}{(l_-^2+k^2)^{5/2}}\right.\\
&\left.-\frac{16\eta_0\left[\eta^2-\eta_0^2-(\xi-\xi_0)^2\right]}{(l_-^2+k^2)^{5/2}}\right)M_\xi\left(\frac{k^2}{l_-^2+k^2}\right)\Bigg]\\
&-\frac{4}{3}\frac{[f'(\xi)\xi-f(\xi)]}{\sqrt{l_-^2+k^2}}M\left(\frac{k^2}{l_-^2+k^2}\right)\\
&+K[\xi,f(\xi)]\Bigg[\left(\frac{-4f'(\xi)(\xi+\xi_0)}{(l_+^2+k^2)^{3/2}}\right.\\
&\left.+\frac{4(\eta+\eta_0)}{(l_+^2+k^2)^{3/2}}\right)M\left(\frac{k^2}{l_+^2+k^2}\right)\\
&+\left(\frac{32\eta\eta_0(\xi+\xi_0)f'(\xi)}{(l_+^2+k^2)^{5/2}}\right.\\
&\left.-\frac{16\eta_0\left[\eta^2-\eta_0^2-(\xi+\xi_0)^2\right]}{(l_+^2+k^2)^{5/2}}\right)M_\xi\left(\frac{k^2}{l_+^2+k^2}\right)\Bigg]\\
&-\frac{4}{3}\frac{[f'(\xi)\xi-f(\xi)]}{\sqrt{l_+^2+k^2}}M\left(\frac{k^2}{l_+^2+k^2}\right)\Bigg\}\end{aligned}\tag{15}$$

with curvature given by

$$\widetilde{C}=\nabla\cdot\hat{n}=\frac{1}{f(\xi)\sqrt{1+f'(\xi)^2}}-\frac{f''(\xi)}{\left[1+f'(\xi)^2\right]^{3/2}}\tag{16}$$

The boundary conditions are again that $f(\xi)$ approaches a straight line with angle θ_c and $f'(0)=0$.

To solve for the interface shape $\eta=f(\xi)$, the integrodifferential equation was discretized. The integration was performed numerically using the trapezoidal rule on a truncated domain along ξ. L'Hôpital's rule and Taylor expansions in the neighborhood of $\xi=\xi_0$ were used to approximate the effect of the integrable singularity in the numerical method [15]. Newton's method was then used to iteratively solve for $f(\xi)$, starting with a straight line with angle θ_c as an initial guess for the shape.

2.1. *Interface shape prior to pinching: nonzero matrix diffusivity*

We seek solutions of Eq. (13) describing the shape of a rod undergoing pinching where diffusion is solely in the matrix. By analogy with the case where diffusion occurs only inside the rod, solutions prior to pinching are not expected at arbitrary cone angles [14,25], so an iterative process was used to search for solutions. A coarse grid spacing along ξ was used to search for solutions as θ_c was varied through the range where a solution is expected based on the experimental data. Solutions were obtained for some values of θ_c in this range, and these solutions were used as an initial guess for the solution with a finer grid spacing. As the grid spacing was made finer, the boundary condition at $\xi = 0$ was changed, fixing $f(0)$ rather than $f'(\xi) = 0$. The angle and $f(0)$ were iteratively refined until a smooth solution with $f'(0) = 0$ was found. The angle was converged to $\theta_c = 40° \pm 1°$. The interface shape is shown in Fig. 1. We searched for but did not find solutions at larger cone angles. It is expected that solutions with smaller cone angles may also exist. However, based on our experience with the case of liquid rods pinching, only the solution with the largest cone angle – the solution shown in Fig. 1 – will be observed experimentally. This has also been found to be the case for rods pinching by surface diffusion [14]. Thus we did not determine any other solution.

2.2. Interface shape post-pinching: nonzero rod diffusivity

The interface shape of the two receding tips after pinching is also governed by Eqs. (2)–(4), so their shapes are also expected to be self-similar. To find the interface shape of the cones after pinching, the dependent and independent variables of the self-similar coordinate system are reversed, giving

$$\xi = \frac{rB}{(t - t_s)^{1/3}}, \quad \eta = \frac{zB}{(t - t_s)^{1/3}} \tag{17}$$

For a rod of nonzero diffusivity in a zero-diffusivity matrix, the integrodifferential equation is

$$\begin{aligned} 2\pi\widetilde{C}[\xi_0, f(\xi_0)] = \int_0^\infty \xi\,\mathrm{d}\xi \Bigg\{ \widetilde{C}[\xi, f(\xi)] \times \Bigg[\Bigg(\frac{f'(\xi)4(\xi + \xi_0)}{(l_-^2 + k^2)^{3/2}} \\ - \frac{4[f(\xi) - f(\xi_0)]}{(l_-^2 + k^2)^{3/2}} \Bigg) \times M\left(\frac{k^2}{l_+^2 + k^2}\right) \\ + \Bigg(\frac{-16\xi_0 f'(\xi)\left[\xi^2 - \xi_0^2 - [f(\xi) - f(\xi_0)]^2\right]}{(l_-^2 + k^2)^{5/2}} \\ + \frac{32\xi\xi_0[f(\xi) - f(\xi_0)]}{(l_-^2 + k^2)^{5/2}} \Bigg) \times M_\xi\left(\frac{k^2}{l_+^2 + k^2}\right) \Bigg] \\ - \frac{4[f'(\xi)\xi - f(\xi)]}{3(l_-^2 + k^2)^{1/2}} M\left(\frac{k^2}{l_+^2 + k^2}\right) \Bigg\} \end{aligned} \tag{18}$$

In analogy with Ref. [13], a solution for the interface shape is expected at any cone angle θ_c. The same behavior was observed here, as shown in Fig. 2. If the cone angle for the self-similar shapes after pinching is fixed by the shape with the largest cone angle prior to pinching, then the interface shape has $\theta_c = 38°$, as found in Ref. [25].

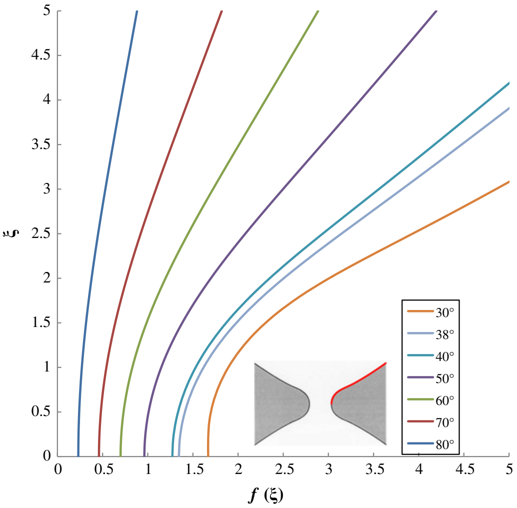

Fig. 2. Shape of the interface for α-phase rods after pinching. Inset, the portion of the interface being plotted is highlighted in red. The interface coordinates are in the self-similar variables of Eq. 17. A solution can be found at any angle θ_c. For each curve, the β phase lies to the upper left and the α phase to the lower right of the curve. The physically observed solution is found at $\theta_c = 38°$, as determined by the stable solution for α-phase rods before pinching. (For interpretation of the references to colour in this figure legend, the reader is referred to the web version of this article.)

It should also be possible to solve for the self-similar shape of a rod after pinching with nonzero diffusivity in the surrounding matrix. However, due to the larger time intervals used in data collection of the sample with multiple solid pinch-offs (Al–26 wt.% Cu) and the faster dynamics of the solid pinching events, insufficient data for solid rods post-pinching was available for comparison to theory. Thus, we did not solve for the theoretically predicted shape for this case.

2.3. The kinetics of pinching

The dynamics of the pinching process can be determined using the self-similar variables. A quantity of experimental interest is the diameter at the center of a pinching rod, $D(t)$, which is given by $\eta(\xi = 0) = f(0)$. Using the definitions of the self-similar variables (5), the diameter decreases in time as

$$D(t) = K(t_s - t)^{1/3} \tag{19}$$

where K is the rate constant for the pinching process,

$$K = 2f(0)(D_\alpha d_0)^{1/3} \tag{20}$$

and the similarity solution for the interface shape at $\xi = 0$ gives $f(0)$. Thus materials parameters and $f(0)$, the interface location at the pinching point in similarity variables at

$\xi = 0$, fix the dynamics of the pinching process. If the α phase is the matrix, as discussed in Section 2.1, $f(0) = 0.88$. If the high-diffusivity phase α is the rod, then the expression for the rate constant is identical except for the location of the interface at the pinching point in similarity variables, which gives $f(0) = 0.60$ in this case [25]. It is also clear that the kinetics of pinching are independent of the difference in concentration between the two phases at the interface (see the mass balance equation at the interface) – a somewhat unusual result. After pinching, the rate constant changes again, due to the change in $f(0)$. If we take the interface shape to be that which is fixed by the shape with the largest cone angle prior to pinching, then $f(0) = 1.3$ for α-phase rods.

3. Experiment

3.1. Experimental procedure

Al–Cu samples of different Cu compositions were directionally solidified to form Al-rich dendrites [27]. In preparation for X-ray tomographic microscopy, 1 mm diameter samples were cut from the original ingots and mounted in a custom-made sample furnace. The samples were then coarsened in situ at 565 °C at the TOMCAT beamline located at the X02DA port of the Swiss Light Source at the Paul Scherrer Institut. Here we analyze data for an Al–26 wt.% Cu sample and an Al–15 wt.% Cu sample, and compare them with the results of Aagesen et al. [25]. These compositions correspond to solid volume fractions of approximately 42% and 74%, respectively, based on the Al–Cu binary phase diagram [28]. These two samples were chosen for analysis because the Al–15 wt.% Cu sample contains multiple liquid pinch-offs and the Al–26 wt.% Cu sample contains multiple solid pinch-offs. Here the high-diffusivity phase, α, is the liquid and the low-diffusivity phase, β, is the solid. For the sample with a 42% solid volume fraction, the liquid is the matrix and the solid rods, remnants of the dendrites, break-up. In the higher-volume-fraction solid sample, the solid becomes the matrix and we examine the break-up of liquid rods. For a detailed discussion of the complex morphology of this high volume fraction sample, see Ref. [29].

X-ray photon energies of 20 keV were used, with 80 ms exposure times, and 721 projections were captured over the 180° of rotation. The detector was a Ce-doped YAG scintillator with a thickness of 20 μm, and a 2048 × 2048 pixel CCD camera with a 280c digital/analog converter and a 10 MHz read-out speed. A total of 1024 slices, with a spatial resolution of 1.48 μm^3 per voxel, were collected every 2 min 30 s and 3 min 52 s for the Al–15 wt.% Cu and Al–26 wt.% Cu samples, respectively. Further information about the TOMCAT beamline and the details of the experiment can be found in Refs. [30] and [31], respectively. Due to the density difference between Al and Cu and the difference in composition between the solid and liquid phases, this alloy system is ideal for X-ray tomographic microscopy. It has been used with great success, for example, to examine the three-dimensional (3-D) morphological evolution during dendrite and particle coarsening [11,32–34].

3.2. Experimental analysis

In preparation for analysis, 2-D grayscale tomograms were segmented (converted to black and white) in Interactive Data Language (IDL), then stacked into 3-D arrays. An IDL program was developed to automatically find pinching events. The program loops through each 2-D $x - y$ slice and searches for small circular cross-sections, which are then fed into a second program that determines if it is a pinch-off by measuring the diameter of the cross-section as well as the diameters of the circular cross-sections in the slices above and below it. If there is a clear minimum in the diameter in the z-direction (as opposed to a maximum, as would be seen in a spherical particle), then it is a pinch-off whose principal axis is aligned with the z-axis. The location of each pinch-off in space and time is then used in a program that measures the diameter as a function of time. At a given time and slice, the program counts the number of pixels across the cross-section at different lines in both the x- and y-directions. The diameters in the x- and y-plane for that slice are then chosen to be the maximum number of pixels. Next, the diameter of the pinch-off at that time step is chosen to be at the slice with the minimum diameter. The smaller of the x- and y-diameters is chosen because, if the pinch-off is slightly misaligned with the z-axis, then the cross-section is elliptical, thus the smaller cross-section diameter is more representative of the actual diameter. t_s is determined for each pinch-off by linearly fitting the diameter cubed vs. t and using the equation of the line to find the time t_s when the diameter is zero. The rate constant is then calculated to be the cube root of the linear slope of the diameter cubed vs. time plot. This program loops through different times and for many pinch-offs, and automatically calculates the rate constant for each, using at least four time steps prior to t_s. Images are produced for each pinch-off in order to verify that they are in fact pinching events.

After pinch-off, the distances between the receding cone tips were also calculated automatically in IDL using the known interface locations and t_s values of the pinch-offs from the pinch-off finder code. Because these pinch-offs are all roughly aligned with the z-axis, the code loops through each z slice until it finds the ends of the top and bottom cones, when it records the locations. It then calculates the difference between the two points and repeats for later time steps, for a total of 5–10 time steps. The post-pinch-off rate constant is then taken as the cube root of the slope of the distance cubed vs. time plot.

Next, the 3-D representation of the theoretically predicted interface shape was created for solid rods with an angle $\theta_c = 40°$, as in Fig. 1. (A comparison between the predicted and measured liquid morphologies is given in Ref. [25].) The arrays of both the experimental data and the theoretically determined shape were then imported into

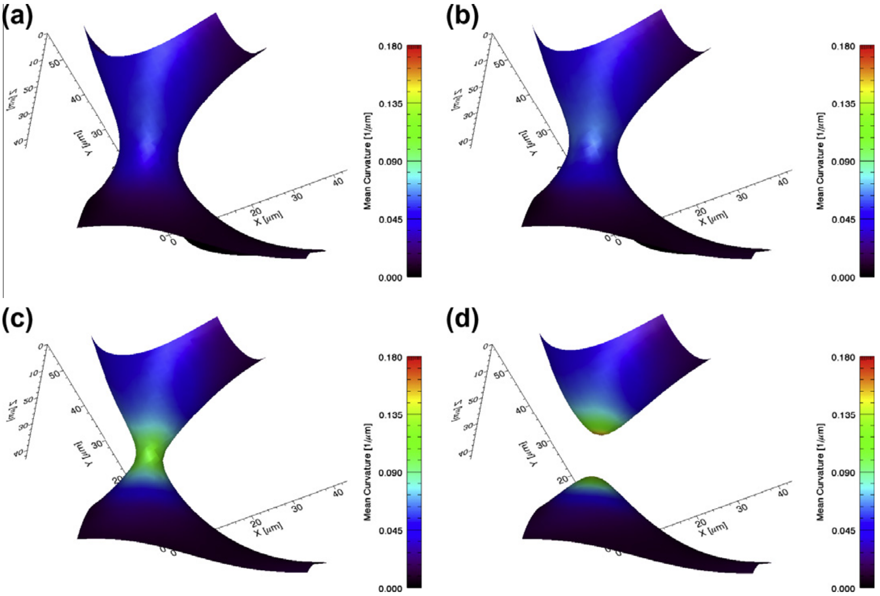

Fig. 3. Time sequence of a solid Al–Cu rod in a liquid matrix pinching due to interfacial-energy-driven bulk diffusion. The steadily increasing curvature with time at the pinching point is evident. Times: (a) 100 min, (b) 104 min, (c) 108 min, (d) 112 min.

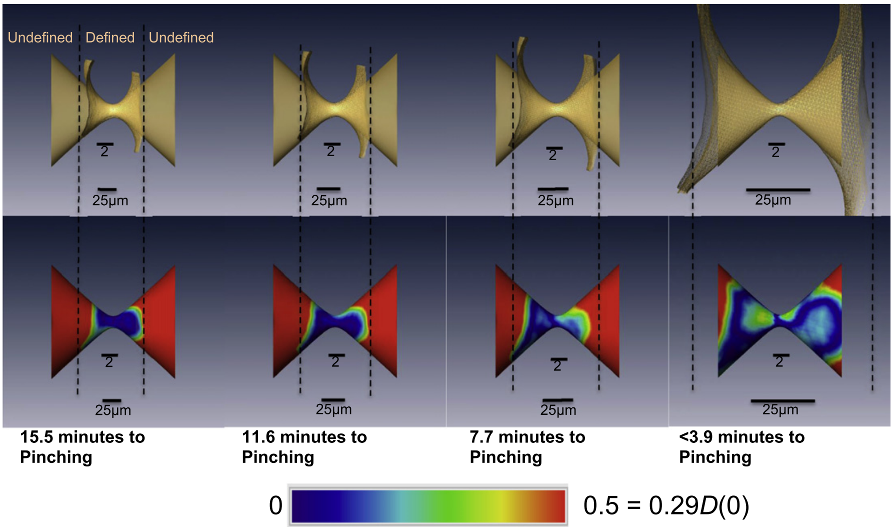

Fig. 4. Color contour plot illustrating the distance between the experimental surface and theoretical surface for a solid pinch-off. $D(0) = 2f(0)$ is the diameter at the center of the pinching rod in similarity variables. Experimental surfaces have been scaled to the theoretical surface, so the similarity scale bar (closer to cone center) is fixed in size, whereas the real scale bar (farther from cone center) is growing as the singularity is approached. (For interpretation of the references to colour in this figure legend, the reader is referred to the web version of this article.)

the visualization program Amira and cropped to the location of individual pinching events.

The pre-pinch-off experimental surfaces were aligned to the theoretically predicted surface by first scaling the experiment to match the diameter of the theory. The surfaces were then aligned using the rigid surface alignment function in Amira. This function changes only the position (not the size) of the experimental shape to align the surfaces. This alignment process was repeated for a series of times leading to the singularity. The distance from the theoretically predicted shape to the closest point on the experimental shape was then calculated and illustrated on the theoretical shape as a color contour plot as a way to demonstrate the extent of the agreement between the two interfaces.

3.3. Experimental results and discussion

3.3.1. Interfacial evolution prior to pinching

An example of a series of images leading to pinching is shown in Fig. 3. The images are colored by the mean curvature, which diverges at the pinching point. This divergence in curvature leads to a divergence in the interfacial concentrations and interfacial velocities; as a result, the evolution of the interface is dominated by the interfacial morphology in the neighborhood of the singularity, and an evolution process that is independent of the initial shape of the interface. This can lead to the predicted self-similar interfacial evolution. To determine if this is the case, we examine the evolution shown in Fig. 3 quantitatively.

Before proceeding to compare theory and experiment, we first address the validity of the quasi-stationary approximation. By scaling the time-dependent diffusion equation by the characteristic time for the evolution of the pinching process, τ, where

$$\tau = \frac{l^3}{8f(0)^3 D_L d_0} \qquad (21)$$

and l is the characteristic length scale, which is the diameter of the pinching rod, we find that the diffusion field is quasi-stationary when $8f(0)^3 d_0/l \ll 1$ [25]. Using the materials parameters for Al–Cu (see below), we find the quasi-stationary approximation fails when the diameter of the rod is less than 12 nm, well below the 1.48 μm resolution of the tomography. Thus the results presented in Section 2 are valid for the experimental data presented here.

We first compare the self-similar shape predicted theoretically for a solid rod pinching in a high-diffusivity liquid. Here the distances are recorded in similarity variables, which have a fixed scale as the variable real-space scale bar grows in time, as seen in Fig. 4. The images are shown in similarity variables to illustrate that the improved agreement as t_s is approached is not just a result of the changing length scale. The agreement is quite good at the final time step before pinching. Fig. 4 illustrates this approach to the theoretical shape; at the latest time there is a large region where the difference between experimental and theoretical surfaces is approximately 0.3 or less, which is less than half of the experimental spatial resolution of 1.48 μm pixel^{-1}. It is difficult to determine whether the theoretically calculated cone angle has the correct value due to spatial and temporal resolution limits. This also means that we cannot differentiate between the solid and liquid shapes by their cone angles alone. However, in almost all of the solid and liquid pinching events found, the angle approaches the theoretical angles of 80° and 76°, respectively, and the overall fit to the theoretical shape improves as the singularity is approached.

We compare the kinetics predicted by the similarity solutions to the experimental data. Fig. 5 shows a plot of one solid pinch-off diameter as a function of $(t - t_s)^{1/3}$, showing images corresponding to a few data points. The excellent fit to a straight line indicates that the temporal exponent of 1/3 holds for a surprisingly long time. Thus the kinetics seem to be described by the similarity solution long before the interface shape is described well by the similarity solution. The ability of the similarity solution to describe the kinetics of the pinching process is further examined by determining the rate constant, K, as given in Eq. (20), from the slope of the line shown in Fig. 5. We employ 19 pinching events, which gives an average rate constant of 2.28 μm s$^{-1/3}$,with a standard deviation of 0.290 μm s$^{-1/3}$. To compare with the theoretical predictions, we use the liquid diffusion

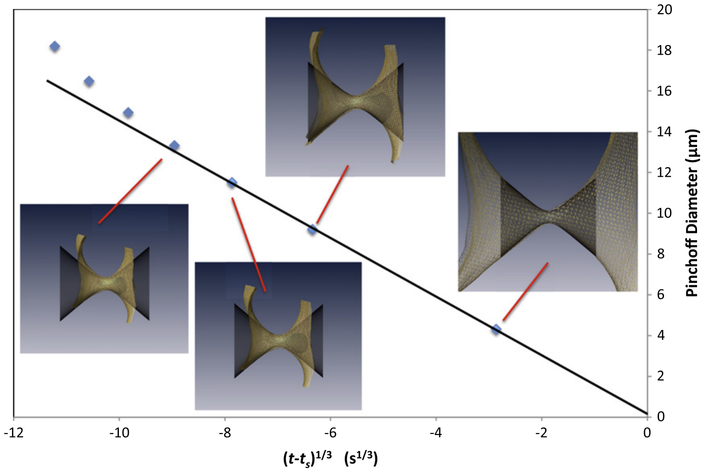

Fig. 5. Plot of the pinch-off diameter vs. $(t - t_s)^{1/3}$ for a solid Al–Cu rod pinching off in a liquid matrix.

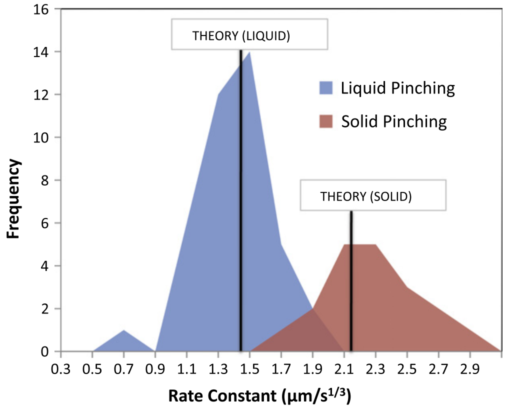

Fig. 6. Frequency of both the solid and liquid rate constants, illustrating the excellent fit to theory.

coefficient $D_\alpha = 8.3 \times 10^{10}\ \mathrm{m^2/s}$ [35] and capillary length d_0=2.27 nm [36], along with $f(0) = 0.88$ for a rod of solid (β) pinching by diffusion in a liquid (α) matrix. This gives $K = 2.15\ \mu\mathrm{m\ s^{-1/3}}$, which is only 6% smaller than that measured experimentally.

The ability of the similarity solution to describe the kinetics of the process is further examined by comparing the experimentally measured and theoretically predicted rate constants, K, for both solid rods embedded in a liquid and liquid rods in a solid. It is possible to predict the dependence of the rate constant on the materials parameters D_α and d_0 simply using the fact that the process occurs by interfacial-energy-driven bulk diffusion and dimensional analysis. The key prediction of theory is that the kinetics depend on the factor $2f(0)$ that appears in the rate constant (see Eq. (20)). As mentioned above, $f(0)$ is different depending on whether diffusion occurs inside or outside the rod. Thus a particularly stringent test of the theory is to determine if the rate constants for pinching are different for solid rods pinching in a liquid and liquid rods pinching in a solid.

We found 40 liquid rods (21 new liquid rods, in addition to the 19 analyzed in Ref. [25]) and 19 solid rods undergoing pinching. The average solid-rod rate constant was $2.28\ \mu\mathrm{m\ s^{-1/3}}$, with a standard deviation of $0.290\ \mu\mathrm{m\ s^{-1/3}}$, and the average liquid-rod rate constant was $1.40\ \mu\mathrm{m\ s^{-1/3}}$, with a standard deviation of $0.236\ \mu\mathrm{m\ s^{-1/3}}$. Using the predicted values for $f(0)$ gives a solid-rod rate constant of $2.15\ \mu\mathrm{m\ s^{-1/3}}$ and a liquid-rod rate constant of $1.47\ \mu\mathrm{m\ s^{-1/3}}$. Note that the materials parameters appearing in both rate constants are identical and thus the reason why the rate constants are different are the values of the diameters of the rods in similarity variables at the pinching point.

The solid-rod and liquid-rod rate constants are 6% greater and 5% less than the theoretically predicted rate constants, respectively. This indicates an excellent agreement between theory and experiment, given the uncertainties in the materials parameters and error in the experiment. To determine if these two rate constants are different due to the differences in $f(0)$, we examine a histogram of the rate constants shown in Fig. 6. It is clear that the distributions are distinct and that the theoretically predicted rate constant falls in the center of each distribution. Additionally, a one-tailed t-test of the experimental solid and liquid rate constants results in a p-value of 6.3×10^{-13}. The p-value essentially represents the probability that the two groups of data (the liquid and the solid pinch-off rate constants) are from the same group, so this low p-value indicates that the difference between the average solid and liquid pinch-off rate constants is quite statistically significant.

We thus show that the rods are pinching in a self-similar fashion; that the kinetics are well described by theory and the known materials parameters; and that the path through

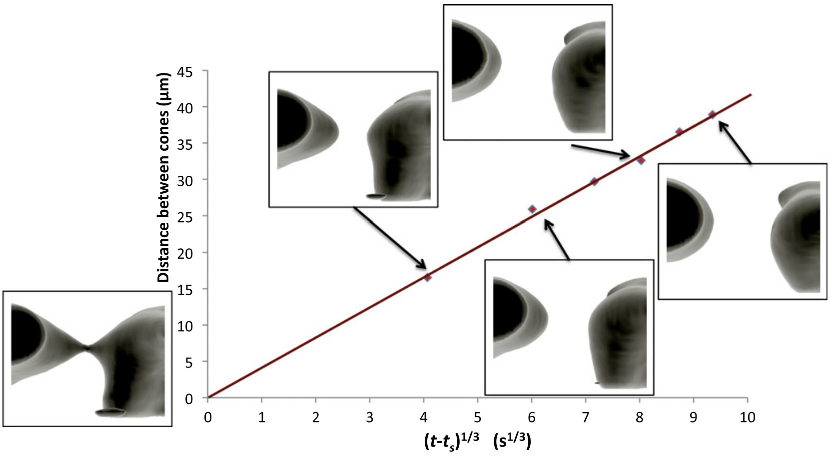

Fig. 7. Plot of the distance between receding cone tips vs. $(t - t_s)^{1/3}$, showing images that correspond with the points. Image to the left of the y-axis shows the rod just before pinching.

which diffusion occurs affects the dynamics of the pinching process, but not the temporal power law.

As seen in both Figs. 4 and 5, the agreement between theory and experiment improves as the singularity is approached, since initial conditions have less influence and the shape becomes locally determined. In some cases, the mean deviation between shapes just before pinch-off is less than the 1.48 μm resolution of the X-ray tomography scan. In other cases, the initial shapes of the rods were asymmetric about the pinching axis and thus the singularity did not achieve high degrees of self-similarity under the time and space resolution constraints of the experiment. However, in all 59 cases examined the agreement between theory and experiment improved as the singularity was approached. Interestingly, despite the apparent disagreement in the shape of the interface in some cases, the kinetics are still described well by the similarity solution, as shown above. We therefore conclude that the pinching process under interfacial-energy-driven bulk diffusion is governed by a unique self-similar solution dependent only on whether diffusion occurs inside or outside the rod.

3.3.2. Interfacial evolution post-pinching

The distance between the tips of the receding cones was calculated in IDL for all 40 liquid pinch-offs and the results show that the tips recede with a temporal exponent of 1/3. Shown in Fig. 7 is one post-pinching event for illustration. The average rate constant for the separation process is 3.46 $\mu\text{m s}^{-1/3}$, with a standard deviation of 1.34 $\mu\text{m s}^{-1/3}$. The theoretically calculated rate constant for receding liquid cones is 3.31 $\mu\text{m s}^{-1/3}$ using $f(0) = 1.3$ for $\theta_c = 38°$. This choice is based on the assumption that the interface shape after pinching is set by the physical observed shape before pinching. The theoretically predicted value is only 5% less than the measured value. (Due to the larger temporal resolution used in the experiments for the sample that contained solid pinching events, the solid rod post-pinching rate constants were not calculated.)

The good agreement between theory and experiment after pinching shows that the shape after pinching is set by the universal shape prior to pinching, even though we cannot describe the evolution very close to the pinching event because the quasi-stationary approximation breaks down. Although the kinetics match the theory quite well, the post-pinching shape deviates from the theoretical shape relatively quickly and thus we did not compare the shapes as with the pre-pinching shape. This shows, as with the pre-pinching case, that the kinetics predicted by the similarity solution hold very well despite the interfacial morphology differing from that predicted by theory.

4. Conclusions

The dynamics of rods pinching by diffusion either inside the rod or in the surrounding matrix were examined. Self-similar shapes and the dynamics of the pinching process, prior to and after pinching, were determined theoretically and compared to experiment. From the excellent agreement between theory and experiment, we conclude the following.

- Sufficiently close to the pinching point, the pinching process, both prior to and after pinching, is universal. The shape of the interface is independent of the materials system and initial conditions. The dynamics are described by unique temporal power laws.
- The shape of the interface after pinching is fixed by the universal shape prior to pinching, despite the breakdown of the similarity solution very close to the pinching point.
- The dynamics of the pinching process are described well by the theoretically predicted power laws surprisingly far from the pinching point.

Using these results, it is possible to estimate the time required for a wide range of microstructures to break-up by capillary-driven bulk diffusion. Such two-phase mixtures include dendritic solid–liquid mixtures, rod-like eutectics and bicontinuous two-phase mixtures, such as those found following spinodal decomposition in polymer blends.

Acknowledgements

This work was partially supported by NSF RTG Grant DMS-0636574 (L.K.A.). M.J.M. acknowledges support from US National Science Foundation RTG grant DMS-0636574 and NSF Grant DMS-0616468. A.E.J., J.L.F. and P.W.V. acknowledge the US Department of Energy, Grant DE-FG02-99ER45782, for financial support, and J.L.F. also acknowledges the National Science Foundation Graduate Research Fellowship. E.M.L. and S.O.P acknowledge the Danish National Research Foundation for supporting the Center for Fundamental Research: Metal Structures in 4D, within which part of this work was performed. The authors thank the Paul Scherrer Institut for beamtime at the TOMCAT beamline. We would also like to thank Gordan Mikuljan from the TOMCAT team for his technical expertise during the initial setup of the experiments at the beamline.

References

[1] Cline HE. Acta Metall Mater 1971;19(6):481.
[2] Nakagawa YG, Weatherly GC. Acta Metall Mater 1972;20(3):345.
[3] Majumdar B, Chattopadhyay K. Metall Mater Trans A 1996;27(7):2053.
[4] Liu HY, Li Y, Jones HJ. Mater Sci 1998;33(5):1159.
[5] Toimil-Molares ME, Balogh AG, Cornelius TW, Neumann R, Trautmann C. Appl Phys Lett 2004;85(22):5337.
[6] Karim S, Toimil-Molares ME, Balogh AG, Ensinger W, Cornelius TW, Khan EU, et al. Nanotechnology 2006;17(24):5954.
[7] Qin Y, Lee SM, Pan A, Gosele U, Knez M. Nano Lett 2008;8(1):114.
[8] Kattamis TZ, Coughlin JC, Flemings MCT. Metall Soc AIME 1967;239(10):1504.
[9] Chernov AA. Kristallografiya 1956;65:567.

[10] Schwarz M, Karma A, Eckler K, Herlach DM. Phys Rev Lett 1994;73(10):1380.

[11] Terzi S, Salvo L, Suery M, Dahle AK, Boller E. Acta Mater 2010;58(1):20.

[12] Nichols FA, Mullins WWT. Metall Soc AIME 1965;233(10):1840.

[13] Wong H, Miksis MJ, Voorhees PW, Davis SH. Scr Mater 1998;39(1):55.

[14] Bernoff AJ, Bertozzi AL, Witelski TP. J Stat Phys 1998;93(3–4):725.

[15] Keller JB, Miksis MJ. SIAM J Appl Math 1983;43(2):268.

[16] Eggers J. Phys Rev Lett 1993;71(21):3458.

[17] Chen YJ, Steen PH. J Fluid Mech 1997;341:245.

[18] Day RF, Hinch EJ, Lister JR. Phys Rev Lett 1998;80(4):704.

[19] Zhang WW, Lister JR. Phys Rev Lett 1999;83(6):1151.

[20] Cohen I, Brenner MP, Eggers J, Nagel SR. Phys Rev Lett 1999;83(6):1147.

[21] Leppinen D, Lister JR. Phys Fluids 2003;15(2):568.

[22] Sierou A, Lister JR. Phys Fluids 2004;16(5):1379.

[23] Maris HJ. Phys Rev E 2003;67(6):066309.

[24] Ishiguro R, Graner F, Rolley E, Balibar S. Phys Rev Lett 2004;93(23):235301.

[25] Aagesen LK, Johnson AE, Fife JL, Voorhees PW, Miksis MJ, Poulsen SO, et al. Nat Phys 2010;6(10):796.

[26] Abramowitz M, Stegun IA. Handbook of mathematical functions with formulas, graphs, and mathematical tables. National Bureau of Standards Applied Mathematics Series 55. Washington, DC: US Dept. of Commerce: U.S.G.P.O.; 10th printing, with corrections ed.; 1972.

[27] Mendoza R, Alkemper J, Voorhees PW. Metall Mater Trans A 2003;34(3):481.

[28] Murray JL. Al–Cu binary phase diagram. In: Okamoto H, editor. Desk Handbook: Phase Diagrams for Binary Alloys. Materials Park (OH): ASM International; 2000. p. 29.

[29] Mendoza R, Thornton K, Savin I, Voorhees PW. Acta Mater 2006;54(3):743.

[30] Stampanoni M, Groso A, Isenegger A, Mikuljan G, Chen Q, Bertrand A, et al. Trends in synchrotron-based tomographic imaging: the SLS experience. Develop X-Ray Tomogr V 2006;6318:U199.

[31] Fife JL. Three-dimensional characterization and real-time interface dynamics in aluminum–copper dendritic microstructures. Ph.D. Thesis, Northwestern University; 2009. <http://ostwald.ms.northwestern.edu/thesis.html>.

[32] Ludwig O, Dimichiel M, Salvo L, Suery M, Falus P. Metall Mater Trans A 2005;36A(6):1515.

[33] Limodin N, Salvo L, Suery M, DiMichiel M. Acta Mater 2007;55(9):3177.

[34] Limodin N, Salvo L, Boller E, Suery M, Felberbaum M, Gailliegue S, et al. Acta Mater 2009;57(7):2300.

[35] Aagesen LK, Fife JL, Lauridsen EM, Voorhees PW. Scr Mater 2010;64(5):394.

[36] Gunduz M, Hunt JD. Acta Metall Mater 1985;33(9):1651.